

UNIVERSITY OF
BIRMINGHAM

Recycling the Anode from Electric Vehicle Lithium Ion Batteries for a Circular Economy

by

Alexander Thomas Sargent

Supervisors: Dr. Phoebe Allan and Prof. Peter Slater

A thesis submitted to The University of Birmingham for the degree of Doctor of Philosophy

The School of Chemistry
College of Engineering and Physical Science
The University of Birmingham
April 2024

UNIVERSITY OF BIRMINGHAM

University of Birmingham Research Archive
e-theses repository



This unpublished thesis/dissertation is under a Creative Commons Attribution 4.0 International (CC BY 4.0) licence.

You are free to:

Share — copy and redistribute the material in any medium or format

Adapt — remix, transform, and build upon the material for any purpose, even commercially.

The licensor cannot revoke these freedoms as long as you follow the license terms.

Under the following terms:



Attribution — You must give appropriate credit, provide a link to the license, and indicate if changes were made. You may do so in any reasonable manner, but not in any way that suggests the licensor endorses you or your use.

No additional restrictions — You may not apply legal terms or technological measures that legally restrict others from doing anything the license permits.

Notices:

You do not have to comply with the license for elements of the material in the public domain or where your use is permitted by an applicable exception or limitation.

No warranties are given. The license may not give you all of the permissions necessary for your intended use. For example, other rights such as publicity, privacy, or moral rights may limit how you use the material.

Unless otherwise stated, any material in this thesis/dissertation that is cited to a third-party source is not included in the terms of this licence. Please refer to the original source(s) for licencing conditions of any quotes, images or other material cited to a third party.

“This for everybody going through tough times Believe me,

been there, done that

But every day above ground is a great day,

remember that.

— **PitBull**

American Rapper

Abstract

Lithium ion batteries are a vital part towards a decarbonised future. However, contained within are materials of critical importance, these include: cobalt, nickel, lithium, phosphorous and graphite (both synthetic and natural). Recycling of lithium ion batteries is essential to both ease the pressure on these unstable feedstocks and to ensure lithium ion batteries are sustainable. An often overlooked critical material within industry is graphite. This is due to the current economically low value of the material, however it's monopolised supply chain and large greenhouse output warrants the case for graphite recycling. Another sentiment for graphite recycling is the specialist grade required for lithium ion batteries, requiring many energy taxing processing steps to create spherical, pitch coated particles for the anode. Academic research on graphite recovery mainly focuses on the extraction of graphite for use in alternative applications despite it being the active anode material in the vast majority of lithium-ion batteries. This is derived from the concept that use within a battery induces significant deterioration, including particle cracking and exfoliation.

Within this thesis, the quality of anode material recovered from cells of various states of health will be analysed in order to determine whether this material could act as a future source for battery-grade graphite. After which, a method to reclaim and reuse this graphite will be developed.

Cells used within this work include quality control rejected, Envision AESC, first generation lithium ion pouch cells, and used (to various states of health) end of life lithium ion pouch cells obtained from a first generation electric Nissan Leaf.

The findings show that under normal and over-normal use, the graphite shows no substantial ageing. Degradation on the anode primarily occurs via solid electrolyte interface growth, metal deposition and particle disconnection. These factors can be easily addressed by recycling, rejuvenating and re-coating the anode. Therefore further focus was given to establishing a sustainable, quick and cost effective technique to extract and reuse the graphite for electrochemical use.

The difficulty in recycling graphite lies with the poly(vinylidene difluoride) binder. Poly(vinylidene difluoride) lacks solubility in non-harmful solvents making it difficult to separate the graphite from the other anode components. Within this work, it was found that when a discharged cell is dismantled, trace amounts of lithiated graphite remained in the anode. This lithiated graphite will react with water to produce hydrogen when submerged in water, which creates localised area of heat and pressure that can cleave the active material away from the current collector. The technique requires only water and its efficiency can be altered by increasing the time the anode is exposed to air. With increased air exposure, lithiated graphite will react with the moisture in the air and reduce the amount of hydrogen gas produced when submerged in water, decreasing the effectiveness of the delamination.

After delamination, the copper current collector was left bare and ready to collect, although with an oxidised surface. Anode active material (containing the graphite) could also be collected as large sheets. Lithium could be extracted from the delamination solution using sodium carbonate and phosphoric acid. As a proof of concept, ($0.14\,\mathrm{g}$ of $\mathrm{Li_2CO_3}$ and $0.34\,\mathrm{g}$ of $\mathrm{Li_3PO_4}$ were extracted from an end of life anode weighing $13.5\,\mathrm{g}$.

Water delamination also cleaned the graphite surface of most contaminates, although the poly(vinylidene difluoride) binder and metal contamination still remained. Annealing to $500\,^{\circ}\mathrm{C}$ removed the binder and produced graphitic material similar to virgin battery-grade graphite. This recovered graphite was used to create second-life anodes, whose electrochemical performance was tested. Half cell performance showed that graphite

recovered from a cell with only 30% of its original capacity could perform close to the theoretical capacity of graphite after water delamination and annealing. This demonstrates that End-of-Life lithium ion batteries can provide high-performing battery-grade graphite, helping to secure future supplies of this critical raw material and alleviating concerns over future accumulation of battery waste.

Water delamination was ineffective after exposing the anodes to air for more than four weeks. It was found that the use of acids allowed for an extended period of delamination that provided graphite of similar quality.

Up-cycling of the graphite material was attempted via delamination within colloidal silica. Here, nanoparticles of silica would coat the graphite allowing for increased capacity during second life use. However, the deposited silica particles were too large to be electrochemically active and therefore future avenues for optimising this procedure are suggested.

Acknowledgements

I extend my deepest gratitude to my family, whose support has been the cornerstone of my journey. Their patience and encouragement have been a constant source of strength for me. To the friends I have made and lost along the way, I owe a debt of gratitude. Each interaction, whether fleeting or enduring, has left an indelible mark on my life. A special mention goes to those from floor 5, whose camaraderie and support have been instrumental in sustaining me through this project.

My heartfelt appreciation also goes to my esteemed supervisors, Phoebe Allan and Peter Slater, whose wisdom and steadfast guidance have been pivotal in navigating the complexities of my project. I am equally indebted to the post-doctoral community on floor 5, including Abbey Jarvis, Emily Giles, and Laura Driscoll, as well as Rob Sommerville from the School of Metallurgy and Materials. Their collective expertise and collaboration have played an integral role in realising the fruition of my ideas.

Lastly, I extend my thanks to the organisers of the ReLiB project and all its contributors, particularly Paul Anderson. The passions shown have illuminated the broader significance of my project, igniting a deeper sense of purpose and enthusiasm.

Contents

Abstract iv

Acknowledgements vii

1 Introduction **1**

1.1 Lithium ion batteries 1

1.1.1 An emerging technology 1

1.1.2 Fundamentals 2

1.1.3 Components 4

1.1.4 Thermodynamics 5

1.1.5 First generation Nissan Leaf components 7

1.1.6 Cathode and anode active material 9

1.2 Transition to net zero 14

1.3 End-of-Life lithium ion batteries 16

1.3.1 Cell ageing 16

1.3.2 Electric vehicle ageing 18

1.3.3 The need for recycling 18

1.4 Current recycling methods 19

1.4.1 Industrial Recycling 19

1.4.2 Lack of anode recycling 21

1.5 Current anode recycling 22

1.6 Chapter conclusion 24

2 Project aims **25**

3 Experimental theory **27**

3.1 Raman spectroscopy 27

3.1.1 Fundamentals 27

3.1.2 Raman active vibrations in crystal structures and graphite 29

3.1.3 Instruments 37

3.2 Scanning electron microscopy and energy dispersive X-rays 38

3.2.1 Fundamentals 38

3.2.2 Instruments 40

3.3 X-ray photoelectron spectroscopy 43

3.3.1 Fundamentals 43

3.3.2 Spectral analysis 44

3.3.3 Chemical environments 47

3.3.4 Hard X-ray photoelectron spectroscopy 48

3.3.5 Instruments 48

3.4 X-ray diffraction 50

3.4.1 Fundamentals 50

3.4.2 Pattern analysis 55

3.4.3 Instruments 57

3.5 Inductively coupled plasma - optical emission spectrometry 59

3.5.1 Fundamentals and instrument 59

3.5.2 Data collection 60

3.6 Particle size analysis 61

3.6.1 Fundamentals 61

3.6.2 Instruments 63

3.7 Thermal gravimetric analysis . . . 64
3.8 Electrochemistry . . . 64
3.8.1 Half-cells . . . 64
3.8.2 Galvanostatic analysis . . . 65
3.8.3 Differential capacity . . . 69
3.8.4 Other electrochemical procedures . . . 70

4 Anode materials entering the recycling stream 72
4.1 Disclaimer . . . 72
4.2 Introduction . . . 72
4.3 Chapter aim . . . 74
4.4 Experimental . . . 75
4.4.1 Dismantling, storage and handling of anode materials . . . 75
4.4.2 Inert atmosphere Raman experimental . . . 75
4.4.3 SEM, EDX, and cross-sectional analysis . . . 78
4.4.4 XPS and HAXPES experimental . . . 79
4.4.5 PXRD experimental . . . 80
4.5 Inert atmosphere studies . . . 81
4.5.1 Bulk Raman study . . . 81
4.5.2 SEM, EDX and a cross-sectional study . . . 88
4.5.3 XPS and HAXPES surface study . . . 96
4.5.4 PXRD analysis of graphite . . . 105
4.6 Air exposed studies . . . 109
4.6.1 Air exposure changes through SEM . . . 110
4.6.2 Changes to XPS and HAXPES . . . 113
4.7 Chapter conclusions . . . 120

4.8 Chapter appendix 121

5 Obtaining graphite via water delamination 123

5.1 Disclaimer 123

5.2 Introduction 123

5.3 Chapter aims 126

5.4 Experimental 126

5.4.1 Water delamination process 126

5.4.2 ICP-OES 127

5.4.3 Lithium recovery experimental 128

5.4.4 Delaminated Material PXRD and XPDF Analysis 129

5.4.5 Delaminated material Raman analysis 129

5.4.6 XPS analysis of delaminated material 130

5.4.7 SEM image collection 130

5.4.8 Graphite PSA analysis 130

5.5 Water delamination 131

5.5.1 Delamination efficiency 132

5.6 Lithium recovery 136

5.7 Quality of the copper current collector 142

5.8 Study of the recovered film 146

5.8.1 Raman analysis 146

5.8.2 XPS and HAXPES 150

5.8.3 SEM analysis 160

5.8.4 PSA analysis 161

5.9 Chapter conclusions 163

5.10 Chapter appendix 165

6 Reuse of recovered graphite **171**

6.1 Disclaimer . . . 171

6.2 Introduction . . . 171

6.3 Chapter aims . . . 172

6.4 Experimental . . . 173

6.4.1 TGA study . . . 173

6.4.2 Graphite treatment . . . 173

6.4.3 Electrochemical data collection . . . 174

6.4.4 Graphite characterisation . . . 175

6.5 Recasting recovered EoL graphite . . . 176

6.6 Improving performance of EoL graphite . . . 181

6.6.1 Further processing . . . 181

6.6.2 Electrochemical performance . . . 188

6.7 Reuse of all recovered anode material . . . 192

6.7.1 Annealing recovered anode materials . . . 192

6.7.2 Electrochemical performance . . . 195

6.7.3 Long term cycling . . . 198

6.8 Chapter conclusion . . . 203

6.9 Chapter appendix . . . 204

7 Acid delamination **208**

7.1 Introduction . . . 208

7.2 Chapter Aims . . . 209

7.3 Experimental . . . 209

7.3.1 Acid delamination procedure and ICP analysis . . . 209

7.3.2 Graphite characterisation . . . 210

7.3.3 Electrochemical data collection . . . 210
7.4 Delamination . . . 210
7.5 Recovered active material . . . 213
7.6 Electrochemical performance . . . 216
7.7 Chapter conclusion . . . 220

8 Colloidal silica delamination 222

8.1 Introduction . . . 222
8.2 Chapter aim . . . 225
8.3 Experimental . . . 225
8.3.1 Colloidal silica delamination procedure . . . 225
8.3.2 Graphite treatment . . . 226
8.3.3 Graphite characterisation . . . 226
8.3.4 Electrochemical data collection . . . 226
8.4 Colloidal silica delamination . . . 227
8.4.1 Delamination . . . 227
8.4.2 TGA of recovered material . . . 227
8.4.3 Electrochemical performance . . . 228
8.4.4 SEM images . . . 231
8.5 Steps to improvement . . . 234
8.5.1 SEM images . . . 234
8.5.2 Electrochemical performance . . . 235
8.6 Chapter conclusion and future work . . . 238
8.7 Chapter appendix . . . 240

9 Overall discussion 243

10 Conclusion and future work **247**

10.1 Conclusion 247

10.2 Future work 249

11 Publication list **252**

12 References **253**

List of Figures

1.1 Diagram of a lithium ion battery 3

1.2 Common commercial lithium ion battery cell designs 5

1.3 Energy diagram for a working battery 7

1.4 Generation 1 Nissan Leaf battery pack breakdown 8

1.5 Layered rock salt unit cell 9

1.6 Graphite and lithiated graphite unit cell 11

1.7 Schematic of a graphite particle 12

1.8 Lithiation staging mechanisms in graphite 13

1.9 Electrification using lithium ion batteries 15

1.10 Ageing mechanisms within lithium ion batteries 17

1.11 Current industrial lithium ion battery recycling 20

1.12 Circular economy schematic 21

3.1 Rayleigh scattering, Stokes and anti-Stokes shift 28

3.2 CO_2 vibrational modes 29

3.3 Vibrational modes of graphene and graphite 31

3.4 Raman graphitic peaks 32

3.5 Scattering mechanisms for Raman modes in graphene 34

3.6 Raman instrument schematic 37

3.7 Escape depth of various interaction signals 39

3.8 SE, BSE and EDX atomic interactions 40

3.9 SEM instrument schematic . . . 41
3.10 Schematic diagram of photo-electron emission . . . 43
3.11 XPS survey, $C\ 1s$, $S\ 2p$ and $Mn\ 2p$ scans . . . 45
3.12 XPS instrument schematic . . . 49
3.13 Graphite unit cell . . . 50
3.14 Lattice planes and their Miller indices . . . 51
3.15 Wave diffraction . . . 52
3.16 Bragg diffraction . . . 54
3.17 Graphite PXRD pattern . . . 54
3.18 PXRD instrument schematic . . . 58
3.19 Schematic diagram of the ICP torch . . . 60
3.20 Rayleigh and Mie scattering . . . 62
3.21 A schematic of a PSA . . . 63
3.22 Phase transitions of graphite during lithium intercalation . . . 68
3.23 Phase transitions on a dQ/dV plot . . . 70

4.1 Bulk Raman analysis method . . . 76
4.2 Graphite Raman peak fit used for analysis . . . 77
4.3 QCR II and EoL III bulk Raman spectra . . . 81
4.4 Bulk I_D/I_G histogram plots for QCR II and EoL III . . . 83
4.5 *P. Attidekou et al.*'s thermal study . . . 86
4.6 SEM images of anode materials after cell dismantlement . . . 88
4.7 Cross sectional SEM images of anode materials after cell dismantlement . . . 90
4.8 EDX mapping of anode materials after cell dismantlement . . . 92
4.9 EDX mapping of the cross sections of anode materials after cell dismantlement 93
4.10 $C1s$ XPS and HAXPES spectra obtained for anodes after dismantlement . . . 97

4.11 F 1s XPS and HAXPES spectra obtained for anodes after dismantlement . . 100
4.12 Mn 2p XPS and HAXPES spectra obtained for anodes after dismantlement . 101
4.13 In-house PXRD patterns for all anodes 106
4.14 Synchrotron PXRD patterns for all anodes 108
4.15 SEM images of air exposed anodes 112
4.16 C 1s XPS and HAXPES spectra obtained for anodes after air exposure . . . 115
4.17 F $1s$ XPS and HAXPES spectra obtained for anodes after air exposure . . . 116
4.18 EDX mapping of the DMC washed anode materials after cell dismantlement 122

5.1 Water delamination 132
5.2 Water delamination efficiency 133
5.3 Li concentrations of delamination water, analysed using ICP 134
5.4 Lithium extraction from delamination water 137
5.5 XRD of recovered lithium salts 141
5.6 Copper current collector after delamination 142
5.7 Full sheet of copper current collector 143
5.8 Copper current collector Raman analysis 145
5.9 Raman spectra of anode active material before and after water delamination 147
5.10 Raman histograms for anode active material before and after delamination . 149
5.11 $C\ 1s$ XPS spectra obtained for anodes after water delamination 151
5.12 $C\ 1s$ HAXPES spectra obtained for anodes after water delamination 153
5.13 SEM images of anode active material before and after water delamination . 161
5.14 Particle size distributions for recovered active material 162
5.15 Oxidation tests on pristine copper foil 165
5.16 SEM images of pristine copper foil 165
5.17 More Raman spectra of anode active material before and after delamination 166

5.18 Raman spectra of MAGE3 graphite 167
5.19 QCR XPS survey scan 167
5.20 More SEM images of anode active material before and after delamination . . 168
5.21 Elemental mapping of recovered EoL after delamination 169
5.22 More particle size distributions for recovered active material 170

6.1 Mass loss of PVDF, EoL and annealed EoL studied with TGA 176
6.2 Cycling performance of recovered EoL compared to MAGE3 177
6.3 Voltage profiles and dQ/dV plots of EoL and MAGE3 180
6.4 SEM images of EoL after NaOH hydrothermal decomposition and annealing 183
6.5 Raman spectra of NaOH hydrothermal decomposed and annealed EoL . . . 185
6.6 XRD patterns of NaOH hydrothermal decomposed and annealed EoL 187
6.7 Cycling performance of NaOH hydrothermal decomposed and annealed EoL 188
6.8 Voltage profiles and dQ/dV plots of NaOH hydrothermal decomposed and annealed EoL 191
6.9 SEM images of annealed anode active material 193
6.10 Raman I_D/I_G ratios of annealed anode active material 195
6.11 Cycle performance of annealed anode active material against MAGE3 . . . 197
6.12 Long term cycling performance of annealed active materials against MAGE3 201
6.13 Voltage profiles and dQ/dV plots for the long term cycling of EoL and MAGE3 202
6.14 Elemental mapping of annealed EoL III 204
6.15 More SEM images of annealed anode active material 205
6.16 Raman spectra for each annealed anode active material 205
6.17 Voltage profiles for QCR II 206
6.18 Voltage profiles for EoL 206
6.19 Voltage profiles for EoL II 207

6.20 Voltage profiles for EoL III 207

7.1 Ionic concentrations of acid delamination solution, analysed with ICP 211
7.2 SEM images of anode active material after acid delamination 214
7.3 Raman spectra of acid delaminated anode active material 215
7.4 Cycle performance of annealed acid delaminated anode active material . . . 218
7.5 Voltage profiles and dQ/dV plots of annealed acid delaminated anode active material 219

8.1 Voltage profiles of EoL delaminated in colloidal silica 229
8.2 dQ/dV plots of EoL delaminated in colloidal silica 231
8.3 SEM images of EoL delaminated in colloidal silica 233
8.4 SEM images of colloidal silica delaminated EoL after annealing and ball milling 234
8.5 Voltage profiles of improved colloidal silica delaminated EoL 237
8.6 Mass loss of colloidal silica delaminated EoL, studied with TGA 240
8.7 dQ/dV plots of colloidal silica delaminated EoL 241
8.8 Magnified SEM images of EoL delaminated in colloidal silica 242

List of Tables

3.1 Character table for point group D_{6h} 36

3.2 XPS and HAXPES peak constraints 47

4.1 Anode materials used within thesis 74

4.2 EDX Atomic percentages of anode materials after cell dismantlement 91

4.3 Chemical compositions within XPS and HAXPES data for anodes prior to air exposure and DMC washing 103

4.4 Atomic compositions within XPS and HAXPES data for anodes prior to air exposure and DMC washing 104

4.5 Anode crystallographic data extracted from in-house XRD 107

4.6 Anode crystallographic data extracted from synchrotron XRD 109

4.7 Chemical compositions within XPS and HAXPES data for anodes after air exposure 118

4.8 Atomic compositions within XPS and HAXPES data for anodes after air exposure 119

5.1 Quantitative EDX data of recovered copper current collector 145

5.2 XPS chemical compositions for recovered anode films 156

5.3 HAXPES chemical compositions for recovered EoL anode film 157

5.4 XPS atomic compositions for recovered anode films 158

5.5 HAXPES atomic compositions for recovered EoL anode film 159

5.6 Particle size distributions collected via PSA 163

6.1 Characteristics of electrodes used for the recovered anode active material electrochemical study 175
6.2 Quantitative electrochemical data for recovered EoL 178
6.3 Quantitative electrochemical data for recovered EoL with post-treatment . . 189
6.4 Quantitative electrochemical data for all recovered and annealed anode materials 196
6.5 Quantitative electrochemical data for recovered and annealed anode materials during long term testing 199

7.1 Characteristics of electrodes used for the acid delamination electrochemical study 210
7.2 Quantitative electrochemical data for recovery using acid delamination . . . 216

8.1 Quantitative electrochemical data for all recovered and annealed anode materials 227
8.2 Percentage of PVDF in colloidal silica delaminated EoL samples 228
8.3 Quantitative cycling data of colloidal silica delaminated EoL 230
8.4 Quantitative cycling data of improved colloidal silica delaminated EoL 235

Acronyms

BM black mass

BSE back scattered electrons

CB carbon black

CCD charge coupled device

CE coloumbic efficiency

CMC carboxymethyl cellulose

DEC diethyl carbonate

DI deionised

DIA dynamic image analysis

DMC dimethyl carbonate

DMI dimethyl isosorbide

DMSO dimethyl sulfoxide

EC ethylene carbonate

EDX energy dispersive X-rays

EoL End-of-Life

ESS energy storage systems

EV electric vehicles

FWHM full width at half maximum

gen-1 first-generation

HAXPES hard X-ray photoelectron spectroscopy

HOMO highest occupied molecular orbital

ICE internal combustion engine

ICP inductively coupled plasma

ICP-OES inductively coupled plasma – optical emission spectrometry

LDA laser diffraction analysis

LiB lithium ion battery

LUMO lowest unoccupied molecular orbital

NG natural flaked graphite

PC propylene carbonate

PSA particle size analysis

PVDF poly(vinylidene fluoride)

PXRD powder X-ray diffraction

QCR quality-control-rejected

SBR styrene-butadiene rubber

SE secondary electrons

SEI solid electrolyte interface

SEM scanning electron microscopy

SG synthetic graphite

SoH state-of-health

TM transition metal

XPS X-ray photoelectron spectroscopy

CHAPTER 1

Introduction

1.1 | Lithium ion batteries

1.1.1 An emerging technology

The first lithium ion battery (LiB), using lithium against iodine, was a primary battery created to satisfy the need for a long-lasting, high energy and specifically dense battery, required for implantable cardiac pacemakers. Originally a primary zinc-mercury battery was used, however, this created heavy and bulky pacemakers that needed replacing every two years, requiring an invasive operation, amounting to large stresses for the patient. The lithium-iodine powered pacemakers provided significant comfort to the patient as well as increased efficiency and operational life (lasting 6 to 7 years).[1,2]

Riding the success of the lithium-iodine battery further developments into other lithium battery technologies were explored in order to advance military and consumer electronics. Initially, advances included changing the cathode chemistry to create higher-capacity batteries, however, the real breakthrough was to create a secondary (rechargeable) battery. Changing the active cathode material to an intercalating structure allowed lithium to be released and accepted by the same electrode. Here the structure acts as a host framework in which the working cation can reversibly be removed. Multiple battery chemistries were proposed, but it wasn't until the highly reactive, volume-changing lithium metal anode was

replaced by graphite, that these batteries saw commercial use.[2–5] Founded through the collaborative work of John Goodenough, Stanley Whittingham and Akira Yoshino, winning them the Nobel Prize in chemistry in 2019, the LCO ($LiCoO_2$) - Graphite battery found great success after its initial commercial release by Sony in 1991.[2–9]

LiBs have allowed for an exponential increase in both the amount of portable electronics and their technical capabilities. $16\,\%$ of households in the UK owned a mobile phone in 1996, increasing to $80\,\%$ in 2006.[10] Capabilities of phones have increased, switching from a basic, call and text only Nokia "brick" to advanced smart devices such as the iPhone, commercially launched in 2007.[11] This has resulted in a rampant demand for more, and more energy dense LiBs summing $> 2,000$ million units of LiBs for portable electronics in 2016.[12]

1.1.2 Fundamentals

Figure 1.1 illustrates a schematic reminiscent of the initial cell design employed in the inaugural commercial battery. The battery is comprised of four pivotal components: the cathode and anode, both electronic and ionic conductive; also in the battery is the separator and electrolyte, which both support ionic conduction while maintaining electronic isolation.[9]

The cathode (on the left) consists of an aluminium current collector and $LiCoO_2$ active material. Poly(vinylidene fluoride) (PVDF) is used as a binder and carbon black (CB) would be used to increase the conductivity. The anode (on the right) consists of a copper current collector, graphite active material, a PVDF binder and CB. In newer generations, a mix of carboxymethyl cellulose (CMC) and styrene-butadiene rubber (SBR) is used as a binder. Inert, porous, and thin materials are used as the separator, these typically consist of either single layer or multi-layer polymer sheets consisting of polypropylene (PP) and/or polyethylene (PE). Carbonates such as propylene carbonate (PC), diethyl carbonate (DEC) or ethylene carbonate (EC) are used as the electrolyte (typically a mixture) with a dissolved lithium salt like lithium hexafluorophosphate ($LiPF_6$) used for lithium ion transport.[2,8,13]

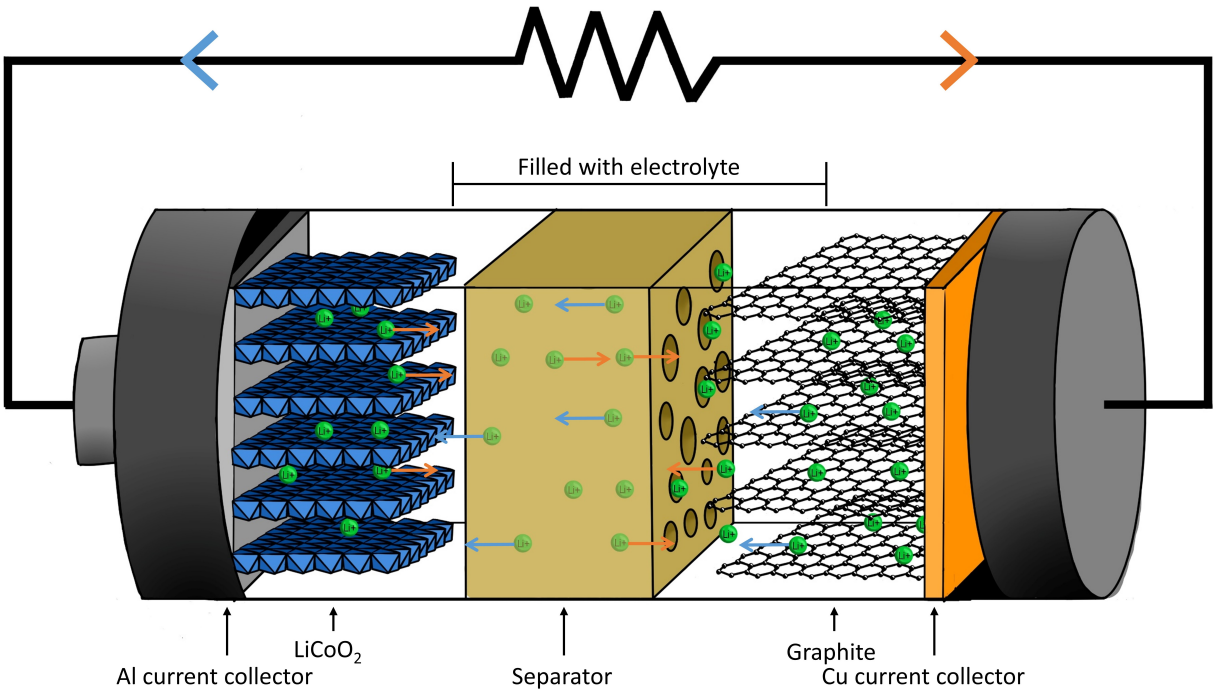


Fig. 1.1. *A simplified diagram of the inside of a lithium ion battery, only showing the major components and the flow of ions. Blue arrows represent both the flow of electrons and the flow of ions upon spontaneous discharge when connected to a circuit. The orange arrows represent that of the charging process.*

During charging, an external power source is used to remove the lithium from the $LiCoO_2$ framework (sometimes known as the "lithium source") and into the graphite ("lithium sink"). The power source delithiates the cathode by providing a potential, *i.e.* removing its electrons, and increasing the concentration of electrons on the anode. This charge imbalance can be countered by the transfer of lithium cations which can only flow through the battery, causing the lithiation of the graphite anode.[9] Once full capacity is reached, either when all lithium ions have transferred (inventory limited) or when all vacancies on the lithiating electrode are filled (site limited), polarisation occurs, idealistically increasing the resistance to infinite and halting the current.[14]

Once fully charged, the battery occupies a higher energy state. Consequently, upon attachment to an external circuit, the battery can spontaneously return to its ground state.

Accomplished by the transfer of lithium cations back to the cathode, which in turn propels the flow of electrons through the external circuit. In effect, stored chemical energy is converted to electrical.[15]

1.1.3 Components

Since the first commercial secondary lithium-ion battery design (shown in figure 1.1), only incremental variations to the chemistry have been made.

These include the addition of Ni and Mn to cathode metal oxide, reducing the amount of cobalt used and giving additional properties like more thermal stability. This has given a range of commercial nickel manganese cobalt oxide cathodes, for instance; NMC(532) ($Ni_{0.5}Mn_{0.3}Ni_{0.2}O_2$) (as used in second-generation Nissan Leaf electric vehicles), NMC(111) ($Ni_{0.33}Mn_{0.33}Ni_{0.33}O_2$) and NMC(811) ($Ni_{0.8}Mn_{0.1}Ni_{0.1}O_2$). Other commercial cathode chemistries also exist, for instance; LFP ($LiFePO_4$), LMO ($LiMn_2O$) and NCA ($LiNiCoAlO_2$).[16]

Separators are typically polymer sheets however ceramic coatings or fully ceramic separators have also been used, as well as glass microfibers for small scale laboratory use.[17]

Fine tuning of battery performance is commonly achieved with the addition of additives and coatings, for instance, sulfur containing polymers are added to breakdown and form an elastic coating on the anode. Pitch coatings are also added to the graphite to reduce first cycle loss, this leads to a multitude of intricate battery compositions.[18,19]

A variety of cell shapes and electrode stacking methods also exist. Cylindrical cells contain wound electrodes in a "jelly roll" stored within a cylindrical metal casing. Prismatic cells have electrodes that are either wound or folded within a rectangular metal case. Pouch cells use a vacuum sealed aluminium-polymer pouch containing stacked electrodes. Images of each are given in Figure 1.2.[20,21]

In contrast to all these differences, in almost all LiBs graphite makes up most of the anode active material, currently dominating the anode market shares by $96\,\%$. LTO ($Li_4Ti_5O_{12}$) makes up the other $4\,\%$.[22,23] More energy dense anode materials like lithium metal and silicon are promising additions, however, have yet to reach commercialisation due to stability issues within an electrochemical environment.[24]

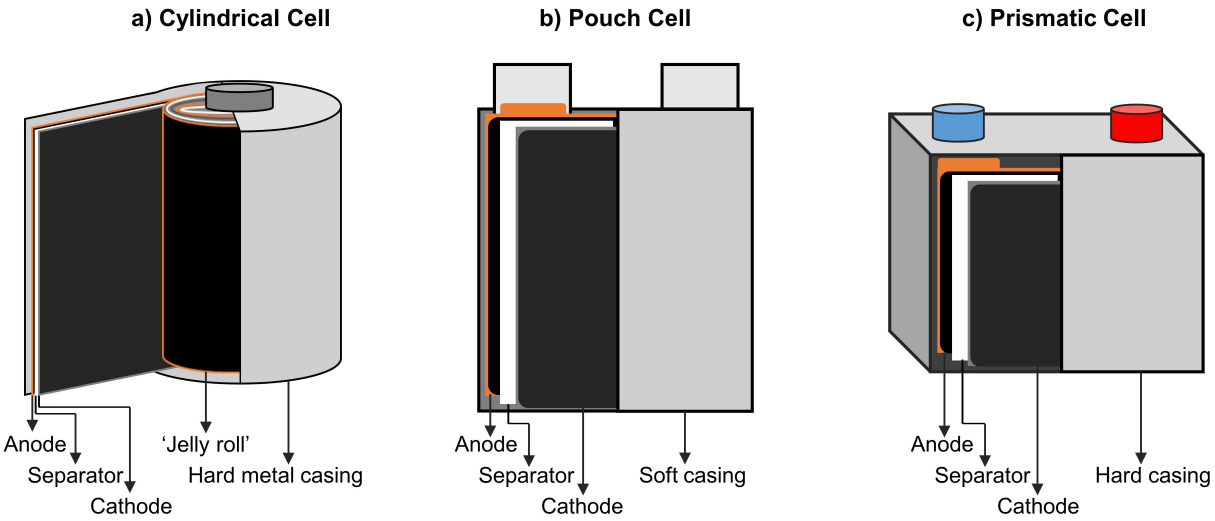


Fig. 1.2. *Common commercial LiB cell designs. a) cylindrical cell, b) pouch cell and c) prismatic cell.*

1.1.4 Thermodynamics

The main factor determining cathode and anode chemistry are the reductive potentials of the active materials on their constituent electrodes.[9] Typically, these potentials are found and quoted as a comparison to a standard secondary electrode like lithium metal (Li/Li^+). The Gibbs free energy determines whether a reaction is spontaneous (denoted by $-\Delta G^\circ$) under standard conditions and is given below:

$$\Delta G^\circ = -nFE^\circ \tag{1.1}$$

Where ΔG° is the change is Gibbs free energy, n is the number of moles of transferred electrons, F is the Faraday constant and E° is the standard electrode potential. The Faraday constant is defined as the elementary charge of 1 mol of electrons which can be written as $N_A e$ and is equal to $96485C$.[25]

Where the discharge process will have the spontaneous oxidation of the anode and spontaneous reduction of the cathode. Under non-standard conditions ΔG is given by:

$$\Delta G = \Delta G^\circ + RT \ln Q \tag{1.2}$$

Where R is the universal gas constant, T is temperature and Q is the reaction quotients.[25] By substituting the Gibbs free energy under standard conditions and expanding Q for a battery containing $\mathrm{LiCoO_2}$ and $\mathrm{C_6}$, the following is gained:

$$E = {E^\circ}_c - {E^\circ}_a + (RT)/F \ln \frac{[\mathrm{LiC_6}][\mathrm{CoO_2}]}{[\mathrm{C_6}][\mathrm{LiCoO_2}]} \tag{1.3}$$

This is the Nernst equation and gives the cell reduction potential (E).[25] In terms of chemical potentials of an anode (μ_a) and a cathode (μ_c), the Nernst equation can also be given as:

$$V_{OCV} = \frac{\mu_c - \mu_a}{e} \tag{1.4}$$

Where V_{OCV} is the open circuit voltage and e is the charge of an electron.[25] The terms μ_a and μ_c, expressed in electron volts (eV), denote the Fermi levels in a battery system. Under thermodynamic equilibrium, these energy levels correspond to states where there is a $50\,\%$ probability of occupancy. The difference between the Fermi levels in the cathode and the anode represents the voltage window.[9]

As the energy of a battery can be given by:

$$\text{Energy}(Wh) = \text{Capacity}(Ah) * \text{Voltage}(V) \tag{1.5}$$

Preferably, components are chosen to give as large of a voltage window as possible to increase the energy of the battery. However, the size of the voltage window is limited by the highest occupied molecular orbital (HOMO) and lowest unoccupied molecular orbital (LUMO) of the liquid electrolyte. A diagram of this is given in Figure 1.3. If the chemical potentials falls outside of this range, unwanted side reactions will occur between the electrode and the electrolyte.[9]

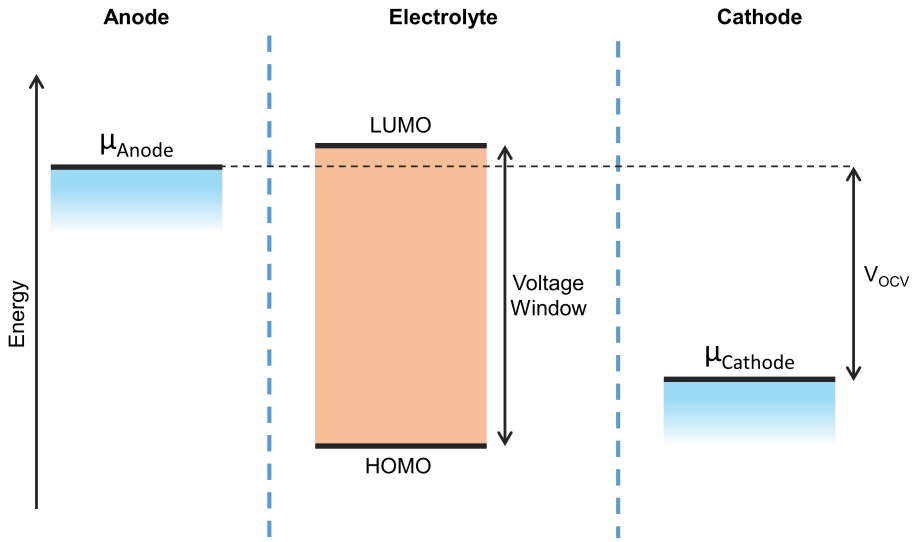


Fig. 1.3. *A simplistic energy diagram showing the voltage window and allowed open cell voltages between an anode and a cathode.*

Mechanical effects like expansion or heat production may also determine whether an electrode can be used.

1.1.5 First generation Nissan Leaf components

An early transition to electric transport was seen with the launch of the first-generation (gen-1) electric Nissan Leaf (2011-2017).[26] The 2017 Leaf contained a $22\,\mathrm{kW\,h}$ battery pack supporting a driving range of 155 mile but took $31\,\mathrm{h}$ to charge to full capacity.[26,27] As of writing, the modern electric vehicles (EV) contain a $69.7\,\mathrm{kW\,h}$ battery pack (on average) with top of the range EVs like the Lotus Eletre supporting a $109.0\,\mathrm{kW\,h}$ pack.[28] These packs also

take less time to charge due to improvements in chemistry, battery management systems and pack layout.

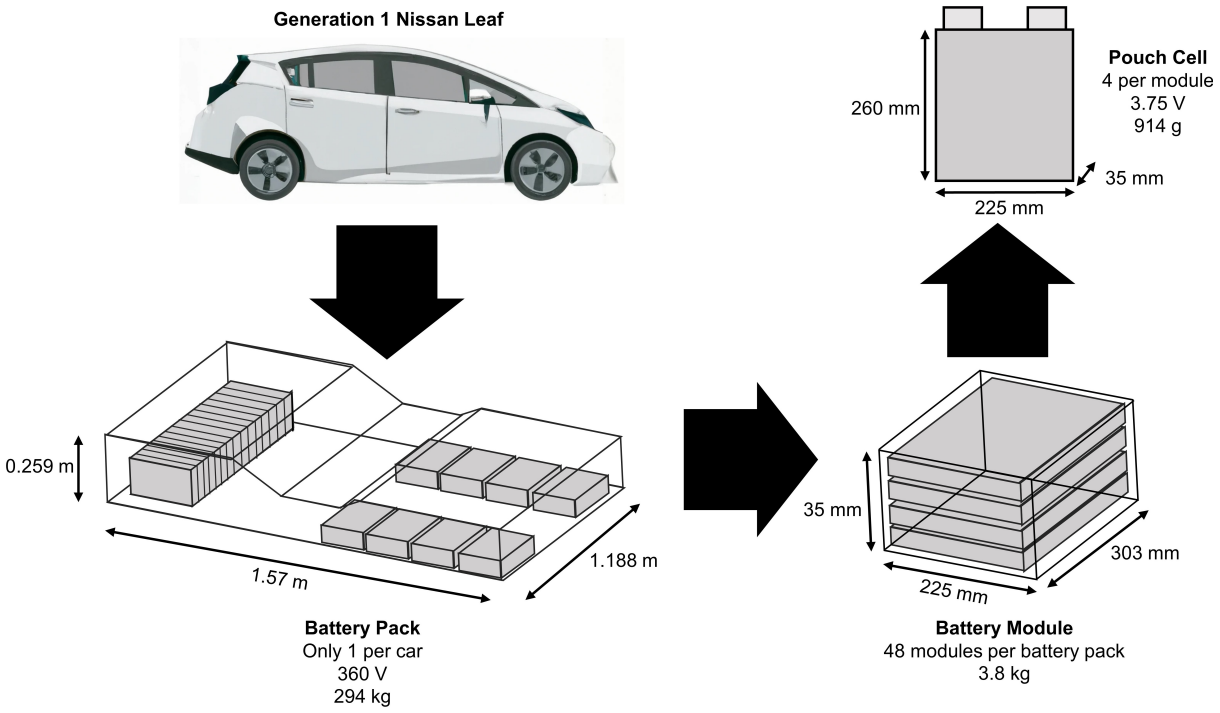


Fig. 1.4. *The breakdown of a gen-1,* $22\,\mathrm{kW\,h}$*, electric Nissan Leaf car into its battery pack, modules and cells. Pack information obtained from Harper et al.*[21]*.*

A breakdown of a gen-1 electric Nissan Leaf propulsion system is given in Figure 1.4. In this example, the $360\,\mathrm{V}$ battery pack weighs around $294\,\mathrm{kg}$ and contains 48 battery modules, a cooling system, various wiring and electrical components,a battery management system and a casing used to contain and protect the components.[21] Inside each module are four laminated aluminium pouch cells.[21] These pouch cells contained a mixed cathode chemistry of lithium manganese oxide (LMO) and lithium nickel cobalt manganese oxide (NMC) coated onto an aluminium current collector using a PVDF binder.[21,27,29,30] The electrolyte consist of an organic solvent with $\mathrm{LiPF_6}$ salt. A polymer separator is also used. The anode consisted of pitch coated sphericalised graphite coated onto a copper current

collector, again, using a PVDF binder. In all three components non-publicly disclosed additives were likely added.[27,29,30]

1.1.6 Cathode and anode active material

LMO ($LiMn_2O_4$) has a spinel structure, while NMC532 ($Ni_{0.5}Mn_{0.3}Ni_{0.2}O_2$) is an ordered layered rock-salt structure with a space group of $R\bar{3}m$. Both materials feature a close-packed array of oxygen atoms with alternating lithium and transition metal (TM) layers. The stacking sequence follows an ABC pattern, resulting in a hexagonal arrangement. In these structures, both the TMs and lithium occupy octahedral sites, with the TMs positioned in edge-sharing octahedral sites. The (de)intercalation of lithium ions during charge and discharge is facilitated by the redox activity of the TMs, with the lithium layers acting as channels for ion conductivity. The structure of the latter is given in Figure 1.5.[9,16]

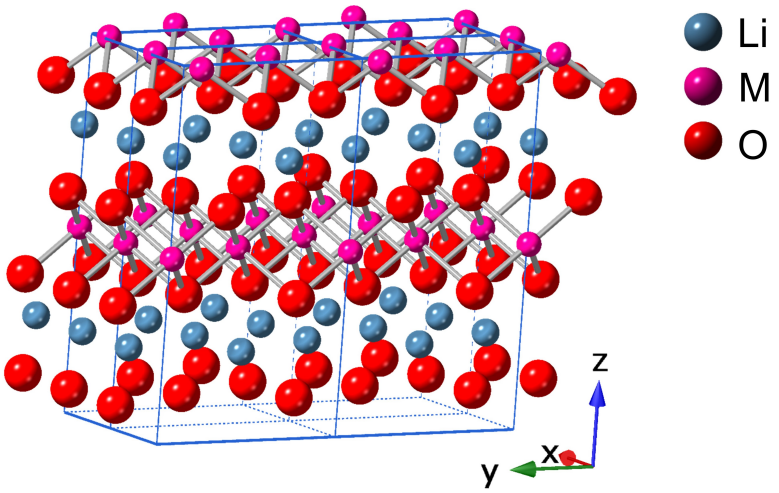


Fig. 1.5. *Layered rock salt structure of* $Ni_{0.5}Mn_{0.3}Ni_{0.2}O_2$ *a common cathode within LiBs. M refers to metal, in this case either manganese, cobalt or nickel.*

Graphite makes up the active material in the anode. Graphite is a three-dimensional structure of layered graphene sheets held together via van der Waals forces. Graphene sheets consist of a two-dimensional covalent sp^2 network of carbon atoms, forming a repeating lattice of 6 membered, hexagonal rings with a nearest neighbour atomic distance

of 1.42 Å and bond angles of $120°$. Each carbon atom is bound to three other carbon atoms via σ bonds within the same plane. The last remaining valence electron in each atom form a delocalised, conductive π band directly above and below the graphene layer. This π band leads to resonance stability, leading to increased van der Waals interactions between layers, enhanced conductivity of graphite, and creates additional quantum interactions, for instance the double resonance effect during Raman analysis. Graphene sheets stack vertically in the C axis, with an interlayer spacing of 3.35 Å for crystalline graphite. Two stacking orders exist for graphite; hexagonal close pack ($ABAB$) and rhombohedral (ABC), the former is more thermodynamically stable and typically makes up $80\,\%$ of natural flaked graphite (NG) with rhombohedral existing at $14\,\%$. The other $6\,\%$ exists as turbostatic stacking, here the layers stack with no long-range order and typically contain a large amount of rotational disorder. Another stacking arrangement of sheets called simple hexagonal (AAA) occurs upon intercalation of lithium between the sheets.[22,31,32] This shift in stacking leads to the observed staging mechanisms discussed later in this section. When graphite is fully lithiated, lithium ions occupy the space above and below the centre of every third hexagonal ring in the graphene layers, therefore, for every 6 carbon atoms one lithium atom can be hosted, leading to a complete lithiation of $\mathrm{LiC_6}$.[24]

The unit cells and extended structures of hexagonal, rhombohedral and lithium intercalated graphite are given in Figure 1.6. Hexagonal graphite is defined by a hexagonal unit cell with $a = 2.456$ Å, $c = 6.694$ Å and 4 carbon atoms. This arrangement conforms to the space group $P6_3/mmc$. Rhombohedral graphite also occupies a hexagonal unit cell, however not in line with the stacking direction. The unit cell contains 9 carbon atoms, unit cell parameters of $a = 2.566$ Å, $c = 10.062$ Å and falls within the $R\bar{3}m$ space group. Lithium intercalated graphite still falls within the $P6_3/mmc$ space group, however, unit cell parameters are $a = 4.305$ Å and $c = 3.706$ Å.[22,24,31,32]

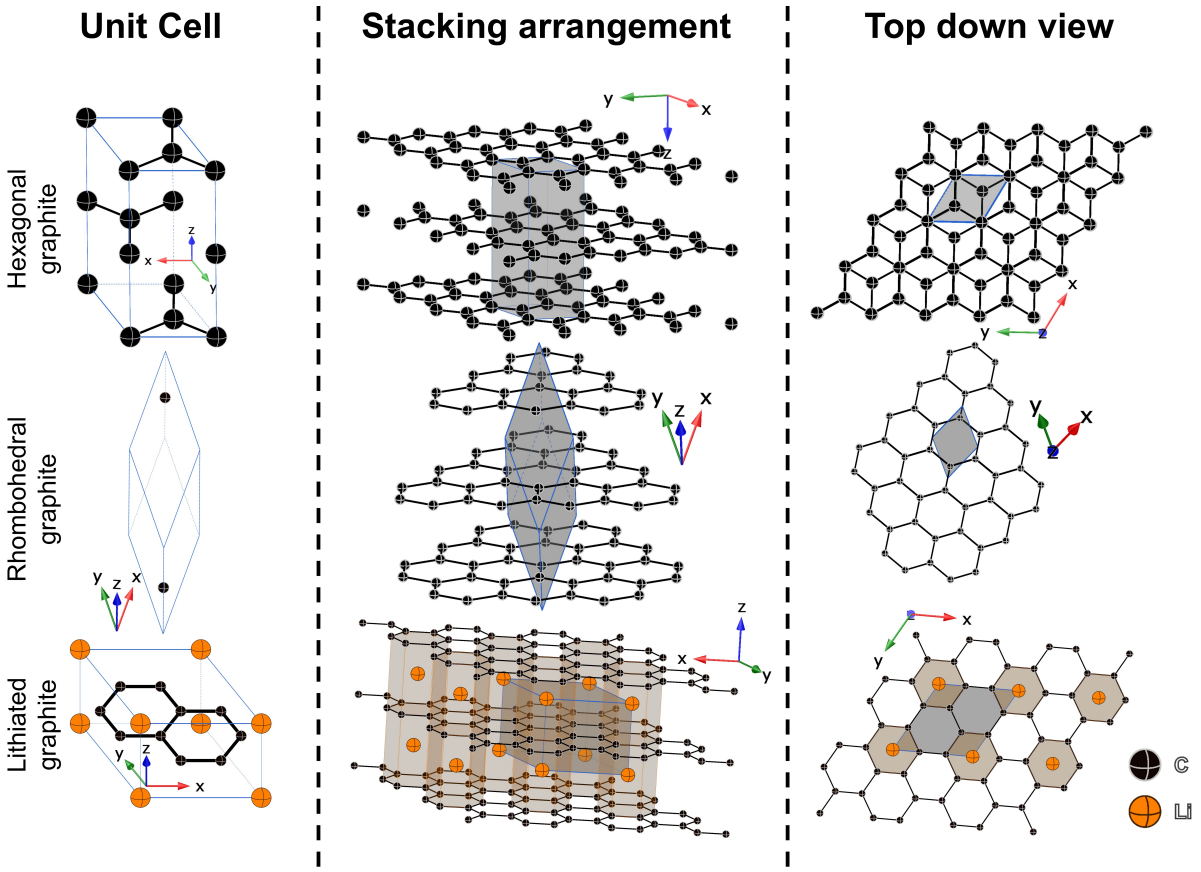


Fig. 1.6. *The unit cells and expanded crystal structures for hexagonal, rhombohedral and lithiated graphite.*

Consequently, this layered structure of all morphologies leads to a flake like particle, consisting of a flat basal plane (lining with the c axis stacking) and an edge plane (in line with the b and c graphene planes).[24] The edge planes can be further split into either a zig-zag or arm-chair configuration depending on the edge being viewed.[24] This anisotropy leads to a large variation in properties and surface energies on a graphite particle.[24] With basal planes showing higher electronic and thermal conductivity compared to the edge plane which shows higher reactivity and also allows for the intercalation of species within the structure.[24] A schematic of the components of a graphite particle are given in Figure 1.7.

Generally, there are two types of graphite materials, NG and synthetic graphite (SG), both of which are used in LiBs (after further processing) with the latter used to a greater

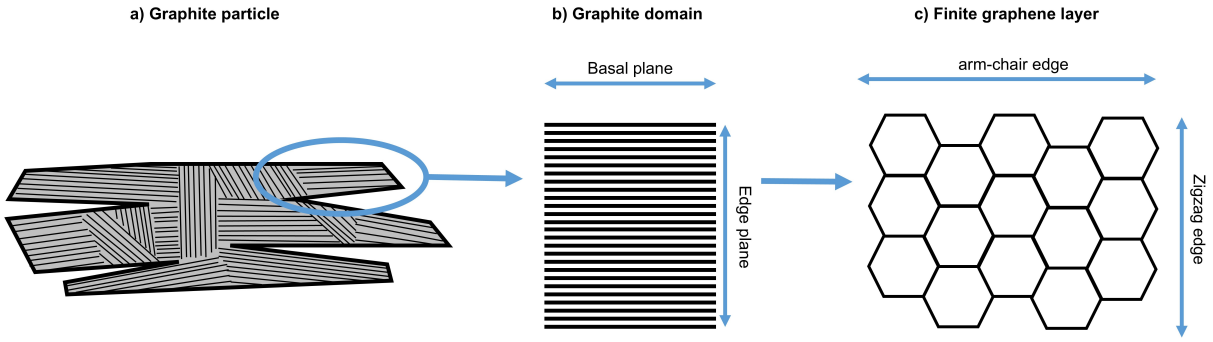


Fig. 1.7. *(a) Schematic of a graphite particle, showing a combination of crystallites forming a larger particle. (b) The basal and edge planes highlighted on a graphite crystallite. (c) The two possible edges created by finite sheet of graphene.*

extent.[24,33–35] NG originates from the ground, although abundant, NG is mined in a limited number of countries like China, Madagascar, Brazil, and Canada. SG can be synthesised by the graphitisation of green coke (a by-product of fractional distillation of hydrocarbon obtained at temperatures below $600\,^{\circ}$C), this is achieved by high temperature and pressure calcination.[24,33–35] NG is cheaper and less energy intensive to obtain, within a battery it also offers higher energy density and power output, however the cycle life and performance at higher cycle rates are worse than SG.[24] Typically, a blend of the two are used.[33,34] For both, further processing is required to form 'battery-grade graphite'.[24,33] A low-yield, high-energy jet-milling process called sphericalisation is used to convert flakes into uniformed spherical particles.[24,33,35] Spherical particles lead to better electrode packing, where otherwise the basal planes would align with the current collector, hindering Li-intercalation through the edge planes.[24,33] A carbon pitch derived coating is also added to 'battery-grade graphite'. The pitch coating is typically composed from petrochemical by-products and predominantly consists of aromatic hydrocarbons. This coating provides high conductivity, volumetric expansion moderation as well as reducing access to the graphite edge plane where parasitic reactions can occur.[19,24,33]

Rüdorff's and Hofmann's staging mechanism was the first description of lithium intercalation into graphite, published in 1938.[36] Here, lithiation occurs via distinct phases indicated by 'nth stage compounds'. In each compound, periodic layers are filled, separated by 'n' number of non-intercalated layers.[36] This is shown in Figure 1.8(a). This mechanism emerged by considering the energy required to expand the gap between two graphene layers and the repulsive interaction between intercalant layers.[36] However, the mechanism fails to explain the transition from stage 3 to stage 2, where layers would have to de-intercalate whilst others intercalate which would be impractical if the layers spanned the entire particle. Daumas and Herold modified the model, allowing the graphene sheets to flex around domains of intercalated species.[24,37] This is shown in Figure 1.8(b).

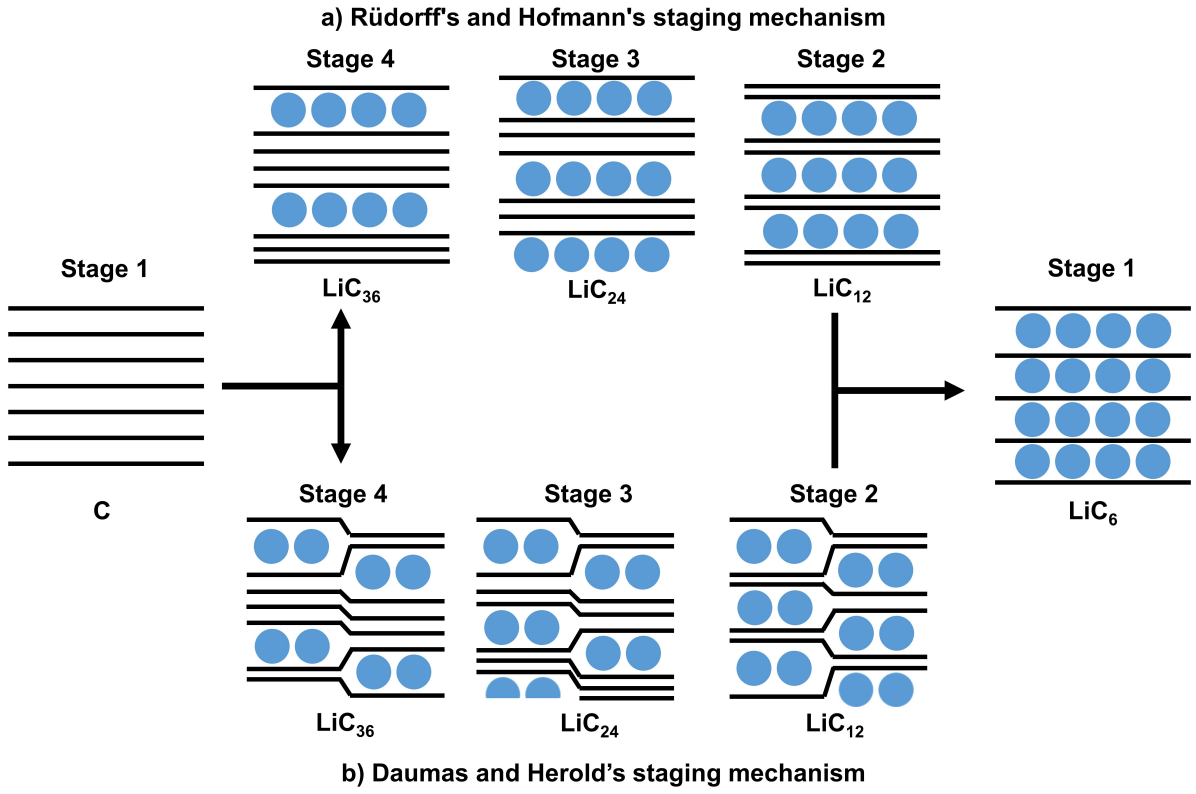


Fig. 1.8. *Two different proposed staging mechanisms for the lithiation of graphite. At the top (a) Rüdorff's and Hofmann's proposed mechanism and on the bottom (b) Daumas and Herold's proposed mechanism. Graphene sheets are shown with black lines and lithium ions as blue circles.*

The voltage window of the carbonate electrolyte: EC/DEC (1 M $LiPF_6$) sits at around 1.0 V to 5.8 V relative to the Li/Li^+ potential.[38] The electrode electrochemical potentials for carbon sits outside this range at around 0.2 V.[38] This may indicate an invalidity for use within a battery, however, after the degradation of some electrolyte on the anode surface during the first charge cycle, a film is created that provides kinetic stability.[38,39] This thin, amorphous layer is known as the solid electrolyte interface (SEI) layer.[38] SEI formation is beneficial during the first cycles, known as formation cycles and the properties of which can be changed by the addition of additives.[39] However, further SEI formation will decrease lithium inventory and increase internal resistance, leading to a loss in battery capacity and performance.[39]

1.2 | Transition to net zero

The UK's net-zero strategy, the EU's green deal, the US's policies like the Inflation Reduction Act of 2022 and China's commitment to peak its carbon emissions by 2030, collectively highlight the global acknowledgment of the impact of carbon dioxide emissions on the climate.[40–43] These initiatives aim to fund new energy technologies, aiming to reduce dependence on fossil fuels and establish an energy infrastructure with zero total carbon dioxide emissions. These policies are motivated by the urgent need to address the effects of global warming, which has already increased (as of the time of writing) by 1.1 °C since 1880, resulting in devastating consequences such as more frequent floods and more severe forest fires.[44]

In every nation the LiB has been recognised as a significant stepping stone towards this ideal decarbonised future. LiBs can be easily integrated into the current energy infrastructure, offering clean transport within EVs, being integrated into the grid, allowing intermittent clean energy sources like wind and solar to supply a continuous stream of energy, and being used

as clean generators and back-up energy systems as energy storage systems (ESS). Figure 1.9 shows the array of uses for LiBs to decarbonise the current energy system.[45]

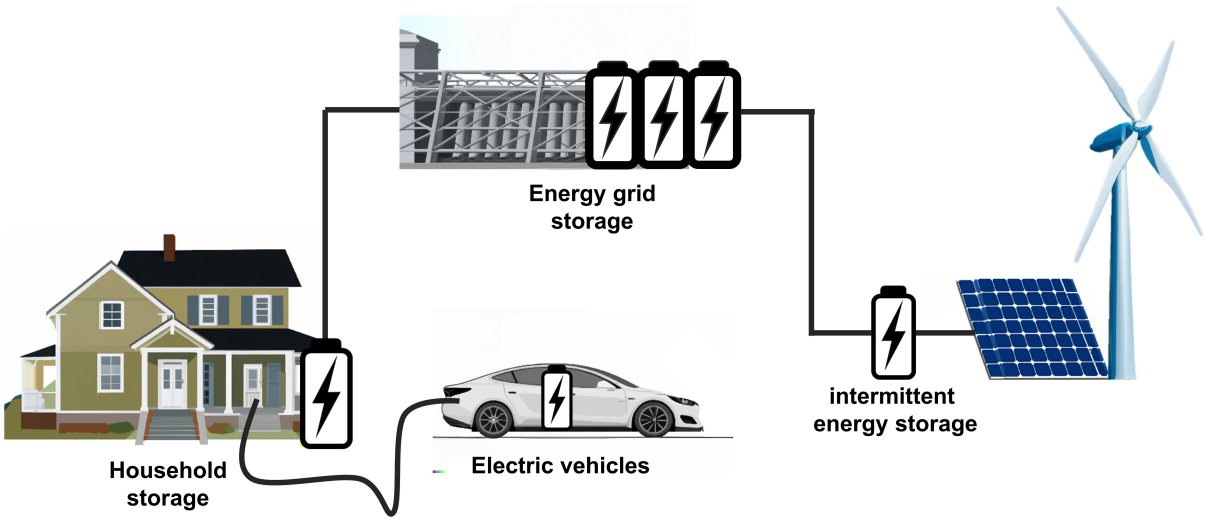


Fig. 1.9. *Proposed usages of LiBs to decarbonise the energy system. LiBs can be used to store intermittent energy from sustainable resources like solar and wind energy, allowing constant output current to the grid. LiBs can also be used as energy grid storage to curb demand peaks in energy usage. LiBs can also be used as battery storage within the home and to isolate houses from the grid. LiBs can also be used to power vehicles.*[45]

In the UK, the transport sector accounted for $26\,\%$ of the $426.5\,\mathrm{Mt_{CO_2e}}$ total domestic greenhouse gas emissions in 2021.[46] This was by far the biggest contributor to $\mathrm{CO_2}$ emissions followed by the energy supply sector, contributing $20\,\%$ to this value.[46] Therefore the majority of strategies for decarbonisation tackle the transport industry, incentivising the production and use of EVs rather than traditional internal combustion engine (ICE) vehicles. For instance, at the time of writing, the UK has mandated that all new car sales must be electric by 2035 and the US offers tax credits for tax payers that purchase qualified electric vehicles.[40,42]

The implementation of these policy changes, coupled with the evolving societal perspective, has already spurred an exponential increase in the EV and LiB markets. Registration of new electric vehicles, in the UK, rose by $87\,\%$ in 2020 compared to 2019. This

is in conjunction with the 51 % and 35 % decrease in new registrations of diesel and petrol vehicles in that same year. It is predicted that in 2040, EVs could dominate the automotive industry, capturing 95 % of the market. This leads to a forecast scenario that the production of EVs could increase to 1.6 million units per year by 2040 in the UK alone.[47–49]

1.3 | End-of-Life lithium ion batteries

1.3.1 Cell ageing

Battery cycling is not a completely reversible process, numerous complex irreversible side reactions can occur during cycling which can be enhanced by irregular environments, caused by factors such as pressure and positioning. Non-ideal cycling conditions, such as faster charging/discharging rates and low temperatures, also lead to increased irreversibility. These side reactions can lead to loss of lithium inventory, loss of active material, and increased internal resistance, all of which decrease the performance of the battery and lead to so called ageing of the cell.[34,50–58]

Many ageing mechanisms are discussed within the literature and illustrated in Figure 1.10. One key ageing mechanism that effects the anode is SEI formation. Whilst beneficial during the initial formation cycles, constant formation consumes both lithium and electrolyte, and increases internal resistance within the cell. Another ageing mechanism that effects the anode is the loss of contact of active material, occurring due to the around 10 % expansion during lithiation. This leads particles to shift, disconnect and potentially crack. Other irreversible effects discussed within the literature include lithium plating, graphite exfoliation, copper dissolution, and metal deposition (where TMs from the cathode deposit onto the anode). The cathode may also deteriorate via similar ageing mechanisms.[34,50–58]

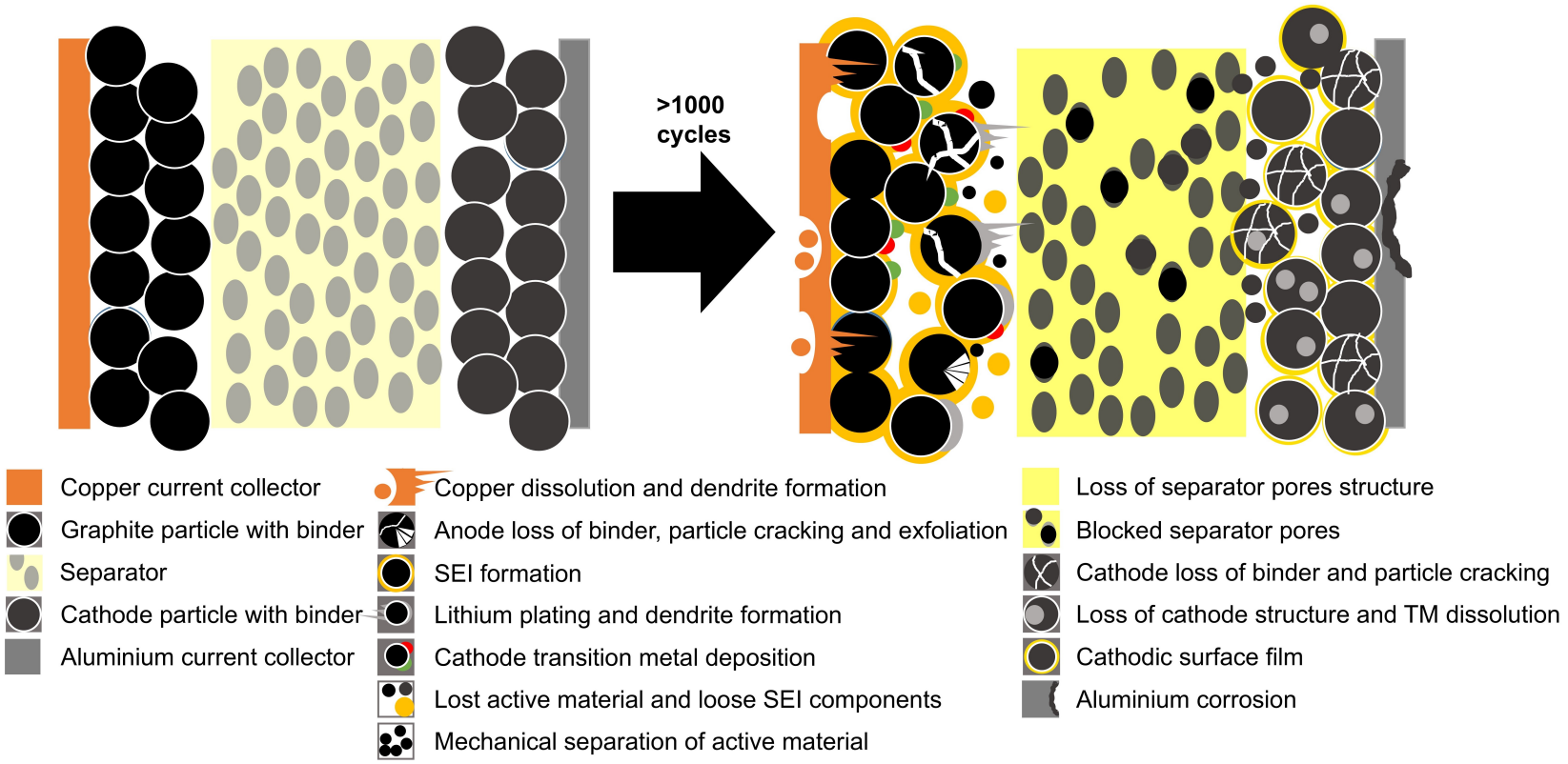


Fig. 1.10. *An artistic impression of the ageing effects discussed within the literature for LiBs. On the left is a fresh cell and on the right is a heavily aged cell. The legend at the bottom can be used to identify ageing mechanisms illustrated within the figure. Components are not to scale.*

1.3.2 Electric vehicle ageing

The most notable effect of cell ageing is the gradual loss in cell capacity, within an EV this results in a decrease in the capacity of the battery pack and therefore a loss in the driving range per charge of the car. Typically, EVs do not operate using the entire battery capacity and a series of operational modes are used during discharging/charging. The battery pack is cycled within a mid-range with a lower and upper band known as a grace capacity. Therefore, the decreasing capacity falls outside the usage capacity and the user would not notice a decrease in car mileage. However, when the capacity drops to around $80\,\%$ of the battery packs original capacity, a drop in driving range will be noticed. When the battery pack reaches this point it is termed End-of-Life (EoL) and unusable within a vehicle. At this point, replacing the battery is suggested.[59–61]

1.3.3 The need for recycling

Current EV battery packs have a lifespan of approximately 10 years. At present, the available options for managing the resulting waste are relatively constrained. The global stock of EVs reached 16.5 million in 2021, which will result in an estimated generation of 16.5 million EoL battery packs in 2031. If current trends are followed, this will amass to around 240 million in 2040. This, combined with the rising volume of waste from production scrap, recalls, factory rejects, and discarded batteries from handheld devices, will contribute significantly to the overall waste pool. However, not only is the amount of waste generated an issue, but the contents of these battery packs raises larger concerns.[47,48,62]

The air and water sensitive components (electrolyte and lithium salts) as well as the toxic and carcinogenic TMs used lead to the generation of dangerous waste that can both leak into the environment and spontaneously catch fire. Not only this, but the majority of components used within LiBs are non-sustainable, controversial and have poor geo-political

security. Materials found in current gen LiBs such as cobalt, nickel, manganese, copper, graphite (both natural and synthetic), phosphorus and lithium all appear on the EU Critical Raw Materials List for 2023, meaning the European Committee has agreed that these raw material have strategic value but are highly susceptible to supply disruption.[63–68]

The establishment of a circular economy, where EoL batteries are recycled to produce materials for new batteries, holds the potential to address both supply chain and waste generation concerns effectively. Generation of EoL batteries is currently in its preliminary stages, this marks a crucial juncture in the electrification revolution where it is imperative to integrate recycling initiatives right from the outset. This will lay the foundation for a circular economy in battery materials with minimal waste.[67]

1.4 | Current recycling methods

1.4.1 Industrial Recycling

The increase in EoL waste and the continuous stream of scrap material generated during the construction of LiBs has already created an emerging recycling industry consisting of multiple players.[69] Initially headed by large, already established, steel smelting companies like Umicore and Posco, LiBs were initially shredded to create a powder known as black mass (BM). This BM is either sold as a commodity or smelted in a process called pyrometallurgy. During pyrometallurgy the BM is heated to $150\,^{\circ}$C-$500\,^{\circ}$C to remove organic components like binders and electrolyte before further heat treatment at $1400\,^{\circ}$C-$1700\,^{\circ}$C to remove plastics and carbon. The main product is an alloy containing $\mathrm{Co/Cu/Ni/Fe}$ which is then sold off for the value of the metals contained. Lithium is often lost within the slag. Many of the battery components are lost during this process.[60,66–68,70]

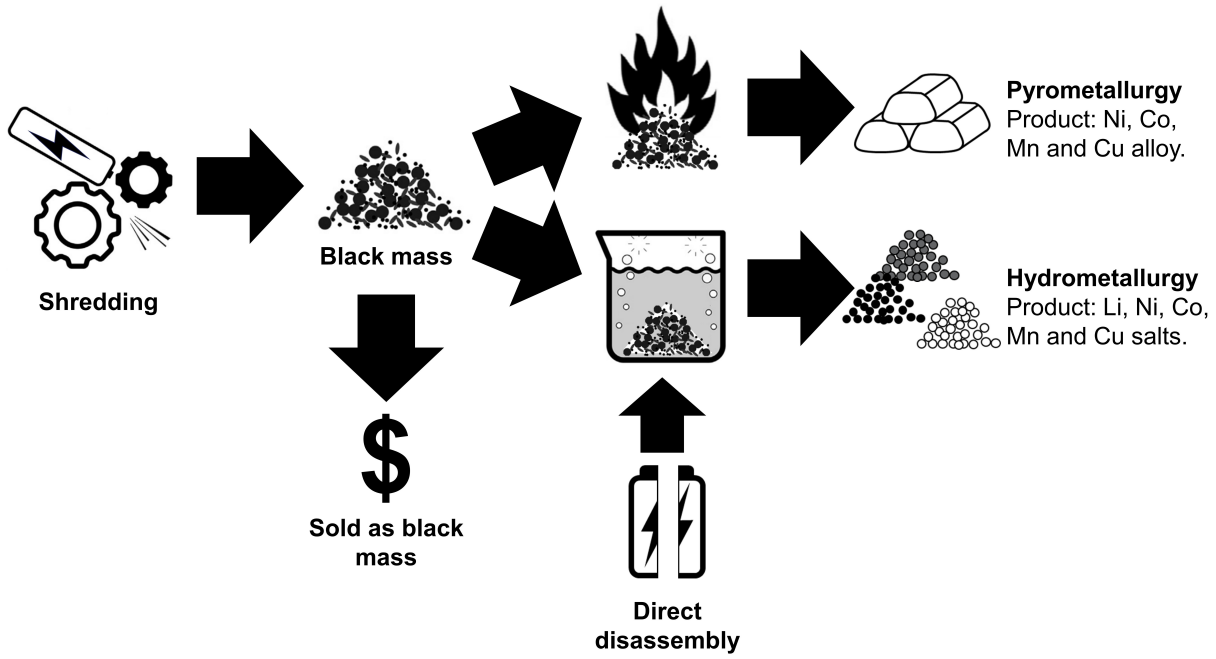


Fig. 1.11. *Current processes used for industrial recycling.*

Hydrometallurgy is a developing industrial technique designed to recover a greater number of components from LiBs with enhanced purity and in forms more relevant to battery applications. Here, an aqueous solvent is used to leach the metals from the BM which are subsequently precipitated out to give Co/Ni/Mn/Li salts which can be used as precursors for generating new cathode material. Cirba solutions, Redwood Materials and Green Li-ion are examples of industrial practitioners out of an ever growing list of hydrometallurgists.[60,66,68,70–72]

Some hydrometallurgists may dismantle cells before hydrometallurgy instead of shredding. This allows for less contamination of components and allows for different processes to be used on the anode and cathode. However, the lack of conformity between battery modules, battery shapes and battery chemistry by manufacturers, as well as the hazardousness of components, makes this a less seen practice.[60,68,70,72]

Current LiB recycling routes are shown in Figure 1.11. How these routes contribute to a circular economy is given in Figure 1.12. Hydrometallurgical processes are favourable over

pyrometallurgical process for a circular economy as less processing is needed to regenerate a fresh battery. However, a direct route, where the material can be integrated back into a battery would be even more favourable.

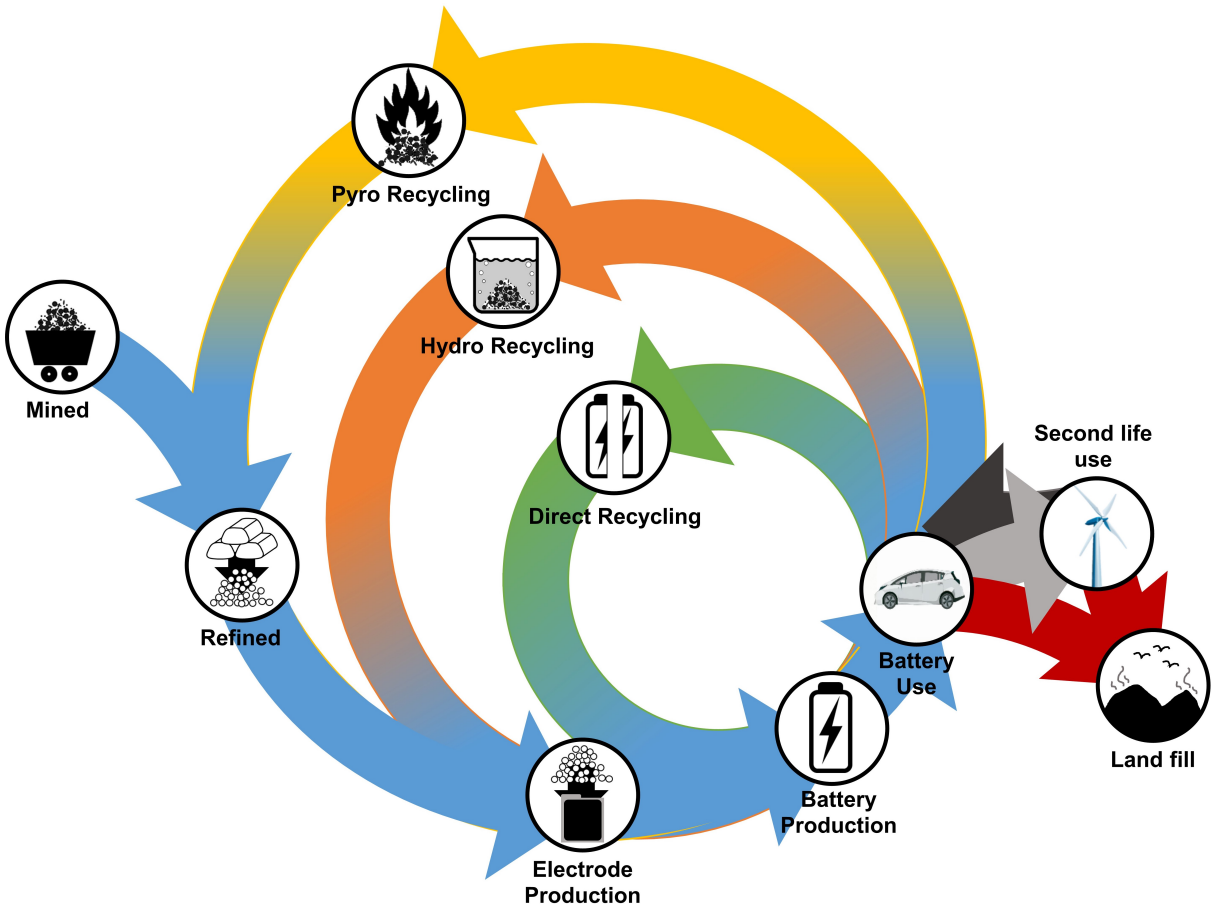


Fig. 1.12. *A schematic of how current recycling techniques can be integrated to create a circular economy for LiBs. An adapted image from ReCell*[73]*.*

1.4.2 Lack of anode recycling

In almost all practices, graphite is either discarded or pyrolyzed. This is likely due to the low economic value ($3400/Tonne) of graphite and the required standard for "battery-grade" being very high.[34,60,74,75]

Graphite makes up the largest composition by weight of a LiB (11 times more graphite than lithium). This resulted in a consumption of 437,000 tonnes of graphite by the EV battery sector in 2021. With the expected exponential increase in demand for LiBs, the demand for graphite is also expected to rise quickly. As already mentioned, graphite is considered a critical raw material by the EU, this is due to supply risks that may hinder meeting future demand. China holds an over $90\,\%$ monopoly on battery-grade graphite, giving China complete control of the market. In 2023, China implemented export controls over their graphite, incentivising the diversification of the supply stream.[34,63,76,77]

Both SG and NG formation require lengthy processes with toxic chemicals and high CO_2 production. NG requires the use of hydrochloric acid, chlorine gas and sodium fluoride for both mining and purification. SG requires temperature of $2500\,^{\circ}\mathrm{C}$ for several days and is a product of hydrocarbons. In 2018, the Argonne National Laboratory Greenhouse Gases, Regulated Emissions, and Energy Use in Transportation (GREET) project reported large global warming potentials for both SG and NG.[24,34,35,57,78]

If high-grade graphite could be recovered from battery scrap and reused within a circular economy, future supply issues could be resolved and the CO_2 cost of batteries could be reduced.

1.5 | Current anode recycling

Graphite recovery within industry has only recently been commercialised with companies like Altilium and LOHUM. However, publicly disclosed information on the process has not been given. Likely high graphite percentage portion of BM are sold that are not reusable for LiBs.[79,80]

Graphite recycling within academia is more common. Although, many papers within the literature focus on extracting graphite from the anode for use in alternate applications, for

instance converting the spent graphite into graphene, active carbons or carbon aerogels or only focus on the quality of the copper current collector.[57,78,81,82] This is due to the idea that EoL graphite contains inherent defects, leading to it being a better precursor for graphene production rather than virgin graphite.[57] These approaches, however, do not contribute to establishing a circular economy.

A major challenge for extracting non-deteriorated graphite from the anode for reuse within a LiB is delaminating the active material film (containing the graphite) from the copper current collector and rejuvenating the graphite. All of which must be done in a cost-effective manner for industrial use. The difficulty of this lies with the PVDF binder, which lacks solubility in non-harmful solvents. Currently NMP is most commonly used for delamination. Dimethyl sulfoxide (DMSO) and dimethyl isosorbide (DMI) have been proposed as less toxic candidates.[83] However, dangers remain due to the alternative solvents high dermal absorption, providing a route of entry into the body for PVDF and any other toxic compounds dissolved within the solvents.

Other approaches follow closely to the already established techniques of industry. These include, but not limited to: Fenton and floatation, leaching and filtration, oxygen free roasting and H_2SO_4 curing leaching. However, these techniques either have large global warming potentials or require non-environmentally friendly reactants. As well as this, it is unclear whether the graphite obtained is suitable for LiB use.[57]

Mechanical delamination, aimed to be industrially scalable, focusing on sonication has been reported, showing promising electrode delamination. Acoustic pressure created by a sonotrode in an aqueous environment creates vapour-filled cavities to form and randomly implode. The implosions near the surface of the electrode release a large amount of energy in the form of high local pressure which can breakdown the binder and release the film from the current collector. However, the high ultra-sonication appears to not cleanly delaminate

the anode, leaving copper contamination on the graphite and graphite contamination on the copper. As well as this, electrochemical data is often not provided.[84–86]

1.6 | Chapter conclusion

Although graphite is a critical raw material, industrial recycling of the material from the ever increasing stock of EoL batteries is relatively unexplored. Techniques discussed in the literature either lack the cost effectiveness required for industry, or use toxic solvents unsuitable for establishing a clean circular economy. As well as this, there is uncertainty as to whether the graphite that can be recovered from EoL LiBs can be reused within the same electrochemical conditions, due to ageing mechanisms causing internal defects within the particles. Often papers that focus on extracting graphite from LiBs do not provide electrochemical data or try to convert graphite into alternate materials like graphene.

CHAPTER 2

Project aims

This work aimed to play a role in easing the pressure on critical raw materials caused by the current rapidly growing demand for LiBs. This was accomplished by establishing an efficient closed-loop circular economy, where all components of LiBs that would otherwise be disposed of could be repurposed to secure future supply chains, reducing the need for mining non-sustainable materials.

The lack of sustainability, contentious political control, and environmental impact linked to the graphite utilized in LiBs sparked industrial interest in graphite recycling. However, despite this growing interest, there remained limited industrial implementation of its recycling practices. Academic focus in graphite recycling lay in using the obtained material for alternate processes rather than to create a circular economy. To address this gap, this project focused on creating an economically viable method for extracting graphite from discarded cell anodes that would often be wasted within the current recycling system, thereby preventing its loss in the recycling process.

Firstly, anodes of varying state-of-health (SoH) that would commonly be found within the recycling stream were studied in order to determine if the quality of the obtained active material was comparable to battery-grade graphite and worth recycling.

The second objective of this project was to identify a technique that would facilitate the easy extraction of this active material from LiB anodes while optimising the performance of the recovered graphite in electrochemical applications. This was achieved through

characterising anodes that would typically enter the recycling stream (but not recycled) and identifying characteristics that could allow for easy separation of graphite from other components. Subsequently, efforts in rejuvenating the obtained graphite were made to ensure its effectiveness within a new cell.

Thirdly, to incentivise the recycling of graphite, an easy and scalable way of up-cycling the recovered anode active material was studied and described.

CHAPTER 3

Experimental theory

3.1 | Raman spectroscopy

3.1.1 Fundamentals

If monochromatic laser light of wavelengths within or close to the visible spectrum ($405\,\mathrm{cm}^{-1}$-$1064\,\mathrm{cm}^{-1}$) is directed onto a sample, the incident photons ($h\nu$) may either be absorbed, transmitted or scattered. The small percentage of photons that are scattered can either scatter elastically (Rayleigh scattering), where the energy of the photon emitted is the same as that absorbed ($\nu_i = \nu_R$), or scatter inelastically. Two inelastic processes can occur, Stokes radiation and anti-Stokes radiation, where Figure 3.1 can be used to visualise the differences.

During Raman scattering, a photon interacts with a molecule, momentarily promoting it to a virtual state—a temporary, non-quantized energy state. From this virtual state, the molecule may relax back to the same electronic state, leading to either elastic or inelastic scattering of the photon. In elastic (Rayleigh) scattering, the molecule returns to its original vibrational state, emitting a photon with the same energy. In inelastic scattering, the molecule returns to a different vibrational state: Stokes scattering occurs if the final state is higher than the original, and anti-Stokes scattering if it is lower, resulting in a scattered photon with a detectable energy difference. Stokes scattering, which represents an energy loss for the photon, is more common than anti-Stokes scattering, especially at room temperature, where

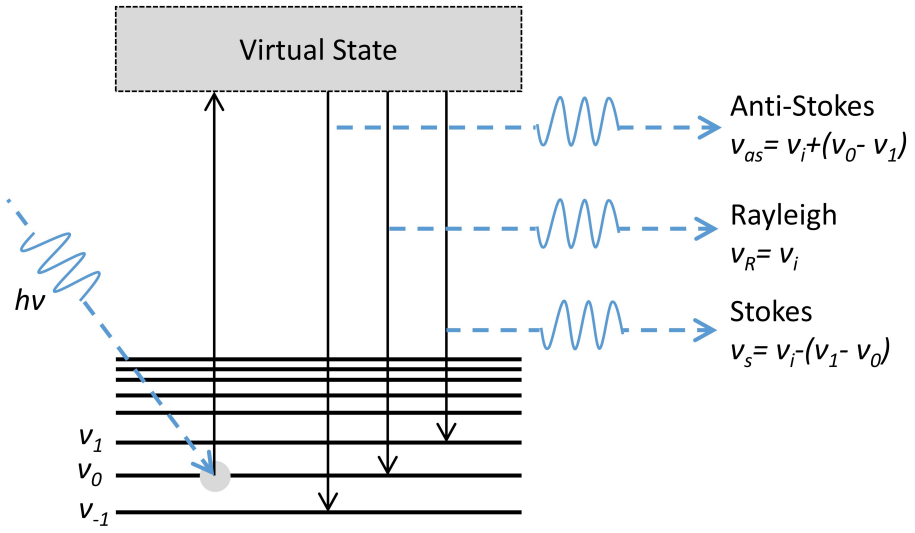


Fig. 3.1. *Perrin-Jablonski diagram showing the vibrational relaxation leading to Stokes shift, anti-Stokes shift and Reyleigh scattering adapted from Atkins' Physical Chemistry, P. Atkin*[87].

only about one in every $\sim 10^7$ photons exhibits this effect, necessitating high-intensity laser illumination.

Typical Raman spectroscopy focuses on Stokes scattering, recording the intensity of changed energy via the Raman shift (cm^{-1}). The Raman shift, and therefore the position of a peak, varies depending on the frequency of the molecular vibrations, *i.e.* the bond strength, bond length, bond angle and the mass of the atoms within the molecule. Note that it does not depend on the energy of the photon of incidence.

Each peak within a Raman spectrum will correspond to a specific vibrational mode of a specific bond within the molecule, leading to a 'fingerprint' spectrum that can be used to identify it. Not all vibrational modes are Raman active, however. A Raman transition occurs only when there is a change in the polarizability of a molecule during its vibration. Similar to this is infra-red (IR) spectroscopy, which records the absorption of absolute frequencies that correspond to vibrations that cause a change in dipole moment.

Whether a bond vibration is IR or Raman active can be found with group theory, by studying the symmetry of the molecule itself. A molecule of N atoms will have $3N$ modes

of displacement, where each atom can move within x, y and z orthogonal directions. For a non-linear molecule, three of these displacements will cause the entire molecule to move and three more displacements will lead to a rotation of the molecule, leaving $3N-6$ displacements that lead to vibrations and deformation. For a linear molecule, this is $3N-5$ as there is no rotation around one of the axes. If the linear molecule CO_2 is considered, there will be 4 vibrational modes corresponding to a symmetric stretch, antisymmetric stretch and two bend modes (all shown in Figure 3.2). IR active vibrations will change the position of electrical density, therefore $\nu 2$, $\nu 3$ and $\nu 4$ are all IR active, with $\nu 1$ being IR inactive. Raman active vibrations are hard to determine but are normally resultant of a change in overall volume. Therefore only $\nu 1$ is Raman active.

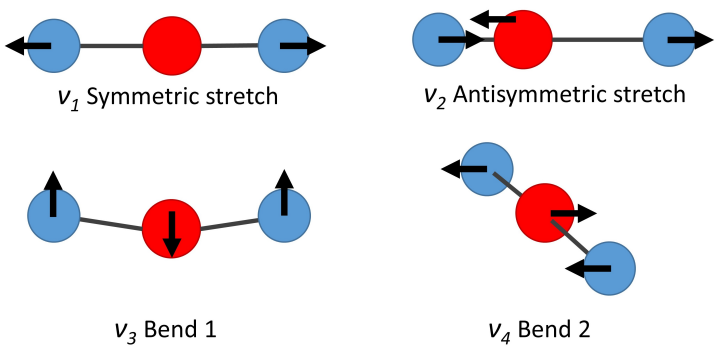


Fig. 3.2. *CO_2 vibrational modes adapted from Inorganic Chemistry, M. Weller[88].*

3.1.2 Raman active vibrations in crystal structures and graphite

Raman spectroscopy is not exclusive to discrete molecules, Raman analysis can also be conducted on solid state materials. The same principles apply to these materials however the relatively infinite lattice make the interactions more complex. Energy absorption leads to a quantum of vibrations within the lattice known as phonons. These phonons propagate through the entire lattice with defined velocity, wavelength, wave vector, and frequency characteristics. In this case, Stokes and anti-Stokes scattering refers to the generation or

annihilation of these phonons. Modes similar to those observed for individual molecules (although transcend through the entire lattice) are known as internal vibrations. More vibrational modes can occur through shear, interlayer breathing or rotation, these are known as external vibrations. Due to these external vibrations, the quantity of vibrational modes within the lattice can be denoted as 3N, where N is the number of atoms within the unit cell.[89]

Calculating Raman active vibrational modes also becomes more complex. Although there are $3N$ vibrational modes, the space group of the unit cell and the irreversible representations of each vibrational mode in comparison to the first Brillouin zone within the reciprocal lattice is required to determine whether the band is Raman active, IR active or neither. As well as this, if graphite is considered, the delocalised π-band can act as a real state for electron excitation, leading to a number of other Raman active mechanics.[31,90–93]

To calculate Raman active phonons a graphene monolayer will be used as an example, which displays a hexagonal unit cell with D_{6h} symmetry and two atoms. Figure 3.3 can be used to aid visulisation of the graphene sheet, where the Bravais lattice and unit cell is given in Figure 3.3(a) and the reciprical lattice with the first Brillouin zone is given in Figure 3.3(b). The two atoms lead to six vibrational phonons, each shown in Figure 3.3(c). If one atom is used as the centre of the vibration (i.e. the centre of the first Brillouin zone or where the wavevector (q) is equal to zero) then the irreducible representations associated with the vibrational modes, found using the character table given in Table 3.1, is given as:

$$\Gamma_{Graphene} = A_{2u} + B_{2g} + E_{1u} + E_{2g} \tag{3.1}$$

Only the doubly degenerate E_{2g} band, where the atoms move in plane, is Raman active. This accounts for the peak given at $\sim 1587\,\mathrm{cm}^{-1}$ commonly denoted as the G (graphite) band. The A_{2u} and E_{1u} are IR active.[31,90–93]

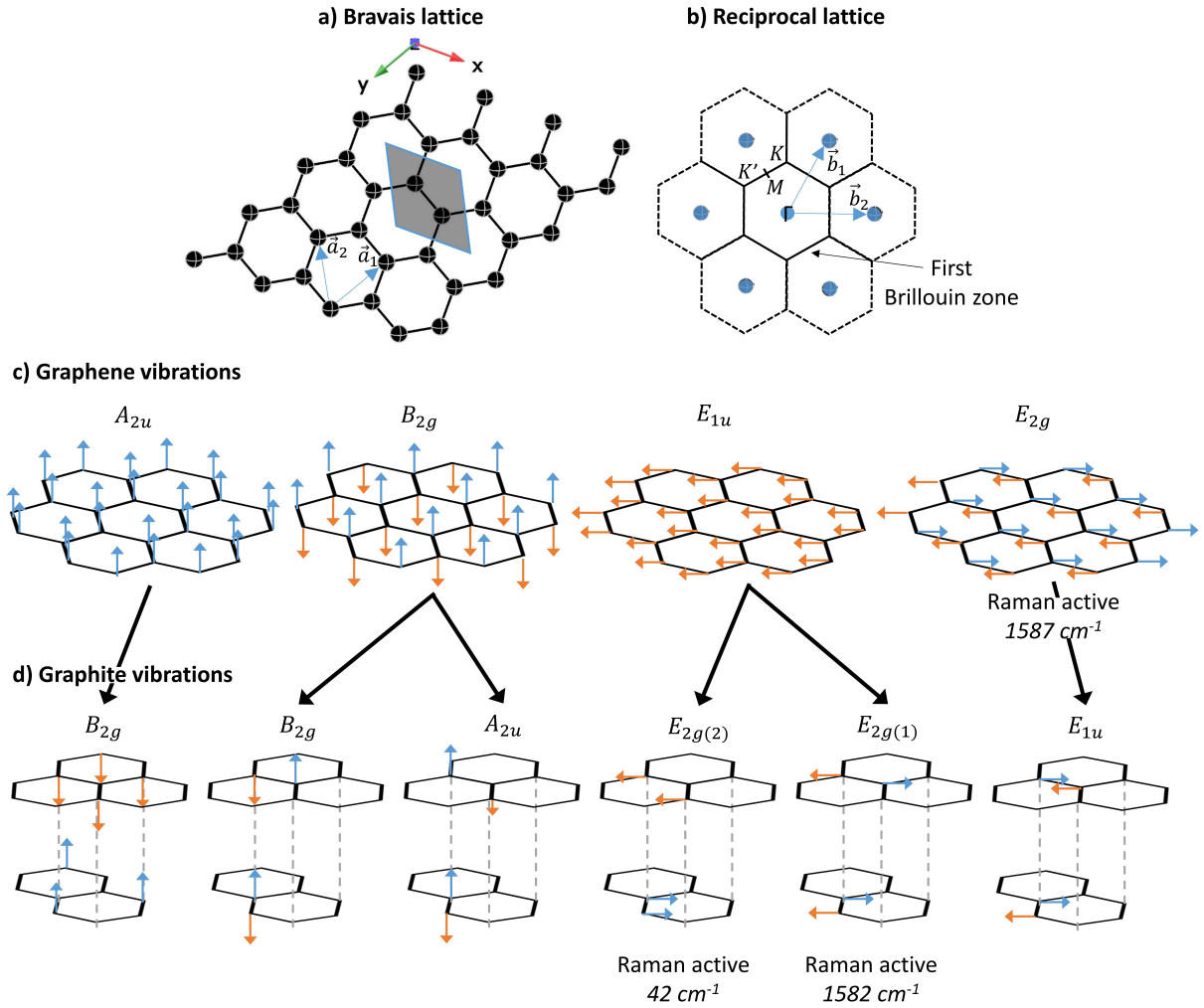


Fig. 3.3. *(a) The Bravais lattice and (b) the reciprocal lattice of graphite. (c) The vibrational modes of graphene. (d) The vibrational modes of graphite adapted from the work of S. Reich*[91]*.*

Graphite falls within the same D_{6h} space group with 4 atoms within the unit cell. The symmetrically irreducible phonon modes of graphite can be visualised by combining two planes that either resonate in phase or out of phase with each other (this is shown in Figure 3.3(d)). This creates 4 more modes, giving a total irreducible representation described by:

$$\Gamma_{Graphite} = 2A_{2u} + 2B_{2g} + 2E_{1u} + 2E_{2g} \tag{3.2}$$

Here again, only the E_{2g} phonons are Raman active and lead to peaks; the $2E_{2g}(1)$ at $\sim 1582\,\text{cm}^{-1}$ and the $2E_{2g}(2)$ at $\sim 42\,\text{cm}^{-1}$. The Raman spectra of a graphite sample obtained from this study is given in Figure 3.4. Although there are peaks that result from non-graphite related phonons i.e. the pitch coating at $\sim 800\,\text{cm}^{-1}$, salts peaks below $700\,\text{cm}^{-1}$ and other small peaks relating to small contamination (discussed later in section 5.8.1), all the peaks labelled in Figure 3.4 result from graphite. Therefore, not all Raman signals can be described with just phonon symmetry.

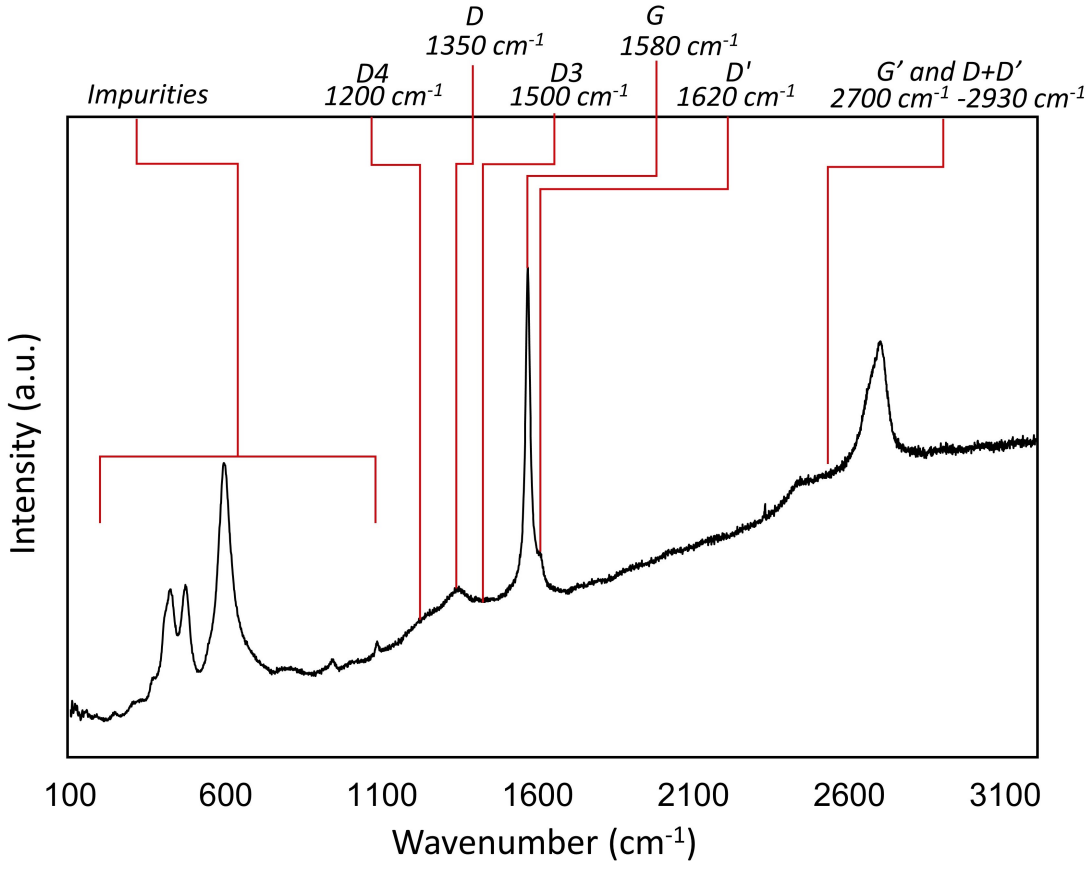


Fig. 3.4. *A Raman spectrum obtained for EoL anode exposed to air for 2 weeks. Peaks relating to graphite are highlighted.*

Within Figure 3.4, the D4 ($\sim 1200\,\mathrm{cm}^{-1}$), D ($\sim 1350\,\mathrm{cm}^{-1}$), D3 ($\sim 1500\,\mathrm{cm}^{-1}$), G ($\sim 1580\,\mathrm{cm}^{-1}$), D' ($\sim 1620\,\mathrm{cm}^{-1}$) and the G' and D+D" ($\sim 2700\,\mathrm{cm}^{-1}$ and $\sim 2930\,\mathrm{cm}^{-1}$) are highlighted as bands corresponding to graphite.[94]

The origin of the G band has already been explained; however the origin of D (disorder) band is more complex. The D band is first mediated by an in plane transversal phonon typically assigned to E_{2g} symmetry, however originating from the K point of the Brillouin zone. The Brillouin zone is a mathematical representation of the allowed states of a periodic structure in reciprocal space and is useful for determining electronic band structures and vibrational properties of crystals (this is shown in Figure 3.3(b)). At the K point, point group symmetry is reduced to C_{2v} and the phonon raises to an A_{1g} symmetry mode which simulates breathing of the rings. The K point also represents the Dirac point of a Dirac cone where the HOMO-LUMO gap drops to zero. At this point, the excited electron is promoted to the conduction band, where with additional resonance through phonons of arbitrary energy, the electron can scatter. The probability of scattering is higher if it results in the transition to another real electronic state, typically from one Dirac cone to another ($K \rightarrow K$). To preserve momentum, the electron can be backscattered elastically via defects (breaks in the sp^2 structure) or inelasticly by another phonon and once the electron-hole pair recombine, a photon of reduced energy is produced. Therefore, the D band results from a double-resonance mechanism either aided by defects or a double-phonon process. Diagrams of a first order response, defect aided one-phonon double-resonance and a two-phonon double-resonance are given in Figure 3.5. The position of the D band varies with excitation wavelength and its intensity (however not linear) varies with disorder.[31,90–93]

The D' peak also results from a two-phonon double-resonance process, however mediated from an in-plane longitudinal (to the phonons direction) phonon that arise at points closer to the Γ point but not so that $q = 0$. Here the phonon's wave vector is smaller and the excited electron transitions between electronic states within the same Dirac cone.[31,90–93]

The G' and D+D" region originates from overtones of both the D and D' bands. An overtone refers to the combination of multiple similar phonons, resulting in a multiplication of the energy.[31,90–93]

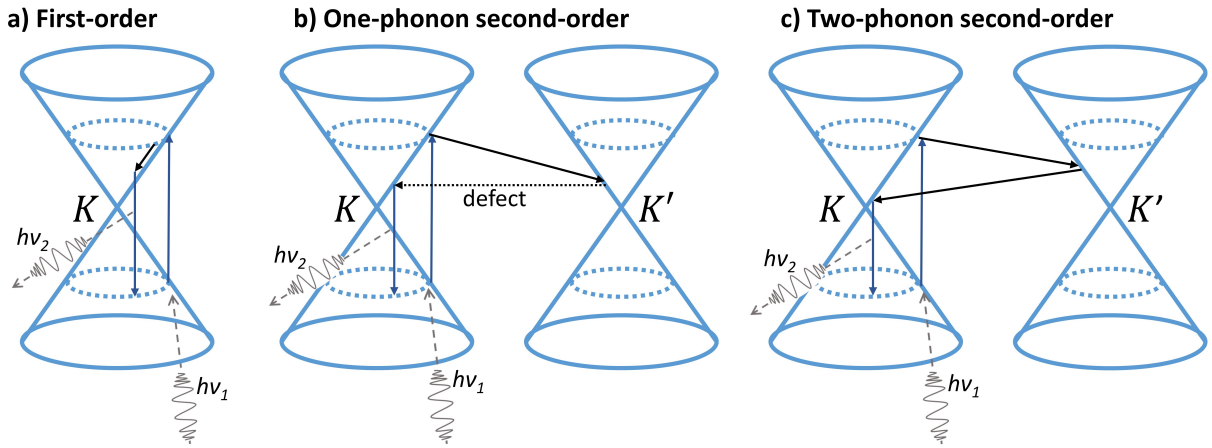


Fig. 3.5. *Scattering mechanisms for photo-excited carriers for various Raman modes. Each cone represents two near-neighbour Dirac cones. (a) First-order G band mechanism. (b) One-phonon second-order double resonance process for the D band. (c) Two-phonon second-order double resonance mechanism. The dotted line represents elastic defect induced scattering whereas the solid black lines show inelastic phonon scattering and the solid navy blue lines represent photon interactions. Figure was adapted from the work of S. Reich[91].*

The nomenclature of graphite Raman is to denote a peak at $\sim 1200\,\mathrm{cm}^{-1}$ as $D4$, originating from further disorder induced A_{1g} double resonance and $D3$ at $\sim 1500\,\mathrm{cm}^{-1}$ due to the presence of amorphous carbon.[94–96] However, these peaks appear to be added to resolve spectral features instead of arising from phonon theory. Changing the peak shapes, for instance, using an asymmetric Fano shaped peak for the G band and a double Lorentzian peak for the D band would remove the need to fit a $D3$ and $D4$ peak.[97] The double Lorentzian peak can be rationalised by the double scattering caused by the double resonance; and the Fano peak results from excitation to a continuum from discrete energy levels.[97]

As all six peaks are the norm within the literature and asymmetric parameters can lead to over-fitting, this fitting will be used for this study.[94] As this study only compares the order within similar origin material, if the fitting is consistent, a perfectly rationalised fitting is not required and only the changes between samples are important.

Table 3.1. *Character table for point group* D_{6h}

D_{6h}	E	$2C_6(z)$	$2C_3$	C_2	$3C_2'$	$3C_2''$	i	$2S_3$	$2S_6$	$\sigma_h(xy)$	$3\sigma_d$	$3\sigma_v$	linear functions, rotations	quadratic functions	cubic functions
A_{1g}	+1	+1	+1	+1	+1	+1	+1	+1	+1	+1	+1	+1	-	x^2+y^2, z^2	-
A_{2g}	+1	+1	+1	+1	-1	-1	+1	+1	+1	+1	-1	-1	Rz	-	-
B_{1g}	+1	-1	+1	-1	+1	-1	+1	-1	+1	-1	+1	-1	-	-	-
B_{2g}	+1	-1	+1	-1	-1	+1	+1	-1	+1	-1	-1	+1	-	-	-
E_{1g}	+2	+1	-1	-2	0	0	+2	+1	-1	-2	0	0	(Rx, Ry)	(xz, yz)	-
E_{2g}	+2	-1	-1	+2	0	0	+2	-1	-1	+2	0	0	-	(x^2-y^2, xy)	-
A_{1u}	+1	+1	+1	+1	+1	+1	-1	-1	-1	-1	-1	-1	-	-	-
A_{2u}	+1	+1	+1	+1	-1	-1	-1	-1	-1	-1	+1	+1	z	-	$z^3, z(x^2+y^2)$
B_{1u}	+1	-1	+1	-1	+1	-1	-1	+1	-1	+1	-1	+1	-	-	$x(x^2-3y^2)$
B_{2u}	+1	-1	+1	-1	-1	+1	-1	+1	-1	+1	+1	-1	-	-	$y(3x^2-y^2)$
E_{1u}	+2	+1	-1	-2	0	0	-2	-1	+1	+2	0	0	(x, y)	-	(xz^2, yz^2) $[x(x^2+y^2), y(x^2+y^2)]$
E_{2u}	+2	-1	-1	+2	0	0	-2	+1	+1	-2	0	0	-	-	$[xyz, z(x^2-y^2)]$

3.1.3 Instruments

Raman studies were conducted using two Raman microscopes, both were Renishaw inVia confocal Raman Microscopes. Air exposed samples used a basic inVia Microscope (using a green 100 mW, 532 nm laser, also equipped was a red 50 mW, 633 nm laser) whereas the inert air study used an inVia Qontor Microscope with an automated platform for taking a matrix of images and a blue 30 mW, 488 nm laser.

A schematic of a typical Renishaw microscope is given in Figure 3.6.

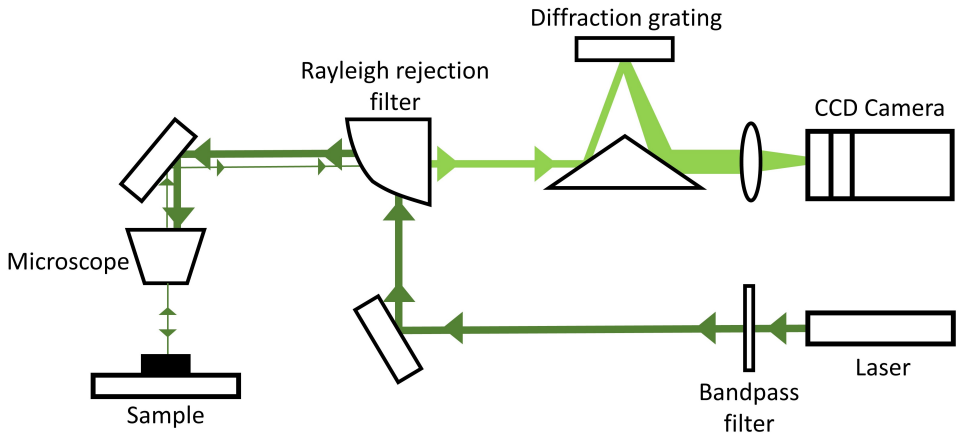


Fig. 3.6. *Raman instrument schematic adapted from Renishaws' website*[98].

A dipole-pumped solid-state laser is used to create monochromatic light to irradiate the sample. The green 532 nm light is typically made by exciting an aluminium gallium arsenide (AlxGa1_xAs) crystal which then irradiates a yttrium aluminium garnet (Nd:YAG) with infra-red light, producing 1064 nm wavelength light; the frequency is then doubled by irradiating a potassium titanyl phosphate (KTP) to create a beam of intense 532 nm. The blue 488 nm light is created in a similar way, however a differently Nd-doped garnet is used and a β-barium borate (BBO) can be used to convert 946 nm light into 473 nm light.

The light it reflected and magnified onto the sample with a series of mirrors and lenses, The resulting light then passes through a Rayleigh rejection filter, which removes

non-Raman scattered light. Typically, a volume phase holographic grating that diffracts certain wavelengths is used, so that unwanted light can be removed. A series of motorised spectrometer lenses are then used to focus the light onto a diffraction grating, which is then capable of splitting Raman light into its constituent colours. The diffraction grating uses a series of grooves to refract the light, (de)constructive interference in effect, spreads the light.

This light is detected with a charge coupled device (CCD). A photon that hits a defined area known as a pixel will produce an electron. The number of electrons produced from one pixel will determine the intensity of that area. The CCD is then scanned, and the data is constructed into a spectrum. These pixels typically consist of p-type silicon attached to metal gates on a metal oxide board.

3.2 | Scanning electron microscopy and energy dispersive X-rays

3.2.1 Fundamentals

Electron microscopy acts similarly to conventional optical microscopy. However, unlike traditional microscopy that is limited by the wavelengths of visible light causing a low depth of field, an electron microscope can image smaller structures with higher magnification. When a sample is bombarded with a beam of electrons a number of interactions can occur. Figure 3.7 displays these interactions. Scanning electron microscopy (SEM) is concerned with two of these interactions; inelastic secondary electrons (SE) scattering and elastic back scattered electrons (BSE) scattering “Back Scattered Electrons (BSE)”.

Low energy electrons ($\sim 10\,\text{keV} - 50\,\text{keV}$) are typically used to instigate SE interference, where upon collision of the incident electron, the specimens atom is ionised, releasing an

outer bound electron as a detectable SE. SE typically reflect with a wide angle and due to their low energy, only originate from the surface; allowing for Topographical analysis.

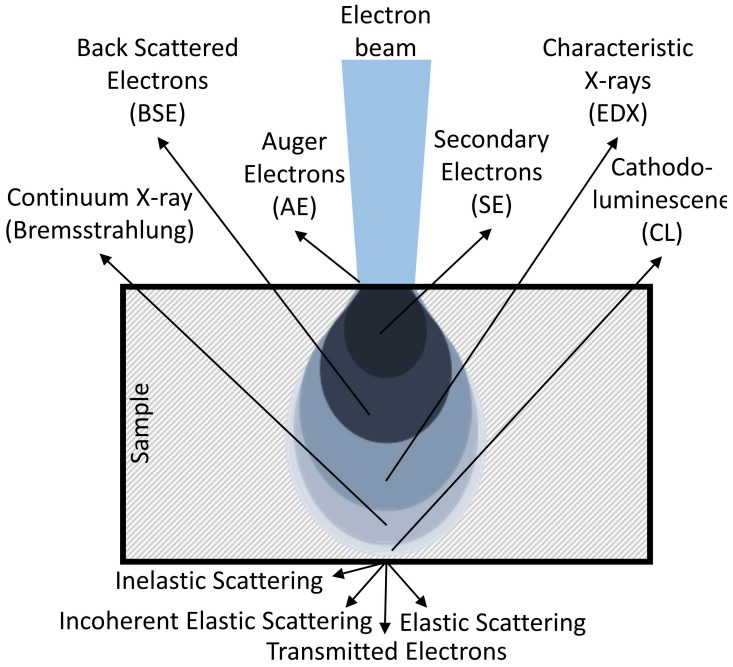


Fig. 3.7. *Escape depths of various types of emissions after interactions between a sample a beam of electrons adapted from Thermo Fisher: electron-microscopy 101*[99]*.*

Higher energy electrons are used for BSE analysis. Here elastic collisions between the smaller incident electrons with the larger atoms causes a change in trajectory. If the trajectory change is larger than $180°$ then they may escape from the surface of the sample and be recorded as a BSE. The likelihood of BSE interactions is less than SE due to the restricted angle of approach, leading to less resolved images. However, useful compositional data can be acquired from BSE as larger atoms are more likely to scatter and therefore lead to brighter images or spots within the sample.

Energy dispersive X-rays (EDX) also occur when bombarding a sample with a beam of electrons. Here, the incident electron excites a core electron to a higher energy state creating a low-energy vacancy in the atoms' electronic structures. Thereafter, an outer electron cascades to fill the vacancy and return to ground state; in doing so, to maintain

energy conservation, an X-ray photon is emitted. X-ray emission is discrete for each element, therefore, EDX allows for a surface sensitive (due to the low mean free path of the electron beam) qualitative or quantitative compositional study of a given sample. Quantitative analysis is limited due to technical limitations compromising resolution and the need for high-quality standards.

Figure 3.8 shows the atomic interactions with the incident electron to produce SE, BSE and EDX interference.

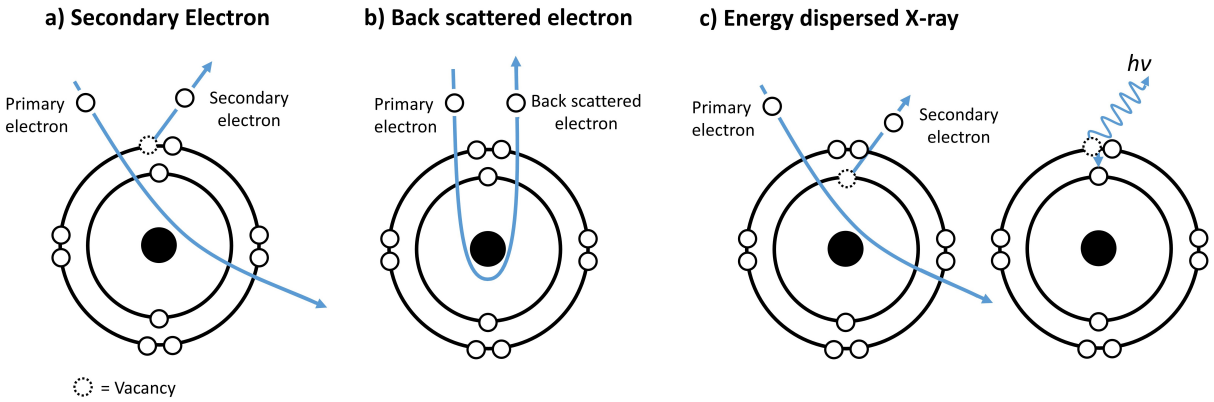


Fig. 3.8. *Atomic mechanisms that lead to (a) secondary electron, (b) back scattered electron and (c) energy dispersed X-ray emission adapted from Thermo Fisher: electron-microscopy 101*[99].

3.2.2 Instruments

For this thesis a FIB Tri-beam SEM, a Philips XL30 FEG SEM and a Hitachi tabletop TM4000Plus was used. For image collection all three are set up using an electron column; a simplified and generic electric column is given in Figure 3.9.

Similar to an optical microscope where light is reflected off a sample and focused onto a detector with the use of a series of (typically curved glass) lenses, electron microscopy reflects electrons from a sample onto a detector using a series of (magnetic or electrostatic) lenses.

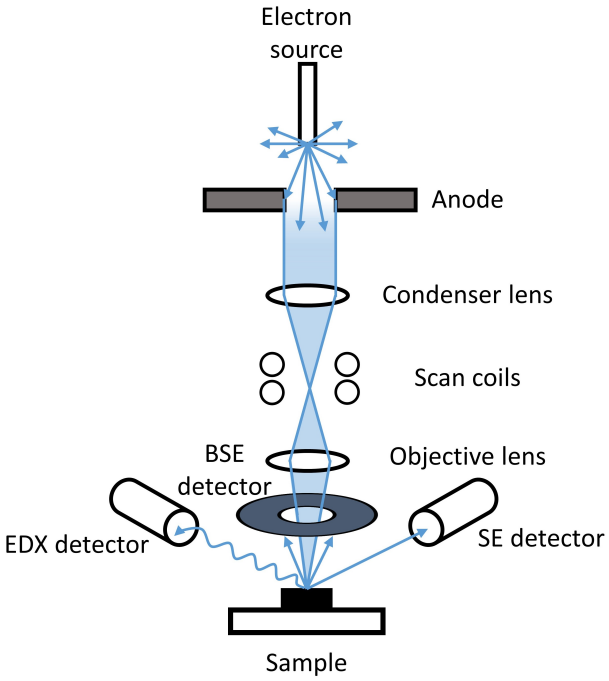


Fig. 3.9. *SEM instrument schematic adapted from Thermo Fisher: electron-microscopy 101*[99].

Both the FIB Tri-beam SEM and the Philips XL30 FEG SEM used a Schottky-based thermionic field electron gun and the Hitachi tabletop TM4000Plus used a pre-centred cartridge tungsten filament. The former is categorised as a field emission source and the latter as a thermionic source. The thermionic source uses heat to excite electrons to exit the surface of either a tungsten filament (as used in the Hitachi tabletop TM4000Plus), LaB6 or a CeB6 crystal. An anode placed nearby is needed to make the electrons flow in the same direction and therefore create a beam. A field emission source uses a strong electrostatic field to induce electron emission. A sharp tipped tungsten wire is used as the cathode allowing high-energy electrons to be released via quantum tunnelling. Field emission sources can be aided via the Schottky effect by coating the tip with zirconium oxide. The Schottky effect lowers the work function at a metal-semiconductor interface under the influence of an electric field. This occurs due to the flow of electrons from the metal to the semi-conductor, once equilibrium is reached a positively charged region is left on

the metal surface and a negatively charged depletion region of lower barrier height at the semiconductor surface.

Much like optical microscopy, electron microscopy uses lenses. Unlike optical microscopy the lenses are used before reaching the sample to focus the beam onto an area of the sample, whereas optical microscopy uses the lenses to focus the image collected from the sample. Another key difference is that although curved, transparent materials that can refract light like glass are used for optical microscopy, magnetic or electrostatic lenses are required to alter the electron beam. As electrons are negative, when they move through a magnetic field, they are subjected to the Lorentz force, forcing the particle along a curved trajectory determined by the magnetic field direction. The field in a microscope is generated by a series of coils or solenoids in which an electric current flows through. The established magnetic field can be altered in order to curve the electrons together, focusing the beam, or away from each other defocusing the beam. Electrostatic lenses use a series of electrodes to produce an electric field this again influences the paths of electron allowing it to be focused or defocused below the electrode plates. Enzel plates are typically used in electron microscopy, consisting of three charged plates, a negative plate sandwiched between two positive plates. The benefit being that the electrons experience a similar electrical potential upon entering and exiting and therefore allows control and stability in the electron beam.

Backscattered electron detector (BSD) is typically placed above the sample and uses p-n junctions to absorb electrons and create electron-hole pairs which can generate a measurable current. A secondary electron detector (SED) (typically a Everhart-Thornley detector) is placed to the side of the sample and uses a scintillator inside a Faraday cage. A positive bias is applied to the Faraday cage, attracting low-energy electrons which upon hitting the scintillator creates detectable luminescence. A silicon drift detector (SDD) is used for EDX analysis. This is a solid-state detector consisting of monolithic silicon crystal

divided into several individual segments. Upon irradiation the X-ray is absorbed producing an electron-hole pair, these electrons drift to an electrode, producing a readable current.

3.3 | X-ray photoelectron spectroscopy

3.3.1 Fundamentals

X-ray photoelectron spectroscopy (XPS) is a surface sensitive technique that makes use of the photoelectric effect. This is where upon incidence of light, from the surface of a sample, electrons are emitted if the energy supplied by the light is above the work function (the minimum energy required to liberate an electron from the material). For XPS a sample is irradiated with monochromatic soft X-rays (Mg Kα:1253.6 eV or Al Kα:1486.6 eV) and detects the resulting emitted photoelectrons to determine elemental composition.

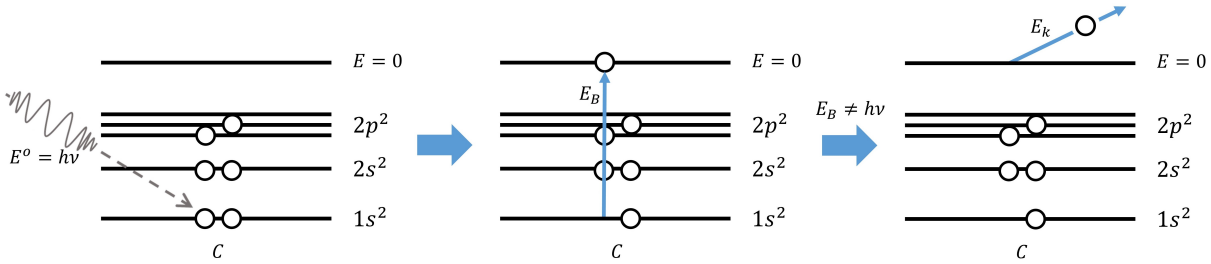


Fig. 3.10. *Schematic diagram of photo-electron emission and associated energy conservations adapted from Handbook of X-ray Photoelectron Spectroscopy, J. Moulder*[100]*.*

A diagram of photoelectron excitation is given in Figure 3.10. Here a core electron is excited by the incident photon. If the energy is greater than the attractive forces between the electron and the nucleus, known as the binding energy, then a photoelectron may escape the atom with a kinetic energy that is equivalent to the excess energy gained from the photon. Resulting in the following equation:

$$H\nu = BE + KE \tag{3.3}$$

In effect the binding energy is the energy difference between the initial core energy state and the fermi level. As core energy states are discrete, only photoelectrons of discrete kinetic energies will be emitted. Therefore, if the kinetic energy of the emitted photoelectrons can be measured, then the resulting binding energy can be used to determine the parent element, its oxidation state, and its chemical environment. It must be noted that an experimental work function correction must be added which will account for the electrons low mean free path length, any spectrometer interference as well as energy requirements caused by material characteristics such as composition, surface smoothness, temperature and any external fields that may alter the photoelectron energy. Therefore, binding energy is calculated via the following equation:

$$BE = h\nu - KE - \Phi \tag{3.4}$$

Where Φ is the work function.

The low energy incident X-rays have a penetration depth on the order of $1\,\mu$m-$10\,\mu$m. However the surface sensitivity arises from the path length of the low kinetic energy electrons, typically around $10\,$Å, meaning only ionisation from the very surface is detectable via XPS analysis. This also requires the analysis chamber to be held under ultra-high vacuum

3.3.2 Spectral analysis

A survey scan ($0\,$eV-$1200\,$eV), a carbon $1s$ scan ($280\,$eV-$300\,$eV), an sulfur $2p$ scan ($155\,$eV-$175\,$eV) and a manganese $2p$ scan ($635\,$eV-$660\,$eV) are given in Figures 3.11(a), (b), (c), (d). A survey scan is used to identify what elements are present in a sample. Each element has a distinct region corresponding to specific core energy levels with lighter elements at lower binding energies (to the right). Each peak corresponds to photoelectrons from discrete energy level that has lost no energy, the stepped background corresponds to similar electrons but for those that have lost kinetic energy upon travel and therefore correspond to

pseudo higher binding energies. Once the elements are identified a more local and higher resolution scan can be used to identify elemental environments.

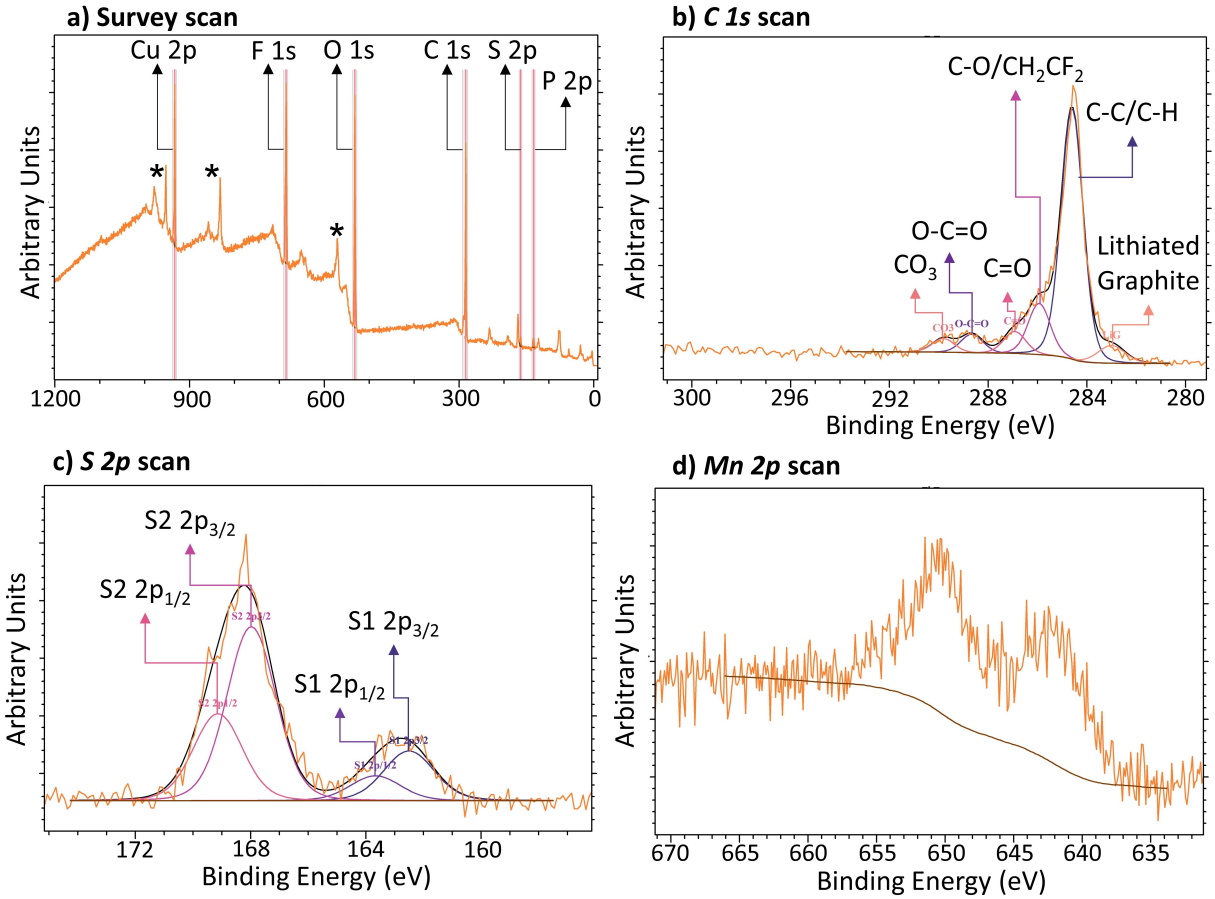


Fig. 3.11. *Fitted experimental XPS data of an air exposed anode sample. (a) A survey scan of the entire XPS spectrum, showing the regions of relevant atomic environments as well as Auger peaks highlighted with an asterisk. Scans were also taken within the (a) $C\ 1s$, (b) $S\ 2p$ and (c) $Mn\ 2p$ regions.*

Electrons from $1s$ environments give rise to a single peak where shifts in the binding energy corresponds to the local environment of the originating atom. Higher oxidation, higher hybridisation, adjacency to higher electronegative functional groups will all increase the binding energy of the electron and therefore the corresponding peak. Complex molecules will lead to a number of environments, this can be seen in the $C\ 1s$ scan (Figure 3.11(b)).

Peaks resulting from core levels of higher angular momentum *i.e.* from p, d and f, will split due to spin-orbit coupling. The interactions of the electrons spin and the orbitals angular momentum leads to a splitting of energy levels that would otherwise be degenerate. Both peaks are denoted by nl_j, where n is the principal quantum number, l is the angular momentum and j is the total angular momentum calculated by $|s + l|$. Therefore, the two peaks resulting from $S2p$ excitation gives $2p_{1/2}$ and $2p_{3/2}$, as shown in Figure 3.11(c). The degeneracy and therefore area ratios of the two peaks can be calculated via the total angular momentum (j). More specifically the area is proportional to the sum of all magnetic quantum numbers (mj) associated with a total angular momentum, which can be calculated by $2j + 1$. Equating to 2 for $2p_{1/2}$ and 4 for $2p_{3/2}$, therefore a 1:2 area ratio. Spacing between the two peaks is constant and determined by the difference in energy between the two energy levels. This allows determination of environments by setting ratio and spacing constraints.

Multiplet splitting is similar to spin-orbit coupling, arising due to interactions between spin and magnetism. Multiplet splitting occurs when the emitting atom contains an unpaired electron, as seen from the manganese signal given in Figure 3.11(d), indicating an oxidised manganese. Here a valance electron can couple with the generated core-hole, giving rise to several final states. This gives rise to complex patterns. Within transition metals, ligand charge-transfers leads to variance in peak spacing and intensity, often leading to misinterpretation if assumed as typical spin-orbit coupling.

Other spectral features include Auger peaks and satellite peaks. Within XPS, Auger peaks are an interference caused by Auger radiation. This is where a valance electron drops into a generated core-hole within an excited atom, where energy conservation occurs via the emission of a second electron. These produce discrete peaks that are independent from the energy of the ionising photon. These peaks are labelled in 3.11(a) with an asterisk. Satellite peaks arise from various physical processes occurring simultaneously to excitation. A number of satellite peaks can occur, but one example is the shake-up peak. This peak

arises from the interaction of the outgoing photoelectron and its parent atom, where some of the energy transfers back to the atom causing it to enter an excited sate.

3.3.3 Chemical environments

The binding energy of XPS and HAXPES chemical environments will shift depending on the surrounding environment, often leading to a range of values for a certain environment within the literature.

In order to accurately account for each environment, FWHM and positional constraints are often used to limit the fitting of peaks. The constraints used within this thesis and the corresponding chemical environments is given in Table 3.2. The reasoning for each corresponds to environments discussed within the literature.

Table 3.2. *The constraints used within casaXPS for the assigned peaks for XPS and HAXPES analysis. Similar peak positions found in the literature are also shown. Literature positions following '~' were obtained from the figures binding energy axis as the binding energy value were not stated.*

Chemical environment	Peak position constraint (eV)	FWHM constraint (eV)	Values found in literature (eV)
Lithiated graphite	283.5-281.0	0 to 2	282 [101] 281.9-282.0 [102]
C−C/C−H	285-284.6	0 to 2	284.8 [103][104] 284.4 [102]
C−O	286.2-285.8	Same as C−C/C−H	285 [103] 286 [105] 285.5 [104] 286.1-286.2 [102]
C=O	287.5-285.9	Same as C−C/C−H	286.5 [106] ~286.5 [105] 288.7 [102]
O−C=O	288.7-288.3	Same as C−C/C−H	~288.9 [106] ~288.5 [105]
$CO_3{}^{-2}$	290.2-289.8	Same as C−C/C−H	~290 [105] 292.9-293.3 [102]
Fluorocarbons	294-290	Same as C−C/C−H	287.2- 294.2 [107]
$LiPF_6$	692.0-676.2	Same as Li_yPF_x/ $LiPF_x(OR)_y$	~688 [106]
Li_yPF_x/ $LiPF_x(OR)_y$	692.0-676.2	0 to 2	~686.6 [106] 687.0-687.5 [102]
LiF	692.0-676.2	Same as Li_yPF_x/ $LiPF_x(OR)_y$	~685 [106] 684.6 [101] 684.1-684.9 [102]

3.3.4 Hard X-ray photoelectron spectroscopy

Hard X-ray photoelectron spectroscopy (HAXPES) is an extension of XPS that uses higher energy X-rays (for instance Ga Kα: $9250\,$eV). This technique results in deeper sample penetration due to producing photoelectrons of higher kinetic energy and therefore larger mean free path length. This leads to a technique that can study the buried surface of a sample. HAXPES also provides the benefit of exiting deeper core electrons, for instance the sulfur $1s$ orbital.

Simplistically the intensity of photoelectrons emitted can be determined via Beer-Lamberts law, given below:

$$I_s = I_d e^{-d/\lambda} \tag{3.5}$$

Where I_s refers to the intensity of photoelectrons at the surface, I_d intensity at a depth of d below the surface and λ is the inelastic mean free path. For photoelectrons emitted via Al Kα radiation a λ of around $1\,$nm-$3.5\,$nm is obtained resulting in a depth of around $3\,$nm-$10\,$nm. For XPS and other electron spectroscopy techniques the exponent is commonly quoted and termed the electron attenuation length. The use of Ga Kα effectively triples the electron attenuation length, increasing the elastic depth profiling to between $10\,$nm-$51\,$nm for C $1s$ signals from graphite. The inelastic electron attenuation length is expected to be twenty times this value, effectively increasing depth profiling to hundreds of nm.[108]

A disadvantage to HAXPES is the increased peak broadening and background intensity. This is due to the increase in inelastic interactions caused by the escape of deeper electrons moving through the material. The use of hard x-rays also leads to greater charge effects on the sample.

3.3.5 Instruments

A schematic of an X-ray photoelectron spectrometer is given in Figure 3.12.

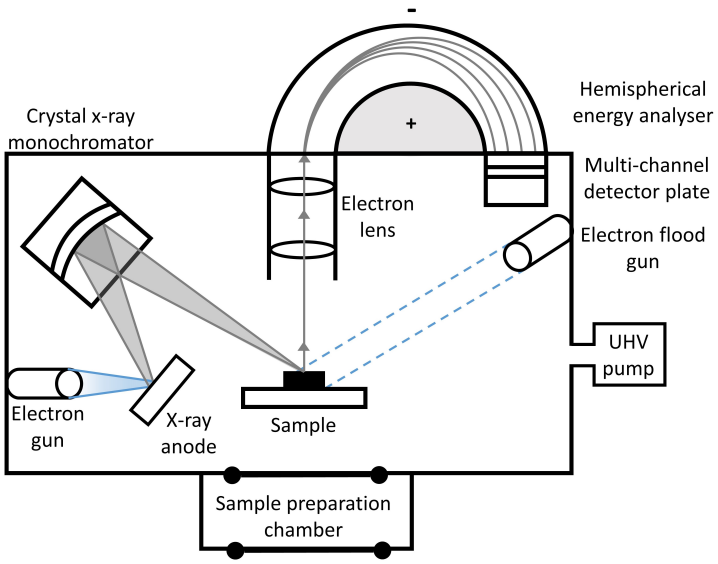


Fig. 3.12. *XPS instrument schematic adapted from Handbook of X-ray Photoelectron Spectroscopy, J. Moulder*[100].

X-rays are produced by bombarding a water-cooled anode metallic plate with a beam of electrons sourced from an electron gun (electron guns are described in Section 3.2.2). The energy of the produced x-rays depends on the anode plate and the intensity depends on the electron current. Typically, a curved quartz crystal is used to monochromate the light using Bragg diffraction via constructive interference (discussed in Section 3.4).

The sample is placed in a chamber under ultra-high vacuum where the x-ray beam interacts with the sample. After a series of transfer lenses, a concentric hemispherical analyser (CHA) is used to disperse photoelectrons of different energies via electrostatic interactions caused by two conductive hemisphere electrodes held at a potential. Multichannel electron detectors are placed at the end of the track, allowing kinetic energy detection via which detector is hit.

A low voltage flood gun is often required to prevent charge build-up within the sample. This provides a flood of low energy electrons that can charge balance the surface. If not used, the release of electrons will disproportionally charge the surface. This may cause

shifts in binding energy, broadening of peaks and a loss of intensity. This charge build up affects insulating samples more than conductive samples.

3.4 | X-ray diffraction

3.4.1 Fundamentals

X-ray diffraction (XRD) is a non-destructive technique that allows for the study of structural information within crystalline material.

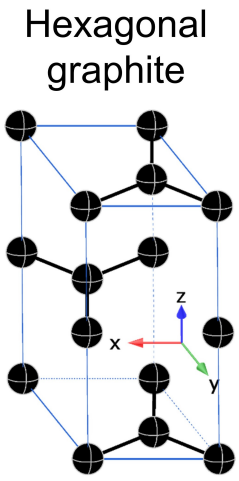


Fig. 3.13. *Graphite unit cell.*

Crystalline structures are created by translational symmetry of repeating unit cells. A lattice point is a space within the unit cell and can be defined via fractional coordinates; a three dimensional coordinate consisting of (a, b, c) where a value of 0 generally refers to the bottom left corner of the unit cell and a value of 1 for a, b and c indicates the other side of the unit cell in the x, y and z axis, respectively. A unit cell for graphite is given in Figure 3.13. Unit cells have modes of symmetry, for instance, inversion centres, n-fold rotations and mirror planes. Combining all symmetry elements allows the unit cell to be characterised into a space group of which there are only 230. The hexagonal unit cell of graphite contains a

six-fold rotation, mirror planes, a six-fold screw axis, and fits within the Hermann-Mauguin notation, space group of $P6_3/mmc$. Where the P refers to a primitive unit cell (1 lattice point per unit cell), 6 refers to the six-fold rotation around the c axis, the 3 subscript refers to a three-fold screw axis around the same axis, $/m$ refers to a mirror plane normal to the rotation axis, the second m refers to a mirror plane in the a axis and c refers to a c axis glide plane.

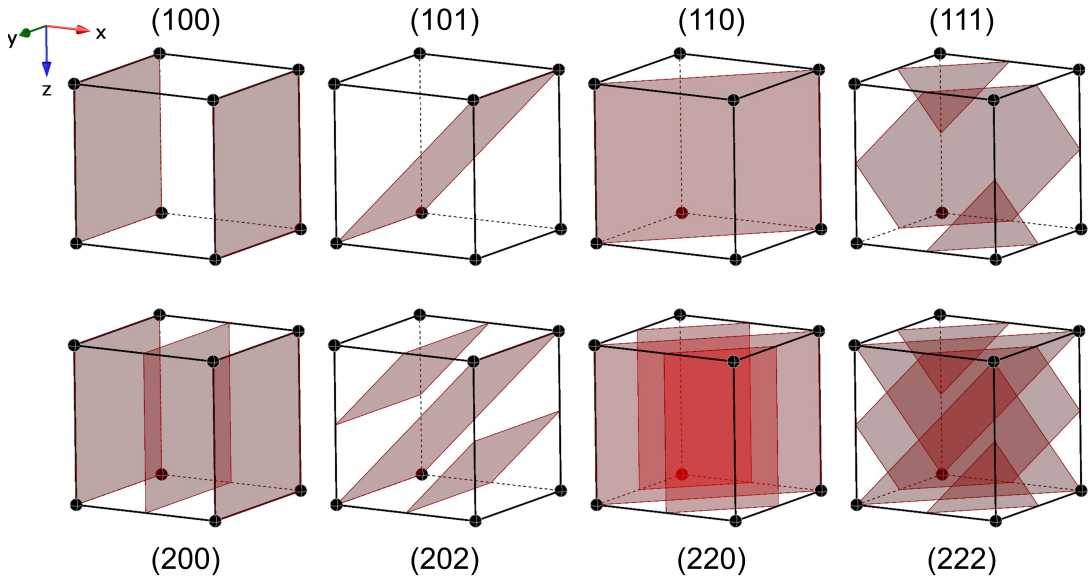


Fig. 3.14. *Examples of lattice planes and their Miller indices.*

Lattice planes are mathematically constructed periodic parallel planes that pass through groups of lattice points describing the arrangement of atoms within an entire crystal lattice. Examples of lattice planes are given in Figure 3.14. One member of the set must pass through the unit cell origin $(0, 0, 0)$ and the interplane distance is denoted by d. Miller indices are used to label these crystal planes. Miller indices can be found by finding where the plane containing the origin passes through the edges of the unit cell in the a, b and c direction, the reciprocal of these fractional coordinate is taken and denoted by $(\frac{1}{a}\ \frac{1}{b}\ \frac{1}{c})$ to give (hkl). Examples of these are given in Figure 3.14. The d spacing between planes can be found by using the relation of the geometry of the unit cell and the Miller indices of the

planes. Some of these relationships are given below:

$$\text{Cubic: } \frac{1}{d_{hkl}^2} = \frac{h^2 + k^2 + l^2}{a^2} \tag{3.6}$$

$$\text{Tetragonal: } \frac{1}{d_{hkl}^2} = \frac{h^2 + l^2}{a^2} + \frac{l^2}{c^2} \tag{3.7}$$

$$\text{Orthorhombic: } \frac{1}{d_{hkl}^2} = \frac{h^2}{a^2} + \frac{k^2}{b^2} + \frac{l^2}{c^2} \tag{3.8}$$

$$\text{Hexagonal: } \frac{1}{d_{hkl}^2} = \frac{3}{4}\frac{h^2 + hk + k^2}{a^2} + \frac{l^2}{a^2} \tag{3.9}$$

Diffraction is the observed behaviour of a wave bending when passing by an edge or through a narrow opening, such as a slit in a wall. If a wave passes through a slit with a width similar to the wavelength of the wave, the wave will diffract considerably, causing a circular or radial spreading of the wave past the slit. When a wave passes through multiple slits in an object, known as a diffraction grating, the wave will diffract from all the slits. A diffraction pattern arises through the constructive or destructive interference of superimposed waves on the other side of the slits. A diagram of this effect is given in Figure 3.15.

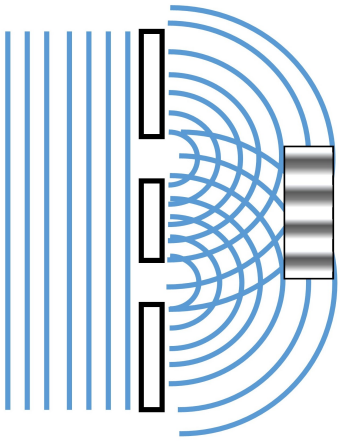


Fig. 3.15. *A diagram of the propagation of waves through two slits and the resulting diffraction pattern.*

The wavelengths of X-rays typically fall in the range of 0.01 nm to 1 nm. The spacing between atoms in crystal lattices is on the order of Angstroms (Å); therefore, a a crystal lattice can act as a diffraction grating. This phenomenon leads to the production of interference patterns upon the incidence of X-rays. The regular atomic arrangement, indicated by lattice planes, results in an overall measurable diffraction pattern that can be analysed to study crystalline features. Constructive interference of X-rays diffracted by a crystal lattice leads to a quantifiable diffraction peak. This occurs when the path difference between two waves, one reflected from one plane in the crystal lattice and the other reflected by a neighbouring plane, is an integer multiple of the wavelength. This is known as Bragg's law and is expressed mathematically by:

$$n\lambda = 2d_{hkl}sin(\theta) \tag{3.10}$$

Where n is an integer reflecting the order of the diffraction, λ is the wavelength of incident light, d is the interlayer spacing, hkl is the Miller indices of the planes and θ is both the angle of incidence and diffraction in respect to the plane. Therefore, by scanning through a series of θ angles (typically 2θ is used), the presence, and angles of all lattice planes within a crystalline lattice can be found. A diagram of incidence that leads to a diffraction peak is given in Figure 3.16.

If a large, highly ordered single crystal is used, the diffraction pattern results in a two-dimensional image that, when analysed, reveals the arrangement of atoms, thereby showing the crystalline structure of the material. However, it is difficult and impractical to develop most materials into a single crystal. Powder X-ray diffraction (PXRD) is much more commonly used. X-rays are incident onto smaller crystals/powder of a sample and a diffraction pattern is collected. However, as the particles are randomly orientated, a radial pattern is obtained where each ring corresponds to diffraction from a lattice plane. An example of a PXRD pattern obtained for graphite is shown in Figure 3.17.

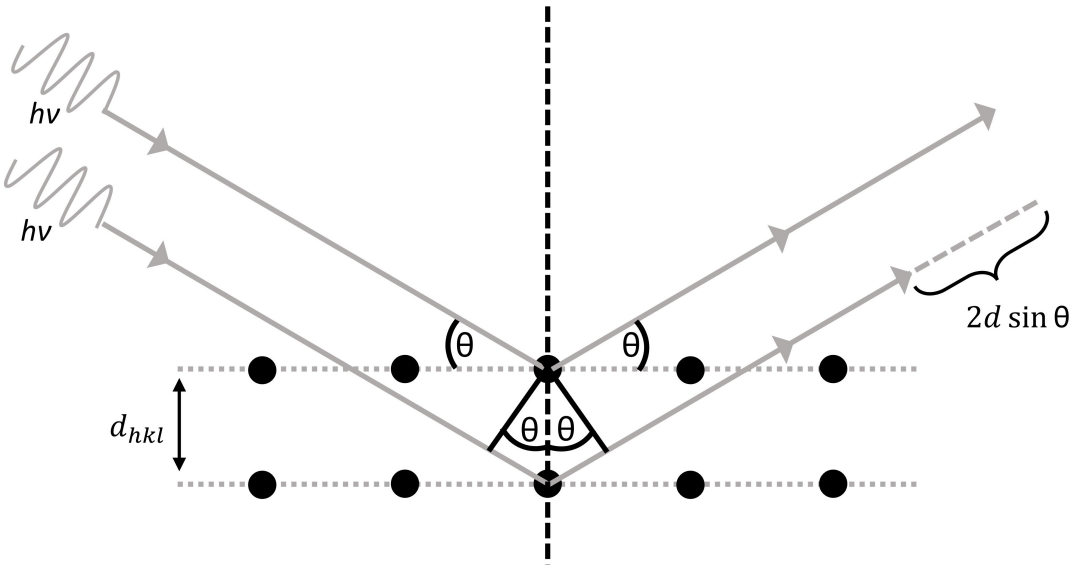


Fig. 3.16. *Two beams of identical wavelength approaching and diffracting off a crystalline structure adapted from Inorganic Chemistry, M. Weller[88].*

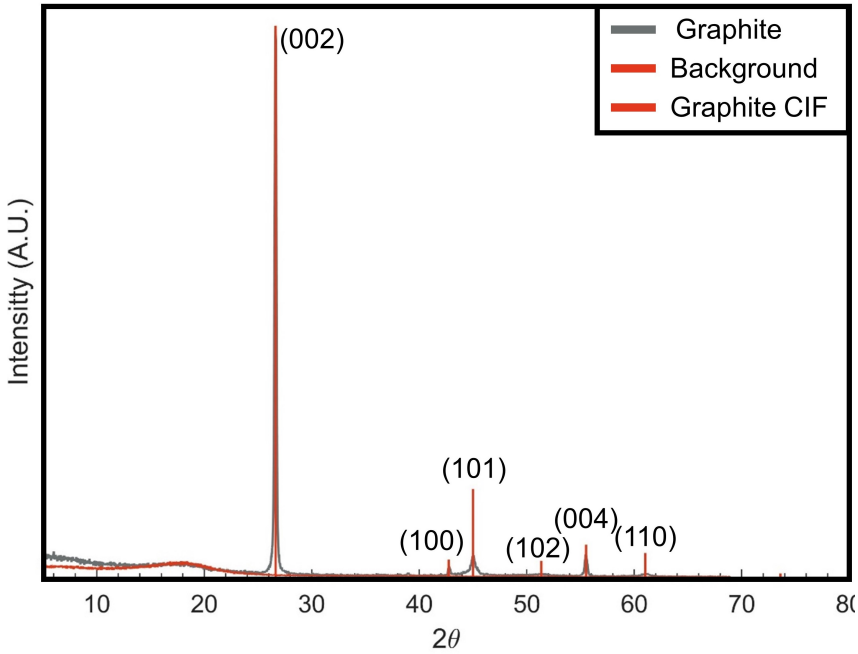


Fig. 3.17. *Graphite PXRD pattern. Experimental data was collected from an annealed EoL sample. Crystallographic Information File (CIF) taken from Fayos.[109].*

3.4.2 Pattern analysis

Peaks within a diffraction pattern

The d spacing correlating to a peak can be found by resolving Braggs law with the 2θ positions of peaks found in a PXRD pattern. Each crystal lattice will give a unique set of d spacing, allowing for a search and match routine to identify the sample.

Crystal symmetry and orientation determine which planes give rise to a measurable peak. Similar symmetries between planes can give rise to degeneracy, mean that one peak may arise from multiple planes of the same symmetry. Systematic absences also occur, where the spacing between planes will lead to destructive interference. The response a plane will have is determined by the structure factor (F_{hkl}), which corresponds to the resulting wave after being scattered by all atoms in the unit cell (f) in the direction $2\theta_{hkl}$. The intensity of a peak is proportional to the squared value of F_{hkl}. F_{hkl} for a given plane can be resolved using the following equation:

$$F_{hkl} = \sum_{j=1}^{m} N_j f_j e^{\frac{2\pi}{hx_j+ky_j+lz_j}} \tag{3.11}$$

Where m is the number of atoms in the unit cell, N_j is the occupancy of atom j in the unit cell, f_j is the scattering factor of atom j, (x_j, y_j, z_j) are the fractional coordinates and (hkl) are the plane indices. This process can be simplified as symmetry within the unit cell typically led to rules in symmetrical absences. For graphite of symmetry $P6_3/mmc$, the primitive (P) centring allows for all (hkl) values, the 6_3 rotational symmetry allows for only even l values on ($00l$) planes parallel to the c axis and the c glide plane only allows even l values for ($0kl$) and ($h0l$) planes perpendicular to the a and b axis, respectively. By determining the d spacing and thereby Miller indices (by using the relationships given in Equations 3.11) of the present peaks in a pattern, structural identification can be attempted.

Once the samples unit cell has been identified, peak shape and position can be used to identify a number of lattice effects. The observed pattern is a time-dependent average diffraction, resulting from the interaction of X-rays with the probability distribution of the electron cloud; therefore, vibrations of atoms from thermal effects, distortions to the crystal lattice either via impurities, amorphous structure or small crystallite sizes give rise to broadened peaks. Lattice strains can lead to either an increase or decrease in peak positions when uniform or result in peak broadening when non-uniform. Intensity is primarily determined by the scattering factor of an atom which can be affected by atomic number, the spatial distribution of electrons, crystal orientation, and phase fraction of the corresponding sample. Preferred orientation occurs in graphite and is a whole spectrum effect where certain crystallographic planes are preferentially aligned, leading to non-uniform intensities in the diffraction pattern often increasing the preferred planes and decreasing the rest. This occurs with particles of acicular (needle-like or plate-like) shape meaning certain crystallographic planes may have a higher likelihood of aligning in a specific direction. This phenomenon can also be observed in thin films and textured polycrystalline samples where deposition or mechanical processes promote alignment.

PXRD refinement

Refinements are whole pattern fits that can be adjusted via A least-squares iterative process to match the experimental data. Variables like atomic displacement (thermal parameters), unit cell parameters and atomic fractional coordinates are refined to match the theoretical pattern to the data allowing for a more accurate representation of the crystal structure.

There are two refinements that are normally used. Rietveld refinement where the intensity is bound to crystal structure, often used to refine a known pattern to experimental data. The other, Pawley fitting, where the intensity is a free parameter for fitting, allowing unit cell fitting without a known structure.

PXRD Single peak analysis

For the analysis of graphite using PXRD, structural parameters are often extracted from the reflections themselves. Calculations found in the literature for the interplane distance (d_{00l}), crystallite size in the c-axis (L_c) and a-axis (L_a), packing density (ρ), and the number of polyarene layers within a crystallite (N) are given below.[110,111]

$$d_{00l} = \lambda/2 \sin \theta_{00l} \tag{3.12}$$

Where λ is the wavelength and θ_{00l} is the reflection angle of reflection $00l$ where l= 2, 4 or 6.

$$L_c = 0.9\lambda/(\beta_{00l} \cos \theta_{00l}) \tag{3.13}$$

Equation 3.13 is the Debye-Scherer equation. The 0.9 is the K constant and corresponds to the crystallite shape; here it refers to a spherical particle with a cubic unit cell. β_{00l} represents the full width at half maximum (FWHM) of reflection $00l$

$$L_a = 0.9\lambda/(\beta_{100} \cos \theta_{100}) \tag{3.14}$$

While β_{100} represents the FWHM of reflection (100) and θ_{100} represents the reflection angle of reflection (100).

$$\rho = 0.762/d_{00l} \tag{3.15}$$

Where 0.762 is a constant representing the density of a spherical particle with a cubic unit cell.

$$N = L_c/d_{00l} + 1 \tag{3.16}$$

3.4.3 Instruments

A schematic of a Bruker D8 Advance X-ray diffractometer is given in Figure 3.18. This X-ray diffractometer as well as a synchrotron source X-ray diffractometer were used within this

thesis. Whilst the synchrotron produces high intensity X-rays via accelerating a charged particle, the D8 diffractometer uses an electron gun and a (copper) anode metal plate, similar to that discussed within the XPS section. A monochromator is then used before the beam hits the sample. The sample is placed on a rotating platform, to aid in preferred orientation removal. Detectors on both diffractometers use scintillators and photodetectors to count photons. These detectors typically use detector strips to acquire positional data. Both the detector and emitter are attached to a rotating wheel so that the whole 2θ range can be scanned.

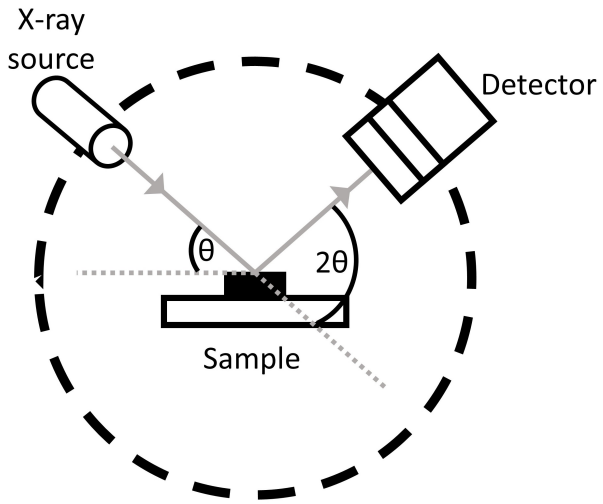


Fig. 3.18. *PXRD instrument schematic adapted from Inorganic Chemistry, M. Weller*[88].

3.5 | Inductively coupled plasma - optical emission spectrometry

3.5.1 Fundamentals and instrument

Inductively coupled plasma – optical emission spectrometry (ICP-OES) is an analytical technique used to determine the quantity of multiple elements within a given sample to the ppm scale.

Again, the principle of an excited electron returning to ground state and producing a discrete photon is used, however, with this technique, ionisation is achieved by providing large thermal energy. Heat is produced via the use of inductively coupled plasma (ICP). There are two definitions for a plasma, the first is a conductive gaseous mixture containing both ions and unbound electrons. The second description, primarily used in spectroscopy, is a partially ionised gas with sufficiently high temperatures to atomise and ionise most elements in the periodic table.

An ICP burner is used to create an ICP from argon gas fed through the burner. A diagram of this burner is given in Figure 3.19. Radio frequency (RF) induction coils are wrapped around the quartz torch and a current is fed through to induce a strong magnetic field. A spark is used to initially ionise the gas, then the magnetic field accelerates and oscillates the released electrons which collide with other atoms, ionising those atoms and creating a steady plasma. The temperature of the plasma varies reaching up to $8000\,\mathrm{K}$-$10\,000\,\mathrm{K}$ at the core and dropping down to $5000\,\mathrm{K}$-$6000\,\mathrm{K}$ around the tail region. the stability of the tail region means sample is fed through and analysed within this section of the flame.

Samples analysed are typically in an aqueous solution which are fed into the burner as an aerosol using a nebulizer and spray chamber. The nebulizer uses a thin capillary and

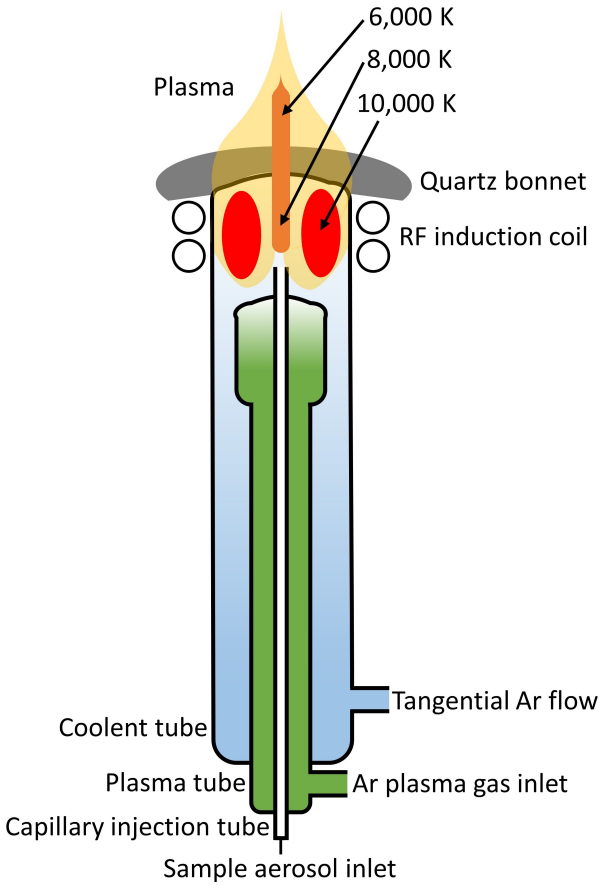


Fig. 3.19. *Schematic diagram of the ICP torch adapted from Instrumental Analysis, D. Harvey*[112]*.*

suction created by the flow of argon gas; the spray chamber is used to capture particles that are too big for analysis.

Light produced from the torch is dispersed using a polychromator (diffraction grating) and a CCD detector is used to identify wavelengths and therefore atoms.

3.5.2 Data collection

ICP may not ionise all atoms within a sample, this is determined by the ionisation energy and Boltzmann distribution given in Equation 3.17

$$\frac{N_i}{N_0} = \frac{g_i}{g_0} e^{-\Delta E/kT} \tag{3.17}$$

As well as this, most atoms return to ground state via collisions, affecting the intensity of the signal. Other effects like spectra overlap, matrix effects and background interference also change the intensity of the signal, leading to a decrease in accuracy.

These interference effects can be removed by analysing standards of known concentration to produce a calibration curve. The intensity of the unknown sample can then be compared to this curve to calculate the concentration of certain atoms.

3.6 | Particle size analysis

3.6.1 Fundamentals

particle size analysis (PSA) can be achieved in multiple ways, the two techniques discussed here are dynamic image analysis (DIA) and the use of lasers with the principle of Mie scattering. Both techniques could be utilized using the Microtract Flowsync particle size analyser.

Both techniques require the sample dispersed in an aqueous solution. This is achieved firstly via mechanical separation by using agitation and ultrasonic vibrations, then secondly by using physico-chemical separation via the addition of a dispersing agents. A sodium phosphate salt was used which upon addition into water ionises, resulting in positive cations and negative anions within the solutions. These ions will exaggerate any electrostatic interactions between particles, leading to a more stable diffusion.

DIA uses a back light and a short exposure, high acquisition camera to effectively image the shadow of particles. By using algorithms that take into account Brownian motion (random motion of particles caused by the collision of fast-moving particles within a medium) particles can be tracked and all angles of the particle can be captured, allowing for size

and morphology studies. Distributions of values can be made by tracking a large number of particles within a sample.

Rayleigh scattering refers to the elastic scattering of light by a particle. If the particle is spherical and smaller than the wavelength of light, the radial scattering of light is determined by the following simplified equation:

$$I = \frac{I_0 8\pi 4 N_a 2}{\lambda 4 R 2}(1 + cos2\theta) \tag{3.18}$$

Where I is the intensity of resulting light, I_0 is the intensity of incidence, N is the number of scatters, a is the polarizability, R is the distance from the scatter and θ is the angle of scattering. Therefore, the particle scatters light in all directions but the scattered light is more intense parallel to the light of incident. The amount of scattering is also dependant on the wavelength of light. In effect, the incident wave acts as a propagating electrostatic field which polarizes the small particle into an electric dipole. This (Hertzian) dipole oscillates with the frequency of the incident wave, emitting light in all directions.

Mie scattering refers to the scattering of light by particles that have a comparable or slightly larger size to the wavelength of incident light. Here scattering is much more complex and leads to a more pronounced forward lobe with less dependence on the wavelength of light. Scattering effects based on particle size is given in Figure 3.20.

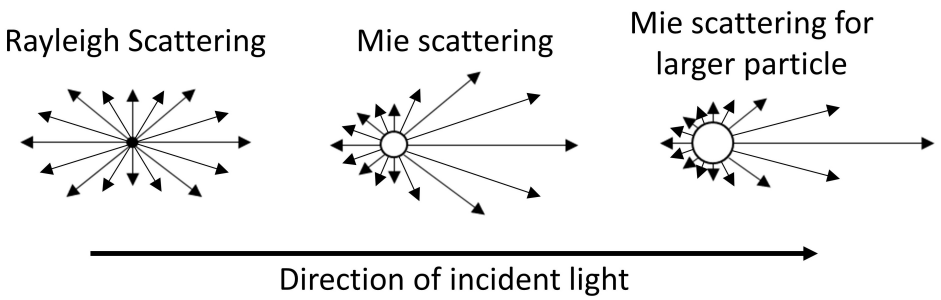


Fig. 3.20. *A schematic diagram of Rayleigh and Mie scattering adapted from microtrac*[113].

For PSA, the Mie scattering pattern can be collected and related to the size distribution of the sample. This is known as laser diffraction analysis (LDA).

3.6.2 Instruments

A schematic of a particle size analyser using both LDA and DIA is given in Figure 3.21.

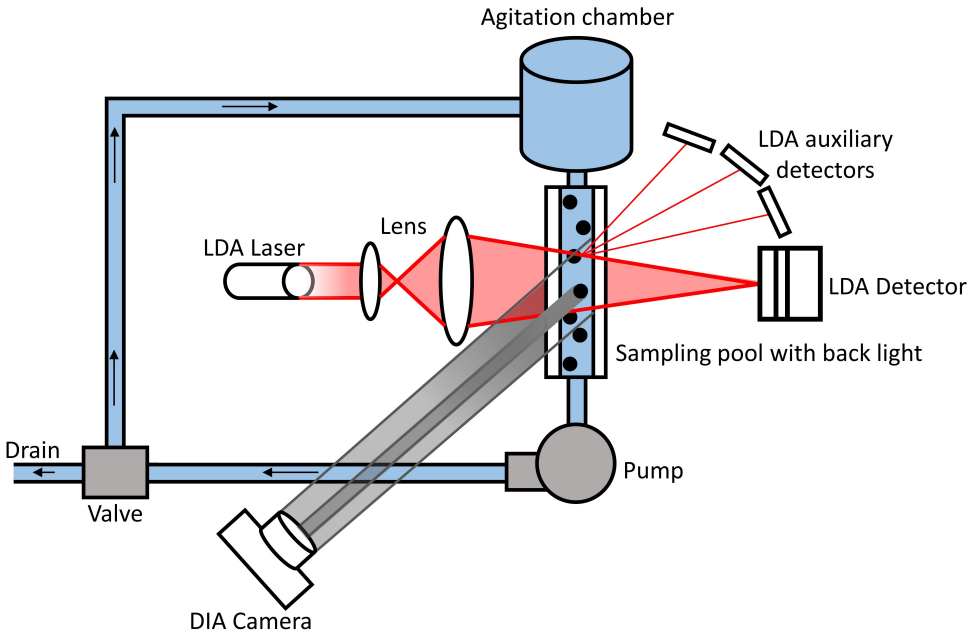


Fig. 3.21. *A schematic of a PSA adapted from microtrac*[113].

The sample for analysis is kept in an agitated pool, before analysis. For analysis, the sample is continually run through a piping network, where sample analysis is conducted in a flow cell sensing zone.

Two cameras are used for DIA, one is used to capture large particles and the second zoomed in camera detects smaller particles.

For LDA, two lasers are commonly used: a red 780 nm and a blue 405 nm (these lasers are also used to provide the backlight for DIA). Auxiliary detectors and a main detector are used to gather the resulting pattern and determine the size of particles.

3.7 | Thermal gravimetric analysis

Thermal gravimetric analysis (TGA) is a technique that studies the mass of a sample as a function of temperature or time. A sample is typically put under a controlled temperature program under a controlled atmosphere. This allows for a study of thermal stability, composition, and decomposition characteristics of a sample within a controlled environment.

The SII EXSTAR 6000 used within this thesis places the sample in a platinum pan and compares the mass to a standard platinum pan. These pans are placed on balance beams, where the change in mass changes the height of the sample, this is then recorded by an optical sensor and strain gauges to give a value of mass.

3.8 | Electrochemistry

3.8.1 Half-cells

A full lithium-ion cell is one in which the potentials of the cathode, anode and electrolyte are balanced to create a working energy storage device. These cells are perfect for commercial use, typically supplying stable high capacity, however, the number of active components makes electrochemical analysis of a given material difficult. Therefore, half cells are typically used to study electrochemical behaviour. Here, lithium metal is used as the anode and the reference electrode for the active material for study. Lithium metal is used due to the low ionisation potential (-3.04 V vs the standard hydrogen electrode) meaning it can act as a reference electrode for both anode and cathode material. As well as this it has a large specific capacity of $3860\,\mathrm{mA\,h\,g^{-1}}$, meaning the cell is not limited to the lithium ion reservoir provided by the counter electrode.

Half cells provide an intrinsic look into the electrochemical properties of a material but will not be able to fully predict the materials performance in a full cell. Therefore, half cells act as a good initial test of a material before further testing in full cells and higher loaded cells.

3.8.2 Galvanostatic analysis

Procedure fundamentals

Galvanostatic analysis is a technique that uses a constant current to test the electrochemical performance of a material. This is achieved by varying the current and voltage limits for a set of cycles; the capacity, cycling stability, and rate capability of a battery material can be assessed. This technique allows the study of charge-discharge behaviour, capacity fade, and any electrochemical reactions occurring within the battery electrode during cycling. Typically, a trace of the voltage is converted to a "charge-discharge" graph with voltage and gravimetric capacity as the axes. Gravimetric capacity ($mA\,h\,g^{-1}$) can be found by multiplying time by the current and dividing by the active mass.

The voltage profile slope not only shows the capacity and voltages of redox reactions, but can also be used to determine the type of (de)lithiation reactions that occur when an active material is cycled. A sloped profile where the voltage depends on capacity is typical of a solid solution (de)lithiation. This is where lithium ions are removed randomly from the structure. A two-phased (de)lithiation may also occur, this is where lithium ions are removed from certain regions, giving rise to two distinct phases; this is indicated with a plateau, where voltage is independent from capacity. Both mechanisms are seen in graphite during distinct stages of (de)lithiation and shown below in Section 3.8.2.

Both delithiation mechanisms can be simplified to the following equations:

$$\text{two-phased: } LiC_6 \longrightarrow LiC_6 + (1\text{-}x)C_6 + xLi^+ + xe^-$$

Solid solution: $LiC_6 \longrightarrow Li_{1-x}C_6 + xLi^+ + xe^-$

The reasoning behind the observed voltage slopes for each mechanism can be describe through two lines of thought.

First, consider band structure. During the delithiation of a two-phased system, the phase being delithiated remains as LiC_6, and therefore its band energy structure will remain constant. This means the voltage (the difference between μ_c and μ_a) will remain constant throughout the delithiation, resulting in a plateau within the voltage profile. In contrast, if a solid solution phase is considered, the atomic structure of the delithiating species—and therefore the electronic structure—constantly changes during delithiation. This change in the atomic structure will alter μ_c and therefore the voltage, leading to a sloped profile.

The second line of thought involves Gibb's phase rule, expressed as follows:

$$F = C - P + 2 \tag{3.19}$$

Here, *F* represents the number of degrees of freedom, which refers to the number of independent intensive variables required to fully describe the state of a system (*e.g.*, pressure, temperature, or chemical composition). *C* represents the number of components, accounting for the separate species within a system. Finally, *P* represents the number of phases, referring to any part of a system that is immiscible with the other parts.

In the two-phased system, there are two components (LiC_6 and C_6) that are immiscible (*i.e.* two phases), leading to two degrees of freedom. Therefore, if temperature and pressure remain constant, the chemical potential of all species—and, consequently, the cell voltage—remains constant at all states of charge.

In a solid solution system, there will be one phase: $Li_{1-x}C_6$, which consists of two components: LiC_6 and C_6, leading to three degrees of freedom. Therefore, at fixed temperature and pressure, the chemical potential will change, resulting in a variation in voltage.

Generally within the thesis, currents used corresponding to $C/20$ ($18.6\,\text{mA}\,\text{g}^{-1}$) for the formation cycles and $C/5$ ($74.4\,\text{mA}\,\text{g}^{-1}$) for testing. Where C corresponds to the theoretical capacity of the material of interest and $\frac{1}{n}$ is the reciprocal of the theoretical hours it will take to fully (dis)charge the material. For graphite, the lithiation process follows:

$$6\,\text{C} + \text{Li}^+ + \text{e}^- \longrightarrow \text{LiC}_6 \tag{3.20}$$

The theoretical gravimetric capacity (amount of capacity that can be obtained from a fully lithiated sample) can be calculated via:

$$Q = \frac{nN_A e}{M_W} \tag{3.21}$$

Where Q is the capacity, n is the number of moles of electrons released, N_A is Avogadro's constant, e is the elementary charge of an electron and M_W is the molecular mass, in this case, of lithiated graphite ($72\,\text{g}\,\text{mol}^{-1}$). The lithiation of graphite involves 1 mol of electrons, Therefore $nN_A e$ totals $96\,472$ C. A more appropriate unit for electrochemistry is A h, where 1 A h is equivalent to the charge that allows one ampere of current to flow for one hour. As 1 C is equal to 1 A s, then A h is equal to $1/3600$C, converting $96\,472$ C to $26.80\,\text{A}\,\text{h}\,\text{mol}^{-1}$ for graphite. Finally this value can be converted to a theoretical gravimetric capacity, giving $372\,\text{mA}\,\text{h}\,\text{g}^{-1}$.

The choice of the used C-rates was arbitrary; however formation cycles require slower rates so that less irreversible reactions caused by increased over-potential will occur, resulting in the choice of $C/20$. $C/5$ was an adequate rate for testing and was similar to rates seen in other studies within the literature.[24,37,114–120]

Expected graphite electrochemical behaviour

A standard voltage profile for graphite is given in Figure 3.22. This figure shows the third charge and discharge cycle, therefore minimal interference from SEI production is

expected to alter the profile. Found within the literature are five distinct graphite (dis)charge intermediate phases. These correspond to lithiations up to LiC_{6n} structures. Also identified in the literature is two two-phase (de)lithiating mechanisms and one solid solution (de)lithiating mechanism.[24,37,114,118,120] The visibility of these phases are dependent on the cycle rate and external conditions (like temperature) used.[120] These are highlighted in Figure 3.22.

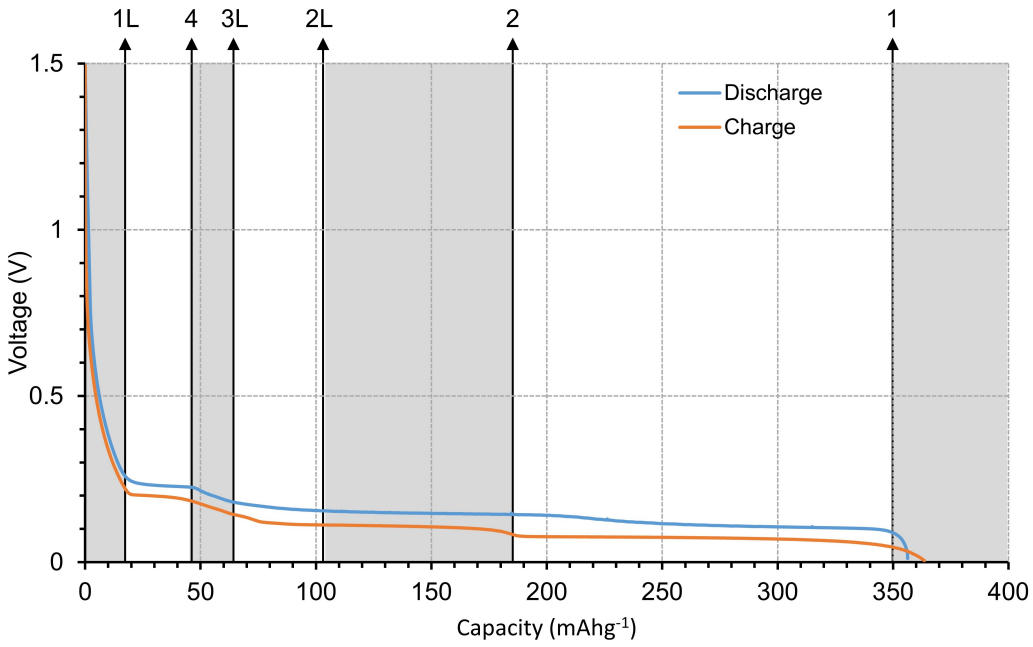


Fig. 3.22. *Phase transitions of graphite during lithium (de)intercalation shown on a voltage profile of EoL extracted using HNO_3 delamination solution.*

As per the norm of graphite analysis, this description of the voltage profile is a simplification. Many higher order phase transitions exist between these phases. This explains why the gradient of the voltage profile cannot be simply described by changes between a two-phase transition and a solid solution transition. As well as this, only the crystal structures of stage 1 and 2 have been proven.[24,37,114,118,120] This leads to a large debate over the mechanisms between stage 4 to stage 2, likely there are many transitionary phases between these stages.[24,37,114,118,120]

A two-phase mechanism can be identified using XRD. The material would produce two patterns, one of the first phase and a second of the next phase when tested at the voltage of transition, for graphite this would be indicated by the presence of two (002) peaks. Peaks within cyclic voltammetry would also indicate this type of transition, which for graphite, can be found for each stage except stage $0 \rightarrow 1L$. Due to resolution issues and the large preferred orientation of the (002) peak, a two-phase mechanism has only been confirmed for the $1L \rightarrow 4$ and the $2 \rightarrow 1$ stages.[24,37,114,118,120]

3.8.3 Differential capacity

Procedure fundamentals

dQ/dV plotted against charge (V) can give a differential capacity plot that can be used to identify electronic mechanisms and cell ageing. This analysis is also termed "differential capacity analysis".

Plots can be created by differentiating raw time series current and voltage data from galvanostatic testing. Smoothing functions (a moving average was used for this work) are required as noise is exaggerated during differentiation. Once collected charge data is plotted and the discharge data is inverted then plotted.

dQ/dV plots give fingerprint patterns where each peak refers to an equilibrium between two transitionary phases. The difference between the positions of the peaks in the charge and discharge profiles can indicate an over-potential. The intensity of the peak indicates the capacity gained from that transition and therefore a decrease in intensity would indicate less capacity and increased resistance.

Expected graphite electrochemical behaviour

Graphite gives a distinctive differential capacity pattern. Each peak in the charge (top) and discharge (bottom) cycle corresponds to the equilibrium between two stages, each are highlighted in Figure 3.23 and discussed in Section 3.8.2.

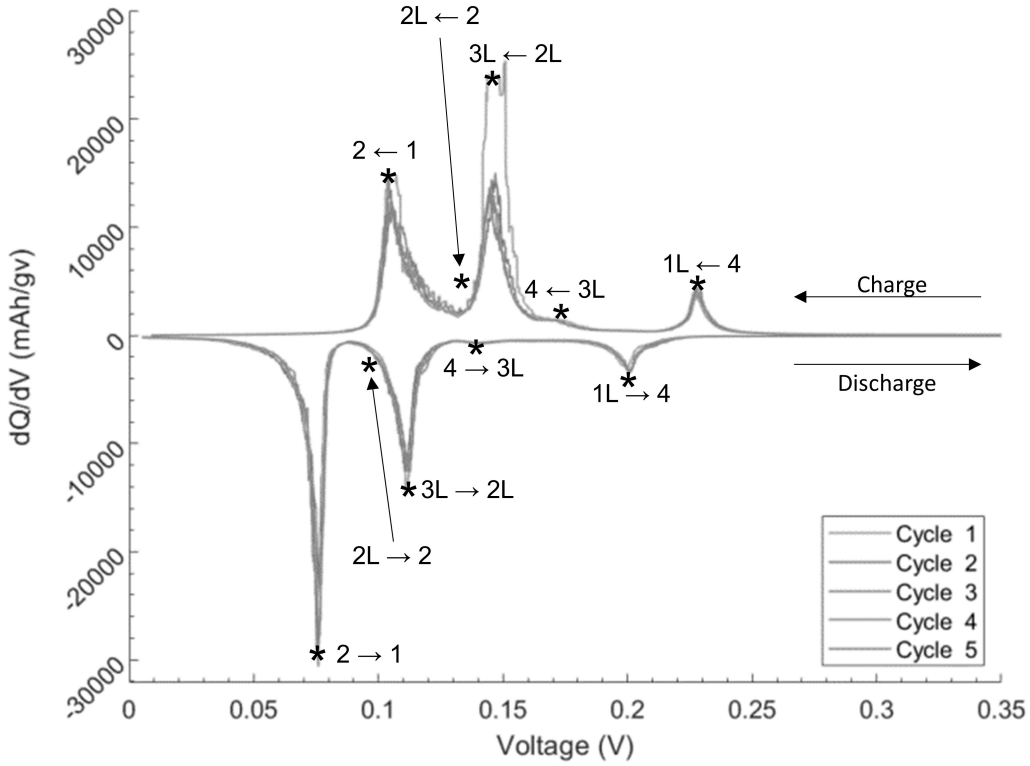


Fig. 3.23. *A differential plot showing the phase transitions of graphite during lithium (de)intercalation. Stars highlight peaks and stage associated with that peak is also given. Charge and discharge is in relation to graphite.*

3.8.4 Other electrochemical procedures

Although no other testing procedures were used in this thesis, other programs can be used to gain more insight into electrochemical behaviour.

dV/dQ "differential voltage analysis" plots can be made in the same way as dQ/dV "differential capacity analysis" however, instead of the peaks representing phase equilib-

ria they represent phase transitions. Perhaps useful for resolving graphite (de)lithiation transitions.

Other programs can be used like potentiostatic analysis which keeps a constant voltage and measures the current output. Dynamic studies can be conducted which sweeps between either different currents (galvanodynamic) or voltages (potentiodynamic). In application, combinations of these charging techniques are used to efficiently charge and discharge batteries, this allows for efficient use, as well as extended lifetime of a cell. Typically, a battery management system is used to control this. Testing using constant current-constant voltage conditions can allow for testing under real life conditions.

Electrochemical impedance spectroscopy (EIS) uses a range of modulated alternating currents to measure the resistance response within the battery. This allows for the individual analysis of multiple mechanisms within the battery, for instance, electrolyte resistance, charge transfer resistance at the electrodes and resistance from SEI formation.

CHAPTER 4

Anode materials entering the recycling stream

4.1 | Disclaimer

Work within this chapter has been published in *Sargent et al.*[121]. Inert-air Raman analysis was carried out in collaboration with Mr Luke Sweeney, a PhD student with Professor Paul Anderson. Both authors have contributed to the collection of data and therefore the analysis will appear both in this thesis and that of Mr Luke Sweeney.

4.2 | Introduction

Predictions indicate that 16.5 million EVs may reach EoL by 2031. If underutilised this could lead to valuable materials being lost and a large amount of scrap to dispose of.[47,48,62] At the time of writing, forecasts also predict that LiB giga-factories will produce 4 %-12 % of production scrap compared to the announced capacity.[69,122] This value is even predicted to be larger for less mature manufacturers, ranging between 15 %-30 %.[122] Production scrap is expected to account for 78 % of the LiB scrap pool in 2025, therefore, much like the vehicles reaching EoL, if underutilised, would lead to a waste of critical materials. Both waste streams highlight a need for a recycling industry.[123] Production scrap will account for most of the material entering the recycling stream in the near term. Within a decade,

this could be overtaken by EoL material, as electric vehicles reach the 10-year maturity mark and giga-factories mature their manufacturing processes.[86] Therefore, it is important to understand the quality of both EoL material and process scrap to create a recycling route that can fully encompass both waste streams.

Ageing can occur through several mechanisms including, but not limited to: particle cracking, lithium plating, active material detachment, dendrite formation and growth, and decomposition, growth and dissolution of the SEI layer.[34,50–58] These degradation pathways could potentially affect the quality of the material obtained via recycling, especially when considering this material for electrochemical reuse. Therefore, a study of these materials after dismantlement is required. This not only allows for an inspection of how ageing affects anode material, but will also indicate whether EoL material can act as a source for battery-grade graphite.

The anode materials used within this study are given in Table 4.1. These represent anode materials that are likely to enter a direct recycling plant if set up within the near-future. The materials used include quality-control-rejected (QCR) material, which will acount for a large majority of production scrap and used EV anodes, sourced from a gen-1 electric Nissan Leaf car (EoL). Two QCR anodes are studied, QCR and QCR II, each distinguished via the process of discharge used before dismantlement. More deteriorated samples are also studied (EoL II and EoL III) which represent the more extreme end, where the cells were cycled further to mimic more extended use.

Table 4.1. *The cycling history of the anodes used within this study. ‡Open cell voltage of the cell before dismantlement. ‡‡State-of-charge.*

Sample ID	Sample History	OCV‡
QCR	Quality control reject pouch cell for a first-generation Nissan Leaf. The cell appeared to have gone through formation cycles. This cell was discharged below 0 % SoC‡‡ to an OCV of 0 V by Envision AESC. The cell was left to rest, causing the OCV to rise.	< 1 V
QCR II	Quality control reject pouch cell for a first-generation Nissan Leaf. The cell appeared to have gone through formation cycles. Electronically discharged to a SOC of 0 %.	3.00 V
EoL	A first-generation battery module was taken from a used Nissan leaf with an odometer reading of $\sim$ 40 000 mile. Electronically discharged to a SOC of 0 %.	2.94 V
EoL II	Same origin as EoL however, was further cycled under a 'mild overcharging regime' by *Attidekou et al.*[124] The cell was run for 500 cycles where only 87.12 % of its original capacity remained. Electronically discharged to a SOC of 0 %.	3.22 V
EoL III	First-generation EoL Nissan leaf pouch cell cycled by *Attidekou et al.*[124] to induce 'severe degradation related to overcharging'. After 250 cycles a knee point was reached and cycling stopped after 300 cycles with only $\sim$ 30 % of its original capacity. Electronically discharged to a SOC of 0 %.	3.27 V

4.3 | Chapter aim

In this chapter each of the anode materials described in Table 4.1 will be studied to understand the spectrum of anode materials entering the recycling stream. Studies were first conducted within an inert environment in order to obtain a snapshot of the material just after dismantlement. Changes to the surface were then studied when exposed to air.

4.4 | Experimental

4.4.1 Dismantling, storage and handling of anode materials

Gen-1 lithium ion EoL pouch cells were acquired from a used Nissan Leaf, driven to an odometer reading of $\sim 40\,000$ mile. The EoL cell was stored in a glovebox whilst EoL II and EoL III were further cycled (as described by Table 4.1). QCR and QCR II were obtained directly from Envision AESC. No extra charging was conducted on QCR an QCR II, these were provided with OCVs of < 1 V (over-discharged) and 3.00 V, respectively.

Dr. Roberto Sommerville and Mr Anton Zorin dismantled the pouch cells within an argon glovebox (< 0.1 ppm H_2O and O_2), opening them using a ceramic scalpel. The sides of the casing were cut so that the electrodes and separators could be pulled out, separated, and left to dry. Each cell contained 18 layers consisting of an anode, a separator and a cathode. The dismantling process was similar to that given in the work of *Marshall et al.*[30].

Anodes consisted of 12 mm thick copper foil with 70 mm of anode film cast on each side. The dimensions of all anodes were 200 mm $\times 228$ mm and each weighed approximately 13.79 g. Each anode was left within the argon environment until required. Samples were washed with dimethyl carbonate (DMC) (Sigma-Aldrich, anhydrous, $\geq 99\,\%$) prior to any air exposure. DMC washing consisted of submerging the anode pieces in DMC and rinsing after 2 min of swirling. This was done twice before a final submersion, where the DMC was left to evaporate overnight. This DMC washing procedure was used for all anodes and before each characterisation technique, unless otherwise specified.

4.4.2 Inert atmosphere Raman experimental

This study was conducted on QCR II and EoL III just after dismantlement within an Ar environment (< 0.1 ppm H_2O and O_2). These samples were washed with DMC. For this

study, anodes from layers 1, 2, 9, 13 and 18 were used. To ensure the same side was analysed the topside of each anode was etched with a scalpel before transfer. For each layer, three evenly spaced spots were punched to create 11 mm disks which were used for analysis. These spots were named Tab, Mid and Cnr in relation to the cathode and the positions of which are given in Figure 4.1. Disks were carried to a Renishaw inVia Raman Microscope via an airtight INSTEC HCS621V cell. A $4\,\text{mm}^2$ 10×10 grid at the centre of each disk was used to collect multiple points (shown in Figure 4.1). For each point scans a 488 nm, 25 mW, laser was used at $100\,\%$ laser power, scanned in a range between $750\,\text{cm}^{-1}$ and $2200\,\text{cm}^{-1}$ (centring at $1450\,\text{cm}^{-1}$) using 1 s acquisitions with 10 accumulations.

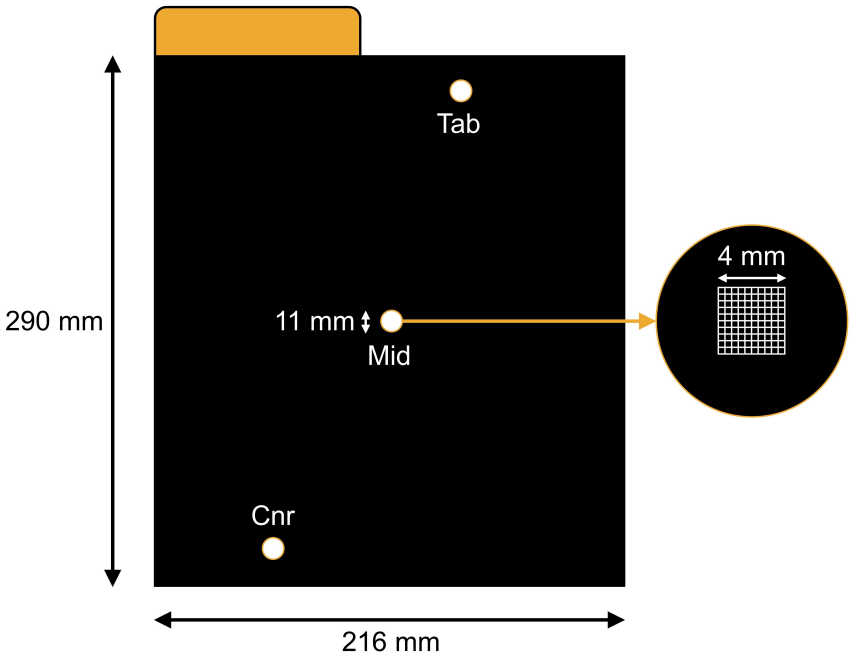


Fig. 4.1. *Diagram of one anode sheet and the disk positions that were punched out for Raman analysis. The 4mm 10x10 grid used on each disk is shown on the right, where each spot was taken at the centre of each square.*

MATLAB software (version 2020a) was used to carry out peak fittings of the obtained Raman spectra.[125] The MATLAB code used modified functions created by Tom O'Haver and John D'Errico.[126,127] A Fourier series background fit was used to represent the shape of the background before five Raman peaks were fitted simultaneously. For each peak, position

and width estimation were inputted, along with peak shape and upper and lower bounds of the fitting area, before running thirty iterations of a boundary constrained scalar minimising function. The peaks fitted correspond to those found within the literature; $D4$ (Voigt, $1150\,\mathrm{cm}^{-1}$-$1310\,\mathrm{cm}^{-1}$), D (Voigt, $1320\,\mathrm{cm}^{-1}$-$1380\,\mathrm{cm}^{-1}$), $D3$ (Voigt, $1450\,\mathrm{cm}^{-1}$-$1525\,\mathrm{cm}^{-1}$), G (Lorentzian, $1525\,\mathrm{cm}^{-1}$-$1590\,\mathrm{cm}^{-1}$) and D' peaks (Lorentzian, $1590\,\mathrm{cm}^{-1}$-$1635\,\mathrm{cm}^{-1}$).[94] The origin of these peaks is discussed in Section 3.1.2. An example of a typical fit obtained with this program is given in Figure 4.2.

Position, width, intensity and integrated intensities were extracted for each peak. I_D/I_G ratios were calculated by combining the $D4$, D and $D3$ bands into a single D region and dividing the combined integrated intensity by the integrated intensity of the G peak. Given the large number of scans (one hundred total measured points for each disk), the fitting procedure was automated and error was concluded from the range of values obtained.

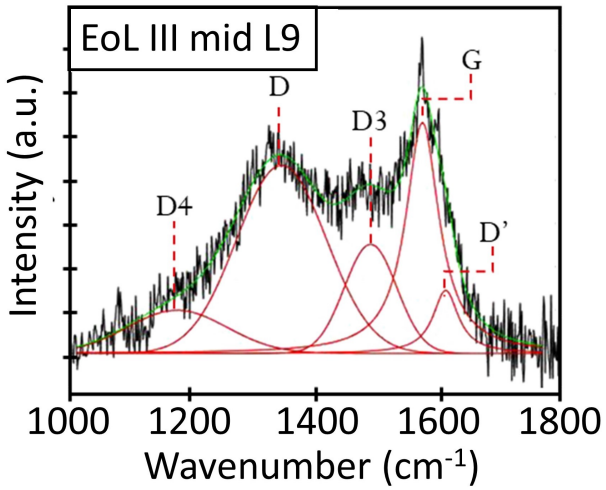


Fig. 4.2. *An example spectrum fit obtained after using the boundary constrained scalar minimising function developed in MATLAB.*

4.4.3 SEM, EDX, and cross-sectional analysis

Inert atmosphere studies

Cells with an identical history to QCR and EoL were used for the inert air study and were therefore given the same sample ID. These QCR and EoL cells were dismantled within an argon glovebox with the aid of Dr. Roberto Sommerville, using the same method as previously discussed (see Section 4.4.1). After which, samples were transferred to a A MBRAUN glove box, fully integrated to a Thermo Fisher Scientific Helios 5 Laser Hydra Laser UX (tribeam system). Samples were affixed to pin stubs via carbon tape (PELCO Tabs, carbon conductive tabs) within the Ar-filled glove box and transferred into the microscope chamber for SEM imaging and composition analysis.

Dr. Wing Kwong Wong operated the instrument. The sample was positioned on a flexible sample holder with movement capabilities in the x and y directions of $100\,\text{mm}$ and a tilt of $60°$. This platform was placed in an antechamber where the sample was purged with nitrogen to displace any residual air before being moved into an ultra-high vacuum chamber for analysis.

The instrument boasted a FEG SEM column with a resolution of $3\,\text{nm}$ at $3\,\text{kV}$, a standard Everhart-Thornley detector, through-the-lens SE and BSE detectors, an Oxford Instrument Symmetry S2 detector for compositional analysis, a plasma-focused ion beam with a beam current of $60\,\text{A}$ for gallium or argon ions, and a femto-second laser.

SEM images were captured using a $5\,\text{kV}$ accelerating voltage, $50\,\text{pA}$ current, SE detector, and a working distance of $3.8\,\text{mm}$. The magnification varied as specified within the figure captions.

Cross-sectional topography analysis was performed using a ytterbium ($1030\,\text{nm}$) oscillating laser at $30\,\text{kHz}$ and $0.6\,\text{W}$ to cut the sample, followed by SEM and EDX analysis of the exposed surface.

SEM after air exposure

DMC-washed samples of each anode were exposed to air for durations of 1 h, 24 h, and 1 week before being transferred into a Philips XL30 FEG scanning electron microscope. A 5 kV accelerating voltage, 50 pA current, SE detector, and a working distance of approximately 10 mm were utilized. Magnification settings were adjusted as specified within the figure captions.

EDX analysis was conducted using a 15 kV accelerating voltage, 50 pA current, an octane silicon drift detector, a working distance of 9 mm, and a magnification of 2,000x.

4.4.4 XPS and HAXPES experimental

XPS and HAXPES analysis was conducted on anodes just after cell dismantling, prior to DMC washing and any air exposure. A second study was conducted on anodes that had been exposed to air (after a DMC wash). These samples were left in air for 1 h and 2 weeks before a vacuum treatment and then transferred into an argon filled glovebox (< 0.1 ppm H_2O and O_2). Samples consisted of 1.27 cm diameter disks cut from near the centre of each anode. XPS and HAXPES measurements were taken at the Department of Chemistry, Photon Science Institute at the University of Manchester, conducted by Dr Zoe Henderson, Dr Alex Walton and Dr Ben Spencer.

HAXPES was performed using monochromated Ga Kα X-ray radiation (9250 eV, 3.57 mA emission at 250 W, micro-focussed to 50 mm) and an EW-4000 high voltage electron energy analyser (HAXPES-Lab, Scienta Omicron GmbH); the instrument has a base vacuum pressure of $\sim 5 \times 10^{-10}$ mbar.[128,129] The entrance slit width used was 0.8 mm, and the pass energies used for survey and core level spectra were 500 eV and 200 eV, respectively, with total energy resolutions of 2.0 eV and 0.6 eV, respectively.[128] The HAXPES instrument also used a monochromated Al Kα X-ray source (1486 eV, 20 mA emission at 300 W) for XPS

scans at the same sample position. Charge neutralisation was achieved using a low energy electron flood gun when required (FS40A, PreVac).

Binding energy scale calibrations were performed by matching the $\mathrm{C{-}C/C{-}H}$ enviroment within the $C\ 1s$ region to 284.8 eV, unless otherwise stated. Analysis and curve fitting were performed using casaXPS[130]. Peak fittings used Lorentzian-approximation shaped peaks (LA(1.53, 243)) for all peaks except lithiated graphite and graphite environments where an asymmetric Lorentzian-approximation (LF(0.65, 1.17, 550, 180, 2)) was used. Peak binding energies and widths were constrained according to environments found in literature; these are given in Table 3.2 in section 3.3.3. Core-level relative sensitivity factors for HAXPES quantification were calculated according to *Cant et al.*[131]. Standard deviations were calculated in casaXPS using a Monte Carlo method to assess the influence of noise on the background and in turn on the fitted peak area.[132]

4.4.5 PXRD experimental

In-house PXRD characterisation was carried out using a Bruker D8 advance diffractometer. A copper anode source was used, generating Cu Kα1 and Kα2 radiation. To create monochromatic Kα1 radiation (1.54 Å) a Johansson monochromator was used. A 1D LYNXEYE_XE_T was used as the detector. 28 min was used for each scan and passed through $5°$ to $80°$. Samples were span at 15 rpm during analysis.

A small segment of each anode with minimal air-exposure was cut and placed onto a Bruker silicon low background holder and held in place with Vaseline for each scan.

The I15-1 XPDF beamline at Diamond Light Source, U.K, was used to collect total scattering data. This was conducted by Javier Castells-Gil. Powder samples were prepared by scraping the anode film off the anode with a scalpel and collecting the active material that came off. Care was taken to not tear the copper foil. Powders were then loaded into borosilicate glass capillaries (1.5 mm outer diameter, 1.17 mm inner diameter) which were

then mounted perpendicular to the beam. Total scattering data collection was carried out at an X-ray energy of 76.69 keV76.69 KeV with two PerkinElmer area detectors. Data collection times of 60 s were used for analysis.

Structural information of graphite was obtained using single peak analysis on both in-house PXRD and and beamline PXRD. Equations used are given in Section 3.4.2.

For each value, a silicon standard was used to remove instrumental broadening.

XRD phase analysis was carried out in DIFFRAC.EVA, peak analysis was conducted in Fityk and Pawley refinements were conducted in Topas Academic v6. [133–135]

4.5 | Inert atmosphere studies

4.5.1 Bulk Raman study

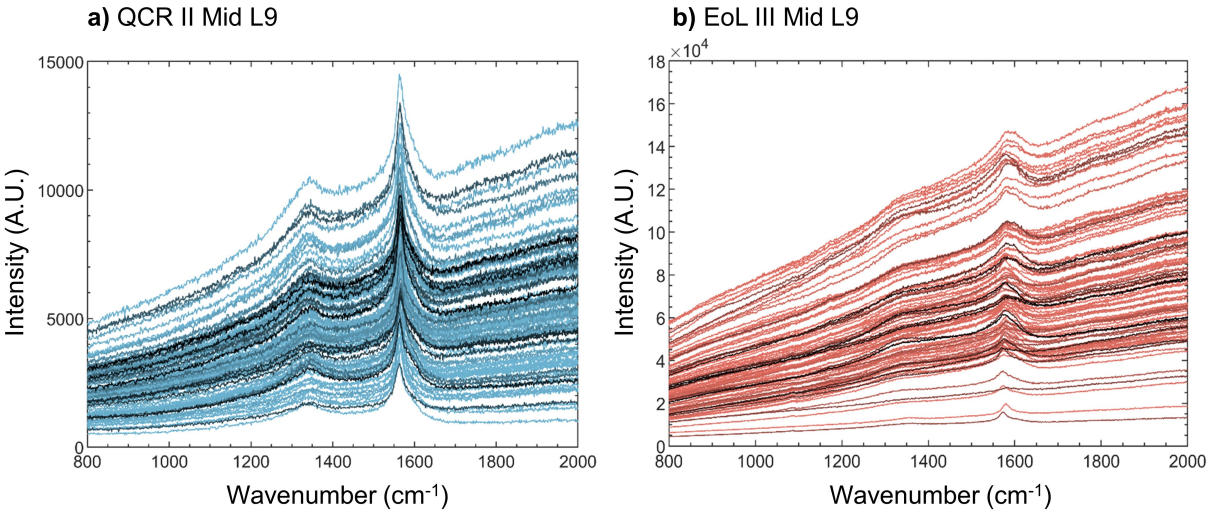


Fig. 4.3. *Waterfall plots of point Raman scans taken from the Mid point of the anode in layer 9 for both (a) QCR II and (b) EoL III cells. Each figure contains 100 point scans taken systematically on a* 4 *by* 4 mm *grid.*

100 Raman point scans taken on the mid point of anodes taken from layer 9 for both QCR II and EoL III are represented as a waterfall plot in Figure 4.3. The most noticeable

differences between the two are the increased background intensity for EoL III and the loss of intensity and sharpness of the graphite region between $1150\,\mathrm{cm}^{-1}$ and $1650\,\mathrm{cm}^{-1}$ for EoL III on comparison to QCR II.[136] This additional noise is likely due to the growth of the SEI layer, depositing amorphous carbons onto the surface that would fluoresce, interfering with the Raman signal, and increasing background noise, reducing peak resolution.[137]

Heavy ageing of the graphite in EoL III was expected. This would include surface amorphous carbon deposition, cracking of particles which would lead to smaller particles (and less order within the graphite), exfoliation, and disorder within the graphene layers; all expected to reduce the intensity of the graphite peaks.[52] These changes will affect the intensities of the D and G bands separately, increasing the former and decreasing the latter. A quantitative study of graphite disorder can be conducted by obtaining the I_D/I_G ratio of a spectrum. The method for this is described within the experimental (Section 4.4.2). The higher the I_D/I_G value, the more the D band contributes, and thereby the more disordered is contained within the carbon material.[31,75,138]

Traditionally, single-point scans are used to identify the ratio. The spatial resolution of the microscope used was around $1\,\mu\mathrm{m}$, and with the $488\,\mathrm{nm}$ beam the penetration depth is quoted to be around $490\,\mathrm{nm}$.[139,140] In reference to PSA data collected and discussed later within this work (Section 5.8.4) it was found that the spherical graphite particles are around $18\,\mu\mathrm{m}$ in diameter. Therefore, the single-point scan will measure a relatively local area compared to the size of the anode and will show interactions from the SEI layer to the sub-surface of the top layer of graphite particles. Within the literature, some suggestions that cell ageing and graphite defects occur locally has been made.[52,53] For instance, lithium plating occurs when the potential drops below $0\,\mathrm{V}$ vs $\mathrm{Li/Li^+}$, this can occur locally from increased resistance caused by spatial variations (like uneven compression of the cell) during fast charging.[141] Therefore, it may be difficult to accurately determine the disorder within the material using a single-point scan.[142,143] This is even evident within Figure 4.3,

where variations in the D region and G peak intensity can be observed. The I_D/I_G ratios for the Mid spots of layer 9 ranged from a max value of 2.43 to a minimum of 1.09 for QCR II and 2.97 to 0.53 for EoL III. This large variation of I_D/I_G ratios supports the notion of local defects.

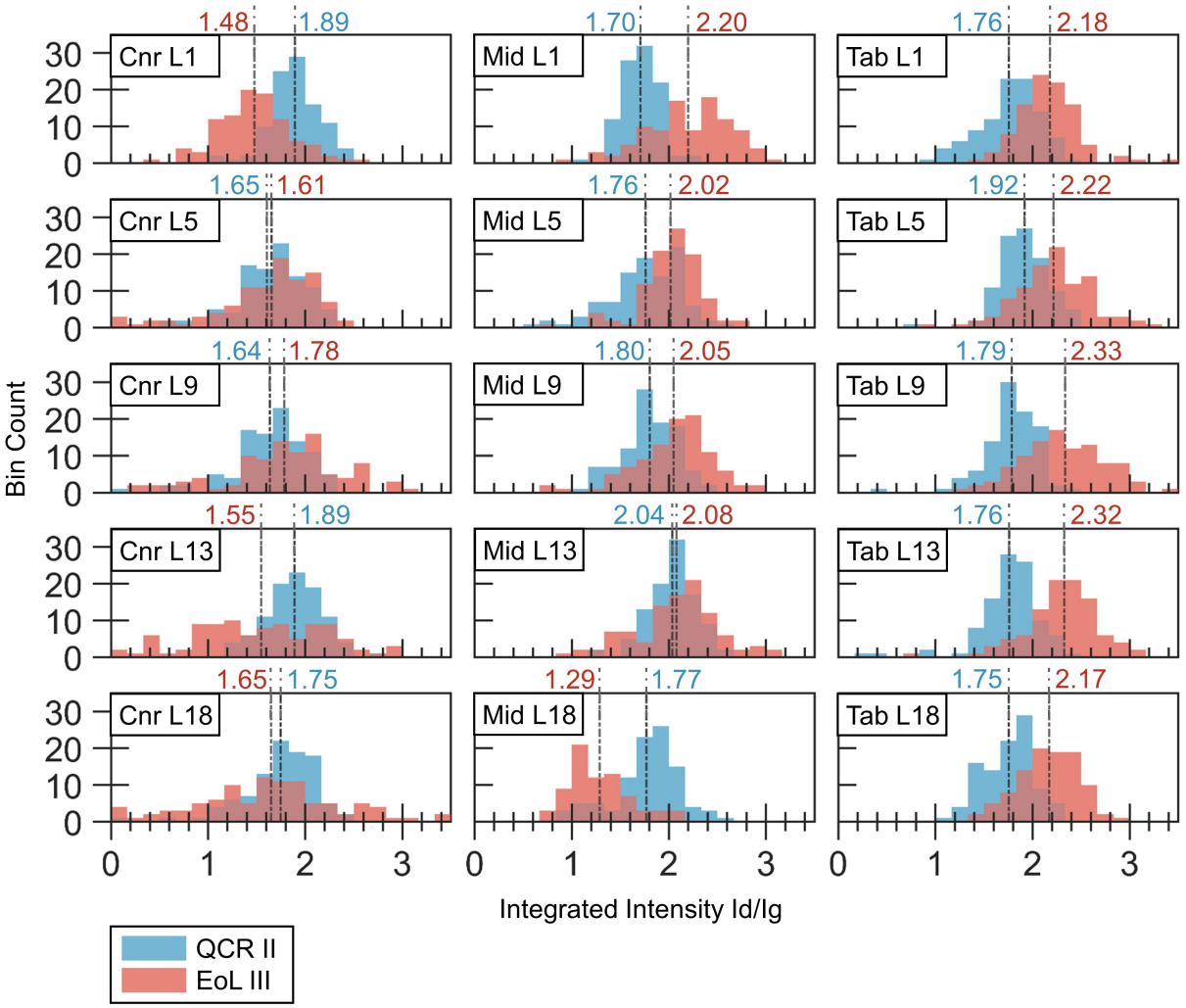


Fig. 4.4. *Distributions of I_D/I_G ratios calculated from 100 Raman spot scans taken using a 10x10 4 mm grid on areas taken from both QCR II and EoL III anode sheets. Cnr, Mid and Tab represent the bottom left corner, middle and top right corner, respectively. L1, L5, L9, L13 and L18 refers to the layer the anode sheet originates from. QCR II is in blue and EoL III is in red.*

By using a 10x10 grid of single-point scans, a distribution of I_D/I_G ratios across a larger area can be plotted to convey a more global property. These distributions are given in Figure 4.4 and show the distributions obtained after 100 single-point scans taken on QCR II overlapped with EoL III for each analysed spot within the cell.

The averages of the QCR II distributions are very similar, ranging around a value of 1.79. The range of I_D/I_G values typically fit a normal distribution with only slight skews for some spots (for instance Cnr L18 skews to the left). The ranges collected for QCRII also typically fall between ±1 of the average. In this example, QCR II acts as the baseline as this sample has only been cycled through the formation cycles and therefore acts as a ready-to-go pristine material. Deterioration is evident for EoL III. Here, a large variation in average I_D/I_G ratios is seen. Averages obtained either shift to lower or higher I_D/I_G values but are generally higher than QCR II. Distributions still typically follow a normal distribution however the range has significantly increased and those that are skewed are more pronounced. These changes in distributions could arise from a number of degradation pathways, for instance, the growth of an in-homogeneous SEI layer, the dislodgement of graphite particles, causing the exposure of other surfaces like the basal plane to the beam, or the desphericalisation of graphite particles.

Due to the surface/sub-surface nature of the Raman analysis, the state of the anode itself showing little graphite dislodgement and the growth of an organic layer evidenced from the proceeding SEM, EDX and XPS studies (Sections 4.5.2 and 4.5.3), a reasonable argument to the cause of this increase in distribution range and I_D/I_G ratios would be surface contamination. This would be through the growth of an SEI layer, depositing amorphous and lithium contaminates on the surface which would mainly favour an increase in the contribution of the D band, but would also add a level of disorder, increasing the range of the distribution. Metal contaminations may also affecting the graphite surface, decreasing its crystallinity and increasing the I_D/I_G ratio.

Average I_D/I_G values for EoL III increase from Cnr < Mid < Tab, apart from L18 which may be anomalous. The range of I_D/I_G values seems to follow an opposite trend, with Cnr spots having the largest variation in values, followed by Mid points then Tab points. The lithiation and delithiation of the anode is heterogeneous, typically not following any discernible patterns due to local spatial variations in charging/discharging.[144] In some occasions, a region of the anode will quickly become fully lithiated/delithiated whereas another region never fully lithiate/delithiate, creating local variations in current density even with a defined value given for the anode current density. This is likely to cause spatial variations in ageing throughout the battery. Interestingly, short-lived local inverted currents were found by *Monasterial et al.*[54], where small regions of the anode lithiates during the anode discharge step and delithiates during charging.

Studies on global variations in degradation within a pouch cell caused by continuous cycling seem lacking within the literature, either focusing on local physical changes like cracking and loss of lithium inventory, or electrochemical studies indicating the overall degradation of the cell. One study conducted by *Charalambous et al.*[144] found that lithium migrates from the centre to the edge nearest the tab on the cathode electrode after continuous fast charging, showing a gradient of degradation could form within a pouch cell. Within cylindrical cells *Bach et al.*[55] found that lithium metal plating first occurred at points of imperfection. Ageing accelerates at these points and the plating radiates out onto surrounding parts of the anode. These points of imperfection included areas of high compression and areas around the tabs. These studies show that ageing within cells does appear to be inhomogeneous as found and shown by the Raman results in Figure 4.5.1.

Prior to dismantling and the work presented here, EoL III was cycled beyond EoL and thermally examined by *Attidekou et al.*[124]. IR thermography was conducted on EoL III (cited as CP1) whilst cycling to obtain full pouch cell mapping of the change in temperature over time (dT/dt) during each discharge cycles. As electrochemical processes, ohmic loss and

polarization generate heat, the cycling behaviour and any degradation processes that may affect that charging can be studied.

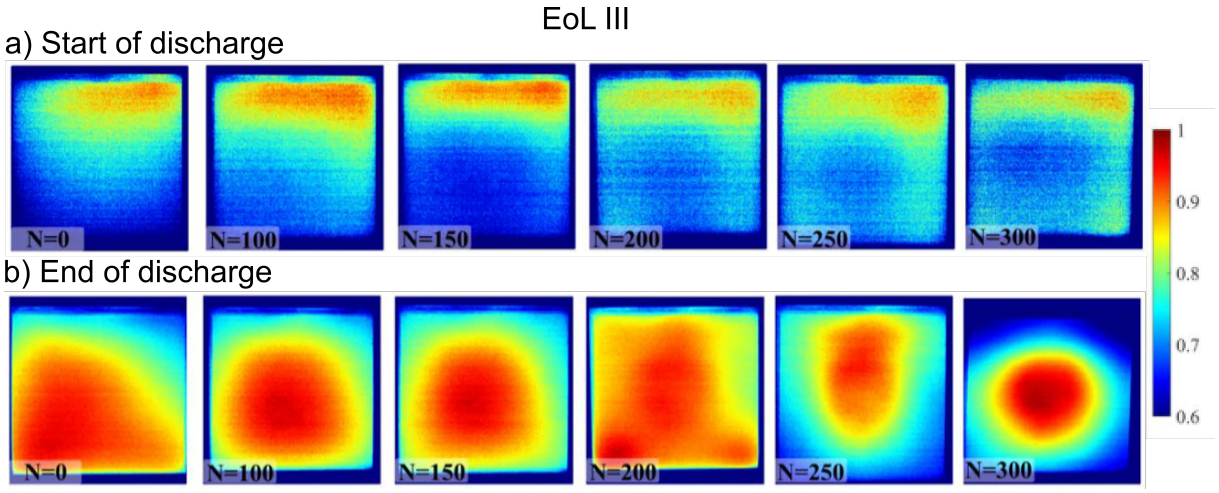


Fig. 4.5. *Normalised dT/dt maps for EoL III (a) 60 s into discharge and (b) at the end of discharge (10 % SoC). Reproduced from Attidekou et al.*[124] *with permission from the Journal of The Electrochemical Society.*

The results of this thermal mapping study normalised to dT/dt_{max} is given within the work of *Attidekou et al.*[124], but a modified version is also given in Figure 4.5. At the beginning of this study, the heat generated at the start of discharge occurred mainly from the top, close to the tabs; as cycling continues, this area becomes more diffused, running down the sides of the cell between cycles 0-150. The heating observed at the start of discharge occurs through local heat generated from battery activity, conduction and resistance within the current collecting tabs. As the cells surface is close to ambient temperature no residual cooling or heating is expected. At the end of discharge (Figure 4.5(b)) local heat generation, heat convection, heat radiation and tab cooling affect the heat distribution. A large trapezoidal hot spot is found centring around the lower centre of the cell up to the 200th cycle. More variation is seen as the cycle number increases, especially at the 200th cycle where the entire cell is heated. After 200 cycles a smaller hotspot is seen with cooling from the bottom at cycle 250 and from both the bottom and tabs at cycle 300. Due to lower internal capacity,

discharge faster for cycle 300 compared to previous cycles; therefore the tabs temperature was significantly colder and therefore, provided a greater cooling effect.

These results may further be used to interpret the gradient in degradation observed within the Raman data (shown in Figure 4.4). If it is assumed that discharge occurs to a greater extent within the hotspots, either due to the production of heat via exothermic electrochemical activity, or via increased kinetics, then a greater extent of discharge can be assumed at the top of the pouch cell, near the tabs during the first $10\,\mathrm{s}$.[145] There are many effects within the cell that will cause heat production including resistance from the active materials, current collector and SEI; heat may also arise from external conditions like the effectiveness of heat conduction, where the tabs will act as both a heat source and heat sink depending on the state of discharge. Therefore, this analysis is only an approximation. However, if this analysis is used then the bottom of the cell appears to be more active during the end of discharge, with the hot spot indicating electrochemical activity. In terms of the graphite anode; graphite at the top of the anode will delithiate at a greater extent at the start of discharge and graphite at the bottom of the anode will delithiate at a greater extent at the end of discharge.

During continual cycling, the start of discharge is fairly consistent, meaning the graphite at the top of the anode is consistently discharged. Therefore, it can be assumed that the top of the anode fully delithiates/lithiates every cycle. This would age the top the most but will also age uniformly. This is seen within the Raman data (Figure 4.4) with Raman distributions at the Tab points showing the largest I_D/I_G but the narrowest distribution. Within the thermal data, the heat map at the bottom of the cell varies through increasing cycles, perhaps suggesting inconsistent delithiation/lithiation. This could be used to explain why the Cnr points have the lowest I_D/I_G ratio but the largest distributions in Figure 4.4.

Ageing within a pouch cell appears heterogeneous and may result from heterogeneous charging/discharging within the cell. For EoL III, it appears more, but more uniformed, ageing occurs at the top and less, but more varied, ageing occurs at the bottom of the cell.

4.5.2 SEM, EDX and a cross-sectional study

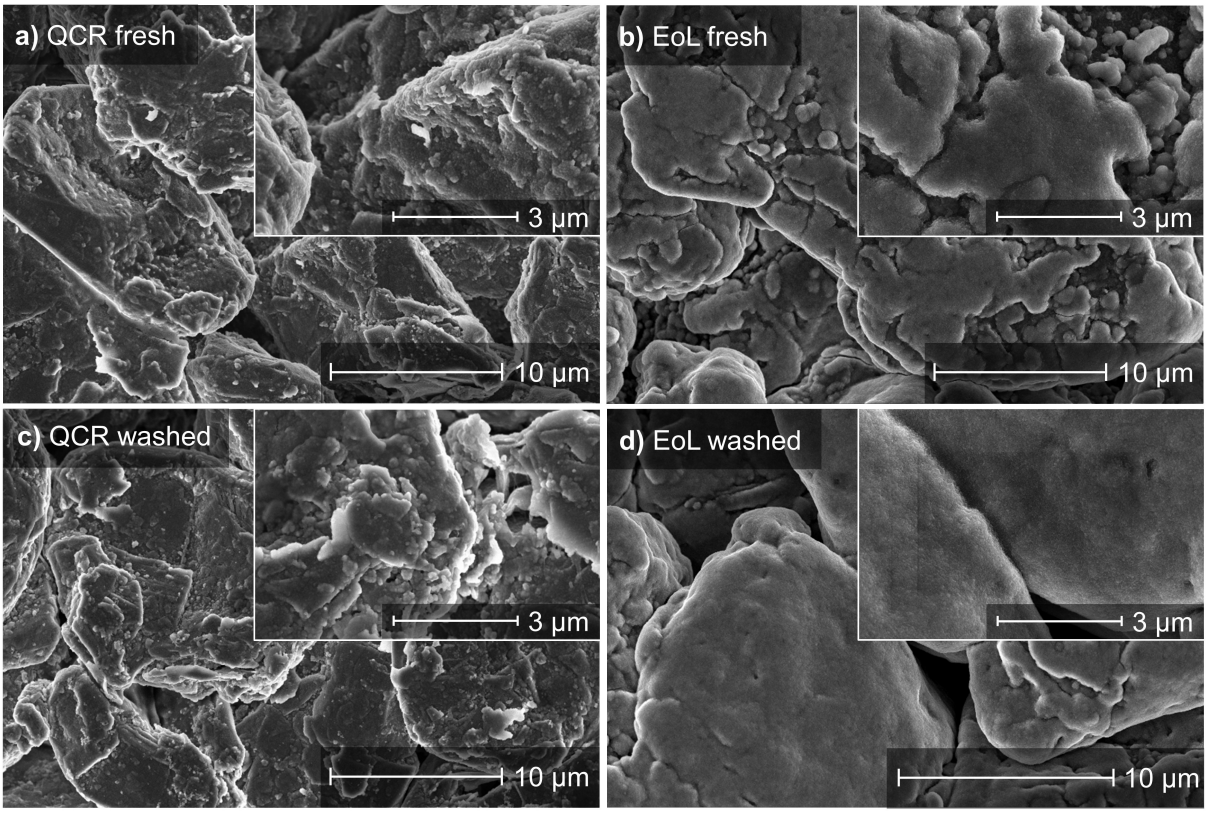


Fig. 4.6. *SEM images taken at 50,000x magnification (small image) and 12,000x magnification (large image) for (a) QCR anode within* 1 h *after dismantlement, (b) EoL anode within* 1 h *after dismantlement c) QCR anode after DMC washing and d) EoL anode after DMC washing. All samples were kept under an inert atmosphere.*

Figures 4.6(a) and (b) show SEM images taken of QCR and EoL anodes within 1 h after dismantlement within an inert atmosphere. In effect, this study pictorially shows the typical ageing experienced by an anode during normal use of an electric vehicle, with the inert

atmosphere preventing excessive ex-situ contamination. As QCR was over discharged, some variance from a ready-to-go pristine anode is expected.

It must be noted that in contrast to the Raman study in section 4.5.1, this is a local study. Samples were taken from the middle of the anodes and upon surveying the area, these images appeared representative of the surrounding area. Local variations are to be expected and should be kept in mind throughout this analysis.

Images taken of QCR anode (shown in Figure 4.6(a)) do not show the expected flat basal planes and stacked edge planes representative of clean graphite particles (which is shown later in Figure 6.9 in Chapter 6). Instead, agglomerates of small particles coat the entire visible surface. Multiple explanations can be made for the presences of these particles, with the three most probable explanations being as follows: a combination of pitch coating and binder, SEI formation from initial cycling before rejection or surface growth caused by the over-discharge.

EoL anode (shown in Figure 4.6(b)) shows more extensive contamination of the surface by agglomerations. The entire surface was coated with an amorphous formulation. The texture of this agglomeration is different to that seen for the QCR anode, showing smoother larger clusters compared to the small hard-edged groups seen in QCR. It is very likely that this is SEI contamination formed from the reduction of electrolyte.

Figures 4.6(c) and (d) show each anode after washing with anhydrous DMC. The surface texture does not change, perhaps suggesting that DMC washing will remove hazardous $LiPF_6$ salt without damaging the structure of the SEI, allowing for air exposed ex-situ analysis of the anode. DMC washing is a common procedure used when dismantling LiBs as if left, $LiPF_6$ salt could react with O_2 and H_2O when exposed to air, presenting a hazard and potentially corroding the anodes due to hydrogen fluoride (HF) production.[146]

Cross-sectional images were taken of both materials after cutting with an Ar beam within the SEM apparatus. Images are given within Figure 4.7. Figure 4.7(a) and 4.7(c)

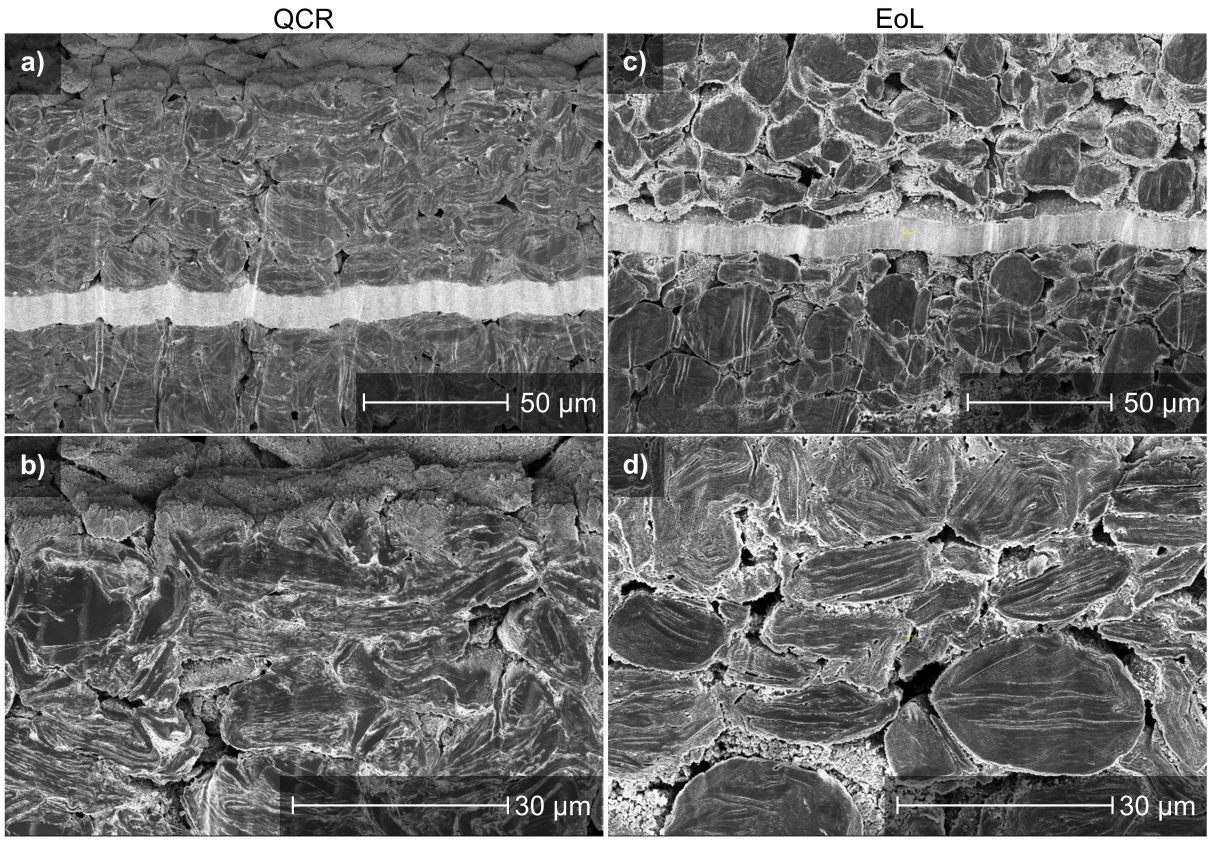


Fig. 4.7. *SEM images taken at 2000x and 12000x of (a-b) QCR and (c-d) EoL anodes, respectively, after milling a cross-section using an Ar milling beam.*

show the cross section of QCR. The use of spherical graphite as the anode active material is apparent. As discussed within the introduction (Section 1.1.6), sphericalisation improves the performance of graphite by allowing better electrode packing and preventing the alignment of the basal plane with the current collector.[24] This cross section also shows that the anode consists of tightly packed graphite particles that also appear to be compressed into the current collector, presumably from the calendaring stage of electrode formation. Evidently, the connectivity across the entire anode is well established. Figure 4.7(c) shows a closer image. Here, it is possible to see the grains within the graphite particles, if damage via exfoliation was present, gaps between these grains would be expected. The top of the QCR

anode is covered with an amorphous layer, this is likely to be fallen debris caused using the Ar milling beam, meaning a depth study of SEI would be inaccurate.

EoL is given in Figures 4.7(c) and (d). Within the literature, as discussed within the introduction (Section 1.3.1) many degradation mechanisms have been suggested that originate from the anode, including: SEI formation, particle cracking, graphite exfoliation, loss of active material, loss of connectivity, lithium plating and metal contamination.[34,50–58] For the EoL anode cycled under a normal EV use case, no particle cracking, exfoliation, or lithium plating can be seen on the anode. However, what is evident is an increased amount of spacing between the particles and less connectivity to the current collector. These appear as voids and are more apparent nearer to the current collector. This spacing indicates a loss of conductivity within the anode, increasing the resistances of the anode and may lead to the loss of contact of some graphite particles. This is likely caused by the $13.2\,\%$ expansion/reduction of graphite during lithiation/delithiation.[147]

Table 4.2. *Atomic percentages gained from EDX analysis of QCR and EoL within* $1\,\mathrm{h}$ *of dismantlement or after DMC washing. All samples were kept under an inert atmosphere. (**10.1 at.$\%$ *of Al was found and removed as this is believed to be an interference perhaps from the holder.* at.$\%$*were normalised after this removal.)*

Sample	C $(K\alpha 1,2)(\%)$	O $(K\alpha 1)(\%)$	F $(K\alpha 1,2)(\%)$	N $(K\alpha 1,2)(\%)$	P $(K\alpha 1)(\%)$	S $(K\alpha 1)(\%)$	Mn $(K\alpha 1)(\%)$	Ni $(K\alpha 1)(\%)$	Cu $(K\alpha 1)(\%)$
QCR Surface	81	4.9	5.5	2.7	0.9	0.7	0.1	0	4.4
QCR DMC washed	81.2	5.9	3.5	2.7	0.4	0.8	0.1	0	5.4
QCR cross section*	87.8	2.0	4.1	0	0.2	0.3	1.8	0	3.9
EoL Surface	55.7	32.2	6.6	0	1.1	1.6	1.5	0	1.3
EoL DMC washed	55.6	34.4	4.2	0	0.8	1.8	1.7	0	1.4
EoL cross section	88.6	2.2	5.2	0.7	0.7	0.4	0.3	0	1.8

Figures 4.8(a) and (b) show the EDX maps of areas on the surface of both QCR and EoL anodes, respectively. Figures 4.9(a) and (b) show the EDX mapping of both QCR and EoL anodes, respectively. EDX maps of DMC washed anodes are given within the appendix (Figure 4.18). The graphite particles' shapes are discernible in the carbon map, appearing almost like irregular, circular pebbles. Qualitatively, consistency can be found within the size

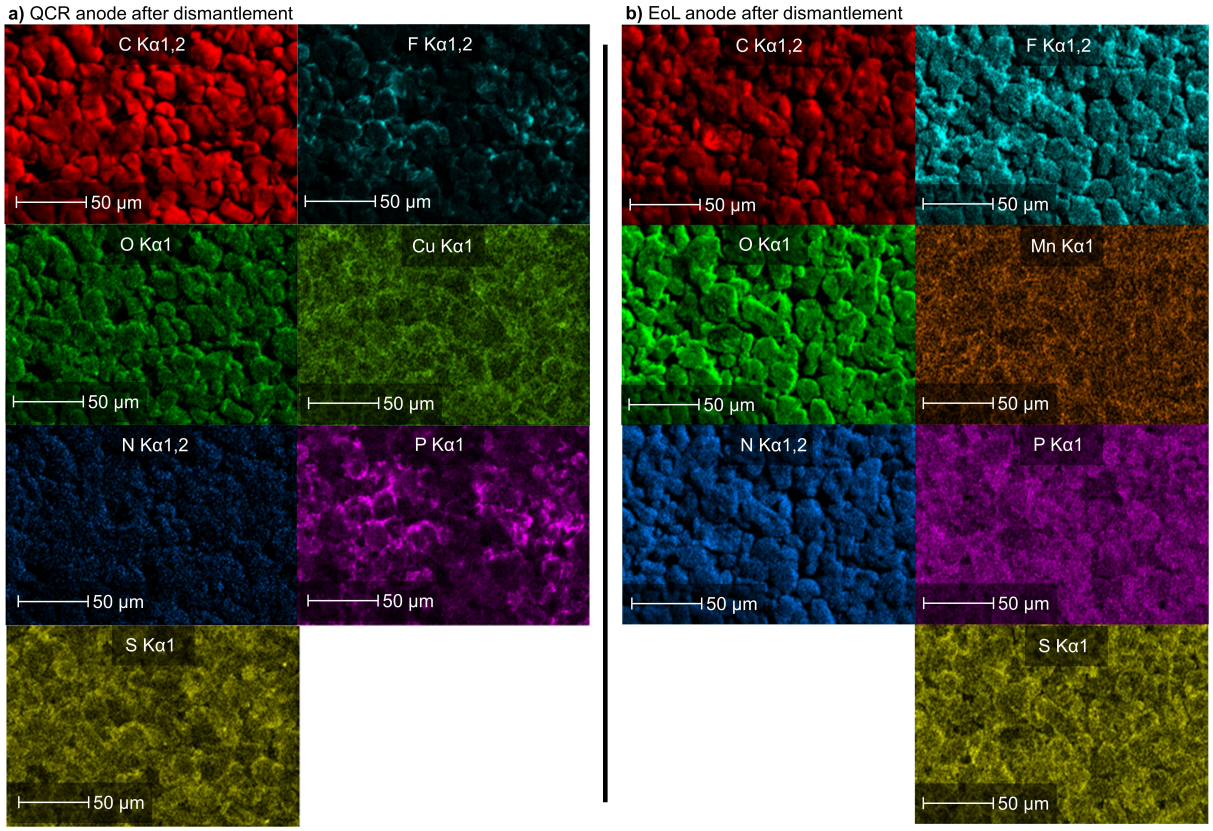


Fig. 4.8. *EDX maps of (a) QCR and (b) EoL anodes taken within* 1 h *after dismantlement within an inert atmosphere. Images were taken at 2,000x magnification.*

of these particles. Graphite particle size also remains consistent between the QCR and EoL anodes. Table 4.2 can be used in conjunction with the EDX maps shown, to give additional quantitative data.

Predictably, carbon has the highest atomic percentage for QCR due to the vast amount of graphite, while for the unwashed surface fluorine follows second. Fluorine will appear due to a number of features; either from $\mathrm{LiPF_6}$, salts, originally within the electrolyte, that may still coat the surface, the PVDF binder or products within the SEI layer. During anode lithiation, the $\mathrm{LiPF_6}$ salt may reduce on the surface to form LiF, $\mathrm{Li}_x\mathrm{PF}_y$ and $\mathrm{LiPF}_x(\mathrm{OR})_y$ components of the SEI.[106] As QCR had undergone formation cycles, contamination of this type could be expected. However, the fluorine map shows higher concentrations of

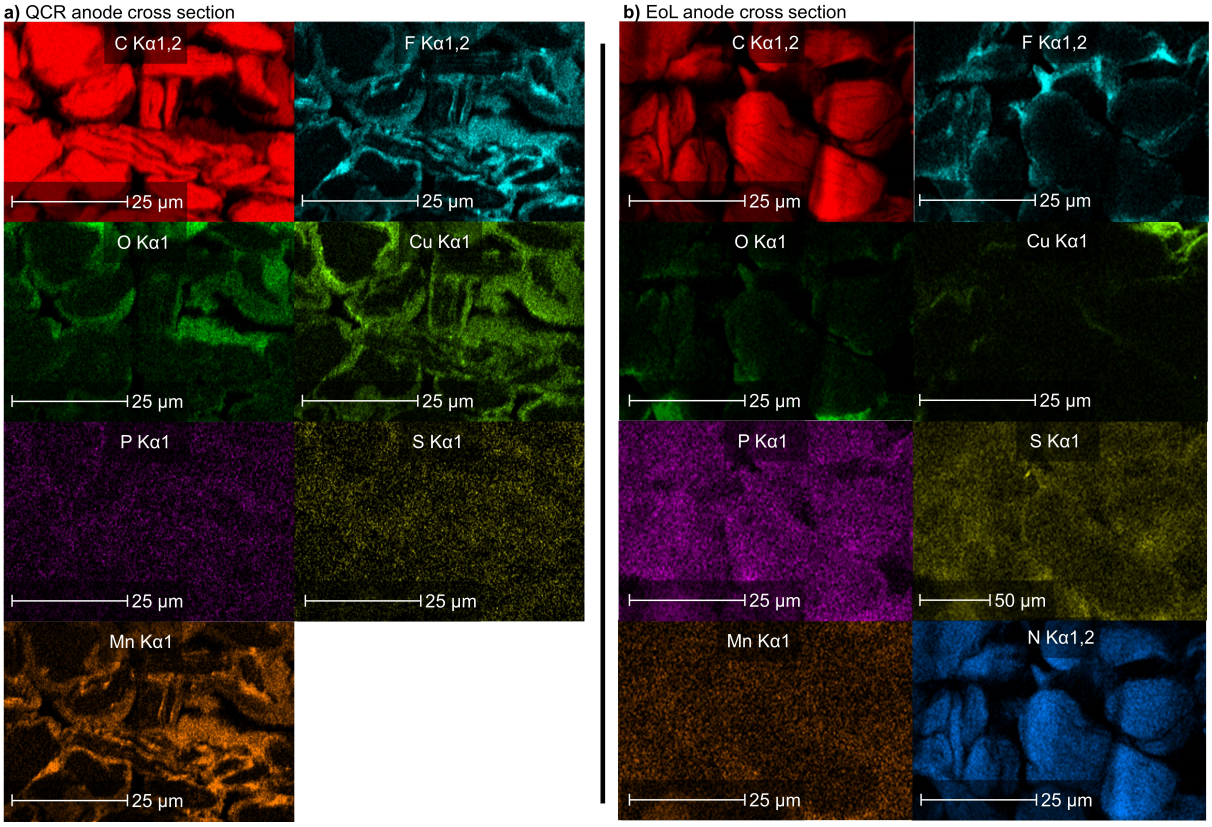


Fig. 4.9. *EDX maps of the cross sections of (a) QCR and (b) EoL anodes within* 1 h *after dismantlement within an inert atmosphere. Images were taken at 6,500x magnification.*

fluorine between the graphite particles, therefore suggesting that the majority of fluorine concentration comes from the PVDF binder that holds the particles together. There is a reduction in the fluorine concentration when washed with DMC. This loss in fluorine is also paired with a loss of phosphorus, consistent with the removal of $LiPF_6$. Evidently the loss in fluorine and phosphorus shows that some electrolyte salt did contaminate the surface and can be effectively removed with DMC.

Nitrogen and sulfur were picked up by EDX analysis. These are likely to appear due to additives added by the manufacturer to improve performance. Sulfur-containing additives are usually added to the electrolyte to reduce before the electrolyte during the first charge, allowing for an initial passivation layer to coat the exposed graphite. This allows

for the properties of the SEI to be altered as well as to prevent a large number of active components like lithium and electrolyte to be used up during formation. Ethylene sulfite ($C_2H_4O_3S$) is a typical additive and is used with PC electrolytes to add a layer that won't allow PC co-precipitation into the graphite.[18]

The presence of manganese and copper on the QCR surface can be an indication of contamination. Copper dissolution occurs during over-discharge, where once a large overpotential is created, the Cu current collector can be oxidised to Cu^+. These ions then dissolve into the electrolyte and deposit on most parts of the cell. This phenomenon is damaging to the cell, producing Cu bridges and dendrites that will short the cell.[148] QCR was taken to $0\,V$ before dismantlement, therefore copper dissolution would have occurred which explains its' presence on the graphite surface. Manganese can be present on the anode via a process called manganese deposition, a common ageing mechanism discussed within the literature.[56,149–151] Here, the $Mn(III)$ at the cathode interface disproportionates during discharge, subsequently leading to $Mn(II)$ dissolving into the electrolyte which can then migrate to the anode.[56] Other processes discussed in the literature may also lead to manganese being present on the surface, including quasi-homogeneous etching of NMC material, which would lead to stoichiometric dissolution. This occurs at $4.7\,V$, where a large number of protic species are present due to electrolyte oxidation. It has also been proposed that electrolyte oxidation at the cathode could lead to the production of water, which upon contact with $LiPF_6$ creates HF which may then etch the cathode.[151] Both these latter processes would lead to stoichiometric deposition, as transport within the electrolyte shows no metal preferences.[103,149] The stoichiometry of the cathode (a mix of lithium manganese oxide spinel (LMO) and a nickel-rich layered oxide) would lead to more manganese deposition even with stoichiometric etching. However, as only a small amount of manganese is present and an undetectable amount of the other metals, it is unknown what process is followed.

Typically, manganese deposition is described as an ageing mechanism, so the presence of manganese on the QCR anode was unexpected but may have been driven by the over-discharge experienced before dismantlement.

The presence of oxygen on the surface of QCR and the decrease of this atomic concentration for the cross sectional study may indicate some SEI formation. The atomic percentages for the QCR cross section is as expected when concerning carbon and fluorine content, making up the majority of the weighting. What is unexpected, however, is the higher manganese within the cross section, perhaps indicating more complexity to the deposition preferences of manganese. In Figure 4.9(a) it is clear that the manganese is found on the surface of each graphite particle within the anode cross-section. Copper deposition shows a preference for the surface of the anode rather than the surface of graphite within the cross-section.

The atomic ratios of the EoL surface obtained via EDX, shows the traces of key ageing mechanisms when compared to QCR. The higher oxygen count suggests more excessive SEI growth and the higher manganese count suggests more manganese deposition. The presence of copper on the surface may suggest that during the cells use, the voltage may have occasionally dropped below the standard voltage window or large over-potentials were experienced on the anode, leading to some copper dissolution and contamination of the surface. The cross section of the EoL anode shows less elemental contamination than the QCR anode. Less copper is seen due to not being over-discharged. Manganese concentrations between the cross section and the surface have reversed when compared to QCR, showing less manganese contamination within the anode. This may indicate differences within the manganese deposition mechanisms, with the over-discharge acting as a shock compared to the gradual deterioration during normal use.

4.5.3 XPS and HAXPES surface study

XPS allows for a surface-sensitive (tens of Angstrom scale) analysis of the atoms and their environments on a given material.[100] HAXPES is similar, but the use of higher energy X-rays (from a Ga Kα source instead of Al Kα source) allows for deeper penetration, allowing for a buried surface XPS study (on the tens of nanometre scale).[152] As seen in previous studies, a major degradation mechanism for anodes arises from the progressive growth of the SEI layer, stripping the cell of reversible Li^+. Within the literature, it is hard to pin the depth of this SEI layer, typically ranging within a few hundreds of angstroms, where to complicate matters, the depth will also change depending on the SoH of the cell.[39,53,101] The study presented here allows for a primitive depth study into the SEI layer, with XPS showing the very top surface of this layer and HAXPES showing the bulk of the SEI to the upper surface of the anode. The use of QCR to EoL III will show how the SEI layer developed with decreasing SoH.

Figures 4.10, 4.11 and 4.12 show the normalised $C\ 1s$, $F\ 1s$ and $Mn\ 2p$ XPS and HAXPES spectra with fitted peaks for each anode. Table 4.3 and 4.4 can be used in conjunction, with the former showing the percentage composition of regions within the $C\ 1s$ and $F\ 1s$ spectra and the latter showing the atomic percentages of lithium, carbon, oxygen, fluorine, phosphorus, sulfur, manganese, nickel and copper. XPS and HAXPES measurements were taken before washing with DMC and before air exposure, so some electrolyte is likely to be present and the SEI is expected to be similar to *in-situ*.

All $C\ 1s$ spectra (shown in figure 4.10) show a peak centring around $284.8\,\text{eV}$. This typically results from an aliphatic environment; however, graphite can also produce an asymmetric peak around this region.[101,102] As some form of SEI was expected to be present on all anodes, the aliphatic peak was fitted and the graphitic contribution was ignored. Adding asymmetry requires more variables and therefore, could over-parameterise the

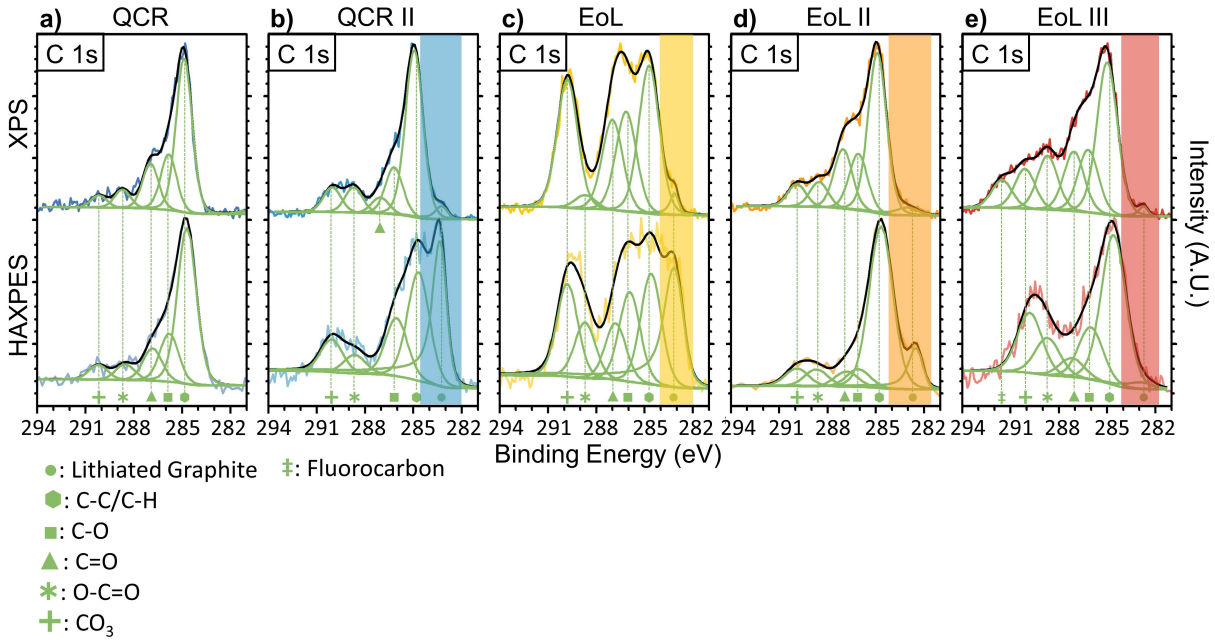


Fig. 4.10. *Normalised photoelectron spectra (XPS and HAXPES) obtained from the surface of anode materials. (a–e) Carbon $1s$ XPS (top row) and HAXPES (bottom row) of anodes before DMC wash and air exposure. Each signal fitting consists of five Voigt peaks with constrained binding energies. An additional Voigt peak was added to EoL III for better fitting and was associated to the presence of fluorocarbons. The lithiated graphite region is highlighted with a transparent band and was fitted using an asymmetric peak. QCR is shown in dark blue on the left, QCR II in turquoise, EoL in the middle shown in yellow, EoL II in orange and EoL III in red on the right. Reproduced from Sargent at al.*[121] *with permission from the Royal Society of Chemistry.*

fit. Four peaks were used to simulate the more oxidised region between 285 eV-291 eV; these were given the nomenclature: C–O (~ 286.1 eV), C=O (~ 287.1 eV), O–C=O (~ 288.7 eV) and CO_3^{2-} (~ 290.0 eV) that is typically found in the literature.[101–107] Literature origins of each peak are given within the experimental chapter (in Table 3.2). These environments correspond to a number of molecules that can be found in the SEI, including but not limited to:$(CH_2OCO_2Li)_2$, $ROCO_2Li$ and other polycarbonates that may form due to electrolyte reduction.[102,104,105] However, it must be noted that these assignments are an oversimplification of the overall $C\ 1s$ spectra, and environments like $C–F_x$, C–SR and C–N could arise from other electrolyte reduction products and molecules originating from

additives.[105] To avoid errors resulting from overfitting, these environments were ignored and the changes in only the plotted oxidised environments were studied. An additional peak had to be added to the EoL III XPS spectrum at 291.6 eV, which has been ascribed to fluorocarbon bonding.[107]

Using Figure 4.10, a comparison between the two QCR anodes and the three EoL anodes seems to show that increased cycling deposits more organic species onto the surface of the SEI, demonstrated by the general increase in the $C\ 1s$ oxidised region in comparison to the aliphatic peak. This trend can also be seen in Table 4.4, showing a decrease in $\mathrm{C{-}C/C{-}H}$ region for the XPS scans on the three EoL samples. For each anode, except EoL III, a comparison of the XPS and HAXPES spectrum of the same sample shows only minor differences in the oxidised region, which perhaps indicates that the composition of carbonaceous species within the SEI is similar within the bulk as on the surface. It is difficult to find a trend in this oxidised region between the anodes. This may indicate the complexity of cell cycling and deterioration. Heterogeneity in the ageing of the anode has already been shown through the Raman study (section 4.5.1), this may explain the differences in composition. Although each sample was taken from the middle of each anode, this heterogeneity is likely to affect the results. A potential route to avoid this effect would be to cycle one cell and analyse the same spot. However, the cycling procedure required to reach the point of degradation shown by the EoL anodes which experienced normal and not accelerated ageing would take a long time.

An interesting peak appears at around 283 eV for all anodes except the over-discharged QCR anode. The intensity of this peak increases under HAXPES measurements in comparison to the other carbon environments. A peak at this binding energy is typically assigned to a metal carbide and in this study has been assigned as lithiated graphite.[101,102] Li-carbides could form in the SEI via a two-electron reduction process of the electrolyte. The following

reaction scheme is given for an EC electrolyte:[153]

$$\mathrm{EC} + 2\,\mathrm{e}^- + 2\,\mathrm{Li}^+ \longrightarrow \mathrm{LiCH_2CH_2OCO_2Li}\downarrow$$

However, this process is the least thermodynamically favourably reduction pathway[153] and the increase in intensity whilst using HAXPES suggests that this environment is found either on the surface of the anode or deeper within the SEI. Therefore, the assumption of lithiated graphite was used. Small amounts of lithiated graphite would be expected in each anode except QCR due to having OCVs of around $3\,\mathrm{V}$. Degradation mechanisms may also lead to higher lithiated graphite concentrations within EoL anodes, due to areas of the anode becoming electronically isolated during continuous cycling. Therefore, it may be expected that the lithiated graphite peak intensity would increase from QCR II < EoL < EoL II < EoL III, however, the opposite is found within the HAXPES measurements (seen clearly in Table 4.4). This can be rationalised by an expected increase in the thickness of the SEI via ageing, obscuring the graphite surface.

$F\ 1s$ spectra acquired for each anode using soft and hard X-rays are given in Figure 4.11. Three environments were chosen to fit the received signals: LiF ($\sim 685.1\,\mathrm{eV}$), $\mathrm{Li}_x\mathrm{PF}_y$ or $\mathrm{LiPF}_x(\mathrm{OR})_y$ ($\sim 686.9\,\mathrm{eV}$) and $\mathrm{LiPF_6}$ ($\sim 688.4\,\mathrm{eV}$). This again, may be an oversimplification, but these peaks were the most common within the literature.[101,102,106] The presence of $\mathrm{LiPF_6}$ was found within the XPS scans of QCR, EoL and EoL III; this environment was also found within the HAXPES of EoL III. As these samples were not washed prior to analysis, $\mathrm{LiPF_6}$ was expected. LiF, $\mathrm{Li}_x\mathrm{PF}_y$ and $\mathrm{LiPF}_x(\mathrm{OR})_y$ are expected reduction products of $\mathrm{LiPF_6}$ and are likely to contribute to the SEI layer. A subtle increase in the $\mathrm{Li}_x\mathrm{PF}_y/\mathrm{LiPF}_x(\mathrm{OR})_y$ environment can be seen between the QCR II < EoL < EoL II anodes, suggesting that as the cell ages, the $\mathrm{LiPF_6}$ reduction products on the surface exhibit increasingly covalent character. This trend can also be subtly seen when comparing the deeper penetrating HAXPES scans of the EoL anodes to their corresponding XPS scans (within Figure 4.11 and Table 4.4).

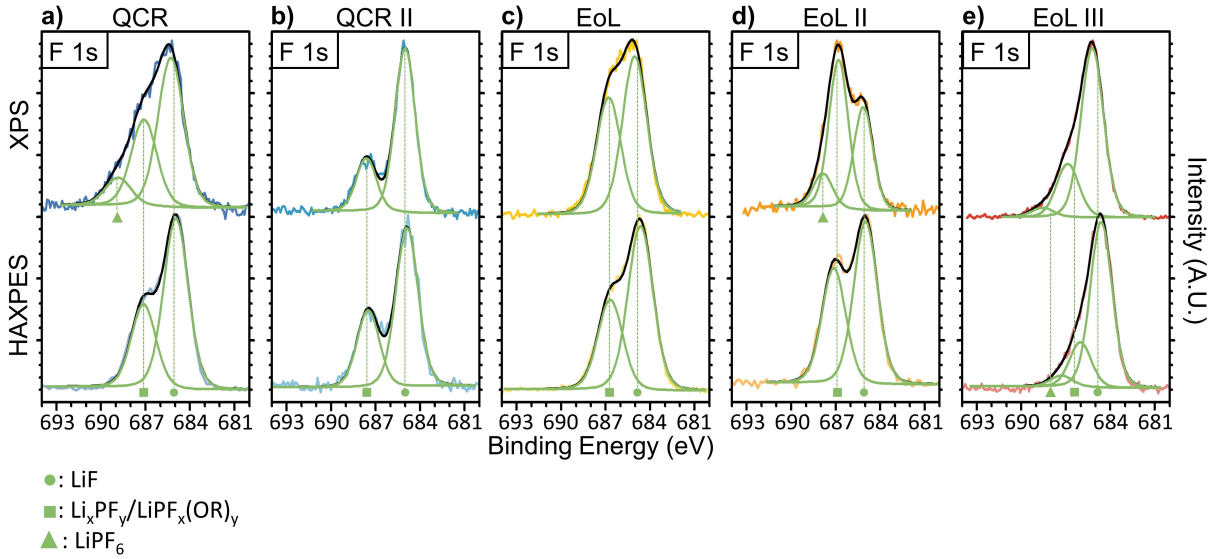


Fig. 4.11. *Normalised photoelectron spectra (XPS and HAXPES) obtained from the surface of anode materials. (a–e) Fluorine 1s XPS (top row) and HAXPES (bottom row) of anodes before DMC wash and air exposure. Two to three peaks were fitted for the calculated signal, representing* $\mathrm{LiPF_6}$*,* $\mathrm{Li}_x\mathrm{PF}_y$*/*$\mathrm{LiPF}_x(\mathrm{OR})_y$ *and* LiF *environments. QCR is shown in dark blue on the left, QCR II in turquoise, EoL in the middle shown in yellow, EoL II in orange and EoL III in red on the right. Reproduced from Sargent at al.*[121] *with permission from the Royal Society of Chemistry.*

Here, the LiF peak makes up a higher percentage composition for the deeper scan, perhaps suggesting more inorganic components are found closer to the anode surface. This would be consistent with studies found within the literature that suggests that SEI formation close to the anode surface has access to desolvated Li^+ ions and salt anions, leading to the formation of more inorganic species, whereas the SEI surface closer to the electrolyte has access to more solvent molecules, leading to a composition with more organic species.[102,154,155]

The presence of manganese on the surface of the anode has been discussed in the previous section (section 4.5.2). Figure 4.12 and Table 4.4 confirm this presence. Mn deposition appears to affect the more aged cells (EoL II and EoL III) with QCR II and EoL showing a manganese atomic percentage below a detectable limit. The peak shapes in Figure 4.12 implies that the manganese is within an oxidised state, likely to be +2.[56,150]

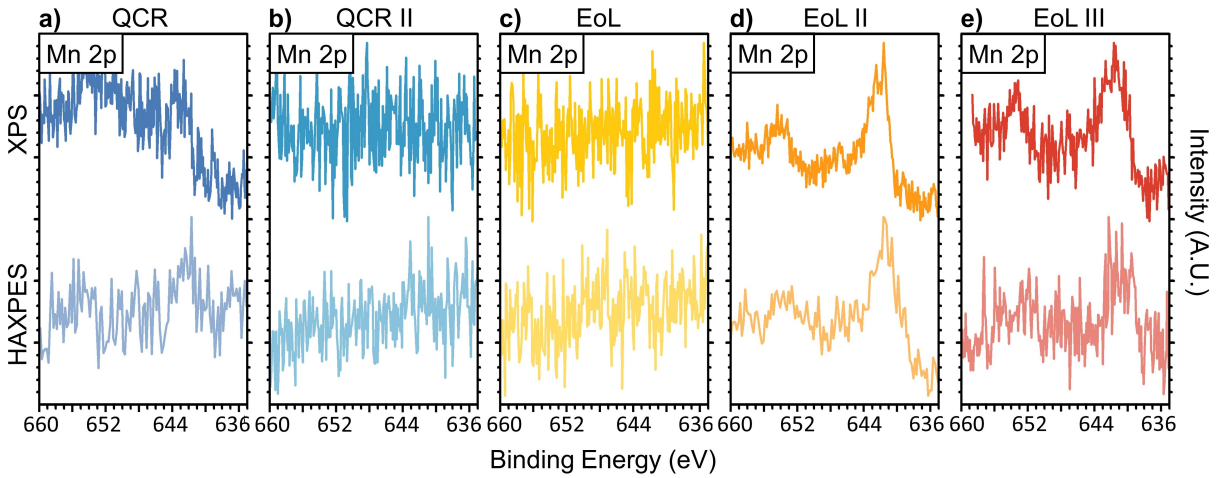


Fig. 4.12. *Normalised photoelectron spectra (XPS and HAXPES) obtained from the surface of anode materials. (a–e) Manganese 2p XPS (top row) and HAXPES (bottom row) of anodes before DMC wash and air exposure. No peaks were fitted due to the asymmetry and complex splitting caused by the d electron band, therefore comparisons to literature were conducted. QCR is shown in dark blue on the left, QCR II in turquoise, EoL in the middle shown in yellow, EoL II in orange and EoL III in red on the right. Reproduced from Sargent at al.*[121] *with permission from the Royal Society of Chemistry.*

However, the low atomic percentage results in noisy data and a high degree of error, making it difficult to accurately assign oxidation states to these peaks and complicating the analysis. As this is an *ex-situ* study, it is unknown whether the manganese deposits first as a metal, later to be re-oxidised by the electrolyte to +2, or deposits into the SEI directly in a (+2) oxidised state. An *in-operando* study by *Wandt et al.*[151] showed that even though other studies show Mn (0) on the lithiated graphite anode when studied within an *ex-situ* environment, manganese is never reduced to 0 during the typical cycling of a full cell. Instead, it is believed that whilst the manganese is continually being reduced by the anode, the electrolyte rapidly re-oxidises the manganese and therefore the manganese acts more as a redox catalyst, reducing the electrolyte.[149,151] This indicates that not only does the cathode lose active material, but constant lithium loss is activated via Mn deposition. HAXPES analysis confirms Mn presences within the SEI and indicates that the manganese does not change its oxidation state, but again, noisy data leads to a large degree of uncertainty. As

seen in previous studies, manganese can be found on the surface of the QCR anode. This manganese appears to also be in an oxidised state similar to EoL II and EoL III. Unlike these two anodes, however, the atomic percentage is depth sensitive. Perhaps for the aged cells deposition occurred gradually, where the manganese will deposit onto the surface and further SEI growth covers these metal ions, whereas for QCR deposition occurs on the final over-discharge, only covering the SEI surface.

The presence of cobalt was not found, at least not to a detectable amount. However, nickel was detected and the atomic percentages are given within Table 4.3. Nickel was found on the less aged samples (QCR II and EoL), suggesting that nickel deposition occurs before manganese. The extraction of nickel from the cathode is likely to be via etching as discussed in the previous section. In contrast to manganese, counts of nickel are found only on the surface of each anode except QCR. It is hard to tell the oxidation state of the nickel via the spectra due to the large background and F Augur overlap (at $858.0\,\mathrm{eV}$). *Wandt et al.*[151] discussed that *in-operando* deposited nickel remains in a +2 oxidation state whilst the cell cycles. The reasoning for this inactivity is that the ions are trapped within the outer layer of the SEI, with no contact to the anode, and therefore are unable to reduce. This trapping is also shown within these results. As no oxidation to Ni^0 occurs, it is expected that no reduction of the electrolyte will be induced and therefore less lithium loss will occur when compared to manganese.

This XPS and HAXPES study has shown that nickel deposits early on within the life cycle of the cell, followed by manganese. These contaminates however seem to not make up much atomic percentage so should not be a major contamination within the recycling process. SEI grows during the ageing of the cell, the surface of which seems to consist of more organic species the thicker the SEI becomes. This appears to be a major ageing mechanism for these cells, reducing the lithium content within the cell. An interesting discovery was the presence of trace amounts of lithiated graphite.

Table 4.3. *Percentage composition for each chemical environment obtained for each anode within the $C\ 1s$ and $F\ 1s$ regions under XPS and HAXPES analysis. Analysis was taken before DMC washing and exposure to air. Standard deviations were calculated using a Monte Carlo procedure to simulate the variance from multiple fittings. Both value and standard deviation were calculated in casaXPS. Reproduced from Sargent at al.*[121] *with permission from the Royal Society of Chemistry.*

		Carbon 1s (%composition)							Fluorine 1s (%composition)		
		LiG	C–C/C–H	C–O	C=O	O–C=O	CO_3^{2-}	Fluorocarbon	$LiPF_6$	$Li_xPF_y/LiPF_x(OR)_y$	LiF
QCR	XPS	1.1(9)	53.3(20)	19.3(14)	15.7(8)	6.4(7)	4.3(7)	–	10.5(10)	32.8(12)	56.8(18)
	HAXPES	0	58.3(52)	18.1(67)	12.2(49)	6.0(26)	5.6(21)	–	–	32.8(11)	67.2(14)
QCR II	XPS	4.4(19)	56.9(27)	16.1(39)	5.5(16)	8.7(16)	8.5(12)	–	–	24.4(16)	75.6(18)
	HAXPES	31.2(54)	37.5(50)	16.6(33)	0	5.4(26)	9.4(23)	–	–	32.6(21)	67.4(25)
EoL	XPS	2.6(12)	30.0(19)	20.2(35)	18.3(28)	2.9(11)	26.0(19)	–	–	42.6(13)	57.5(14)
	HAXPES	27.5(48)	19.8(41)	16.0(26)	10.1(44)	10.0(18)	16.6(23)	–	–	35.4(8)	64.7(9)
EoL II	XPS	4.2(12)	47.4(18)	16.7(23)	17.6(18)	7.5(6)	6.6(6)	–	11.8(20)	52.1(21)	36.2(8)
	HAXPES	13.3(27)	61.0(47)	5.8(23)	6.8(34)	6.5(14)	6.7(15)	–	–	41.5(18)	58.5(19)
EoL III	XPS	1.7(15)	37.5(34)	15.7(37)	15.7(24)	13.3(13)	9.9(12)	7.2(3)	4.0(10)	23.0(13)	73.0(23)
	HAXPES	3.2(35)	45.4(55)	15.8(45)	5.9(30)	11.4(28)	18.3(33)	–	5.0(22)	20.1(35)	74.9(70)

Table 4.4. *Surface elemental composition calculated from the lithium $1s$, carbon $1s$, oxygen $1s$, fluorine $1s$, phosphorus $2p$ (XPS), phosphorus $1s$ (HAXPES), sulfur $2p$ (XPS), sulfur $1s$ (HAXPES), manganese $2p$ (XPS), manganese $1s$ (HAXPES), nickel $2p$ (XPS), nickel $1s$ (HAXPES), copper $2p$ (XPS) and copper $1s$ (HAXPES) regions for each anode before DMC washing and air exposure. Standard deviations were calculated using a Monte Carlo procedure to simulate the variance from multiple fittings. Blank values indicate atomic percentages below the limit of detection. Both value and standard deviation were calculated in casaXPS. Reproduced from Sargent at al.*[121] *with permission from the Royal Society of Chemistry.*

		Lithium (at.%)	Carbon (at.%)	Oxygen (at.%)	Fluorine (at.%)	Phosphorus (at.%)	Sulfur (at.%)	Manganese (at.%)	Nickel (at.%)	Copper (at.%)
QCR	XPS	31.7(44)	24.2(8)	13.1(3)	22.4(3)	2.9(7)	2.1(6)	1.00(19)	0.77(13)	1.80(31)
	HAXPES	13.4(54)	28.0(25)	11.1(10)	40.3(6)	2.4(1)	2.3(2)	0.36(3)	0.79(8)	1.34(27)
QCR II	XPS	39.1(16)	28.7(8)	16.7(4)	12.3(3)	0.8(2)	1.9(2)	–	0.45(13)	–
	HAXPES	28.2(49)	29.6(18)	25.4(8)	15.5(6)	0.3(1)	1.0(1)	–	–	–
EoL	XPS	40.3(12)	20.5(6)	18.6(3)	16.9(2)	3.1(2)	0.3(1)	–	0.35(10)	–
	HAXPES	28.0(45)	18.6(11)	16.0(4)	36.2(3)	1.1(1)	0.2(1)	–	–	–
EoL II	XPS	40.7(76)	28.1(12)	15.6(4)	11.5(5)	2.9(4)	–	0.72(8)	0.18(30)	–
	HAXPES	13.8(36)	49.6(16)	17.5(5)	16.7(4)	1.4(1)	0.3(1)	0.79(2)	–	–
EoL III	XPS	46.2(13)	17.7(5)	13.9(2)	20.7(2)	0.6(1)	0.3(1)	0.12(6)	0.56(9)	–
	HAXPES	35.8(33)	18.3(10)	26.6(4)	18.5(4)	0.3(1)	0.2(1)	0.22(2)	–	–

4.5.4 PXRD analysis of graphite

The previous studies have predominately focused on the anode surface. Other degradation techniques like particle cracking and exfoliation have not been seen but are discussed in the literature.[34,50–58] PXRD analysis enables a clearer study of crystallite domain sizes and microstrain within the bulk of the graphite particles. Bulk effects will have a major effect on the quality of the recycled graphite, especially for electrochemical use. As well as providing structural information, PXRD allows for the study of structural anisotropy arising from stress, strain, texture, orientation, and particle size, etc. making PXRD a powerful tool for looking into regional degradation that may occur within crystalline materials. However, the inherent layered structure of graphite leads to a very high preferred orientation, increasing the intensity of the (002) peak and drastically lowering peak intensity corresponding to other crystallographic directions. As this is an intrinsic property, the concentration of this effect cannot decrease beyond a certain limit, making Rietveld refinement (a common PXRD analysis technique) for graphitic material inconvenient.[156]

In-house PXRD for all anodes just after air-exposure are shown in Figure 4.13. As discussed, the intensity of the (002) peak significantly dominates the pattern, meaning diffraction peaks originating from other crystallographic directions such as (101) and (100) are of very low intensity, with the latter positioned at $(\sim 42°)$ not visible in the patterns given in Figure 4.13, making gathering information via refinement difficult. The (111) (positioned at $(\sim 43.3°)$) and the (200) (positioned at $(\sim 50.4°)$) peaks for copper metal are found in the patterns due to the copper current collector and are highlighted with asterisks. The presence of impurities cannot be seen. It is evident from the other studies that impurities are present, so this observation may again be hindered by the preferred orientation.

Due to the difficulty in refinement, unique structural parameters are often extracted from the reflections themselves. These parameters include the interplane distance (d_{00l}),

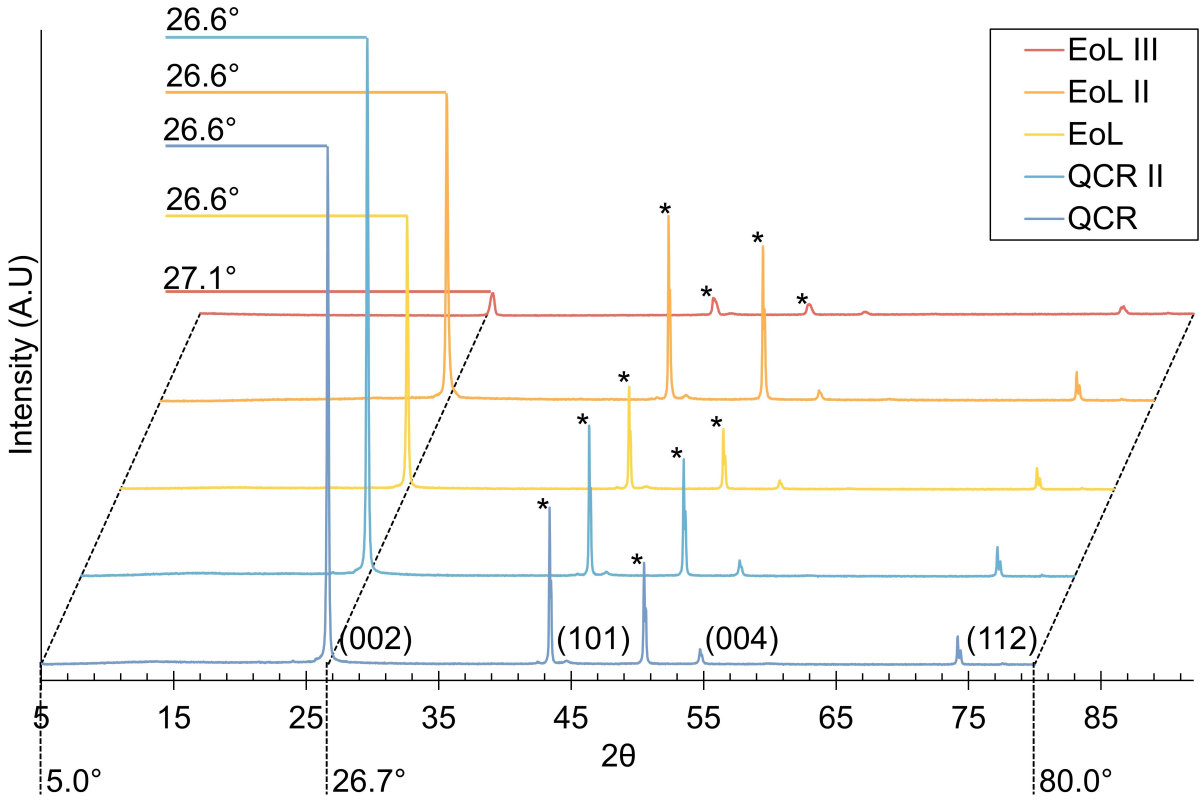


Fig. 4.13. *Stacked in-house PXRD patterns of all anodes, taken with minimal air-exposure. Miller indices for key graphite peaks are annotated to the right of each peak and asterisks are used to indicate copper peaks.* 2θ *positions of the* (002) *peak for each graphite material is also shown.*

crystallite size between layers (L_c) and through layers (L_a), packing density (ρ), and the number of polyarene layers within a crystallite (N).[110,111] The calculations for each value are given within the experimental chapter (Section 3.4.2) and the values obtained for each anode are given in Table 4.5. A Pawley fit was used to determine the percentage of graphite particles compared to copper foil.

Even though L_c values are commonly quoted in literature, *Badenhorst*[157] states that it is ambiguous to what these values are measuring. Due to the complexity in graphite disorder, arising from defects like basal, non-basal edge, prismatic screw, and prismatic edge dislocations, it is hard to distinguish what makes up a crystallite domain and the consistency of this domain within the crystal lattice. It is an oversimplification to think that the

Table 4.5. *Graphite crystallite parameters extracted from in-house PXRD for all anodes and a commercially available battery-grade graphite (MAGE3).*

Anode	Graphite wt.%	d_{002}	L_c (nm)	ρ	N
QCR	73.4(10)	0.33	18.89	2.28	57.47
QCR II	72.7(13)	0.33	17.33	2.28	52.80
EoL	81.2(11)	0.33	16.58	2.28	50.56
EoL II	73.1(12)	0.33	10.88	2.28	33.53
EoL III	73.8(12)	0.33	4.45	2.31	14.52
MAGE3	-	0.34	16.69	2.27	50.76

whole crystal structure is constructed of regular crystallite domains.[110,157] This may lead to the large discrepancy between measured crystallite domains and crystal size within literature when analysing highly crystalline natural graphite flakes.[157] These discrepancies will also be present within this study, however, as the values are used as a comparison between similar graphite particles, L_c values can be used as a measure of disorder rather than real domain sizes.

Excluding EoL III, all parameters for all anodes given in Table 4.5 showed no excessive differences and no trends with cell SoH before dismantling. Values were similar to that of MAGE3, a commercially available battery-grade graphite. This may indicate that no crystalline degradation occurred within the graphite during cycling. EoL III shows lower crystallite size (L_c) and layer stacking (N). This may indicate degradation. However, upon exposure to air, it was observed that organic contaminants began to oxidise, forming a layer of amorphous carbon. This formation would continually occur whilst the PXRD measurements were taken. This may have caused the lower signal intensity and higher background leading to a false crystalline degradation.

PXRD using a synchrotron source and a rotating, horizontal capillary was conducted to increase the intensity of the pattern and minimise the preferred orientation of graphite. The high brilliance of the X-ray beam not only increases the intensity of the reduced reflections

but will increase reflections from impurities.[158] In order to reduce interference via amorphous carbon production, these samples were examined with no air-exposure.

Patterns for each anode are shown in Figure 4.14. The patterns shown here are compressed by $\sim x10$ 2θ compared to those taken within the in-house PXRD patterns. This is due to the use of a 0.16 Å X-ray wavelength instead of 1.54 Å Cu Kα1,2 source. No copper peaks are seen, as the graphite was removed from the anode surface for analysis. The intensity of the (002) reflection has evidently reduced in comparison to the others whilst using a synchrotron source, although it is still the most intense peak. Apart from the large background found at $22°$, resulting from the capillary, no impurities were seen. Although metal contamination was found in previous studies, the percentage of this contamination must be very small or non-crystalline.

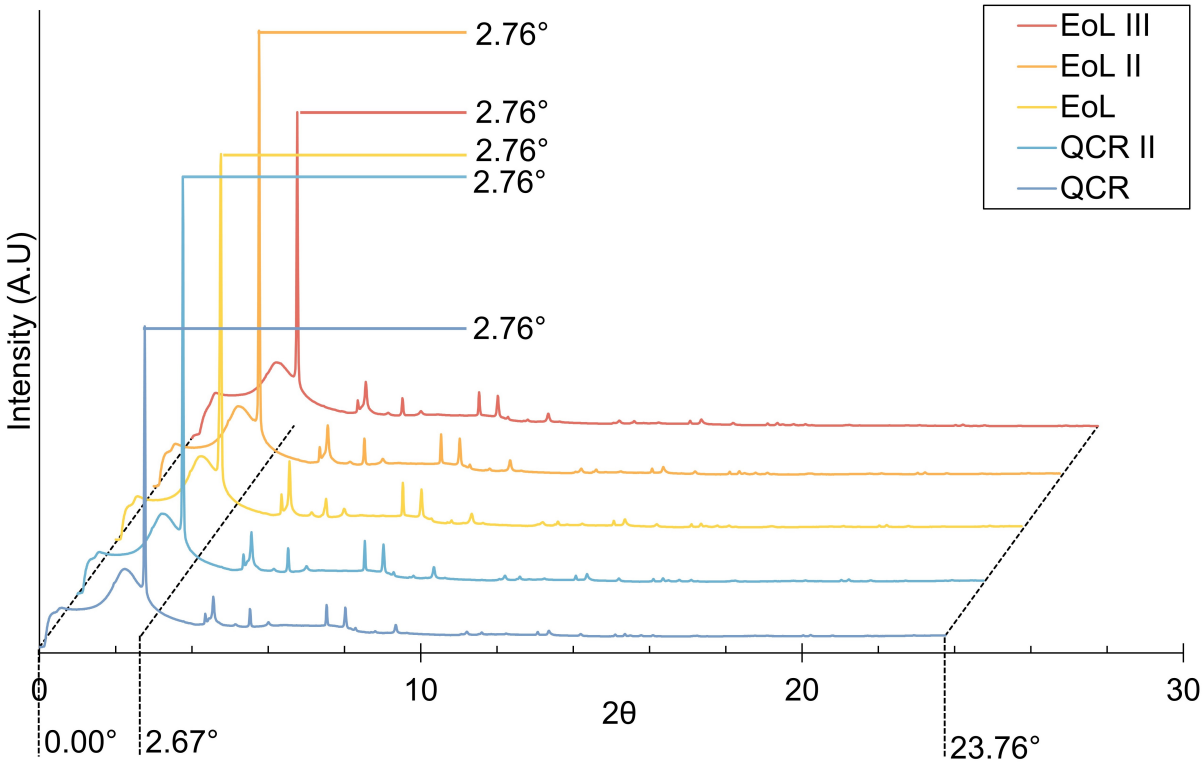


Fig. 4.14. *Stacked synchrotron PXRD patterns of graphite scraped off of all anodes, taken with no air-exposure. 2θ positions of the (002) peak for each graphite material is also shown.*

Crystalline parameters were again extracted using the (002) reflection and are shown in Table 4.6. Here, the variation in values is even smaller than that gained from the in-house study, suggesting that the graphite from EoL cells is crystallographically similar to the less cycled QCR cells. L_c values are higher for all anodes within this study. This may be linked to less preferred orientation and highlights the need for correct experimental set-up for graphite XRD analysis.[158]

Table 4.6. *Graphite crystallite parameters extracted from synchrotron PXRD*

Anode	d_{002}	L_c (nm)	ρ	N
QCR	0.34	47.68	2.27	143.17
QCR II	0.34	47.67	2.27	143.13
EoL	0.34	47.66	2.27	143.05
EoL II	0.34	47.67	2.27	143.11
EoL III	0.34	47.66	2.27	143.05

4.6 | Air exposed studies

It would be impractical to keep these anode materials within an inert atmosphere either throughout the rest of their lifetime (to grave) or during the recycling and rejuvenation process (to cradle). *Sabisch et al.*[159] describes a process of mechanically removing graphite from EoL cells taken from used electronics and washing this recovered material with DMC and NMP before recasting, calendaring and insertion into a new cell, all within an inert atmosphere. Therefore it is possible to reuse the material with no air exposure, and in fact, *Sabisch et al.*[159] states that this could be beneficial; the graphite may be coated in an undisturbed pre-formed SEI layer, reducing lithium loss within the new cell, as well as some graphite remaining lithiated, increasing the amount of lithium within the new cell. However, their recovered material showed a non-disclosed "heavy capacity loss" and the process described for industrial up-scaling would be very expensive within an inert atmosphere. Their recovered material that was exposed to air during the coating and calendaring process

actually performed better, giving a capacity within 30 % of virgin material. Evidently, this SEI layer does not help for further cycling within a new cell, it most likely acts as a point of parasitic reactions, forming unhealthy SEI. The better performance of the exposed samples shows that there are significant changes to the graphite when removed from an inert atmosphere.

Within this section, anode materials will be exposed to air for different amounts of time and the effect of this exposure will be studied. The exposure of this material will also allow for more options for rejuvenation, perhaps leading to better electrochemical performance.

4.6.1 Air exposure changes through SEM

After washing with DMC, segments of each anode were removed from the glovebox and exposed to air for 1 h, 24 h and 1 week before a representative image of each segment was taken using SEM. The images collected are given in Figure 4.15.

QCR and QCR II showed no significant changes to the surface after progressive time exposed to air. However, there is evidently still a surface coating as shown for QCR in section 4.5.2 as soft contours are seen instead of the typical strata and crystalline surfaces of graphite. This could consist of a number of components, either the SEI, a pitch coating or PVDF and carbon black. This resembles that seen within the inert atmosphere study (Section 4.5.2) and indicates that this coating is stable in air.

The EoL anodes are more interesting. After 1 h of air exposure (Figure 4.15(g), (j) and (m)) small clusters of particles are present. On EoL II (Figure 4.15j), these agglomerates have joined to form a surface crust with cracks. Unlike the QCR anodes, the surface changes with increased air exposure. With increased time, the size of these clusters increases so that after 1 week of exposure it almost becomes difficult to distinguish graphite particle grain boundaries. EoL II is of particular interest, as growth appears within the cracks of the crust developed after 1 h of exposure. This growth eventually seals the cracks so that in Figure 4.15(l) the graphite is completely encased within this crust.

The difference in reactivity may be insinuated by the larger complexity of carbon species shown within the previous XPS study (section 4.5.3). These could react with the air, depositing species like carbonates and ethers. Lithium species within the SEI are likely to form more stable inorganic compounds like lithium carbonate and lithium hydroxide.[101]

Lithiated graphite, as identified by the previous XPS study, will react with the air and moisture via a number of oxidation and hydrolysis reactions. This may deposit a number of lithium salts like $LiOH$, Li_2O and Li_2CO_3. However, these salts are likely to be found underneath this coating, on the very surface of the graphite, as observed by *Malmgren et al.*[101].

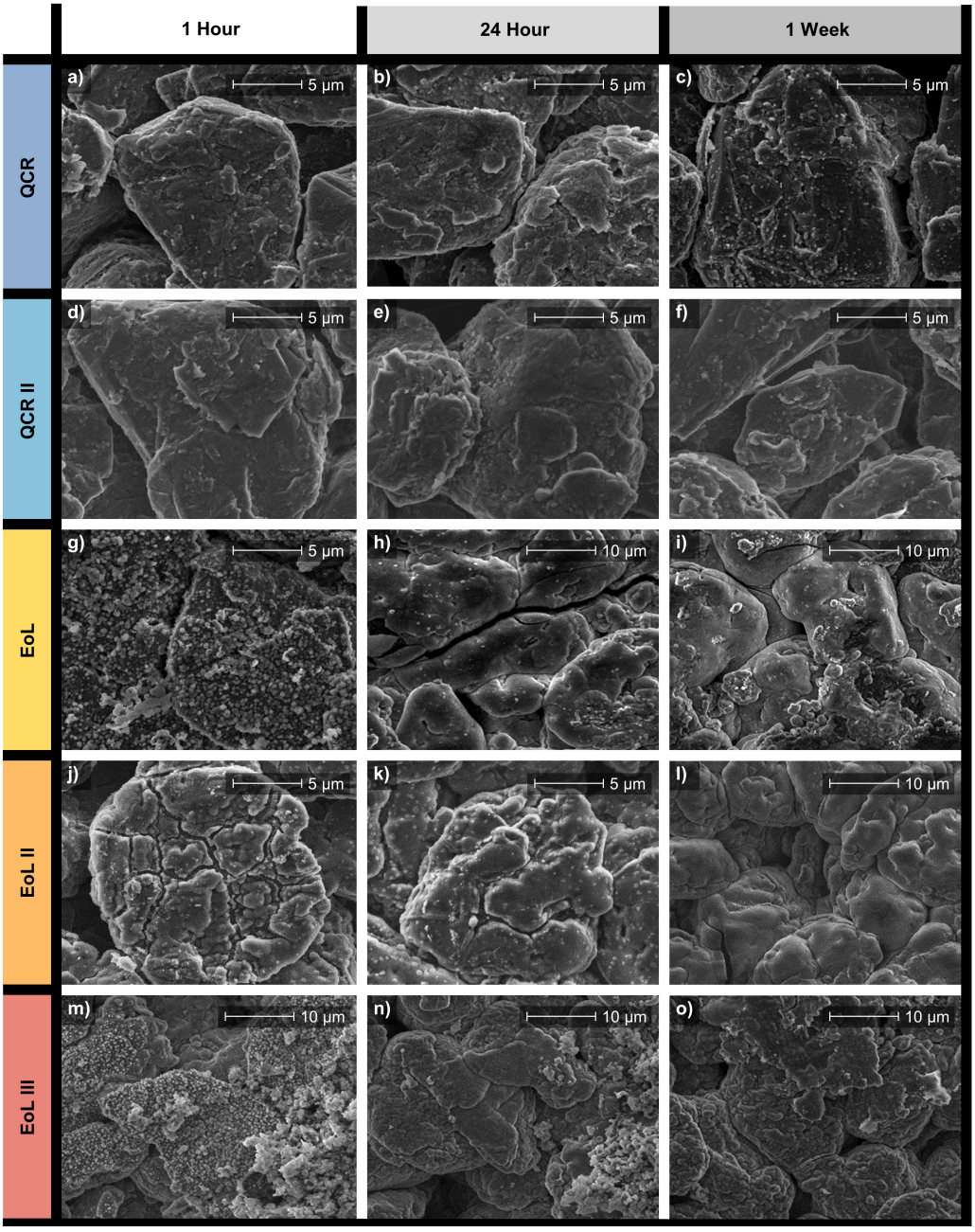


Fig. 4.15. *SEM images taken at either 5000× or 2500× magnification. (a–c) QCR after* 1 h, 24 h *and 1 week of air exposure, respectively. (d–f) QCR II after* 1 h, 24 h *and 1 week of air exposure, respectively. (g–i) EoL after* 1 h, 24 h *and 1 week of air exposure, respectively. (j–l) EoL II after* 1 h, 24 h *and 1 week of air exposure, respectively. (m–o) EoL III after* 1 h, 24 h *and 1 week of air exposure respectively. Reproduced from Sargent at al.*[121] *with permission from the Royal Society of Chemistry.*

4.6.2 Changes to XPS and HAXPES

As shown in the previous section, for EoL anodes, air exposure causes a crust to form on the surface which develops over time. This crust is likely to result from oxidation and hydrolysis of SEI species. For confirmation, anodes were also observed under XPS and HAXPES analysis after 1 h and 2 weeks of air exposure. Normalised plots for the $C\ 1s$ environment are shown in Figure 4.16 and $F\ 1s$ plots are given in Figure 4.17. A table of the percentage composition of each chemical environment for carbon and fluorine is given in Table 4.8 and atomic percentages of surface elements is given in Table 4.7.

As the carbon environment is particularly complex and the point of interest, an unconventional calibration method was employed. Specifically it was difficult to identify the aliphatic ($\mathrm{C{-}C/C{-}H}$) environment, therefore, the $\mathrm{Li}_x\mathrm{PF}_y/\mathrm{LiPF}_x(\mathrm{OR})_y$ in the $F\ 1s$ spectra was used to calibrate the binding energies. This was chosen as the environment was easy to identify and had the least variation, varying around a value of 686.9 eV by 0.4 eV, within the previous study (Section 4.5.3). XPS analysis of EoL 1 h and EoL 2 weeks, used traditional calibration techniques.

In Figure 4.16 the grey area represents the area under the normalised spectra for the equivalent sample before exposing the sample to air. After 1 h of air exposure, the oxidised carbon region (285 eV-291 eV) shows significant differences for each anode. QCR anode showed a reduction in this oxidised region and EoL showed a more exaggerated reduction. EoL II and EoL III anodes showed a shift in environments, with a decrease in $\mathrm{CO_3}^{2-}$ and $\mathrm{O{-}C{=}O}$ environments and a large increase in $\mathrm{C{=}O}$ and $\mathrm{C{-}O}$ environments. Evidently, some organic components react with the air/moisture producing volatile components that come off the surface, changing the surface composition. A similar but less intense change can also be seen within the HAXPES measurements taken after 1 h of exposure. Due to the porous nature of the SEI it may be expected that air would penetrate through and react

with components within the SEI, but to a lesser extent than the surface. The HAXPES scan of QCR after 1 h of air exposure looked almost identical to that of before exposure. Little change was expected as the thickness of the SEI layer would be significantly smaller than that on the EoL anodes.

The percentage composition of the lithiated graphite environment varies per scan with no consistency between sample or air exposure time. It is likely that lithiation within the anode is heterogeneous, leading to varying compositions based off locations of scans. QCR, which previously showed no lithiated graphite, now has a peak at around 283 eV for only the XPS scan. Perhaps the gassing of components within the SEI reduces its thickness, meaning more electrons from the lithiated graphite environment are detected. As this environment is still present after 2 weeks, it indicates that reactions between lithiated graphite and the air/moisture to form lithium salts is slow.

There is a very obvious change to the carbon composition for all EoL anodes when left in air for 2 weeks (in Figure 4.16(f) and (h)), signified by the growth of the $\mathrm{O{-}C{=}O}$ and $\mathrm{CO_3^{2-}}$ regions. This growth would explain the crust formation on the EoL anodes with prolonged exposure to air as seen within the previous SEM section (Section 4.6.1). Evidently, the growing crust on the surface primarily results from the oxidation of organic components within the SEI. This would also likely be seen in EoL II, however, a scan was not taken. The increase was not shown for QCR, which also did not show a growing crust within the SEM analysis.

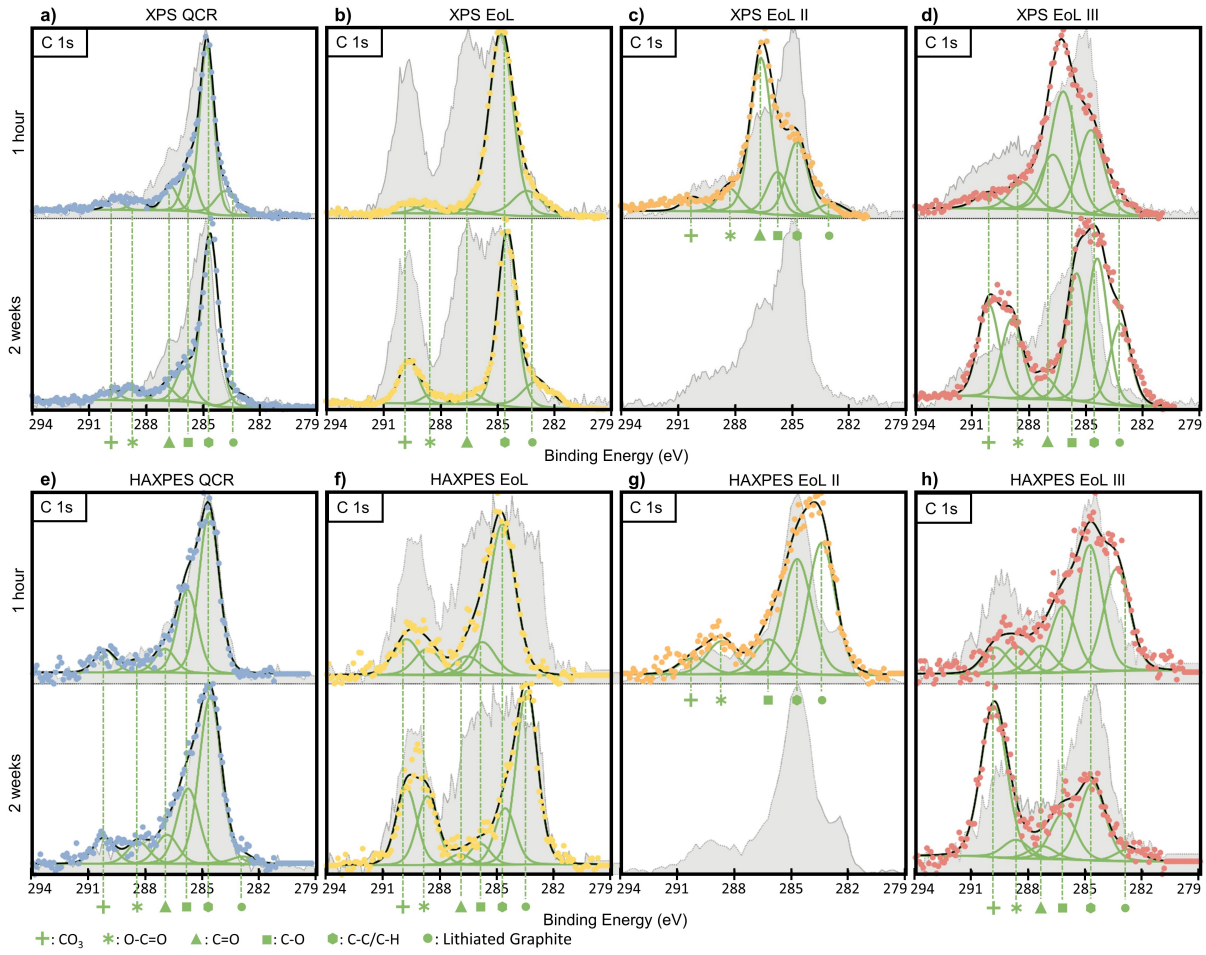


Fig. 4.16. *Normalised photoelectron spectra (XPS and HAXPES) obtained from the surface of anode materials. (a–e) Carbon 1s XPS (top row) and HAXPES (bottom row) of anodes before DMC wash and air exposure. Each signal fitting consists of six Voigt peaks with constrained binding energies. QCR II is shown in turquoise, EoL in yellow, EoL II in orange and EoL III in red. all spectra of QCR and the HAXPES analysis of EoL II was not conducted. The grey area shows the experimental signal before exposure to air.*

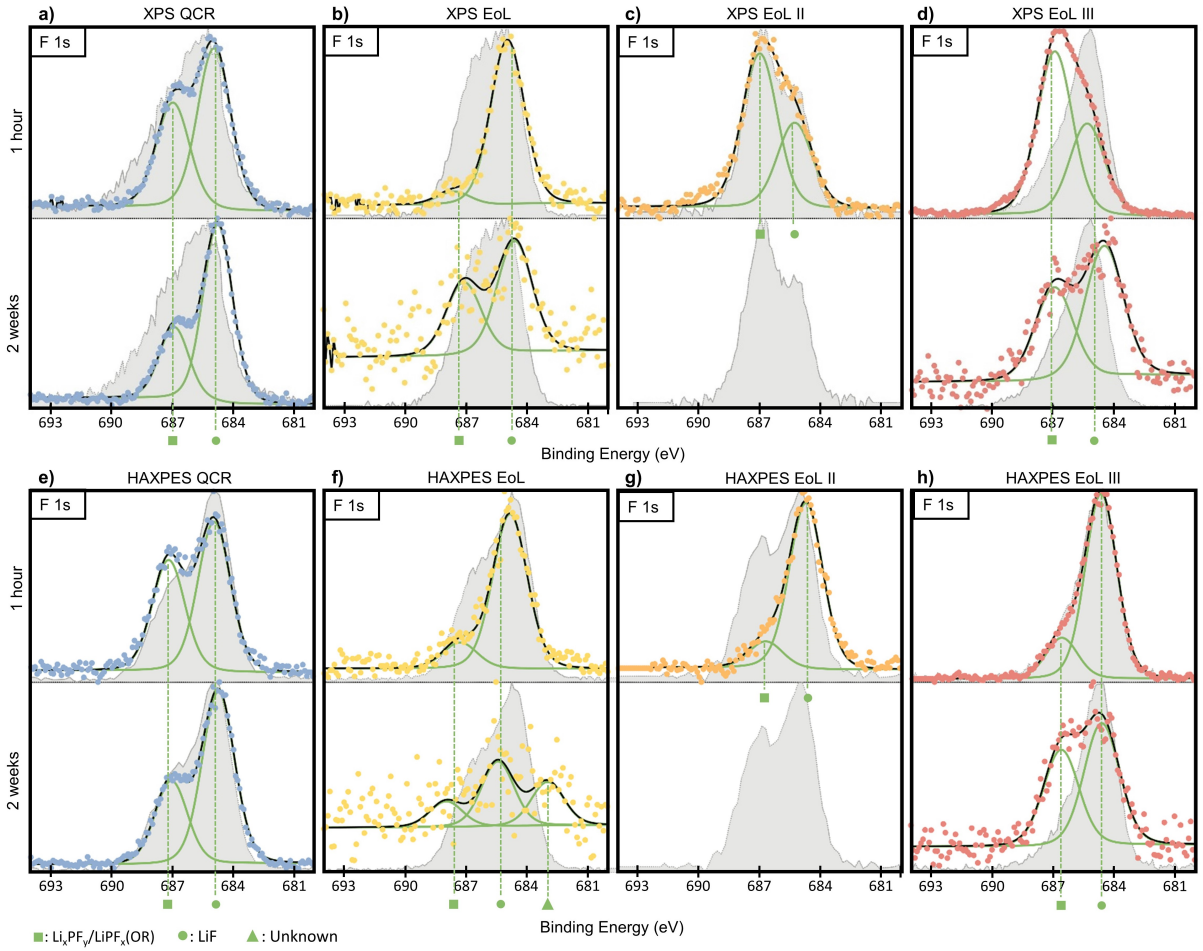


Fig. 4.17. *Normalised photoelectron spectra (XPS and HAXPES) obtained from the surface of anode materials. (a–e) Fluorine $1s$ XPS (top row) and HAXPES (bottom row) of anodes after air exposure. Two to three peaks were fitted for the calculated signal, representing $\mathrm{Li}_x\mathrm{PF}_y/\mathrm{LiP}_x(\mathrm{OR})_y$, LiF and an unknown environment. QCR II is shown in turquoise, EoL in yellow, EoL II in orange and EoL III in red. all spectra of QCR and the HAXPES analysis of EoL II was not conducted. The grey area shows the experimental signal before exposure to air.*

The $F\ 1s$ spectra are given in Figure 4.17. The XPS spectrum for QCR 1 h is similar to that of the non-exposed sample but lacking the $\mathrm{LiPF_6}$ environment. This environment would have predominately been removed via the anhydrous DMC wash conducted before air exposure, but traces may have reacted with the moisture in air to completely remove this environment. Both the HAXPES and XPS spectra show a reduction in the $\mathrm{Li}_x\mathrm{PF}_y/\mathrm{LiPF}_x(\mathrm{OR})_y$

environment after 2 weeks of air exposure, resulting in spectra with very low intensity. This is likely due to the growth of the crust layer observed in the SEM study (Section 4.6.1), which consists primarily of amorphous carbon. This layer obscures lithium-containing components, thereby reducing signal intensity.

Larger differences are seen within the EoL anodes, most notably the large increase in noise when exposed to air for 2 weeks when compared to $1\,\mathrm{h}$. If Table 4.7 is used in conjunction, it is evident that the concentration of fluorine on the surface drops significantly with increased exposure, reducing the intensity of the peaks within the spectra. This again is likely due to the oxidation of organic species, creating a surface crust consisting of $\mathrm{O{-}C{=}O}$ and $\mathrm{CO_3^{2-}}$ environments and not those of fluorine. These fluorine environments are likely to be buried under this crust.

Carbon is the dominant element found on the surface when looking at Table 4.7. Its percentage remains consistent for QCR but increases for the EoL anodes when exposed to air for 2 weeks. This increase is coupled by an increase in oxygen, which again highlights the crust formation. Fluorine, phosphorus and manganese concentrations drop after an exposure of 2 weeks, evidently, all these environments are buried by the crust. Manganese is only present within the HAXPES scans for EoL II and EoL III after 1 hour of exposure so evidently is already buried. Copper is again found on the QCR sample.

Table 4.7. *Percentage composition for each chemical environment obtained for each anode within the $C1s$ and $F1s$ regions under XPS and HAXPES analysis. Analysis was taken after air exposure. Standard deviations were calculated using a Monte Carlo procedure to simulate the variance from multiple fittings. Both value and standard deviation were calculated in casaXPS.*[130] *An extra environment within the EoL 2 weeks HAXPES scan at* 687 eV *with a percentage composition of* $1.38(22)$*. An asterisk represents valuses not collected.*

Sample and scan	**Air exposure**	**Carbon $1s$ (% Composition)**						**Fluorine $1s$ (% Composition)**	
		LiG	C–C/C–H	C–O	C=O	O–C=O	CO_3^{2-}	Li_xPF_y/$LiPF_x(OR)_y$	LiF
QCR XPS	1 hour	9.43(37)	46.3(22)	12.64(24)	7.09(11)	3.36(7)	3.88(8)	6.81(12)	10.48(18)
	2 weeks	4.63(10)	47.3(16)	11.42(21)	7.10(11)	3.83(4)	3.03(4)	6.59(7)	16.10(18)
QCR HAXPES	1 hour	0	37.3(26)	19.32(91)	5.54(19)	2.69(5)	5.21(14)	12.74(20)	17.24(28)
	2 weeks	2.13(6)	31.9(14)	14.37(68)	5.57(16)	4.18(9)	4.91(10)	12.07(16)	24.91(33)
EoL XPS	1 hour	12.83(49)	73.29(10)	0	1.93(2)	3.26(4)	3.19(3)	0.21(1)	5.30(14)
	2 weeks	11.56(14)	64.21(110)	0	3.56(3)	3.15(3)	15.90(19)	0.61(6)	1.03(11)
EoL HAXPES	1 hour	0	45.4(22)	9.91(56)	5.63(20)	7.82(26)	10.72(27)	2.95(11)	17.53(65)
	2 weeks	41.5(16)	13.11(49)	4.94(9)	2.46(5)	15.95(31)	17.80(37)	0.81(13)	2.05(37)
EoL II XPS	1 hour	4.84(13)	20.37(89)	11.69(32)	42.47(49)	6.44(8)	3.81(3)	6.68(23)	3.70(13)
	2 weeks	*	*	*	*	*	*	*	*
EoL II HAXPES	1 hour	29.3(17)	27.7(19)	8.36(32)	0.70(1)	7.96(19)	3.94(7)	3.02(10)	19.10(62)
	2 weeks	*	*	*	*	*	*	*	*
EoL III XPS	1 hour	3.28(18)	18.48(108)	26.36(113)	12.27(29)	5.92(8)	3.28(6)	19.45(39)	10.95(22)
	2 weeks	14.13(96)	25.05(162)	22.05(78)	3.99(7)	13.71(42)	16.08(51)	2.08(13)	2.91(18)
EoL III HAXPES	1 hour	14.71(95)	17.7(13)	9.34(53)	3.81(11)	3.78(9)	3.65(10)	8.50(14)	38.51(62)
	2 weeks	3.05(9)	19.54(86)	11.69(76)	3.28(10)	4.73(19)	38.2(27)	8.59(57)	10.89(72)

Table 4.8. *Surface elemental composition calculated from the lithium 1s, carbon 1s, oxygen 1s, fluorine 1s, phosphorus 2p (XPS), phosphorus 1s (HAXPES), sulfur 2p (XPS), sulfur 1s (HAXPES), manganese 2p (XPS), manganese 1s (HAXPES), nickel 2p (XPS), nickel 1s (HAXPES), copper 2p (XPS) and copper 1s (HAXPES) regions for each anode after air exposure. Standard deviations were calculated using a Monte Carlo procedure to simulate the variance from multiple fittings. Blank values indicate atomic percentages below the limit of detection. Both value and standard deviation were calculated in casaXPS.*[130] *An asterisk represents valuses not collected.*

Sample and scan	Air exposure	Lithium (at.%)	Carbon (at.%)	Oxygen (at.%)	Fluorine (at.%)	Phosphorus (at.%)	Sulfur (at.%)	Manganese (at.%)	Nickel (at.%)	Copper (at.%)
QCR XPS	1 hour	19.9(47)	41.8(40)	18.3(17)	8.54(87)	1.68(54)	6.37(75)	0.91(32)	-	1.52(26)
	2 weeks	18.4(64)	39.4(35)	18.2(17)	11.2(12)	2.50(62)	5.76(86)	1.34(37)	-	1.93(27)
QCR HAXPES	1 hour	20(12)	13.1(25)	9.8(19)	5.5(11)	6.6(25)	39.8(70)	2.3(21)	2.9(27)	0.60(21)
	2 weeks	16(14)	13.2(27)	9.7(20)	7.8(15)	10.5(29)	34.3(71)	3.4(24)	2.9(41)	1.36(32)
EoL XPS	1 hour	25.5(34)	51.3(26)	18.0(11)	2.86(77)	1.10(39)	0.62(43)	0.42(29)	-	-
	2 weeks	-	66.63(96)	33.18(94)	0.19(31)	-	-	-	-	-
EoL HAXPES	1 hour	-	24(11)	27(12)	6.2(32)	12.0(68)	-	23(12)	-	-
	2 weeks	21(18)	31.0(85)	34.3(93)	1.4(14)	-	-	-	-	-
EoL II XPS	1 hour	31.7(42)	43.3(29)	16.9(13)	5.28(65)	1.18(47)	0.69(44)	0.49(25)	6.7(2)	-
	2 weeks	*	*	*	*	*	*	*	*	*
EoL II HAXPES	1 hour	15(10)	21.4(36)	14.2(25)	6.3(12)	9.2(35)	6.6(36)	27.36(530)	-	-
	2 weeks	*	*	*	*	*	*	*	*	*
EoL III XPS	1 hour	38.3(35)	29.7(28)	15.4(11)	12.73(88)	3.03(39)	-	-	0.44(20)	-
	2 weeks	33.2(30)	34.3(26)	29.5(17)	1.72(57)	1.00(32)	-	-	-	-
EoL III HAXPES	1 hour	28(13)	15(3)	13.8(29)	13.3(28)	20.1(48)	-	7.3(45)	-	-
	2 weeks	35(15)	15.4(42)	31.2(78)	3.9(15)	7.0(43)	4.7(40)	-	-	-

4.7 | Chapter conclusions

This chapter has indicated a difference between anode material collected before use within a battery and after. This was expected due to the vast amount of degradation mechanisms discussed within the literature that affect and age the anode during cycling. Mechanisms discussed within the literature include: SEI formation, particle cracking, graphite exfoliation, loss of active material, loss of connectivity, lithium plating and metal contamination.[34,50–58] Particle cracking and graphite exfoliation would be detrimental to the electrochemical performance of the graphite; however, the effects of these two mechanisms were not evident on any of the studied anodes. It was observed that, during normal use of cells, the dominant ageing mechanisms for the anode appear to be SEI formation, metal deposition and a loss of connectivity. The growth of an SEI layer would deteriorate the health of a battery by continuous stripping of useable lithium and increasing resistance, but would likely not change the bulk properties of the graphite.

SEI formation and metal contamination were highlighted within the Raman, SEM, EDX, XPS and HAXPES studies, with the PXRD study showing no crystallographic differences between the obtained graphite anode materials. As expected, SEI thickness increased with increased cell ageing. The Raman study highlighted a less expected phenomenon of inhomogeneous growth of SEI, with more, but more uniformed ageing occurring at the top of the cell and less, but more varied ageing at the bottom of the cell. SEM and XPS studies highlighted metallic contamination and the volatility of this surface layer upon exposure to standard atmospheric conditions.

The observed degradation mechanisms may easily be addressed via a recycling procedure that washes the surface of the graphite. The disparity between this study and those in literature may be the use of real EV cells experiencing a normal use case. Within

the literature, ageing analysis is conducted on cells constructed in the lab or computationally, which may exaggerate certain ageing mechanisms.

The XPS and HAXPES studies highlighted the presence of trace amounts of lithiated graphite. These cells were not taken down to an OCV of $0\,\mathrm{V}$ so some lithiation would be expected, however a larger amount may be contained through the disconnection of lithiated material from the current collector as well as the trapping of lithium within the SEI.

This trace lithiated graphite may provide a potential recycling route as lithiated graphite hydrolysis with water, producing hydrogen. This hydrogen production may act as mechanical leverage to pull the active material away from the current collector. An analysis of this technique is discussed within the following chapter.

4.8 | Chapter appendix

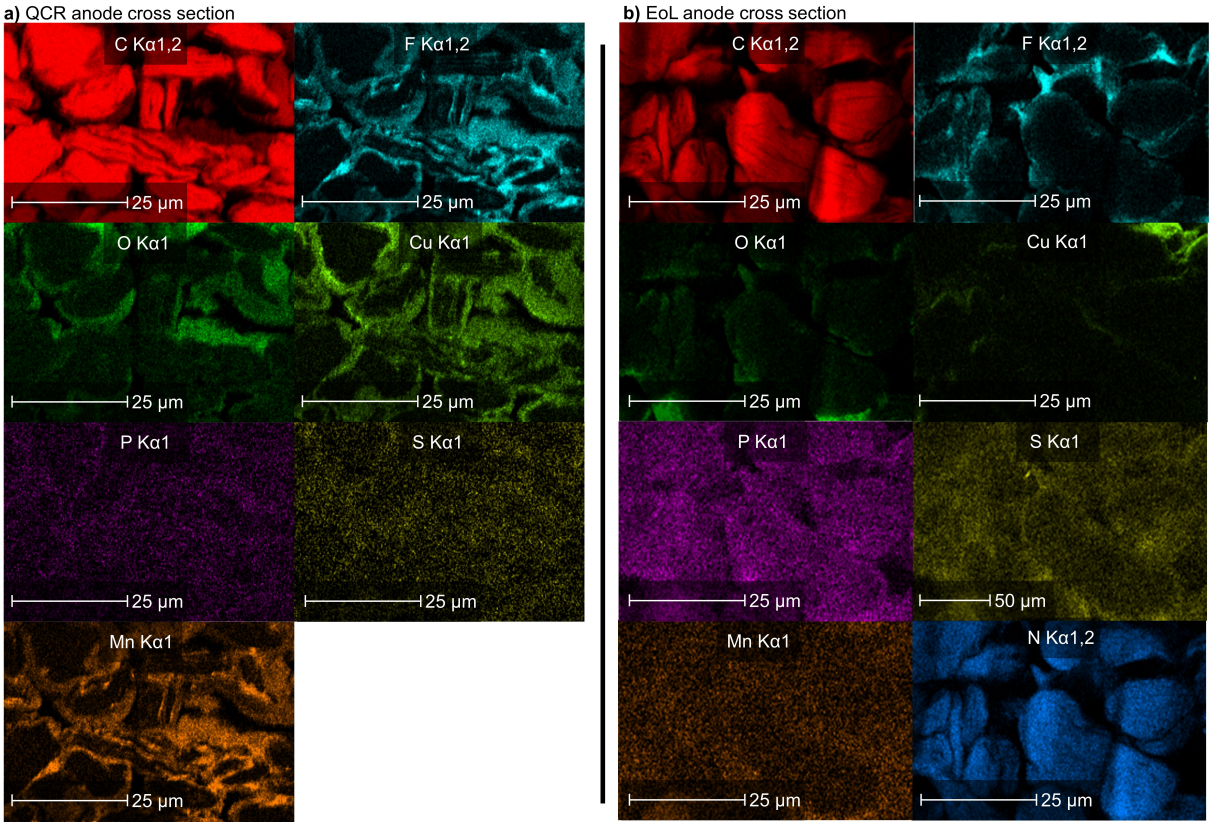


Fig. 4.18. *EDX maps of the DMC washed surfaces of (a) QCR and (b) EoL. Images were taken at 2,000x magnification.*

CHAPTER 5

Obtaining graphite via water delamination

5.1 | Disclaimer

Work within this chapter has been published in *Sargent et al.*[121].

5.2 | Introduction

Current LiB recycling processes typically begin by shredding the disused cell. The collected material can then be separated using techniques such as size, froth and flotation, or magnetic separation before further refinement into distinct components. The alternative and much more common process is to treat this shredded material as BM, where the material is either sold, fired or leached to extract value out of the material.[60]

These techniques bear a resemblance to those used in the already long-established steel refining industry. There is no coincidence here as many industrial leading recycling companies such as Umicore and Posco were primarily metallurgical companies before LiB recycling. Currently, these companies use LiBs as 'ores' to extract valuable materials such as nickel and cobalt.[160,161] *Gaines et al.*[162] estimated that in the US (2019) 54 % of un-usable LiBs were sent for recycling. Although this number is realistically good and likely to have increased over recent years, important components such as graphite, lithium, separator, electrolyte and casing are typically lost due to their poor economic value.[60] However, these

parts need to be recycled for environmental concerns, and future increasing demand for these non-sustainable materials.

Once the hurdles of direct recycling have been overcome, for instance, the ability to open cells and separate the electrodes without the use of intensive and hazardous manual labour, it offers a cleaner and more efficient way to reach 100% LiB recycling.[163]

This chapter will assume that an efficient route to acquiring anodes has been found, where now the anode needs to be separated so that each part can be rejuvenated separately and reused within a new recycled cell. A successful laboratory technique found in the literature is the use of ultrasonication within an aqueous environment.[84,86] Here a combination of convective motion and ultrasonic cavitation pulls the anode film (containing the graphite, PVDF binder, CB and other additives) from the copper current collector.[85] The passing of the negative pressure phase of an ultrasonic wave causes tiny vacuum holes to form within the solution, where dissolved gasses enter these holes. Upon the positive pressure phase, these bubbles are crushed causing a large release of energy in the form of high local pressure.[84,86] The PVDF binder used for gen 1 anodes is weakest at the boundary between the current collector and the anode film, which may aid this technique's delamination ability.[159] It must be noted however, that even though ultrasonication provides a cost-effective and green delamination, the technique still requires external energy and upon inspection of aqueous delamination, ultrasonication causes indentation on the current collector, evidently damaging the foil, and some anode film remains on the copper, evidently not a 100 % separation.[86]

Within the previous chapter, it was noted that discharged anodes still contain trace amounts of lithiated graphite. This lithium source will hydrolyse upon contact with water via a number of reactions, including those given below:

$$2\,\mathrm{Li}_x\mathrm{C}_{(s)} + 2\,\mathrm{XH_2O}_{(l)} \longrightarrow 2\,\mathrm{C}_{(s)} + 2\,\mathrm{XLiOH}_{(aq)} + \mathrm{XH}_{2(g)} \tag{5.1}$$

$$2\,\mathrm{Li}_x\mathrm{C}_{(s)} + 2\,\mathrm{CO}_{2(g)} + 2\,\mathrm{H_2O}_{(l)} \longrightarrow 2\,\mathrm{C}_{(s)} + 2\,\mathrm{XLiHCO}_{3(aq)} + \mathrm{H}_{2(g)} \tag{5.2}$$

$$2\,\mathrm{LiHCO_{3(aq)}} \longrightarrow \mathrm{Li_2CO_{3(aq)}} + \mathrm{H_2O_{(l)}} + \mathrm{CO_{2(g)}} \tag{5.3}$$

The production of gas and the exothermic reactions at the surface of the anodes may provide similar conditions to that of the ultrasonication technique allowing the anode film to be removed from the current collector. The benefit would be the lack of an external power source and potentially less cavitation on the copper.

Within the XPS and HAXPES study of air-exposed anode samples (section 4.6.2) within the previous chapter, it was found that SEI components are sensitive to air and water, leading to an initial formation of volatile species on the surface upon air-exposure. This has also been recorded in the literature; *Herstedt et al.*[164] observed a continuous degassing and a change in the surface chemistry for anodes exposed to air for ~ 3 min, which eventually eased after 3.5 h. They suggest the presence of components like lithium methoxide ($\mathrm{LiOCH_3}$) will react readily with water to produce volatile alcohols. *Malmgren et al.*[101] also suggest that upon air-exposure, lithium alkoxides will combust, producing $\mathrm{CO_2}$, following the equation below:

$$\mathrm{RCHOLi_{(s)}} + \mathrm{O_{2(g)}} \longrightarrow \mathrm{LiOH_{(s)}} + \mathrm{CO_{2(g)}} + \mathrm{R} \tag{5.4}$$

These processes may also aid in cleaving the anode film from the current collector and may also clear the graphite particle surface.

$\mathrm{LiPF_6}$ will also react with water via the following reactions:

$$\mathrm{LiPF_{6(s)}} + \mathrm{H_2O_{(l)}} \longrightarrow \mathrm{LiF_{(s)}} + \mathrm{POF_{3(g)}} + 2\,\mathrm{HF_{(g)}} \tag{5.5}$$

The production of toxic gasses may aid in the delamination but will lead to undesired side reactions like fluorination and will produce potential health risks. However, the kinetics of this hydrolysis is slow, requiring days to equilibrate. As a precaution all samples will be washed with DMC to remove any $\mathrm{LiPF_6}$ contamination.[101,164]

Within this chapter, the hydrolysis of trace amounts of lithiated graphite will be used to remove the anode film from the copper current collector, with the potential aid of the hydrolysis and oxidation of SEI components.

5.3 | Chapter aims

In this chapter, an effective method for removing the anode film from the current collector will be established. This technique will involve the hydrolysis of trace amounts of lithiated graphite (and SEI components) to produce gaseous species. These species will provide pressure changes as well as localised variation in temperature via the corresponding exothermic reactions that will allow the cleaving of the anode film from the current collector.

The efficacy of this water delamination technique as a step within a LiB recycling process will be examined by scrutinising the following key aspects:

- The efficiency, safety, and swiftness of the delamination process.
- Recovery rates and the generation of waste by-products.
- The overall quality of the reclaimed materials.

5.4 | Experimental

5.4.1 Water delamination process

After washing with DMC, portions of anodes were removed from an inert argon atmosphere and left for either 1 h, 24 h, 2 weeks or 4 weeks in air before submersion into a stirred beaker of deionised (DI) water. Typically ~ 2 g of anode was submerged in 80 mL of DI water. Once delaminated, the copper and anode material were separated and washed with more DI water

before drying. If no delamination occurred after 2 h of water submersion it was reported to be unsuccessful.

The single sheet of EoL anode was delaminated using 450 mL of DI water before 1 h of air-exposure. The full EoL sheet, weighing 13.5 g, where 8.6 g of graphite and 4.1 g of copper was recovered. This resulted in a 5.9 wt.% loss.

Delamination water was collected from the full sheet delamination for the lithium recovery experiment. This solution was vacuum filtered.

5.4.2 ICP-OES

ICP-OES (5110, Agilent) was used to determine the chemical composition of the solution resulting from submersion of anodes in DI water for 1 h. After air exposure times of 1 h, 24 h, 2 weeks, and 4 weeks, 10 mm diameter disks of DMC-washed anode samples (QCR, QCR II, EoL, EoL II, and EoL III), each weighing approximately 0.02 g, were submerged for 1 h in 20 mL of DI water. Following submersion, 10 mL of the resulting solution was extracted and filtered using a 10 mL syringe fitted with a Millex®-GP Filter Unit (pore size: 0.22 µm, diameter: 33 mm, polyethersulfone membrane, hydrophilic). To prevent precipitation of metals, 2 µL of ultrapure HNO_3 was added. 1 µL aliquots were then extracted from each filtered solution using Finnpipette F2 Single Channel 0.2 µL – 2 µL micropipettes. Each aliquot was further diluted with 9 µL of ultrapure HNO_3 (VWR Chemicals, 67 % – 69 %) using Finnpipette F2 Single Channel 100 µL – 1000 µL micropipettes to achieve a $100x$ dilution. Standards were prepared using a multi-element standard (10 µg mL^{-1}, 5 % HNO_3 matrix, TruQms). Values and standard errors were calculated based on measurements from three aliquots.

5.4.3 Lithium recovery experimental

An anode sheet weighing $13.79\,\mathrm{g}$ was delaminated using $450\,\mathrm{mL}$ of DI water before $1\,\mathrm{h}$ of air-exposure. During the washing of the recovered anode material and copper current collector from the full EoL anode delamination, $9\,\mathrm{mL}$ of DI water was added to the $450\,\mathrm{mL}$ delamination solution. The solution, initially at pH 13, was reduced to $29\,\mathrm{mL}$ using a rotary evaporator.

ICP-OES was performed on aliquots taken from both the initial and subsequent solutions throughout this study. The method followed was similar to that described above (Section 5.4.2), although further dilutions were required for solutions with high lithium content.

Via ICP-OES analysis it was determined that the initial solution content contained $445\,\mathrm{ppm}$ of lithium and the evaporated solution increased to $5552\,\mathrm{ppm}$. Via the chemical equation below (Equation 5.6) it was determined that $23\,\mathrm{mmol}$ of lithium hydroxide was contained within the concentrated solution. To precipitate out lithium carbonate (Li_2CO_3) a molar equivalence plus a $10\,\mathrm{wt.\%}$ excess of sodium carbonate (Na_2CO_3) ($1.14\,\mathrm{g}$) was added (calculated by using Equation 5.7 in Section 5.6). The solution was stirred at a temperature of $\sim 80\,^{\circ}\mathrm{C}$ for $30\,\mathrm{min}$ before the solution turned cloudy and $0.14\,\mathrm{g}$ of Li_2CO_3 was collected and dried.

$$Li^+_{(aq)} + H_2O_{(l)} \rightleftharpoons LiOH_{(aq)} + H^+_{(aq)} \tag{5.6}$$

ICP-OES determined that a $2768\,\mathrm{ppm}$ lithium concentration remained in the solution, equivalent to $\sim 14\,\mathrm{mmol}$ of lithium hydroxide. Using Equation 5.8 in Section 5.6 it was determined that $0.35\,\mathrm{mL}$ of H_3PO_4 (Sigma Aldrich, $\geq 85\,\%$) was required to add a molar equivalence plus $10\,\mathrm{wt.\%}$ excess in order to precipitate out lithium phosphate (Li_3PO_4). $0.34\,\mathrm{g}$ of Li_3PO_4 precipitated out almost immediately. This was filtered and dried. After further evaporation

via heating, ICP-OES analysis determined a remaining 720 ppm of lithium within the 25 mL solution.

The purity of the collected Li_2CO_3 and Li_3PO_4 was analysed using PXRD and Raman analysis using the methods described in Sections 5.4.4 and 5.4.5.

5.4.4 Delaminated Material PXRD and XPDF Analysis

PXRD was only conducted on the extracted Li_2CO_3 and Li_3PO_4 salts. Characterisation was conducted using the same method for in-house PXRD as discussed in Section 4.4.5. However, analysis and figures were produced using GSAS-II.[165]

5.4.5 Delaminated material Raman analysis

Raman spectroscopy measurements were taken from ten points on the surface of each anode before and after water submersion. Spectra were collected after certain periods of air-exposure (1 h, 24 h, 2 weeks and 4 weeks). For MAGE3, forty point scans were taken at random positions.

A Renishaw inVia Raman microscope with a green laser (wavelength of 532 nm, power of 100 mW) was used. For each spot measured, 5 acquisitions were taken. Analysis used a similar MATLAB code to that developed and discussed in Section 4.4.2.

One broad scan was taken on both Li_2CO_3 and Li_3PO_4 between $100\,cm^{-1}$ and $1800\,cm^{-1}$ using the same settings described above. More local scans were taken between $100\,cm^{-1}$-$300\,cm^{-1}$ and $1050\,cm^{-1}$-$1150\,cm^{-1}$ for Li_2CO_3 and $900\,cm^{-1}$-$1100\,cm^{-1}$ for Li_3PO_4.

Three scans were taken on the copper current collector obtained from the full sheet EoL anode delamination. These points were taken on areas of assorted colours. Two scans were also taken on pristine copper foil (MTI corporation, 9 µm).

5.4.6 XPS analysis of delaminated material

XPS and HAXPES experimental has already been discussed in Section 4.4.4. For air exposed samples, anodes were washed with DMC then exposed to ambient conditions for either 1 h, 24 h, 2 weeks and 4 weeks. After the required period of air-exposure, samples were put under vacuum before storing within an Ar glovebox (< 0.1 ppm H_2O and O_2). When ready, samples were transferred via sealed air-tight bags to the XPS and HAXPES facility. Delaminated anode materials and copper current collectors were dried and put under vacuum before also storing within an Ar glovebox.

Peak binding energies and widths were constrained according to environments found in literature; these are given in Table 3.2 within the experimental chapter.

5.4.7 SEM image collection

A Philips XL30 FEG scanning electron microscope (SEM) was used to gain high resolution images of the surface of the anodes and recovered graphite. An accelerating voltage of 5 kV was used with a secondary electron detector.

Samples were attached to pin stubs on a multi pin mount specimen holder via carbon tape (PELCO Tabs, carbon conductive tabs).

5.4.8 Graphite PSA analysis

PSA was conducted using a Microtract Flowsync laser diffraction particle size analyser.

Graphite for analysis was collected first via water delamination, followed by annealing to $500\,^{\circ}$C in air for 1 h. ~ 0.1 g was added to ~ 10 mL of DI water before 10 min of ultrasonication. Drops of tetrasodium pyrophosphate ($Na_3P_2O_7$) were added as a dispersing agent before the sample was added to the analyser.

5.5 | Water delamination

Figure 5.1 shows the delamination of an entire EoL anode sheet. Before submersion into the container filled with $450\,\text{mL}$ of DI water, the sheet was washed with DMC to remove any LiPF_6 traces, and exposed to air for just under $1\,\text{h}$. The entire process took $3\,\text{min}$, however, delamination began at around 10 s and effervescence occurred instantaneously upon contact with the water.

The anode film came off as a sheet and could easily be scooped out of the bath. Evidently, PVDF still bound the anode film particles together. The copper current collector showed no visible signs of damage and was indistinguishable from lab-sourced copper foil, however upon drying, the surface became discoloured, forming a mosaic pattern of purple, red, orange, and blue hues. This will be discussed later in Section 5.7. After the solid components were extracted from the bath, the delamination solution was filtered, and a yellowish solution with a pH of 14 was collected. Clearly, lithium sources within the anode, such as lithiated graphite, underwent hydrolysis, resulting in the formation of bubbles through the production of H_2 and CO_2 gas, and the elevation of the pH of the delamination solution due to the dissolution of LiOH. The collection of a yellow solution may indicate a loss in carbon content from the anode, either from the loss of CB that may have lost adhesion, or the hydrolysis/oxidation of SEI components causing components to detach and contaminate the delamination solution.



Fig. 5.1. *Snapshots of a* 3 min *video showing the delamination of a full EoL anode sheet via submersion in* 450 mL *of DI water. Prior to submersion the sheet was washed with DMC and exposed to air for just under* 1 h*. (a) Effervescence began immediately after submersion. (b) Shows the clean peeling of one side of the anode film at around* 1 min 30 s*. (c) The peeling of the reverse side of active material at around* 1 min 50 s*.*

5.5.1 Delamination efficiency

To test the efficiency and the applicability of this technique, ~ 0.2 g of each anode (QCR, QCR II, EoL, EoL II and EoL III) were cut, washed and exposed to air before submerging in water. In effect, the versatility to delaminate cells of different SoH and different air-exposure times was examined.

A segment of each anode was exposed to air for 1 h, 24 h, 2 weeks and 4 weeks before submersion into water. The following describes the reactivity of each anode, with Figure 5.2 used as a visual representation of these observations. After 1 h of exposure, all anodes delaminated from the current collector. All anodes also delaminated after 24 h, however, QCR took almost 2 h of submersion to delaminate compared to delamination in under 5 min for all other anodes. After 2 weeks, QCR would not delaminate and the rate of delamination for QCR II, EoL II and EoL III slowed to above 10 min. After 4 weeks QCR II and EoL II would not delaminate. For all anodes the effectiveness of delamination (whether the anode film came off instantly in one sheet or had to be scraped off) decreased with increased air-exposure time. This coincided with the rate of delamination which for all anodes would decrease with increased air-exposure time; the delamination of EoL took only 10 s after 1 h

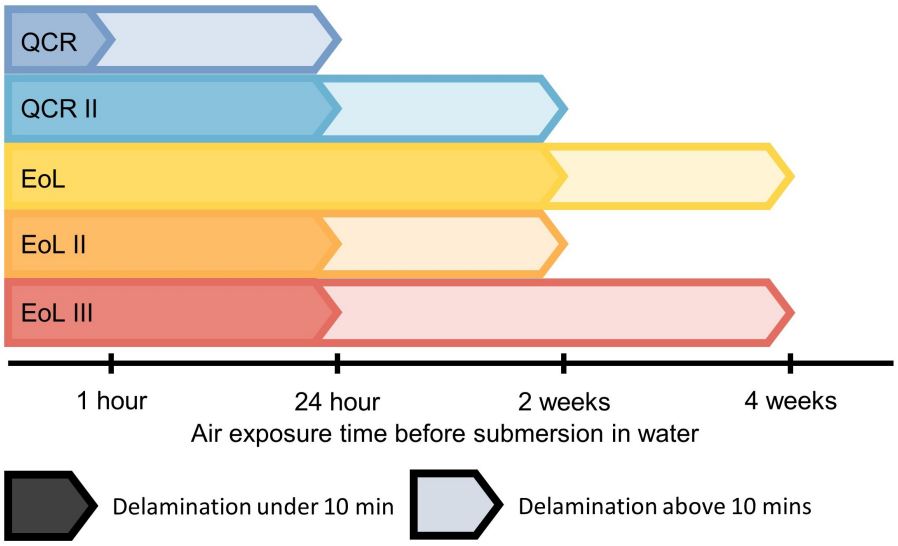


Fig. 5.2. *A visual representation of the observed delamination efficiencies for each anode after certain periods of air-exposure. If no delamination occurred within* 2 h*, it was determined that the anode did not delaminate. The end of the block represents the longest period of air-exposure that still led to a delamination. Delamination after 4 weeks was not studied, therefore EoL and EoL III may still delaminate with further air-exposure times. Reproduced from Sargent et al.*[121] *with permission from the Royal Society of Chemistry.*

of exposure, with both sides coming off as sheets, while after 4 weeks the process took just under 2 h where one side had to be scraped off.

For each anode segment, the pH change during delamination remained fairly consistent across different air-exposure times, increasing from pH 6 to pH 9. However, the amount of effervescence observed decreased with longer air-exposure times, which coincided with a reduction in delamination effectiveness. Therefore, it can be concluded that the amount of effervescence is crucial to the rate of delamination.

ICP-OES analysis was conducted on the solutions obtained after each anode submersion after different air-exposure times. The results from the 610.365 nm Li line are given in Figure 5.3. The concentrations of manganese, copper, cobalt and nickel were also examined, however, values above 0.5 ppm were not observed and therefore it was concluded that these elements did not influence the delamination process.

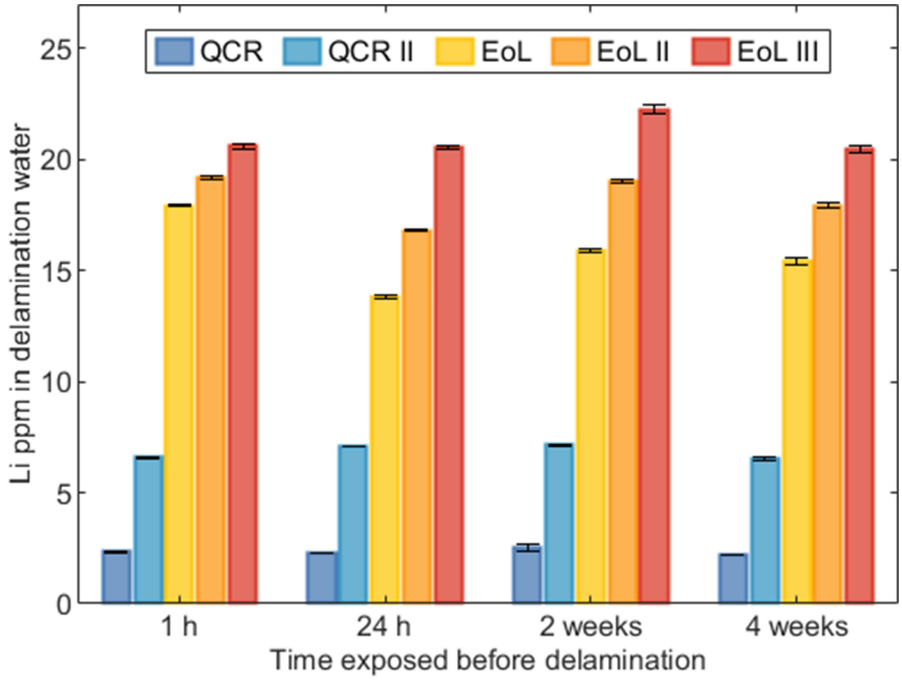


Fig. 5.3. *Li concentrations within* $20\,\text{mL}$ *of water after the submersion of each anode for* $1\,\text{h}$ *after either* $1\,\text{h}$*,* $24\,\text{h}$*, 2 weeks or 4 weeks of air-exposure. Each anode was cut into a* $10\,\text{mm}$ *disk weighing approximately* $0.2\,\text{g}$*. The* $610.365\,\text{nm}$ *analytical line for lithium was used. Error bars represent the standard error between three repeated measurements of the same solution. Reproduced from Sargent et al.*[121] *with permission from the Royal Society of Chemistry.*

Li concentrations within the solution varied depending on the anode used and not the time exposed to air; following an increasing trend from QCR < QCR II < EoL < EoL II < EoL III. Predictably QCR would be the lowest due to being taken down to an OCV value of $< 1.0\,\text{V}$ before dismantling. However QCR II had a similar OCV value to the EoL cells before dismantlement but showed a lower lithium content within the delamination solution. The higher Li concentrations from the EoL anodes are likely to be due in part to the increased thickness of the SEI layer as seen in section 4.5.3, storing more lithium sources for hydrolysis. Active lithium inventory loss is a major ageing mechanism for lithium-ion batteries and can occur via several alternate routes to SEI formation, including lithium plating and the trapping of lithium-ions within electronically isolated graphite particles caused either by

particle cracking, blocking of active sites or loss in electronic contact.[52,166] All degradation processes will lead to an increase in lithium content in the EoL anodes beyond the OCV. This may also explain why the most degraded anodes have the highest concentration of Li within the delamination solution (EoL < EoL II < EoL III).

The delamination efficiency drop due to air-exposure does not correspond to a drop in Li concentration within the delamination solutions. With increased air-exposure time prior to delamination, the Li concentration for a sample remains consistent. This may correspond to the slow hydrolysis and oxidation of lithium species (including lithiated graphite) whilst left out in the air.[101] This will form $LiOH$, Li_2CO_3 and equivalent salts on the surface that will still dissolve when submerged in water but will not provide the needed effervescence caused by the production of gaseous species needed for delamination.

Delamination works more effectively the less time the anodes are exposed to air. With increased air-exposure causing hydrolysis and oxidation of lithium species, therefore leading to the anodes producing less gaseous species upon submersion into water, decreasing the cleavage force applied to the anode film. The lessening efficiency of the delamination may seem like a hindrance but provides control over the production of gases. The safety of this technique is acceptable for one anode sheet, however, up-scaling may increase the amount of H_2 produced and may cause safety issues. This can easily be relieved by either varying the OCV of the cell before dismantlement or by leaving the anode material in the air for a certain duration before submerging in water. H_2 is also a beneficial by-product, once collected and purified from other gaseous species it may be used within the hydrogen storage industry.

5.6 | Lithium recovery

As lithium from the anode dissolves into the delamination water, this provides an excellent opportunity to recover and reuse the lithium. Lithium extraction is already a well-established industrial technique with brine evaporation plants accounting for just under an estimated two-thirds of all commercially extracted lithium.[167] There are many processes used to extract lithium from aqueous resources including; evaporation, ion sieving, ion pumping and electrodialysis. However, evaporation is currently the only technique exploited by industry.[167] Therefore, as a proof of concept, the lithium extraction represented here will follow closely to the evaporation of brine.

The evaporation process typically begins by increasing the concentration of lithium within the brine via solar and wind evaporation of large ponds. Once a concentration of around $6000\,\mathrm{mg_{Li}\,L^{-1}}$ is achieved the brine is pumped through a recovery plant to remove unwanted ions like calcium and boron via precipitation. Na_2CO_3 is then added to the brine to salt out Li_2CO_3 via a simple displacement reaction (given below) which is then re-dissolved and re-precipitated to increase its purity.[167,168]

$$2\,LiOH_{(aq)} + Na_2CO_{3\,(s)} \longrightarrow Li_2CO_{3\,(s)} + 2\,NaOH_{(aq)} \tag{5.7}$$

This technique proves to be cost-effective, however, requires specific environmental conditions (e.g. proximity to a brine basin and specific atmospheric conditions) and the large amounts of water used (half a million litres per ton of recovered lithium carbonate) questions the environmental efficacy of the extraction.[167]

As described at the start of this chapter, an entire sheet of EoL anode was successfully delaminated. Via ICP-OES analysis it was determined that the $459\,\mathrm{mL}$ solution obtained after filtering contained $445\,\mathrm{ppm}$ of lithium. As a wt.% this accounts for $0.04\,\%$ of the delamination solution. Salar de Uyuni brine reservoir in Bolivia contains 0.0321 wt.% of

lithium and Clayton Valley in the USA contains 0.0163 wt.%.[168] The U.S. Geological Survey states that brines from closed basins typically carry 200 ppm-1400 ppm of lithium, similar to the water obtained after delamination.[169] Although not attempted within this study, reusing the delamination water for multiple sheets may offer higher lithium concentrations within the solution and allow for an increase in the Li extracted per ton of water, reducing the environmental impact of water usage per lithium extraction.

If lithium were to be extracted from the delamination solution, it would offer two benefits over traditional brine evaporation. Firstly, the lithium is sourced from waste materials. Secondly, the delamination water does not contain large quantities of ions that could interfere with the lithium extraction like magnesium, potassium, boron, and calcium, therefore, many of the purification steps can be avoided.

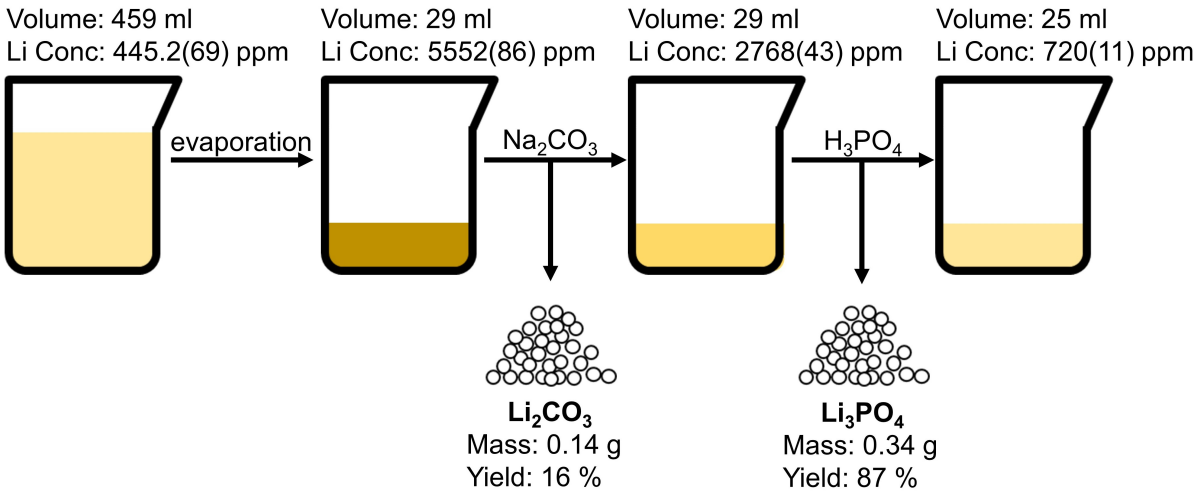


Fig. 5.4. *A diagram showing a basic representation of the process used to extract lithium from the delamination solution. Volumes are given and the lithium concentrations, found using ICP-OES. Masses of precipitates are given as well as the yield calculated by assuming* 100 % *of the lithium in the solution was converted to the precipitate as the theoretical yield.*

Figure 5.4 shows the steps taken to extract lithium from the delamination solution obtained after delaminating one EoL anode sheet. Much like brine evaporation, the solution was evaporated to near $6000\,\mathrm{mg_{Li}\,L^{-1}}$ before precipitation was attempted. After the addition

of Na_2CO_3, only $16\,\%$ of the lithium was extracted from the solution. The mass of Li_2CO_3 collected also only accounted for $33\,\%$ of the loss in concentration analysed via ICP-OES. As this process is non-optimised a small yield could be expected, however the reasoning for the discrepancy between ICP-OES lithium loss and obtained Li_2CO_3 mass is unknown. Many aspects of the process could be optimised, for instance; *An et al.*[168] incorporated many different stirring techniques like an impeller-type stirrer and ceramic balls to reach equilibrium faster. For the process used here, a magnetic stirrer bead was used for $30\,$min, which may have not been enough time. More importantly, the solubility of Li_2CO_3 is high at room temperature (12.9 g/L) but decreases at higher temperatures, allowing for the extraction of the salt at elevated temperatures ($8.5\,g\,L^{-1}$ at $80\,°$C).[170] *An et al.*[168] heated their solution between $80\,°$C-$90\,°$C allowing the extraction of $90\,\%$ of lithium within the brine. Here, the solution was only just heated to $80\,°$C, which may explain the low yield. The low yield in comparison to the loss in Li concentration may arise from the lack of control over the volume and the use of multiple beakers may have caused non-precipitated Li_2CO_3 to be lost.

Li_2CO_3 is the most commercially important lithium salt accounting for $46\,\%$ of the global market in 2015 due to its use in glass, ceramics, drugs and batteries.[171] However, here the solubility of the salt has created issues in its extraction. Another precipitation method discussed in the literature is the use of phosphoric acid to precipitate Li_3PO_4.[171–173] Li_3PO_4 has its use within the battery industry, being used as an easy precursor to $LiFePO_4$, a common cathode. The solubility of Li_3PO_4 is also much lower at room temperature ($0.4\,g\,L^{-1}$ at $20\,°$C) allowing for easier extraction of lithium from this now lower Li concentrated water.[171] An advantage to switching to precipitation using the polyprotic phosphoric acid after Li_2CO_3 is that the formation of Li_3PO_4 requires basic conditions and the remaining delamination water contains both $LiOH$ and $NaOH$. If an acidic/neutral solution is used LiH_2PO_4 and Li_2HPO_4 solutes are formed instead of the Li_3PO_4 precipitate, lowering the amount of lithium that can be extracted.[172,173] It is assumed that the reaction follows the pathway given

below:[172]

$$3\,Li^{+}_{(aq)} + H_2PO_4{}^{-}{}_{(aq)} + 2\,NaOH_{(aq)} \longrightarrow Li_3PO_{4\,(s)} + 2\,Na^{+}_{(aq)} + 2\,H_2O_{(l)} \qquad (5.8)$$

This extraction was much more successful, obtaining a yield of $87\,\%$. Evidently not all the lithium reacted with the added Na_3PO_4 and further refinement of the process may yield higher extraction.[174] The mass of the extracted Li_3PO_4 also accounts for $104\,\%$ of the loss of lithium concentration. This above $100\,\%$ may again arise from errors via dilutions, volume measurements, switching beakers and perhaps hydration.

Through both processes around $91.2\,\%$ of the lithium within the solution was extracted. Therefore, it has been shown that it is easy to extract $0.6\,\%$ of the weight of the anode of lithium via water delamination ($0.14\,g$ of Li_2CO_3 and $0.34\,g$ of Li_3PO_4 from an anode weighing $13.79\,g$). Based on previous literature searches, it appears this is the first-time lithium extraction from a graphite anode has been recorded. $8.8\,\%$ of the lithium from the delamination remains in the water after this study. Therefore, there is room for refinement. Other precipitation processes can be used such as Na_3PO_4 instead of phosphoric acid.[171,174] Alternatively, steps of this process can be used and refined independently as a single-step process.

The purity of the extracted salts were examined with Raman and XRD. This is given in Figure 5.5.

From the XRD patterns (Figure 5.5(a) and (c)), it appears that there are no crystalline impurities in either of the collected salts. For each, a large background occurs from using the low background sample holder. The Raman spectra (Figure 5.5(b) and (d)) show only peaks for their respected salts however these Raman spectra showed large background signals, which likely result from fluorescence, possibly due to organic compounds in the sample.[177] No CB/graphitic peaks were found for both samples, although the discolouration of the delamination water indicates the presence of CB and organic contaminates. Evidently

the organic contamination remains in the sample, whereas the carbon black can be washed off through the filter paper. This organic contamination will likely be removed by heating, which could facilitate the decomposition or removal of the organic material.

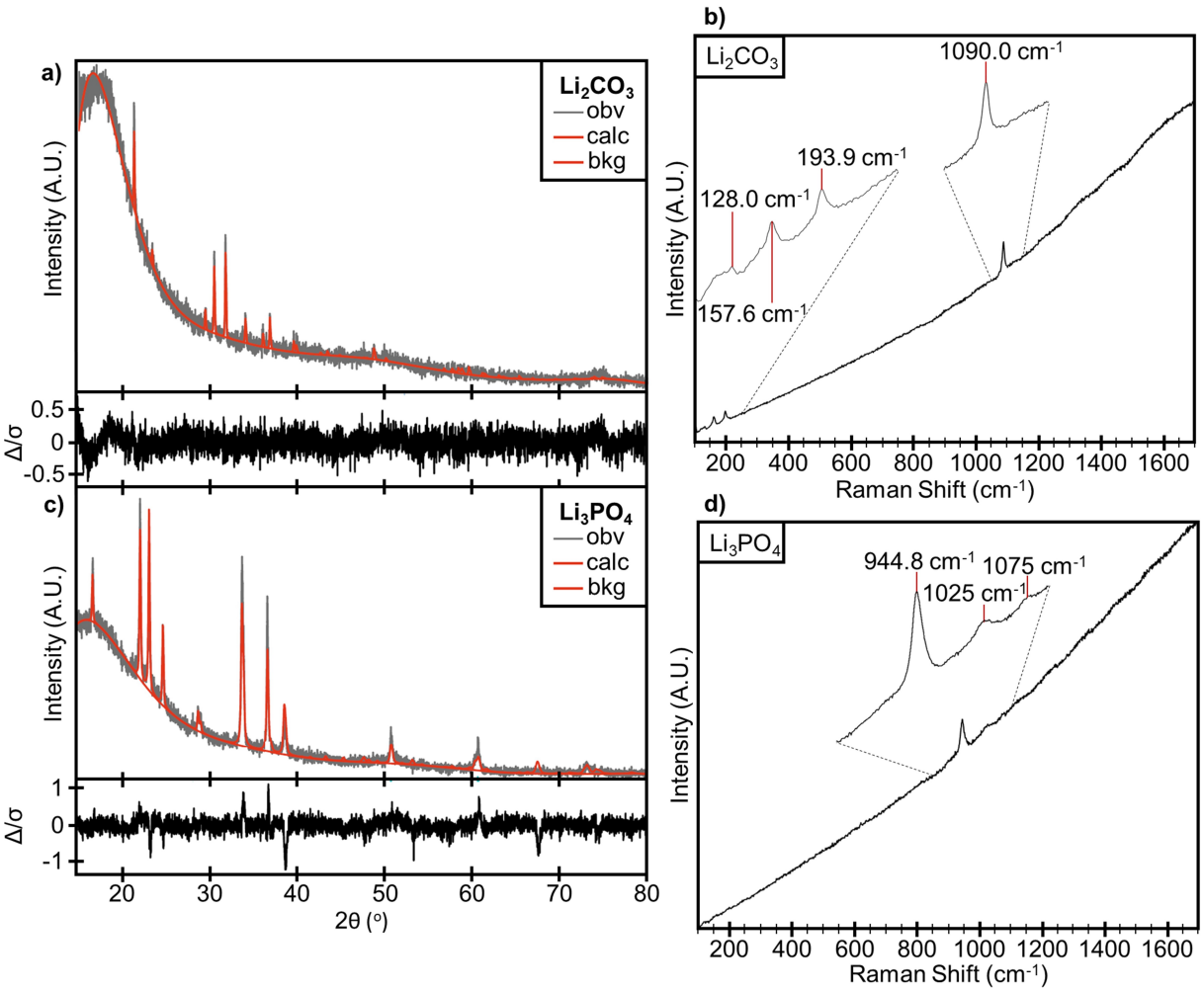


Fig. 5.5. *(a) Refined XRD pattern taken of recovered* Li_2CO_3*, Crystallographic Information File files taken from Idemoto et al.*[175]*. (b) Raman spectrum taken of recovered* Li_2CO_3*. (c) Refined XRD pattern taken of recovered* Li_3PO_4*, Crystallographic Information File files taken from Keffer et al.*[176]*. (d) Raman spectrum taken of recovered* Li_3PO_4*.*

5.7 | Quality of the copper current collector

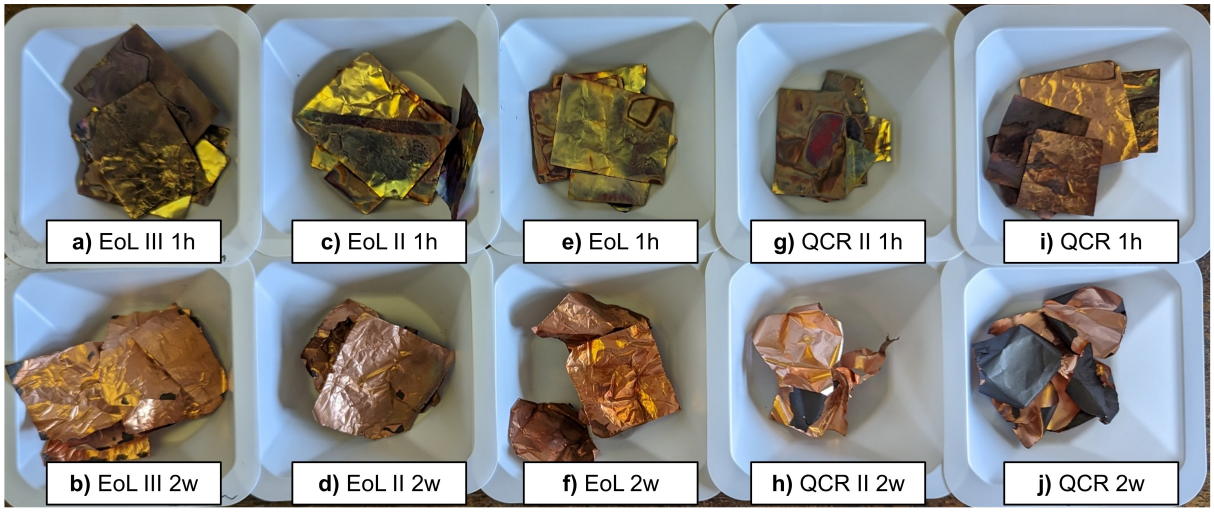


Fig. 5.6. *Images taken of the copper foil obtained from (a)(b) EoL III, (c)(d) EoL II, (e)(f) EoL, (g)(h) QCR II and (i)(j) QCR after delamination in water, washing and drying of the foil. The top images show delamination after* 1 h *of air-exposure and the bottom after 2 weeks of air-exposure.*

Upon delamination, the copper foil shows no signs of deterioration, however, after drying, discoloration appears on the surface. This is shown for each anode in Figure 5.6. The amount of discolouration appears to depend on the efficiency of delamination, with EoL III 1 h (an anode that delaminated well) showing a large discoloration compared to QCR II 2 weeks (a sample that took almost 2 h to delaminate) showing the pink hues of pristine copper. As the pH of the delamination water is fairly consistent for each delamination it might be expected that each copper experiences the same amount of discolouration, however this is not the case. In fact, samples that delaminate less efficiently spend more time within the basic conditions of the delamination water. So perhaps, more discolouration would be expected on these samples, which was not seen.

Figure 5.7 shows the extent of this discolouration. After delamination, the full EoL foil sheet gained a mosaic pattern of blue, red purple and orange hues. These are indicative of

oxidation of the foil, with the variety of colours coming from intermediates between copper and copper (II) oxide.[178] Copper (I) oxide is red, copper (II) hydroxide gives a green-blue colour and copper (II) oxide is black, giving rise to the mosaic pattern.

When pristine copper foil is submerged in a heated, agitated solution of LiOH in order to mimic the delamination conditions, oxidation does not visibly occur. An image of before and after is given within the appendix (Figure 5.15).



Fig. 5.7. *An image taken of the EoL foil collected from the full sheet delamination shown in Figure 5.1 after drying.*

Raman spectroscopy was taken on points of the obtained copper foil and compared to pristine foil. This is given in Figure 5.8. Peaks found at around $218\,\mathrm{cm}^{-1}$, $301\,\mathrm{cm}^{-1}$, $532\,\mathrm{cm}^{-1}$ and $641\,\mathrm{cm}^{-1}$ on the obtained copper are indicative of copper oxidation. Variations in intensities of these peaks, and therefore copper oxide content, lead to the variety in colour.[179] Two broad peaks appear at around $1667\,\mathrm{cm}^{-1}$ and $1896\,\mathrm{cm}^{-1}$, these wavelengths are too high to indicate CB/graphite contamination.

Another peak appears only on the pristine foil at $2898\,\mathrm{cm}^{-1}$. Both pristine and EoL copper foil appear to consist of rolled electrolytic tough pitch copper, indicated by the parallel grains observed on one side of the foil whilst using SEM (shown within the appendix in Figure 5.16).[103,180] On a separate note, the difference in surface structure may explain why one side more readily delaminates. Typically during manufacturing, anti-oxidation pretreatments are required to prevent surface oxidation.[181] A number of processes can be used such as alloying and electroplating, however these degrade physical properties and introduce harmful elements.[182] A much more practical technique for copper used within a conductive environment is the addition of a passive carbon layer to the surface.[182] Both *Peng et al*[182] and *Hong et al.*[183] use formate ions and dodecyl mercaptan ($\mathrm{CH_3(CH_2)_{11}SH}$) to form a protective passive layer on the copper surface that does not hinder electrical or thermal conductivity. As the peak at $2898\,\mathrm{cm}^{-1}$ can be associated to ($-\mathrm{CH}-$) vibrations,[183,184] it is not a stretch to believe that a passive carbon coating has also been applied to the pristine copper. The manufactures web page also quotes that "antioxidation pretreatment is necessary for the rolling copper foils to be used as battery current collector".[181] This coating would prevent oxidation when dipped within the heated LiOH solution.

Oxidation of the recovered films after delamination may indicate that the delamination process also removes this antioxidant passivation layer. Quantitative XPS results of the surface of recovered foil from efficient delamination (EoL III 1 h) and slow delamination (QCR II 2 weeks) are given within Table 5.1. Visually QCR II 2 weeks was pink and EoL III 1 h was oxidised (as seen in Figure 5.6). The XPS results show higher copper and oxygen intensities for EoL III 1 h, evidently from the presence of copper oxide. QCR II 2 weeks shows a slightly higher carbon content as well as the presence of sulfur. This could indicate a carbon and thiol protective layer which is not present on EoL III 1 h. Therefore, more efficient delamination may remove more of this protective layer, describing the relationship between more efficient delamination resulting in a greater extent of copper oxidation. However, whether this process

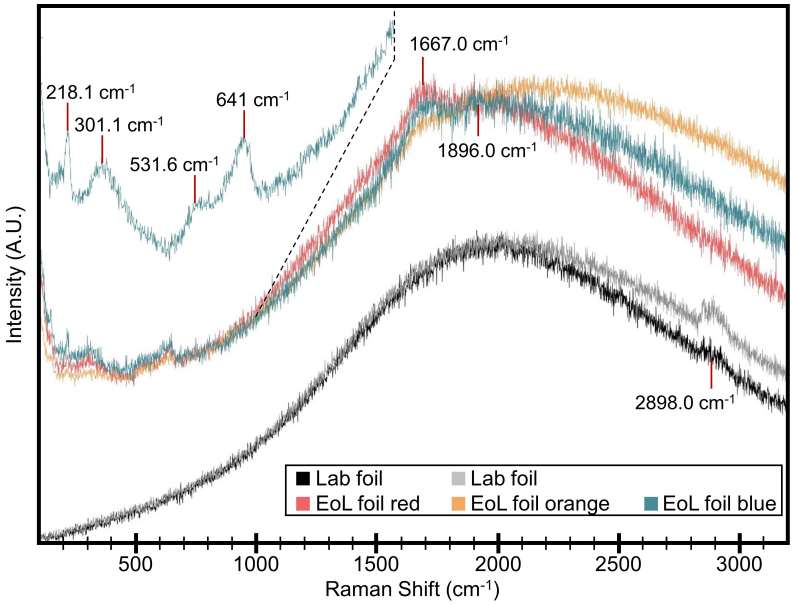


Fig. 5.8. *Point Raman spectra taken on three spots of recovered EoL foil and two spots of pristine foil. The colour of the EoL spectra represent the colour of the copper the spectrum was taken.*

is mechanical or due to the change in chemical environment from the production of reductive H_2, to oxidising $LiOH$ solution and drying under air, is unknown.

Table 5.1. *XPS atomic percentages of obtained copper foil for QCR II after delamination following 2 weeks of air-exposure and EoL III after delamination following* $1\,\mathrm{h}$ *of air-exposure. The percentage only relates to the four elements given within the table.*

Sample	Copper (at.%)	Oxygen (at.%)	Carbon (at.%)	Sulfur (at.%)
QCR II 2 weeks	2.26(1)	15.96(7)	78.28(26)	3.51(1)
EoL III 1 hour	3.88(1)	21.57(1)	74.55(26)	0

Although the copper is oxidised, recycling plants would likely smelt the copper to retrieve the desired metal in its desired form. Therefore, the oxidation layer would easily be removed.

5.8 | Study of the recovered film

5.8.1 Raman analysis

Raman spectroscopy was used to analyse the graphitic material within the anode film before and after water submersion. 10 randomly dispersed point scans of QCR II and EoL II were taken after certain periods of air-exposure (1 h, 24 h, 2 weeks and 4 weeks) and compared to their counterpart after water submersion after the same time periods. The results are shown in Figure 5.9. The same study was conducted on all anodes, these spectra are given within the appendix (Figure 5.17).

As expected, both before and after water submersion spectra are dominated by graphitic peaks, specifically the G (graphite) band found at $1590\,\mathrm{cm}^{-1}$ and the D (disorder) band found between $1320\,\mathrm{cm}^{-1}$-$1440\,\mathrm{cm}^{-1}$.[31,75,185,186] The G band was easily resolved by fitting a Lorentzian peak, however, the D band is much more complex. Three Voigt peaks are commonly quoted in the literature resulting from the D, $D3$ and $D4$ peaks.[186] These peaks were used to resolve this D band. An example fit of this region is shown in Figure 5.9(g). The origin of each graphitic peak is given in Section 3.1.2.

The G' region found between $2500\,\mathrm{cm}^{-1}$-$2800\,\mathrm{cm}^{-1}$ and shown in Figure 5.9(h) has been used to investigate the degree of stacking between graphene layers within the literature.[31,187] However, the bulk nature of graphite as well as the interference of CB and amorphous carbon complicates the obtained G' region, therefore, analysis was not conducted.

Two overlapping broad peaks centring around $800\,\mathrm{cm}^{-1}$ appear after water submersion of both samples (shown in Figure 5.9(b) and (d), with an expanded region shown in Figure 5.9(f)). This was assigned to amorphous sp^2 vibrations which may occur due to a pitch coating applied to the surface of the graphite that is only exposed once the SEI and other

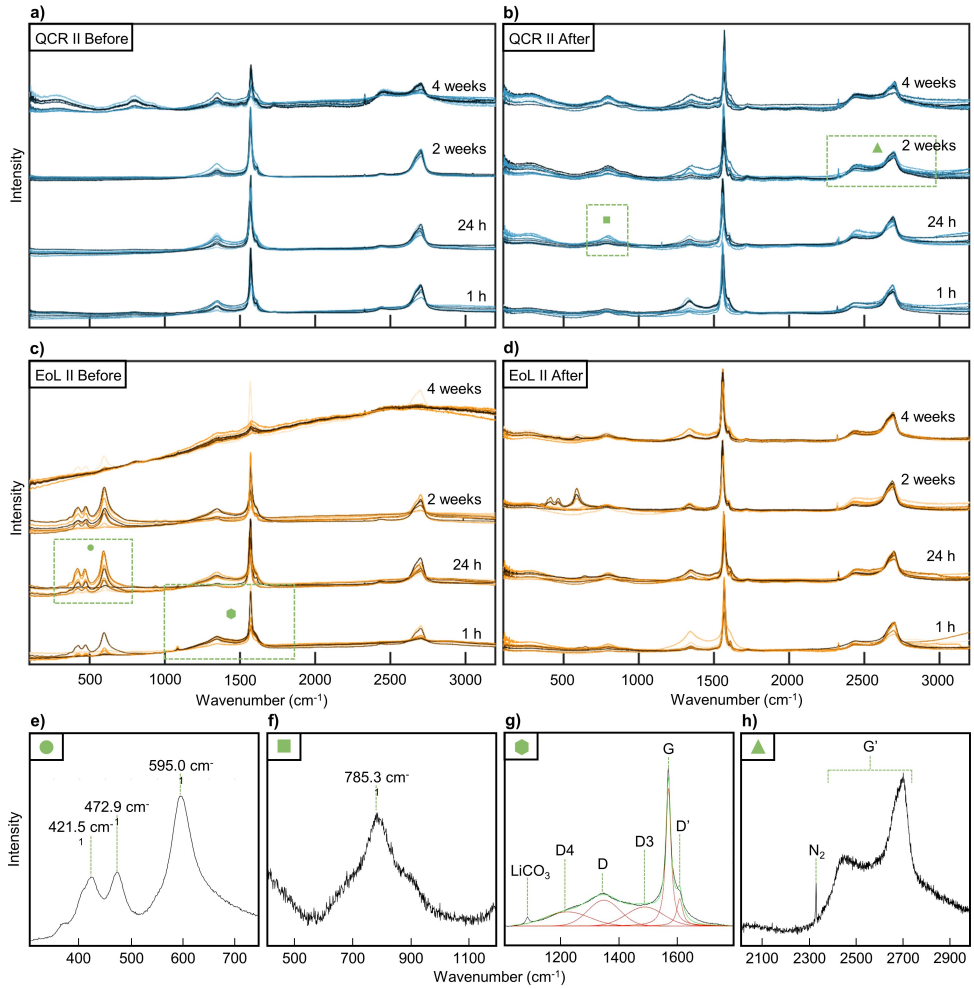


Fig. 5.9. *40 randomly dispersed Raman point scans were taken on (a) QCR II and (c) EoL II before water submersion and (b) QCR II and (c) EoL II after water submersion. For the pre-submerged samples, 10 scans were taken at each of the following time intervals of air-exposure:* $1\,\mathrm{h}$, $24\,\mathrm{h}$, *2 weeks and 4 weeks. Water submersion was also conducted at these time intervals, where once dried, 10 Raman scans were taken of each sample to give the post-submersion figures. Scans taken at the same time interval for each sample are overlapped. (e-h) show regions of interest from the Raman spectra shown in (a-d) which are also highlighted with a green box and a symbol as an identifier. (e) Phosphorus or lithium salt peaks found between* $300\,\mathrm{cm}^{-1}$-$750\,\mathrm{cm}^{-1}$ *in EoL II after* $24\,\mathrm{h}$ *of air-exposure. (f) Amorphous* sp^2 *vibrations found between* $600\,\mathrm{cm}^{-1}$-$1200\,\mathrm{cm}^{-1}$ *for QCR II after submersion after* $24\,\mathrm{h}$ *of air-exposure. (g) The graphitic region found between* $1100\,\mathrm{cm}^{-1}$-$1700\,\mathrm{cm}^{-1}$ *for EoL II after* $1\,\mathrm{h}$ *of air-exposure. Graphitic peak fittings are shown and labelled, as well as a peak originating from* $\mathrm{Li_2CO_3}$. *(h) The G' region found between* $2000\,\mathrm{cm}^{-1}$-$3000\,\mathrm{cm}^{-1}$ *for QCR II after submersion after 2 weeks of air-exposure. Reproduced from Sargent et al.*[121] *with permission from the Royal Society of Chemistry.*

surface contaminates are removed.[19,188] These two peaks were also found in the Raman spectra taken of MAGE3 (Figure 5.18 given within the appendix), a commercial battery-grade graphite used as a standard, which is also likely to have this pitch-derived carbon coating. A pitch coating is typically composed from petrochemical by-products and predominantly consists of aromatic hydrocarbons. This coating provides high conductivity, volumetric expansion moderation as well as reduces access to the graphite edge plane where parasitic reactions can occur, making it a good addition to battery-grade graphite.[19]

In EoL II, before water submersion (Figure 5.9(c)) and to a lesser extent after water submersion (Figure 5.9(d)), three intense peaks can be found at around $422.6\,\mathrm{cm}^{-1}$, $471.8\,\mathrm{cm}^{-1}$ and $596.1\,\mathrm{cm}^{-1}$ (highlighted in 5.9(e)). Within the literature, it was found that PO_4 ν_2 symmetric bending generates a peak at around $431\,\mathrm{cm}^{-1}$ and PO_4 ν_4 asymmetric bending generates a peak at around $594\,\mathrm{cm}^{-1}$, perhaps suggesting the presence of phosphate salts.[189] Multiple phosphate products could appear on the surface after air-exposure including manganese phosphate, nickel phosphate, organic phosphates and organo-fluoro-phosphates, either from the presences of metals, SEI and trace electrolyte.[190] $LiPF_6$ reduction products like LiF, PF_5 and POF_3 could also lead to the generation of these peaks.[191] The complexity of the surface and the history of these anodes makes it almost impossible to confirm the identity of these peaks; as well as phosphates, multiple lithium salts like Li_2O and $LiOH$ produce peaks in this region.[192]

A small sharp peak appears between $950\,\mathrm{cm}^{-1}$-$1085\,\mathrm{cm}^{-1}$ in Figure 5.9(c) which can be associated to the presence of Li_2CO_3.[53] Another small peak intermittently appears at around $1753\,\mathrm{cm}^{-1}$ for all samples, this may correspond to $2\nu_2$ overtones of internal vibrations within CO_3^{2-} groups.[193] This could be linked to the presence of Li_2CO_3 or $MnCO_3$ salts on the surface. The intensity and presence of these peaks vary between scans on the same sample at the same air-exposure time. This shows the heterogeneity of the surface and again, like Chapter 4 suggests, ageing occurs in local clusters and not evenly within the cell.

Submersion of EoL II in water appears to remove most of these impurities, however some traces still remain.

The D region equates to the presence of defects within the graphite, allowing for theoretically disallowed phonons within perfectly stacked crystalline graphite, whereas the G band corresponds to an E_{2g} stretch mode within sp^2 sites which is present in even the most crystalline graphite.[31,75,186] Thus a calculation of the I_D/I_G ratio allows for the quantification of carbon disorder on the anodes surface and sub-surface. Similar to Section 4.5.1, a statistical approach was taken to avoid errors occurring from surface heterogeneity.[143,194] I_D/I_G ratio were calculated for the 40 scans gathered for each sample and combined to create a distribution of before and after water submersion. These distributions as well as the distribution gathered for 40 scans taken on MAGE3 powder are given in Figure 5.10.

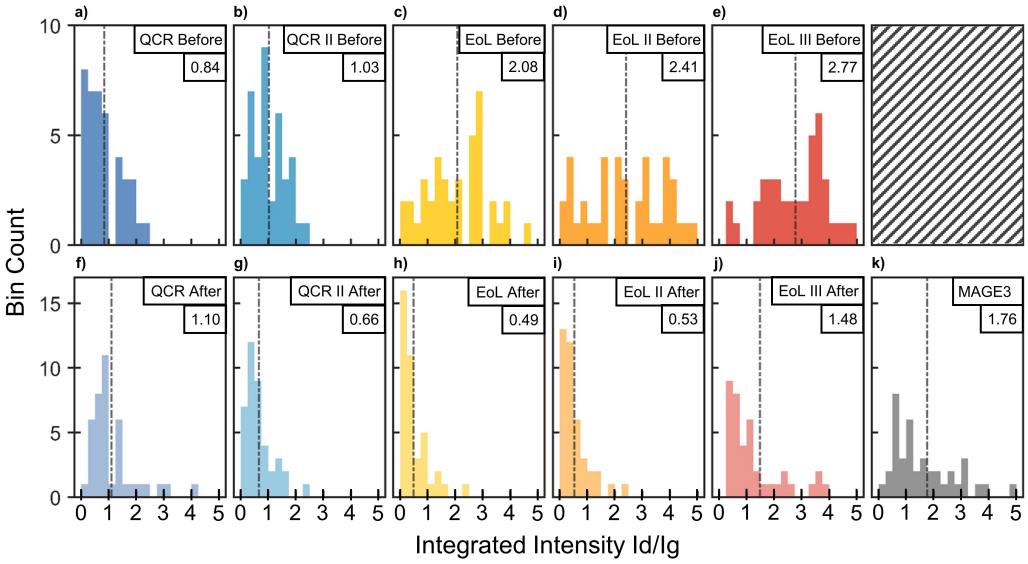


Fig. 5.10. *Distributions of 40 I_D/I_G ratios calculated from randomly distributed Raman scans on (a) QCR, (b) QCR II, (c) EoL, (d) EoL II, and (e) EoL III anode material before water submersion as well as (f) QCR, (g) QCR II, (h) EoL, (i) EoL II, and (j) EoL III anode material after submersion. (k) shows the distribution gathered for a powder of MAGE3. Peak-fittings and integrated intensities were calculated in MATLAB.[125] The mean I_D/I_G ratio is shown via the dash-dotted black line and is given in the top right corner of each distribution. Reproduced from Sargent et al.[121] with permission from the Royal Society of Chemistry.*

QCR and QCR II (Figures 5.10(a) and (b)) show left-skewed distributions with mean I_D/I_G values of 0.84 and 1.03 before water submersion. These are far less disordered than the EoL anodes which show broad distributions (therefore large heterogeneity) with mean values of 2.08, 2.41 and 2.77 for EoL, EoL II and EoL III respectively (Figures 5.10(c) to (e)).

After submersion, all distributions skewed to lower I_D/I_G ratios with EoL, EoL II and EoL III showing significant reduction in distribution widths. Mean values of 1.10, 0.66, 0.49, 0.53 and 1.48 were obtained for QCR, QCR II, EoL, EoL II and EoL III respectively. As Raman is a surface/subsurface technique, the increase in graphitic nature may arise from the loss of SEI/oxidised SEI products and organic contaminates from the surface. After this submersion, the graphite from EoL anodes are almost indistinguishable from those obtained from the QCR anodes when looking at I_D/I_G ratios, suggesting that the graphite itself is relatively unaffected by progressive battery cycling. Providing more evidence to suggest that ageing within pouch cells during normal use is not caused by graphite degradation but more so via SEI production, causing both lithium loss and increased resistance. With a recycling perspective, this suggests that graphite obtained from deteriorated, used cells, may be structurally similar to virgin material, meaning these cells can act as a promising source of graphite. This also highlights the effectivness of water delamination in cleaning the graphite.

EoL III has the highest I_D/I_G ratio after water submersion (1.48), either suggesting more SEI formation or deteraration of the graphite surface. This would likely be caused by the battery hitting the failure knee point near the end of its cycle life, indicated by a rapid drop in capacity per cycle. A higher mean I_D/I_G ratio was also observed for QCR.

5.8.2 XPS and HAXPES

XPS analysis was conducted on QCR, EoL and EoL III after water submersion following 1 h and 2 weeks of air-exposure. Both the EoL and EoL III anode films delaminated from the

current collector whereas only the QCR 1h sample had delaminated, leaving the 2 week QCR anode film attached to the copper current collector. The $C\ 1s$ spectra of each compared to before submersion (shown in grey) are given in Figure 5.11.

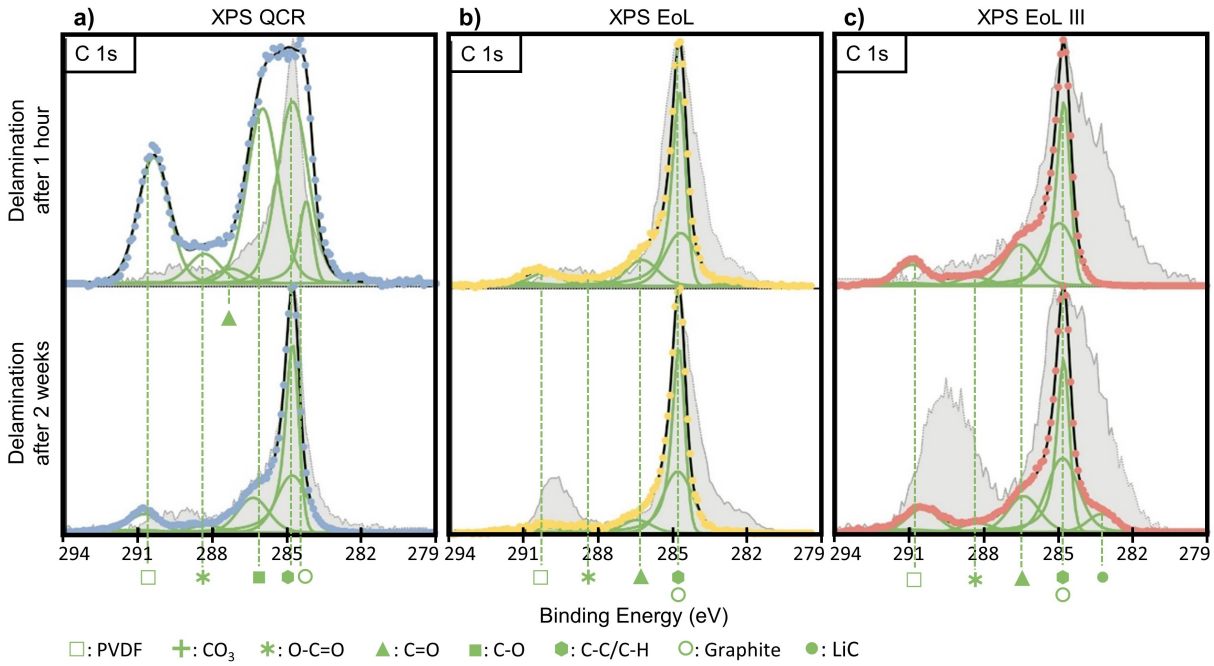


Fig. 5.11. *Normalised photoelectron spectra (XPS). $C\ 1s$ XPS spectra of (a) QCR, (b) EoL, and (c) EoL III after water submersion following* 1 h *(at the top) and 2 weeks (at the bottom) of air-exposure. Spectra obtained before water submersion are shown via the grey area. Peaks were resolved using casaXPS.*[130] *Seven constrained Voigt peaks and a peak fit model for graphite obtained from Biesinger*[195] *was used to create an envelope. The peaks are shown in green, with their corresponding environment highlighted with a symbol and a legend at the bottom. The overall envelope is given in black.*

Excluding QCR 1 h a drastic difference between before and after delamination can be seen. There is a large reduction in all carbon environments previously used in Section 4.5.3 and Section 4.6.2; where the profile is better fitted with a large asymmetric peak paired with a small broad peak at around 291.2 eV to represent both conductive graphite and the associated $\pi \longrightarrow \pi*$ shake-up satellite. A peak model obtained from *Biesinger*[195] was used which contained an asymmetric Voigt peak developed by Ulrik Gelius to increase low-kinetic energy electron contributions as well as a small, broad and linked Voight peak representing

the $\pi \rightarrow \pi^*$ shake-up satellite.[196] This asymmetry occurs due to the conductive band of graphite allowing shake-up processes to occur at a continuum of energies, with the higher energies of the unfilled band less likely to fill with an excited electron and therefore leading to a gradual decay in polarizable probability and therefore a decay in the peaks' tail.[197] A 'shake-up' describes an event where the outgoing photoelectron excites a valence electron from its corresponding ion to a higher energy state. This reduces the kinetic energy of the photoelectron and thereby artificially increases the apparent binding energy deduced from that electron, resulting in a tail towards higher binding energies. The $\pi \rightarrow \pi^*$ shake-up satellite appears due to a shake-up event that excites an electron within the loosely bound, highest occupied π orbital to the lowest unoccupied π^* orbital.[198]

Another carbon environment at ~ 290.9 eV is used for Figure 5.11 that has not been used in previous studies. This relates to a $\mathbf{C}F_2{-}CH_2$ environment found within PVDF.[199] Both the domination of the spectra by the asymmetric graphite peak and the appearance of a peak relating to PVDF shows the removal of most the organic surface contamination via water submersion, confirming the findings from the previous Raman analysis.

The spectrum obtained for QCR 1 h contrasts with the other spectra in Figure 5.11. This may result from differential charge build-up on the sample as evident from the increased noise in the survey scan (as shown in Figure 5.19 in the appendix). This may have occurred due to an unfortunate sample set-up that did not allow the charge compensation system to establish a uniform potential across the sample.[198] To remedy this another scan would need to be taken. The peak at 283.2 eV is still present for the EoL III 2 week delaminated sample which has previously been ascribed to lithiated graphite. As both are reactive to water, it is unknown why this environment is still present on the surface, it could perhaps indicate the presence of an alternative carbide.

$C\ 1s$ spectra gained from HAXPES analysis on EoL after 1 h and 2 weeks of air-exposure preceding water delamination are shown in Figure 5.12. Again, the spectra are

dominated by the asymmetric graphite peaks and the emergence of the PVDF peak. This suggests that the majority of the sub-surface is now graphite.

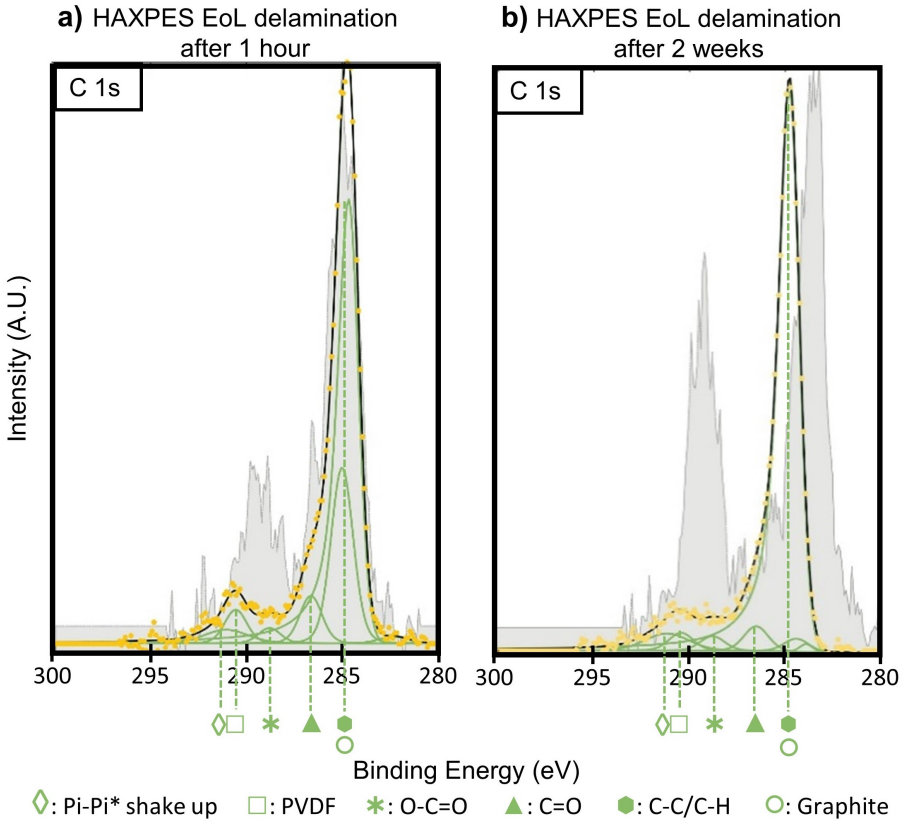


Fig. 5.12. *Normalised photoelectron spectra (HAXPES). $C\ 1s$ HAXPES spectra of EoL after water submersion following (a) 1 h and (b) 2 weeks of air-exposure. Spectra obtained before water submersion are shown via the grey area. Peaks were resolved using casaXPS.*[130] *Seven constrained Voigt peaks and a peak fit model for graphite obtained from Biesinger*[195] *was used to create an envelope. The peaks are shown in green, with their corresponding environment highlighted with a symbol and a legend at the bottom. The overall envelope is given in black.*

Except for QCR 1 h (due to a surface charge differential), the $F\ 1s$ spectra can be fitted with a single peak centering ~ 687.6 eV. Within previous studies this peak had been assigned to $\mathrm{Li}_x\mathrm{PF}_y/\mathrm{LiPF}_x(\mathrm{OR})_y$. However, due to the presence of the **C**$\mathrm{F}_2-\mathrm{CH}_2$ environment in the $C\ 1s$ spectra and the observed cleaning of the anode material of SEI contamination,

this peak was assigned to the more likely $\mathrm{C}\mathbf{F}_2{-}\mathrm{CH}_2$ environment which would also appear at this binding energy.[199]

Tables 5.2 and 5.3 complement the data shown in Figures 5.11 and 5.12, showing a domination of the environments via the graphitic peak. Peaks relating to the $C\ 1s$ $\mathbf{C}\mathrm{F}_2{-}\mathrm{CH}_2$ environments and the F 1s $\mathrm{C}\mathbf{F}_2{-}\mathrm{CH}_2$ environments make up around $7\,\%$-$2\,\%$. This percentage is close to the amount of PVDF found to be in these anodes, $\sim 4\,\%$, via TGA analysis within Section 6.5 later in this work. As this is a single spot surface scan, and some impurities are expected to be present, a large variance in these values was expected. Other carbon environments like the $\mathrm{C}{-}\mathrm{C}/\mathrm{C}{-}\mathrm{H}$ and the $\mathrm{C}{-}\mathrm{O}$ environment still contribute to the overall percentage; where some trace amounts of SEI would be expected. However, these may also arise from the pitch coating and $\mathbf{C}\mathrm{H}_2{-}\mathrm{CF}_2$ environment of the PVDF. Table 5.3 shows a graphite contribution of around $80.5\,\%$ and a $\mathrm{C}\mathbf{F}_2{-}\mathrm{CH}_2$ contribution of around $3.4\,\%$ for EoL when 1 h and 2 week values are averaged. Evidently, showing a depth penetration to within the anode film.

Elemental composition within Table 5.4 consists primarily of carbon, oxygen is the next highest concentration, followed by fluorine. Metal contamination is still present, with manganese appearing on all samples except EoL III 2 weeks. These manganese concentrations are higher than those reported within the previous studies (Section 4.5.3 and Section 4.6.2). This not only shows that the manganese is not washed off via water delamination, but that the manganese is attached to the graphite surface, depositing below or within the SEI via the deposition mechanism. The HAXPES elemental composition for EoL, shown in Table 5.5, shows even greater manganese concentrations. Indicating either that manganese has intercalated into the graphite or that it has deposited within grain boundaries of graphite particles, both suggesting that manganese deposition does not just happen on the surface of the SEI layer but will penetrates through and affects the surface of the graphite. Nickel is also found on QCR and EoL III, shown in Table 5.4, showing higher concentrations than

previously found. Evidently another metal contamination attached to the surface of the anode material that cannot be removed via the delamination process. The same is seen for copper which contaminates QCR.

There are no obvious trends in surface morphology between samples delaminated after 1 h of air-exposure to those after 2 weeks. Evidently the efficiency of the delamination does not majorly affect how much SEI/oxidised SEI is removed. This suggests that these contaminates can be easily washed off, requiring only agitation within a solution rather than requiring the delamination process. Metal contamination, however, is not removed via the delamination process. Perhaps this may lead to further work in establishing a rejuvenation technique that would remove these contaminates. For instance, manganese could be removed by soaking the anode in ascorbic acid ($HC_6H_7O_6$).[200]

Table 5.2. *Percentage composition of assigned chemical environments for the C 1s (shown in Figure 5.11) and F 1s spectra obtained after the XPS analysis of QCR, EoL and EoL III after water submersion following 1 h and 2 weeks of air-exposure. Standard deviations were calculated using a Monte Carlo procedure to simulate the variance from multiple fittings. Both value and standard deviation were calculated in casaXPS.[130] Peak positions and FWHM are given in within the experimental section (Section 5.4.6).*

Sample and scan	**Air exposure**	**Carbon 1s (% Composition)**							**Fluorine 1s (% Composition)**	
		Carbide	Graphite	C−C/C−H	C−O	C=O	O−C=O	CF_2−CH_2	CF_2−CH_2	LiF
QCR XPS	1 hour	-	14.4(15)	22.40(81)	21.6(27)	1.94(62)	3.71(12)	15.58(43)	17.83(14)	1.46(10)
	2 weeks	-	58.7(40)	15.7(13)	7.96(83)	2.26(19)	1.40(10)	4.43(19)	5.39(10)	-
EoL XPS	1 hour	-	65(15)	12.5(32)	5.9(31)	1.81(76)	1.22(20)	3.1(10)	4.76(15)	-
	2 weeks	-	66(12)	15.7(32)	3.6(18)	2.30(85)	1.51(59)	1.64(58)	3.06(21)	-
EoL III XPS	1 hour	-	56.4(28)	15.55(87)	8.48(65)	3.44(24)	1.66(10)	4.83(23)	5.70(10)	-
	2 weeks	3.51(41)	54.9(40)	14.0(15)	7.90(95)	2.42(36)	1.44(10)	5.09(22)	6.95(10)	-

Table 5.3. *Percentage composition of assigned chemical environments for the $C\ 1s$ (shown in Figure 5.12) and $F\ 1s$ spectra obtained after the HAXPES analysis of EoL after water submersion following* 1 h *and 2 weeks of air-exposure. Standard deviations were calculated using a Monte Carlo procedure to simulate the variance from multiple fittings. Both value and standard deviation were calculated in casaXPS.*[130]

Sample and scan	**Air exposure**	**Carbon 1s (% Composition)**							**Fluorine 1s (% Composition)**	
		Carbide	Graphite	C−C/C−H	C−O	C=O	O−C=O	CF_2−CH_2	CF_2−CH_2	LiF
EoL HAXPES	1 hour	0.46(14)	74.9(15)	9.81(81)	-	1.51(62)	0.90(12)	1.82(43)	3.87(10)	-
	2 weeks	-	86(15)	-	-	-	0.88(20)	-	2.88(15)	-

Table 5.4. *Surface elemental composition obtained from the XPS analysis of QCR, EoL and EoL III after water submersion following* 1 h *and 2 weeks of air-exposure. Standard deviations were calculated using a Monte Carlo procedure to simulate the variance from multiple fittings. Both value and standard deviation were calculated in casaXPS.*[130]

Sample and scan	Air exposure	Lithium (at.%)	Carbon (at.%)	Oxygen (at.%)	Fluorine (at.%)	Phosphorus (at.%)	Sulfur (at.%)	Manganese (at.%)	Nickel (at.%)	Copper (at.%)
QCR XPS	1 hour	0.46(26)	23.4(12)	21.2(12)	6.42(34)	0.45(24)	1.80(41)	11.8(14)	6.3(17)	27.9(31)
	2 weeks	-	69.4(25)	9.6(15)	7.00(27)	-	1.04(29)	2.5(17)	7.2(17)	3.3(16)
EoL XPS	1 hour	-	64.9(72)	14.9(54)	6.08(90)	-	-	4.6(41)	-	-
	2 weeks	1.43(48)	64.2(75)	17.7(46)	3.92(75)	-	-	12.0(55)	-	-
EoL III XPS	1 hour	-	61.8(22)	17.2(13)	6.28(26)	-	-	6.6(16)	7.2(19)	-
	2 weeks	-	79.9(57)	4.53(65)	9.87(73)	-	-	-	0.22(10)	-

Table 5.5. *Elemental composition were obtained from the HAXPES analysis of EoL after water submersion following* 1 h *and 2 weeks of air-exposure. Standard deviations were calculated using a Monte Carlo procedure to simulate the variance from multiple fittings. Both value and standard deviation were calculated in casaXPS.*[130]

Sample and scan	Air exposure	Lithium (at.%)	Carbon (at.%)	Oxygen (at.%)	Fluorine (at.%)	Phosphorus (at.%)	Sulfur (at.%)	Manganese (at.%)	Nickel (at.%)	Copper (at.%)
EoL HAXPES	1 hour	-	57(10)	14.7(77)	5.2(12)	-	-	15.7(45)	-	-
	2 weeks	1.73(46)	37.9(73)	12.9(45)	2.87(76)	1.12(59)	2.48(75)	36.9(54)	-	-

5.8.3 SEM analysis

Figure 5.13 shows SEM images of QCR II, EoL II and EoL III before and after delamination. Images of other delaminated anodes are given in the appendix (Figure 5.20). The surface coating formed of oxidised SEI can be clearly seen in Figures 5.13(d), (g) and (j). After delamination, these agglomerations appear to be completely removed. Much like the XPS and Raman analysis, this suggests that the delamination or even just the submersion in water leads to removal of surface contamination caused by the SEI. This is beneficial for electrochemical reuse of the graphite, as if left, would create a larger, more reactive, inhomogeneous surface for more SEI growth during the first cycle. This leftover SEI may also add to the resistivity of the graphite.

When efficient delamination occurs, *i.e.* after a brief exposure to air, the anode material can be removed as a film. This film has two sides; the side that faced the separator and cathode during use and the side that faced the current collector. The former are given in Figures 5.13(b), (e), (h) and (k) and the later in Figures 5.13(c), (f), (i) and (l). The current collector facing side showed pooling of an organic substance between the graphite particles; EDX analysis (Figure 5.21 within the appendix) showed that these regions were high in fluorine content, suggesting that this results from the PVDF binder. Concentrating PVDF closer to the current collector by using low drying temperatures is typically used to provide better adhesion between the anode film and the current collector.[201,202] Evidently, this concentration gradient is retained during the delamination process.

Delamination of QCR II, EoL II and EoL III after 2 weeks of air-exposure provide graphite particles with no obvious signs of degradation/exfoliation. SEM images taken after the delamination of EoL III within 1 h of air-exposure shows a small percentage of the recovered graphite that have lost their sphericalised shape. This may have been caused by

the localised condition of H_2 production when submerged in water. However, this was only observed for EoL III with 1 h of air-exposure.

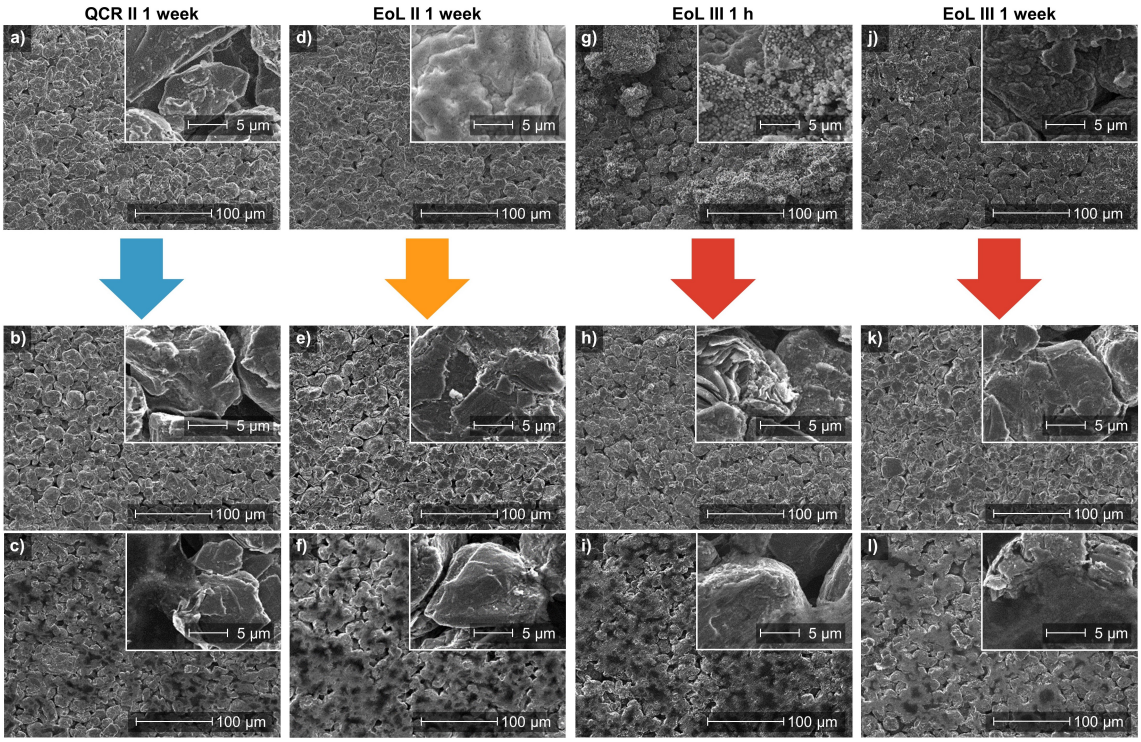


Fig. 5.13. *Large SEM images at 250x magnification with a 5000x magnified SEM image in the top right of each. (a) QCR II after 1 week of air-exposure. (b) Water-delaminated QCR II after 2 weeks of air-exposure, showing the face that originally faced the separator and electrolyte. (c) Water-delaminated QCR II after 2 weeks of air-exposure, showing the face that was attached to the current collector. (d-f) Similar to (a-c) however for EoL II after 1 week of air-exposure for the top image and delamination after 2 weeks for the bottom two. (g-j) Showing EoL III after* 1 h *of air-exposure and delamination after the same time period. (j-l) EoL III after 1 week of air-exposure and delamination after 2 weeks. Reproduced from Sargent et al.*[121] *with permission from the Royal Society of Chemistry.*

5.8.4 PSA analysis

PSA was used to determine whether graphite from EoL anodes had degraded when compared to QCR anodes. This would be apparent from either an increase in size, indicating despherication, or a decrease in size, indicating particle cracking.

Water delamination allowed for the removal of the graphite from the current collector, however, as evident from the SEM study, the graphite particles are still bound together with PVDF. This PVDF was removed by heating the obtained anode material to $500\,^{\circ}\mathrm{C}$ in air for $1\,\mathrm{h}$, leaving a fine powder. This powder was then suspended in water and run through the PSA.

Figure 5.14 shows the particle size distribution of EoL after delamination after $1\,\mathrm{h}$ of air-exposure. Distributions collected for other anodes are given in Figure 5.22 within the appendix. Mn represents the mean based on the number of particles whereas Mv represents the mean weighted by volume. Both values are useful, however, more emphasis has been applied to Mv as the larger particles occupy more of the powder and will therefore have a larger affect on coatings made.

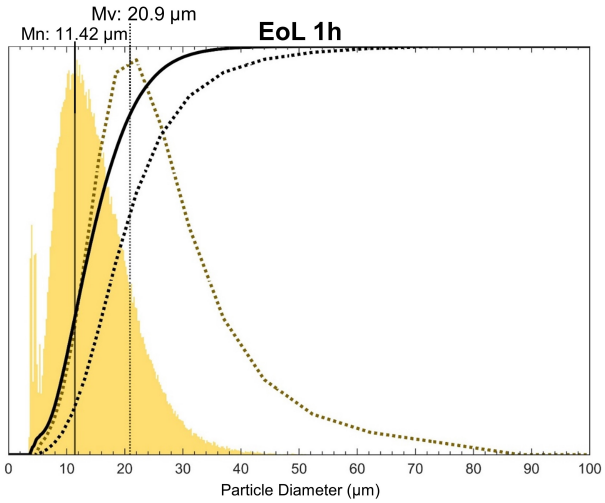


Fig. 5.14. *Particle distributions gathered for EoL after* $1\,\mathrm{h}$ *of air-exposure followed by delamination. After delamination heating to* $500\,^{\circ}\mathrm{C}$ *for* $1\,\mathrm{h}$ *in air was required. The filled distribution represents the number of particles, and the dotted line represents the volume weighted distribution. The mean (Mn) and weighted mean (Mv) are given above the figure.*

Figure 5.14 shows left-skewed Leptokurtic peaks for both the number distribution and volume distribution. A small peak at lower particle diameters can also be seen in the number distribution, which is reduced to a small shoulder for the volume distribution. Presumably, this

results from the presence of CB. This identical peak shape was collected for every anode after both delamination following 1 h and 2 weeks of air-exposure.

The Mn, Mv, and the tenth and ninetieth percentiles for each anodes recovered graphite particle distributions are given in Table 5.6. The variation in both Mn and Mv between anodes is ± 0.32 µm. This distribution is exceptionally small, suggesting that delamination does not lead to particle fragmentation, nor does it cause desphericalisation or particle cracking during prolonged cycling. Highlighting that EoL material can function as a valuable source for battery-grade graphite.

Table 5.6. *Mean (Mn), weighted mean by volume (Mv) as well as the tenth (D10), ninetieth (D90), weighted tenth (Dv10) and weighted ninetieth (Dv90) percentiles for particle distribution data collected on delaminated anodes. Anodes were delaminated after* 1 h *and 2 weeks of air-exposure. After delamination heating to* 500 °C *for* 1 h *in air was required.*

Sample	Mn (µm)	Dn10 (µm)	Dn90 (µm)	Mv (µm)	Dv10 (µm)	Dv90 (µm)
QCR 1h	**11.8**	7.631	22.9627	**20.48**	11.34	31.11
QCR 2w	**11.63**	7.559	22.591	**20.38**	11.23	31.07
QCR II 1h	**11.53**	7.371	21.726	**19.83**	11.01	30.1
QCR II 2w	**11.75**	7.546	22.8216	**20.57**	11.3	31.61
EoL 1h	**11.42**	7.524	23.618	**20.9**	10.93	32.87
EoL 2w	**11.29**	7.197	22.5929	**20.81**	10.77	32.26
EoL II 1h	**11.71**	7.552	22.9747	**20.58**	11.26	31.5
EoL II 2w	**11.6**	7.5	23.025	**20.61**	11.21	31.69
EoL III 1h	**10.73**	7.434	21.603	**20.72**	10.96	31.06
EoL III 2w	**11.71**	7.692	23.453	**20.84**	11.43	31.78

5.9 | Chapter conclusions

Water delamination is an effective way to separate the anode material (containing graphite, CB and PVDF) from the copper current collector. Its effectiveness is determined by the OCV of the cell before dismantlement and the period of time the anode has been exposed to air. This relation occurs as the key component is trace amounts of lithiated graphite, this reacts with the water to produce hydrogen. Much like ultrasonication within an aqueous environment, the production of hydrogen creates local regions of changing pressure and

temperature, mechanically cleaving the anode material from the current collector. The longer the anode is exposed to air, the less lithiated graphite is available due to oxidation within ambient conditions.

It was found that not only could the anode material be separated from the current collector but the lithium within the anode could be extracted from the delamination water. As a proof of concept both Na_2CO_3 and phosphoric acid was used on condensed delamination water to extract $0.6\,\%$ of the weight of the anode in lithium. It is believed that this is the first recording of lithium extraction from the anode. As $8.8\,\%$ of the lithium remained in the solution and the process required two steps, future work in optimising the process is required.

The current collector obtained after delamination initially appeared unaltered. However, after drying the surface appeared heavily oxidised, creating foil with mosaic patterns of red, blue, purple, and orange hues. It was concluded that the delamination process removed an anti-oxidative layer from the coppers surface, causing the copper to oxidise whilst drying. The more effective the delamination, the more oxidation occurred.

The recovered anode material was analysed with Raman, XPS, HAXPES, SEM and PSA analysis. All techniques showed comparable results. Surface contamination created by the SEI could easily be washed off via water submersion. The organic contaminates were removed even when delamination did not occur, suggesting that this contamination was loosely bound and could be removed with agitation within a solution. Metal contamination from manganese, nickel and copper could not be removed, even with efficient delamination. This suggests that the metals are bound to the graphite surface instead of on the surface of the SEI/within the SEI. SEM and PSA analysis showed that the graphite particles are unaffected by both the delamination process and ageing within the cell. Suggesting that graphite from recycled cells may perform well within a second life electrochemical application.

5.10 | Chapter appendix

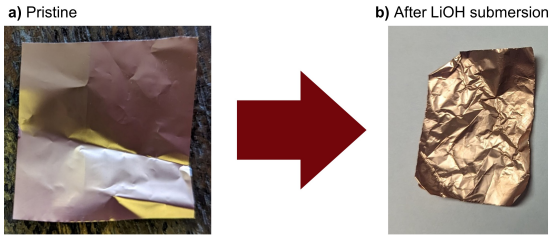


Fig. 5.15. *Pristine copper foil (a) before and (b) after submersion in a heated, agitated solution of* LiOH*.*

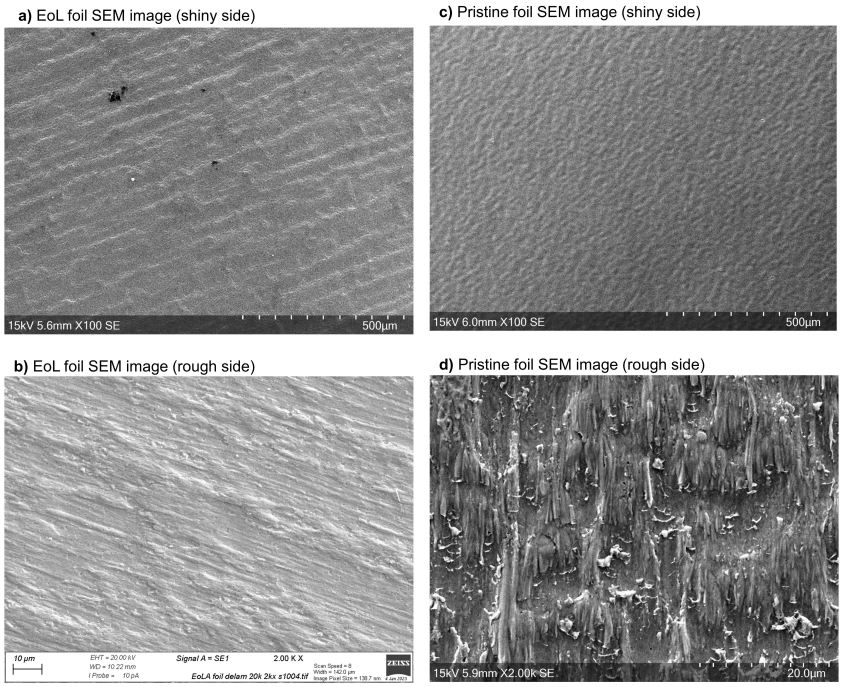


Fig. 5.16. *SEM images taken of delaminated EoL and pristine copper foil using both a HITACHI TH4000plus and a Philips XL30 FEG scanning electron microscope. (a) Shows the shiny side of EoL foil. (b) Shows the rough side of EoL foil. (c) Shows the shiny side of pristine foil. (d) Shows the rough side of pristine foil.*

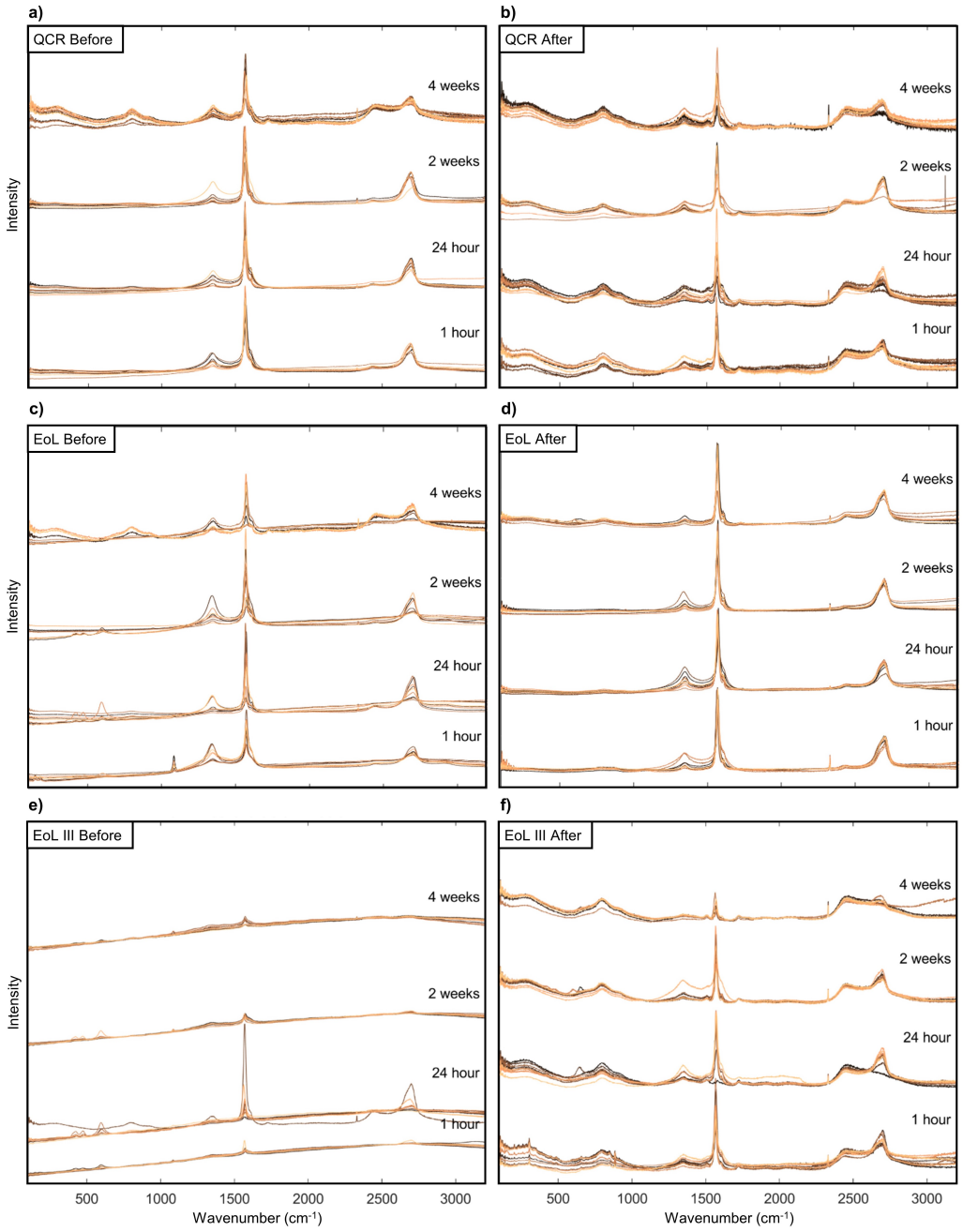


Fig. 5.17. *40 randomly dispersed Raman point scans were taken on (a) QCR, (c) EoL and (e) EoL III before water submersion and (b) QCR, (d) EoL and (f) EoL III after water submersion. For the pre-submerged samples, 10 scans were taken at each of the following time intervals of air-exposure:* 1 h, 24 h, *2 weeks and 4 weeks. Water submersion was also conducted at these time intervals, where once dried, 10 Raman scans were taken of each sample to give the post-submersion figures. Scans taken at the same time interval for each sample are overlapped.*

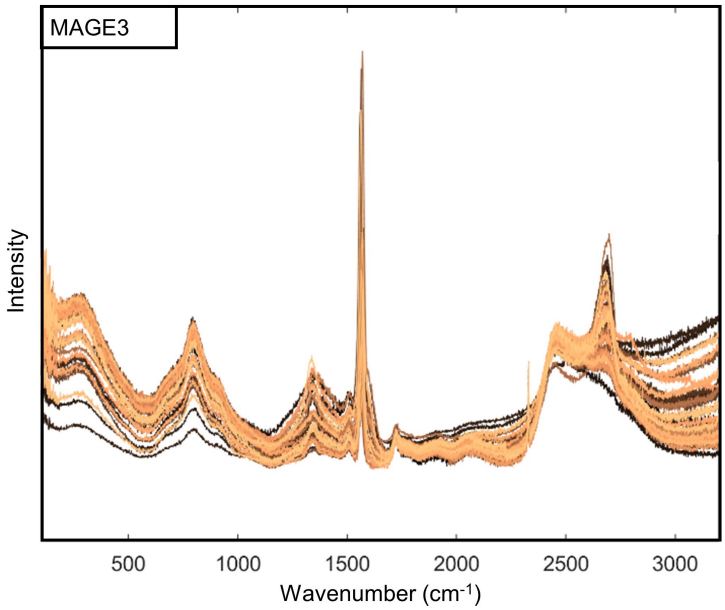


Fig. 5.18. *40 randomly dispersed Raman scans taken of a sample of MAGE3 powder.*

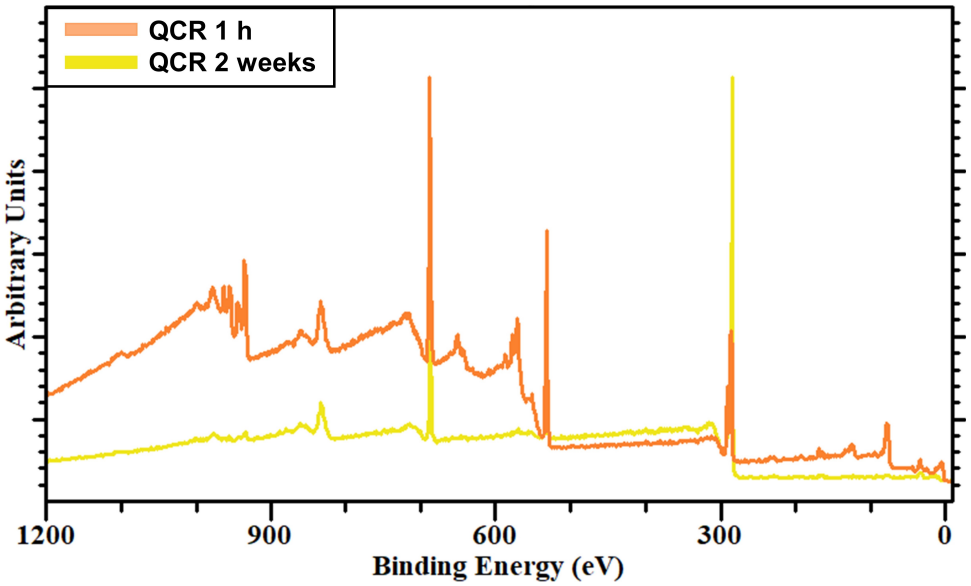


Fig. 5.19. *The XPS survey scan of QCR delaminated after* 1 h *of air-exposure (in orange) compared to that of QCR after water submersion after 2 weeks of air-exposure (in yellow).*

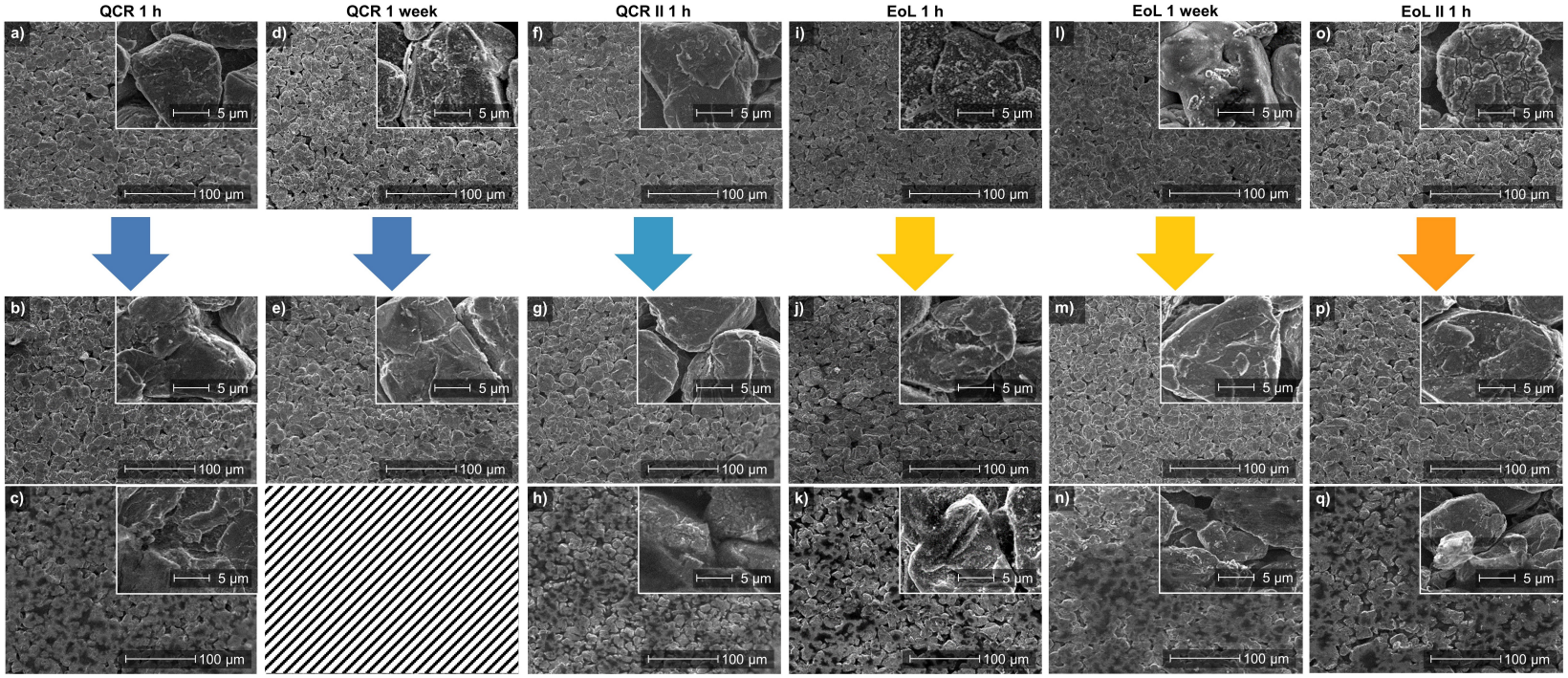


Fig. 5.20. *Large SEM images at 250x magnification with a 5000x magnified SEM image in the top right of each. a) QCR after* 1 h *of air-exposure. b) Water delaminated QCR after* 1 h *of air-exposure, showing the face that originally faced the separator and electrolyte. c) Water delaminated QCR after* 1 h *of air-exposure, showing the face that was attached to the current collector. d-e) Similar to (a-c) however for QCR after 1 week of air-exposure for the top image and delamination after 2 weeks for the bottom. An image of the face that was attached to the current collector was not acquired due to difficulties in delamination. f-h) Shows QCR II after* 1 h *of air-exposure and delamination after the same time period. i-k) Shows EoL after* 1 h *of air-exposure and delamination after the same time period. l-n) EoL after 1 week of air-exposure and delamination after 2 weeks. o-q) Shows EoL II after* 1 h *of air-exposure and delamination after the same time period.*

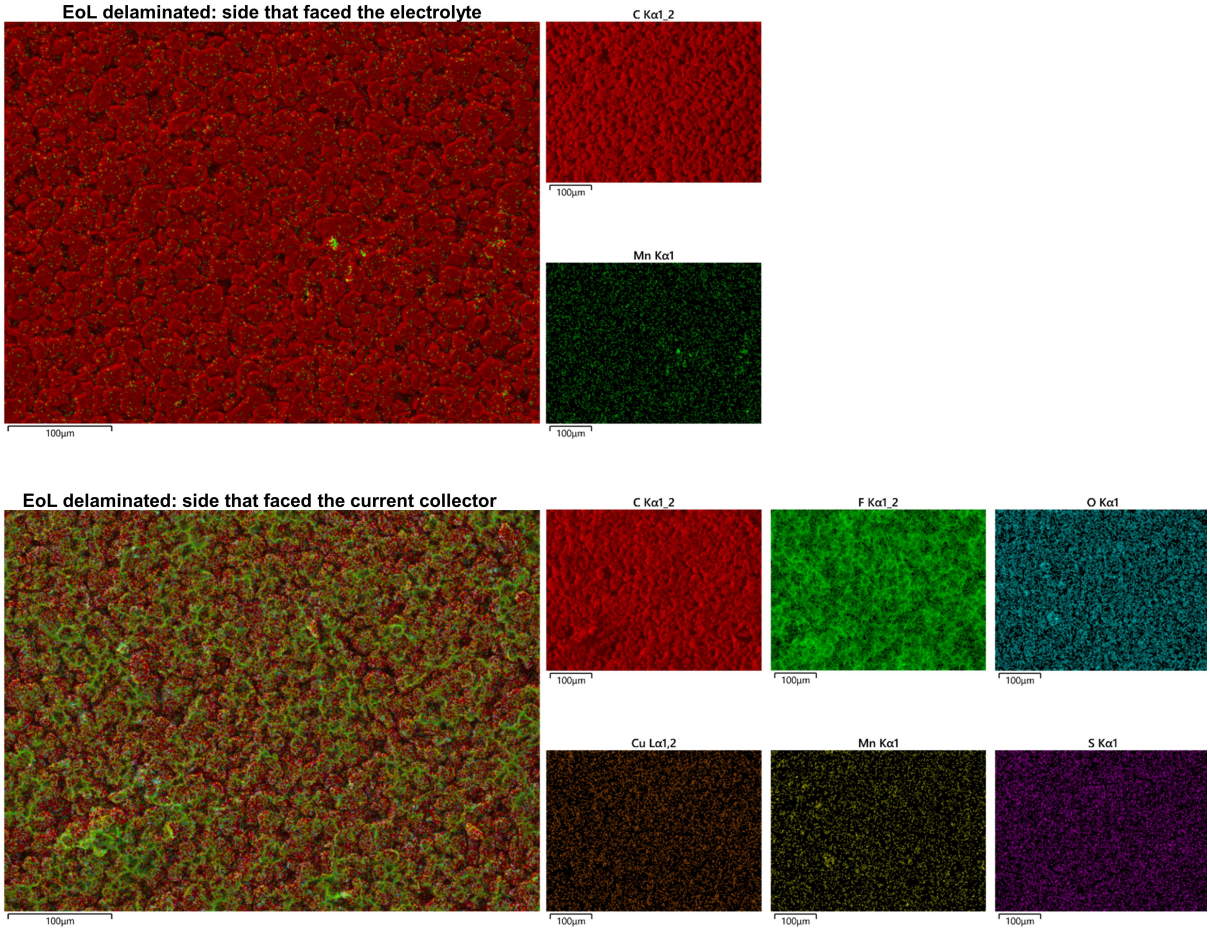


Fig. 5.21. *Elemental mappings were taken using a HITACHI TH4000plus SEM with an energy dispersive X-ray spectroscopy (EDX) detector from AztecOne. The 15 kV backscattered electron mode was used. Shown above are the two sides of anode film from* 1 h *air-exposed EoL after delamination. The top displays the side that faced the electrolyte and separator, where only carbon and manganese concentrations were enough to be picked up via elemental mapping. The images below show PVDF binder keeping the graphite together on the side that faced the current collector before the delamination.*

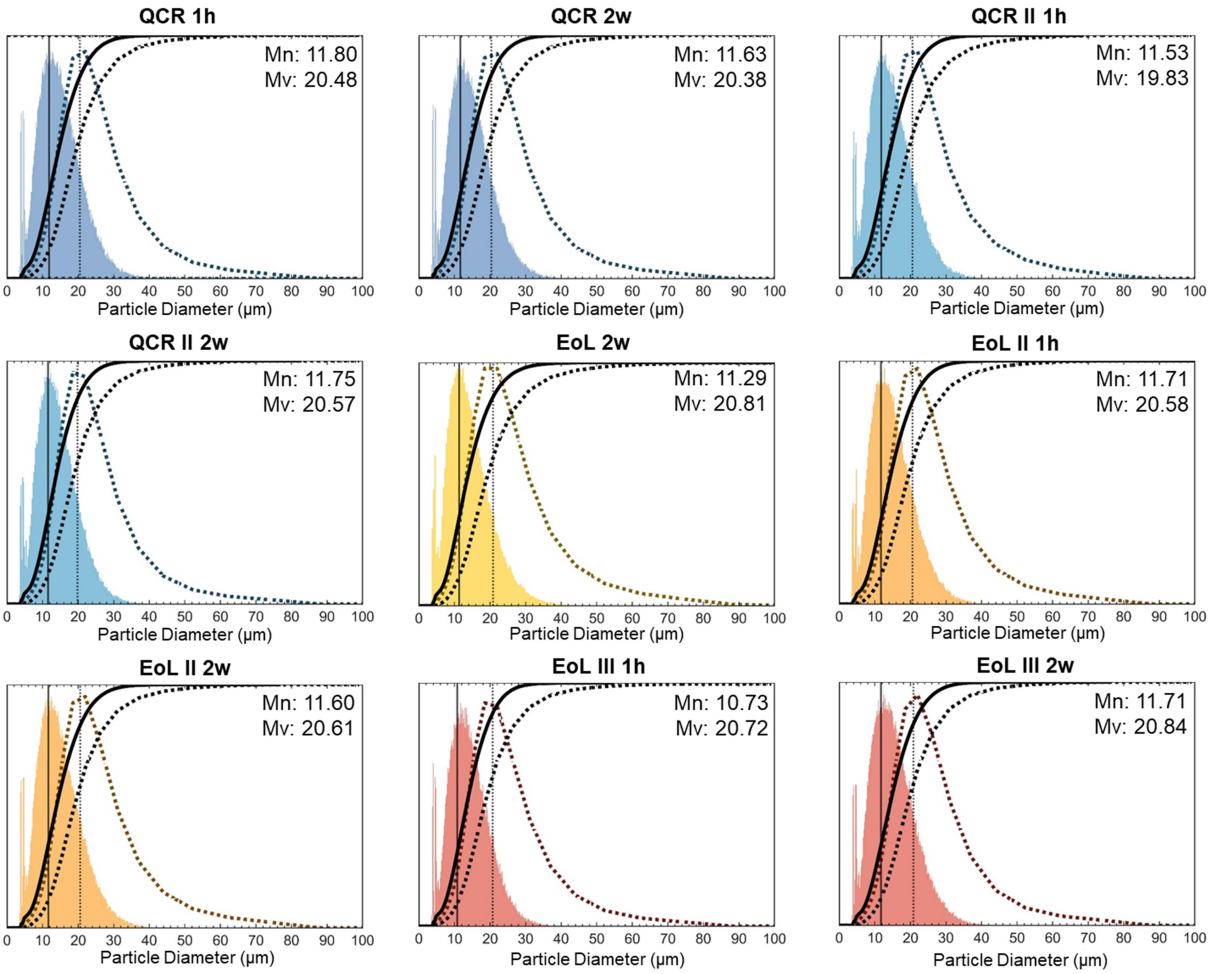


Fig. 5.22. *Particle distributions gathered for QCR, QCR II, EoL II and EoL III after* $1\,\mathrm{h}$ *of air-exposure and QCR, QCR II, EoL II and EoL III after 2 weeks of air-exposure followed by delamination. After delamination heating to* $500\,^{\circ}\mathrm{C}$ *for* $1\,\mathrm{h}$ *in air was required. The filled distribution represents the number of particles, and the dotted line represents the volume weighted distribution. The mean (Mn) and weighted mean (Mv) are given above each figure.*

CHAPTER 6

Reuse of recovered graphite

6.1 | Disclaimer

Work within this chapter has been published in *Sargent et al.*[121].

6.2 | Introduction

The relatively low cost (~8 US$ kg^{-1} for NG and ~13 US$ kg^{-1} for SG in 2020), abundancy and established market, makes graphite an ideal option for mass-produced anode materials.[24] However, a more intrinsic look shows the high environmental impact, high production costs and market instability for graphite. Increasing demand for graphite and China's dominance of the market could lead to political issues in the future.[77] Calcination of coke for SG and the sphericalisation and coating of NG are taxing processes on production costs and the environment.[24] Sphericalisation requires energy intensive jet-milling and extends the production time to produce battery-grade graphite.[35] Calcination produces 13 kg of CO_2 per ton of SG. Sphericalisation and coating produces 57 kg of CO_2 per ton of NG.[203]

Industrial recycling techniques using pyrometallurgical/hydrometallurgical methods either discard the graphite or fail to reclaim the graphite in a reusable way.[24,34] Furthermore, due to theories of electrochemical ageing mechanisms causing changes in the microstructure, crystallinity, and morphology of the used graphite, academic research into the recycling and

reuse of graphite is sparse.[34,50,51] Research has even been conducted to convert this used graphite into graphene as an alternative to reuse in a LiB.[81] As shown in previous chapters, the graphite within QCR and EoL cells that would enter a recycling stream contains graphite with little, to no microstructural, crystalline, and morphological changes. The only ageing experienced on the anode appears to be growth of SEI, metal contamination and mechanical wear, where the former can be easily removed with submersion in water and the latter via reconstructing the anode.

The share of demand for graphite supply from the battery industry is predicted to rise from $\sim 19\,\%$ in 2021 to around $79\,\%$ globally in 2030.[204,205] This has already resulted in a $49\,\%$ increase in 2022, making the LiB anode demand overtake traditional industrial demand like refractory and foundry industries for (natural) graphite supply.[206] This ever increasing market is adding extra demand pressure on an already supply constrained product. Therefore, the need to recycle graphite in a usable way, ideally to satisfy the battery industry, is growing at the same rate as the battery industry.

Water delamination provides a unique and easy method to obtain cleaned, battery-grade graphite. Within this chapter, the recovered graphite will be inserted into new cells in order to determine the efficacy of creating a LiB graphite closed loop economy.

6.3 | Chapter aims

Within this chapter, the graphite recovered from the dismantled cells will be electrochemically tested to determine whether water delamination provides a successful route to establishing a circular economy.

An optimal route for converting graphite, recovered via water delamination, to a well performing reused anode will be investigated by studying. Here, the cell performance of each recovered graphite material will be examined and compared to its material characteristics.

Once established, the viability of each graphite as a reused anode will be assessed. Once established, the viability of each graphite as a reused anode will be examined.

As QCR showed difficulty in delamination, only QCR II, EoL, EoL II and EoL III will be investigated.

6.4 | Experimental

6.4.1 TGA study

A SII EXSTAR 6000 was used to conduct thermogravimetric analysis on Solef® PVDF (Solvay), EoL active material delaminated after 1 h of air-exposure and the same active material after annealing to $500\,^{\circ}$C for 1 h.

Around 20 mg-10 mg of sample was added to a platinum sample pan and zeroed against another platinum pan used as a reference. Samples were then heated to $900\,^{\circ}$C under nitrogen, using a ramp rate of $10\,^{\circ}$C min^{-1}. Time, temperature, mass, and rate of mass loss was collected via TGA.

Temperature, mass and rate of mass loss were transferred and plotted in MATLAB.[125] The width of the PVDF peak in the rate of mass loss was found and the mass loss within this region was assumed to correspond to $86\,\%$ of the PVDF mass, as this was how much was lost in this region for pure Solef® PVDF. The loss within this region was then calculated for the other samples and assumed to also correspond to $86\,\%$ of the PVDF within the sample.

6.4.2 Graphite treatment

Two processes of graphite treatment were used, annealing and hydro-thermal treatment. Annealing involved heating the material in a furnace (within a fume cupboard) in air to $500\,^{\circ}$C for 1 h at a ramp rate of $10\,^{\circ}$C min^{-1}. This technique was used on all 1 h and 2 week recovered

active material except QCR. Hydro-thermal treatment was conducted using 0.8 g of EoL 1 h. This sample was added to 10 mL of 1 M NaOH (≥ 97.0 %, dissolved pellets, Sigma Aldrich) within a sealed polytetrafluoroethylene (PTFE) container in a metallic vessel. This container was added into a furnace and heated to 160 °C (using a ramp rate of 10 °C min^{-1}) for 12 h. Samples were removed and washed with DI water over a vacuum filter. NaOH solution was evaporated in a fume cupboard using a temperature of 80 °C.

6.4.3 Electrochemical data collection

Two types of anodes were made: recast anodes using the PVDF already in the sample and CMC/SBR bound anodes, where the PVDF had been removed by thermal/hydrothermal treatment. For both coatings, a Thinky ARE-250 CE was used to create a homogeneous slurry.

A recast anode was made for EoL 1 h. The PVDF content within this active material was calculated using TGA as mentioned above (Section 6.4.1). Around 0.5 g of EoL 1 h was dissolved in around 0.7 g of NMP (anhydrous, 99.5 %, Sigma Aldrich) in two steps. Within a 12 mL pot , 6 zirconia balls, EoL 1 h and half the NMP was added. This was mixed at a rate of 2000 rpm for 10 min. Next, the remaining half of NMP was added before mixing at a rate of 2000 rpm for 10 min followed by a 3 min degassing step at 2200 rpm. The formed slurry was coated onto copper foil (MTI corporation, 9 µm) using a doctor blade, and calendered once dried.

For the CMC/SBR bound anodes, slurries using the recovered graphite, powdered sodium cellulose (Na CMC) (Sigma-Aldrich, 250,000 Mw, 0.7 degree of substitution), Super P® conductive carbon black (CB) (Sigma-Aldrich, ≥ 99 %) and styrene-butadiene rubber (SBR) (Sigma-Aldrich, 50 wt.%). The slurry was made with a 30 wt.%-20 wt.% with water and a weight ratio of 90:2:5:3 of graphite: CB: Na CMC: SBR respectively. This was again coated

onto copper foil and calendared once dried. MAGE3 graphite (Hitachi Chemical, Sakuragawa, Japan) was used to create a standard CMC/SBR bound anode as a comparison.

CR2032 coin cells were made by first punching a 12 mm disk of electrode and transferring this into an inert atmosphere. Glass microfiber (Whatman, 1.2 µm thick, 55 mm diameter) was used as the separator, 100 µL of 1 M lithium hexafluorophosphate ($LiPF_6$) in EC and DMC (EC:DMC 50:50 (v:v)) (Sigma-Aldrich) was used as the electrolyte. Lithium metal (PI-KEM, 15.6mm x 0.25mm thick) that was scraped and punched to a diameter of 1.27 cm was used as the counter electrode. Before battery testing the coin cells were rested for between 6 h-24 h to equilibrate.

Electrode information for each anode used within this chapter is given in Table 6.1.

Table 6.1. *Averaged electrode information for each of the three lithium-ion half cells used for the electrochemical testing of each active material within this chapter. All active materials except recast EoL* 1 h*, PVDF MAGE3 and hydro-thermal EoL* 1 h *were annealed for* 1 h *at* 500 °C *in air. All anodes except recast EoL* 1 h *and PVDF MAGE3 (which used PVDF) used CMC/SBR as the binder.*

Graphite used	Active Mass Loading (mg cm^{-2})	Coating thickness (µm)	Coating Porosity (%)
recast EoL 1 h	6.56(84)	63.6(21)	49.8(55)
Hydro-thermal EoL 1 h	6.20(18)	64.7(6)	49.3(12)
QCR II 1 h	4.33(9)	30.7(6)	23.6(6)
QCR II 2 weeks	4.28(90)	30.3(21)	22.0(16)
EoL 1 h	5.4(1)	33.3(6)	15.9(4)
EoL 2 weeks	4.30(6)	45.7(6)	34.8(15)
EoL II 1 h	6.0(5)	47.0(26)	31.7(28)
EoL II 2 weeks	6.3(2)	55.0(35)	36.1(24)
EoL III 1 h	4.2(5)	47.0(26)	49.9(53)
EoL III 2 weeks	3.1(1)	36.3(21)	54.4(35)
MAGE3	5.74(4)	57.3(64)	46.4(52)

6.4.4 Graphite characterisation

Graphite was characterised via SEM, XRD and Raman spectroscopy. The techniques used follow the same procedures as those disscused in Section 5.4.7, 5.4.4 and 5.4.5.

6.5 | Recasting recovered EoL graphite

PVDF, a binder commonly used for electrodes within LiBs due to its electrochemical stability and high adhesion to both electrode materials,[207] still remains in the recovered anode material extracted via water delamination. This was shown in Section 5.8.3 and is evident from the sheet like nature of the anode material. Studies within the literature use NMP to remove this binder and any organic impurities from the recovered anodes. The binder is then replaced with fresh binder for use within new LiBs.[81,208,209] Due to the solubility of PVDF in NMP, NMP is also used to create electrode slurries.[210] As most organic contaminates are removed via water delamination and PVDF still remains, NMP can be used to directly recast the obtained active material onto a piece of copper foil to recreate an anode. Therefore, not only is the graphite re-used, but so is the binder.

Anode material extracted from EoL after 1 h of air exposure followed by water delamination was used for this study.

TGA was used to determine the amount of PVDF, and thereby, the amount of active material (graphite) within the recast anodes. This study is shown in Figure 6.1.

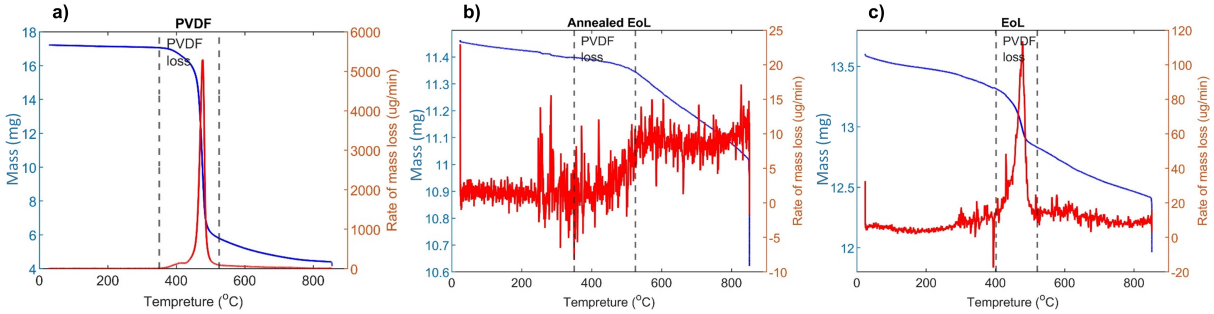


Fig. 6.1. *Mass loss (blue line, left axis) and rate of mass loss (red line, right axis) for (a) PVDF, (b) EoL annealed to* $500\,^{\circ}\mathrm{C}$ *for* 1 h *prior, and (c) EoL anode material exposed to air for* 1 h *before delamination. Each was heated to* $900\,^{\circ}\mathrm{C}$ *at a rate of* $10\,^{\circ}\mathrm{C\,min^{-1}}$.

From Figure 6.1(a) it was determined that $86\,\%$ of pure PVDF is lost between $350\,^{\circ}\mathrm{C}$ and $550\,^{\circ}\mathrm{C}$, as indicated by the peak in rate of mass loss within this region. The study of

annealed EoL (Figure 6.1(b)), where all PVDF was expected to have been removed, showed no real mass loss within this region. Therefore, loss between the $350\,^{\circ}\mathrm{C}$ and $550\,^{\circ}\mathrm{C}$ region in Figure 6.1(c) would result from $86\,\%$ of the overall PVDF mass within the EoL active material. It was calculated that $4\,\%$ of the weight of anode material is PVDF, leaving $96\,\%$ of active material. This calculation excludes any CB or unknown additives that are likely to be present, however, these would only make up a small percentage of the overall mass.

Once recast, electrochemical testing within lithium ion half cells was conducted and compared to standard MAGE3 anode. The results of this study is shown in Figure 6.2 and Table 6.2.

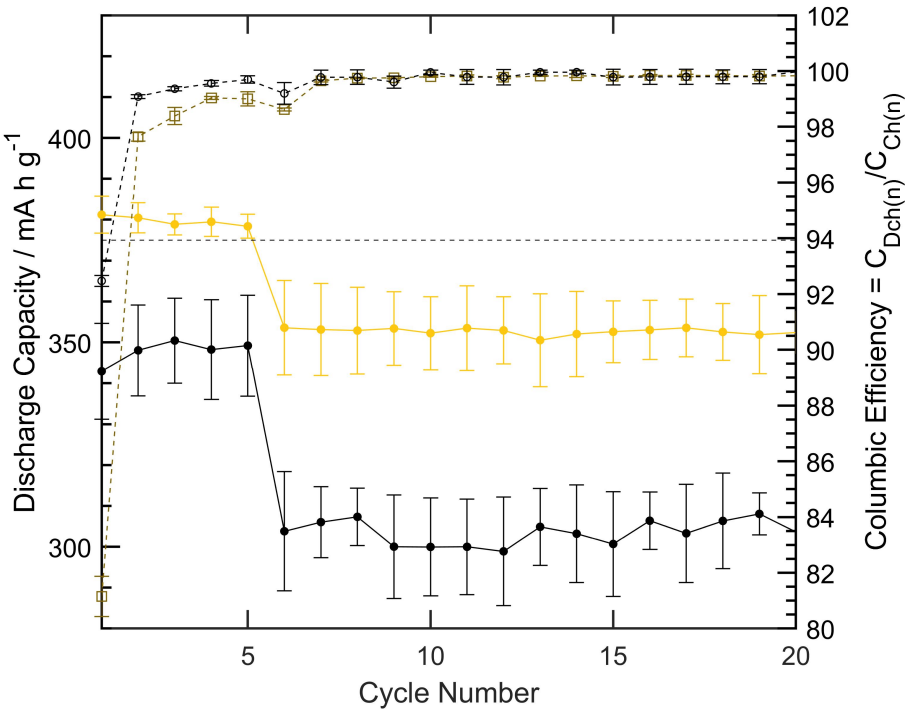


Fig. 6.2. *Specific discharge capacities (referring to the deintercalation of* Li^{+} *from graphite) for triplicate lithium ion half cells made from recast EoL and MAGE3. Each data point represents the average and standard deviation of triplicate data. Using* $372\,\mathrm{mA\,h\,g^{-1}}$ *as the theoretical capacity, the first five cycles were run at C/20 (*$18.6\,\mathrm{mA\,h\,g^{-1}}$*), which was then switched to C/5 (*$74.4\,\mathrm{mA\,h\,g^{-1}}$*) for the remaining 15 cycles. The black dotted line represents the theoretical capacity of graphite. The yellow and black lines represent the specific discharge capacities and relates to the axis on the right. The dotted yellow and black lines represent the coulombic efficiency and relate to the left axis.*

Table 6.2. *Losses during the electrochemical testing of recast EoL and MAGE3 anodes within lithium-ion half cells. Each sample was tested using three half cells; therefore each data point represents an average with standard deviation.*

Anode material	First cycle charge capacity	First cell irreversible capacity loss		C/20 to C/5 capacity loss		Capacity loss after 20 cycles	
	$mA\,h\,g^{-1}$	$mA\,h\,g^{-1}$	% Loss	$mA\,h\,g^{-1}$	% Loss	$mA\,h\,g^{-1}$	% Loss
recast EoL	469.8(97)	88.6(52)	18.86(72)	19.85(35)	4.225(63)	117.4(46)	25.00(47)
Mage3	371(13)	27.9(14)	7.53(20)	42.97(32)	5.353(76)	67.2(60)	31.7(12)

Recast EoL shows a stable specific capacity ($353.0(56)\,mA\,h\,g^{-1}$ on cycle 20) close to the theoretical capacity for graphite ($372\,mA\,h\,g^{-1}$) and far exceeding the capacity of MAGE3 ($303.7(91)\,mA\,h\,g^{-1}$ on cycle 20). A large drop in specific capacity for both electrodes is experienced between cycle 5 and 6, which is due to the electrode polarization caused by the switch to a higher cycling rate (C/5). This increased specific capacity for EoL over MAGE3 is likely not due to water delamination or cell ageing before dismantling improving characteristics of the graphite for increased capacity. More likely, as discussed within a later section (Section 6.7.1), differences in each graphite morphologies, that arise from the origin of each graphite (not the history of each graphite), leads to this increase in performance.

Bar the first six cycles, which represent the formation cycles and equilibration to a higher cycling rate, coloumbic efficiency (CE) varies around $99.89(10)\,\%$ for MAGE3 and $99.80(5)\,\%$ for recast EoL. The CE of commercial cells typically vary between $100\,\%$ to $99.96\,\%$.[211] however, industry uses highly automated procedures focusing on high quality products.[117] This standard also applies to full-cells. Here, half cells are used, where degradation effects occur from the lithium metal counter electrode (due to expansion, shrinkage, dendrites and electrolyte reduction), creating a lower CE.[212] So reaching this $100\,\%$-$99.96\,\%$ goal may be unrealistic. However, similarities of CE between the standard MAGE3 and EoL anode, as well as the stability of these CE through progressive cycles show that EoL graphite has the potential to perform excellently when used to create new LiBs.

From Table 6.2 however, it is apparent that the first cycle capacity loss for EoL is far greater than that of the MAGE3 standard. This is likely due to unhealthy SEI formation caused by metal contamination, leading to irreversible lithium loss. This loss is not detrimental to the performance of a half cell due to the lithium metal providing an effectively infinite amount of lithium ions.[117] However, the performance of a full cell (most commercial cells) are limited by the amount of lithium ions, therefore irreversible loss to SEI growth will have a detrimental effect.[117] It is also evident from the CE of the first five cycles of recast EoL, that this SEI formation/lithium loss continues into further cycles.

Figure 6.3 shows the voltage profiles and differential (dQ/dV) plots for both recast EoL and MAGE3. As proposed by Rüdorff and Hofmann,[36] developed by Daumas and Herold, and discussed within Section 1.1.6, graphite cycling occurs via multiple staging mechanisms, leading to a variety of phase transitions during the lithiation/delithiation. For instance, the uniform solid solution filling/vacating of lithium ions from stage 1L and 2L leads to a sloped loss/gain in voltage compared to the two-phase filling/vacating of stages 4,3,2 and 1 leading to stepped plateaus.[24,37] This can be seen in Figures 6.3(a) and (c). dQ/dV plots (as shown in Figures 6.3(b) and (d)) aid in the analysis of electrochemical thermodynamics and kinetics, where the equilibrium between a transition creates a redox peak in which the position, intensity and FWHM can be analysed. The origin of each peak is given in Section 3.8.3. Each anode gives a three peaked (with one shoulder) fingerprint indicative of graphite, with graphite charging shown on the bottom from right to left and graphite discharging at the top from left to right.[114,118] More peaks and therefore more distingishable transitions would be seen if lower C-rates were used.[114,118]

Differences in the two anodes can be viewed within the voltage profiles at around $0.7\,\mathrm{V}$ of the first graphite charging cycle. Here, a large shoulder can be found on the dropping profile of recast EoL (Figure 6.3(a)) and only a small difference in gradient for MAGE3 on comparison to its second cycle (Figure 6.3(c)). This difference is resultant from irreversible

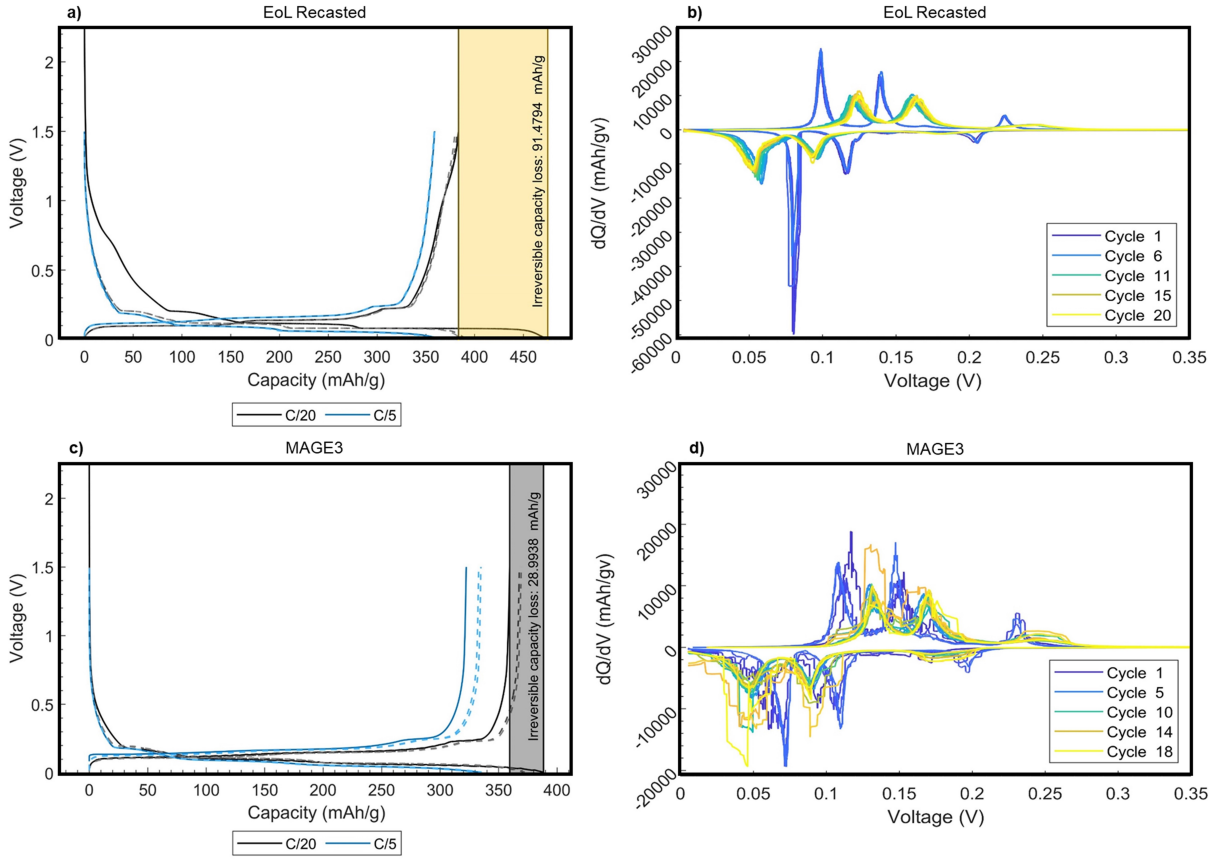


Fig. 6.3. *Capacity plotted against voltage for every cycle on (a) recast EoL and (c) MAGE3. The black line represents the first five cycles at C/20 (18.6 mAg^{-1}) and the coloured line represent the last 15 cycles conducted at C/5 (74.4 mAg^{-1}). The continuous line represents the first cycle of each cycle rate, the dashed lines represents the second cycle and above. Irreversible capacity is shown via a box on the right. The dQ/dV plots for (b) recast EoL and (d) MAGE3 are also shown.*

reduction of electrolyte on the surface of the anode, leading to the growth of an SEI layer, the loss of lithium and an increase in the charge capacity of the first cycle.[37,119] This process is greater for recast EoL, leading to greater definition in the charge profile and a greater irreversible loss.

Peaks in dQ/dV traces indicate an equilibrium between two states of a redox process, therefore the irreversible reduction of electrolyte does not appear in the dQ/dV of Figure 6.3.[116] However, its effects can be witnessed through its effects on the dynamics of further

cycling. For the first five charge cycles of recast EoL (Figure 6.3(b)) the peak at around 0.08 V, that results from the transition from stage 2 graphite (LiC_{12}) to stage 1 graphite (LiC_6),[114,118] decreases and shifts to later in the charge step. This decrease and shift is more apparent in the faster C/5 scans, where the peak propagates to around 0.05 V. This indicates a progressive increase in overpotential during the lithiation of graphite for recast EoL (the shift to lower voltages), which inevitably ends up in less LiC_6 formation per cycle (drop in peak intensity).[115,116] This is likely caused by an increase in resistivity created by the large SEI formation and although no degradation of cell capacity was seen in Figure 6.2, further cycling may result in a decrease in this capacity. This shift was less noticeable for MAGE3 (Figure 6.3(d)).

As the voltage profile and cyclic voltammetry of recast EoL graphite resemble that of pristine (MAGE3) graphite, it indicates, like stated in previous chapters, that the normal use of EV LiBs has no significant effect on the graphite structure.

As unhealthy SEI formation will occur at points of imperfection and this was seen during this study, it is evident that further processing is needed to clean the surface of the graphite particles in order to get better cycling performance.

6.6 | Improving performance of EoL graphite

6.6.1 Further processing

In recent years, CMC/SBR mix has become a common anode binder.[213] This provides a number of benefits, for instance, decreased cost and decreased production toxicity, due to the use of water as a solvent instead of NMP to create the coating slurries.[24] The Polyelectrolytes CMC binder also has electrochemical advantages over the van der Waals binding PVDF; showing decreased initial capacity loss, an increase in thermal stability and

provides suppression for any potential thermal runaway, as unlike PVDF, CMC does not react with lithiated species.[24] However, for this study, the advantage of using CMC/SBR comes from the ease of further recycling. CMC/SBR binder is water soluble, this allows for easy separation and reuse of anode components via submersion in water without the need of trace amounts of lithiated graphite.

Therefore, for improving the recovery of graphite, not only will the surface be cleaned, but the PVDF binder will be removed and replaced with the eco-friendlier CMC/SBR binder.

Two methods were used to rejuvenate the graphite and remove the binder from EoL 1 h active material. The first method annealed the active material in air to 500 °C for 1 h, whilst the second used hydro-thermal conditions (160 °C for 12 h) to decompose the PVDF in a 1 M NaOH solution.

The former will decompose the PVDF at around 450 °C-500 °C.[214] SEI components will also decompose. A study by *Rothermel et al.*[75] showed evaporation of residual carbonates and decomposition of other SEI components below 120 °C. Carboxyl groups, another SEI contaminate, was also seen to decompose between 200 °C and 400 °C.[75] This will result in the production of CO_2, O_2 and ethylene (C_2H_4) gas from the trace amounts of SEI.[215] PVDF is known to act as a fluorinating agent when heated with various metal oxides due to its thermal breakdown into HF gas and various fluorine monomers. The fluorine monomers will then further breakdown into CO, CO_2 and more HF gas.[214,216] Fluorination of graphite however, requires the use of fluorine gas and as this is not a decomposition product of PVDF, no fluorination was expected.[217–219] Graphite also has a relatively high combustion temperature (700 °C-800 °C), so no combustion was expected, however carbon black will oxidise and self-ignite at temperatures of around 400 °C.[220,221] Therefore this method will potentially lose valuable battery material and will also produce a variety of gasses that will need to be collected in order to make the recycling process eco-friendly.

High alkaline conditions have been shown to etch and reduce the binding of PVDF film via a dehydrofluorination processes.[222,223] This elimination reaction produces aqueous HF (which further neutralises to form NaF and $\mathrm{H_2O}$), leaving a double chained polymer which upon further reactions with water, forms carbonyl monomers (likely as a sodium salt).[223] This process intensifies at elevated temperatures, therefore, hydrothermal conditions were used to increase the temperature past the boiling point of water ($100\,^{\circ}\mathrm{C}$).[29,222] For this study, a temperature of $160\,^{\circ}\mathrm{C}$ (using a ramp rate of $10\,^{\circ}\mathrm{C\,min^{-1}}$) for $12\,\mathrm{h}$ was used. This hydro-thermal method will allow for the degradation of the PVDF without loss of CB and will prevent any potential surface oxidation that might occur on the graphite at elevated temperatures. Waste removal will also be easier as decomposition products will be contained within the solution rather than within the produced gas.

SEM images were taken of the products obtained after the annealing and hydro-thermal treatment of EoL $1\,\mathrm{h}$ anode material (Figure 6.4).

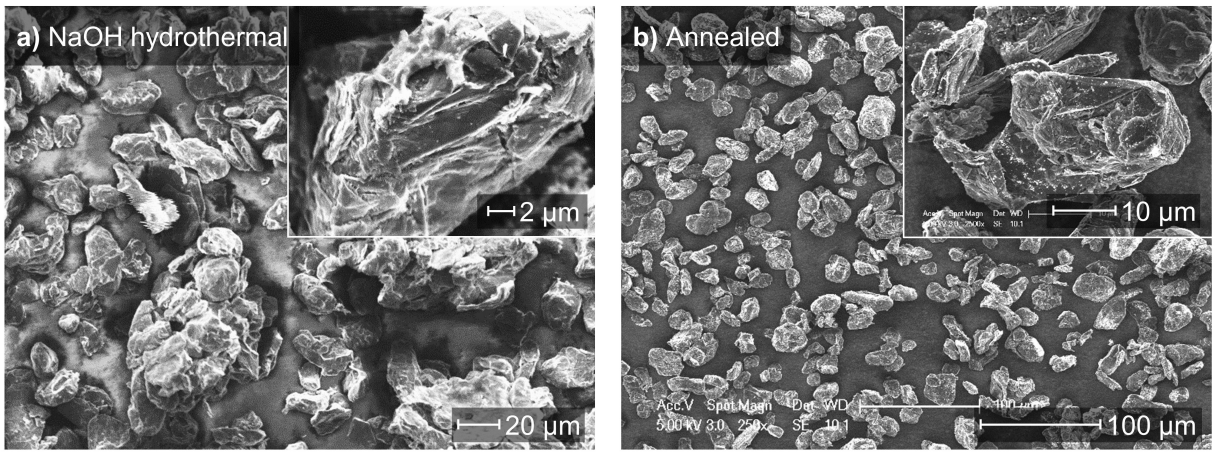


Fig. 6.4. *SEM images taken of (a) hydro-thermally treated in 1 M NaOH and (b) annealed EoL active material delaminated after* $1\,\mathrm{h}$ *of air exposure. Hydro-thermal images were taken at x1,500 and x12,000. Annealed images were taken at x250 and x2,500. All images were taken with a secondary electron detector with an accelerating voltage of 5 kV.*

Annealing of EoL $1\,\mathrm{h}$ anode material (Figure 6.4(b)) created a powder of individual graphite particles, indicating the removal of PVDF. Furthermore, on the particle surface,

layers and flakes of graphite can be observed, suggesting that any coating that remained on the surface had been removed. Apparent agglomerates appear as white specks on the surface of each graphite particle. These indicate regions of reduced electrical conductivity and could result from salts formed from the decomposition products of PVDF, SEI species or lithium and metal salts. EDX analysis conducted on EoL III $1\,\mathrm{h}$ and EoL III 2 weeks, which also experiences the same agglomerations are shown in Figure 6.14 within the appendix. Here these images show that the impurities in the recovered graphite contain traces of manganese and fluorine.

Much like the annealed counterpart, the hydro-thermally treated EoL $1\,\mathrm{h}$ product shows spherical graphite with no obvious surface coating or degradation. However, clumps of graphite particles can be found with obvious strands of PVDF. Evidently, these conditions need to be altered in order to remove all PVDF from the sample. Less white spots can be found on this sample, indicating the presence of less salt contamination.

Raman spectroscopy and I_D/I_G ratio distributions for both recovered materials are given in Figure 6.5.

Both Raman spectra show far more intense graphitic regions than those obtained via water delamination (Figure 5.9), indicating the removal of non-Raman active components, perhaps suggesting the loss of PVDF and trace SEI contaminates from the surface. The mean I_D/I_G ratio actually increases slightly for the annealed graphite (a rise from 0.49 to 0.53). This may arise from surface oxidation or less alignment of the loose graphite particles. A higher intensity in the pitch coating peak around $800\,\mathrm{cm}^{-1}$ is observed for both, compared to the EoL pre-thermal treatment. This may indicate either a loss of surface contamination, revealing more pitch coating, or an increase in pitch coating due to the combustion of organic components on the graphite surface, particularly during annealing.

A difference between the two techniques can be seen in the I_D/I_G distributions, where hydro-thermally treated graphite shows a narrower distribution and a lower mean I_D/I_G ratio

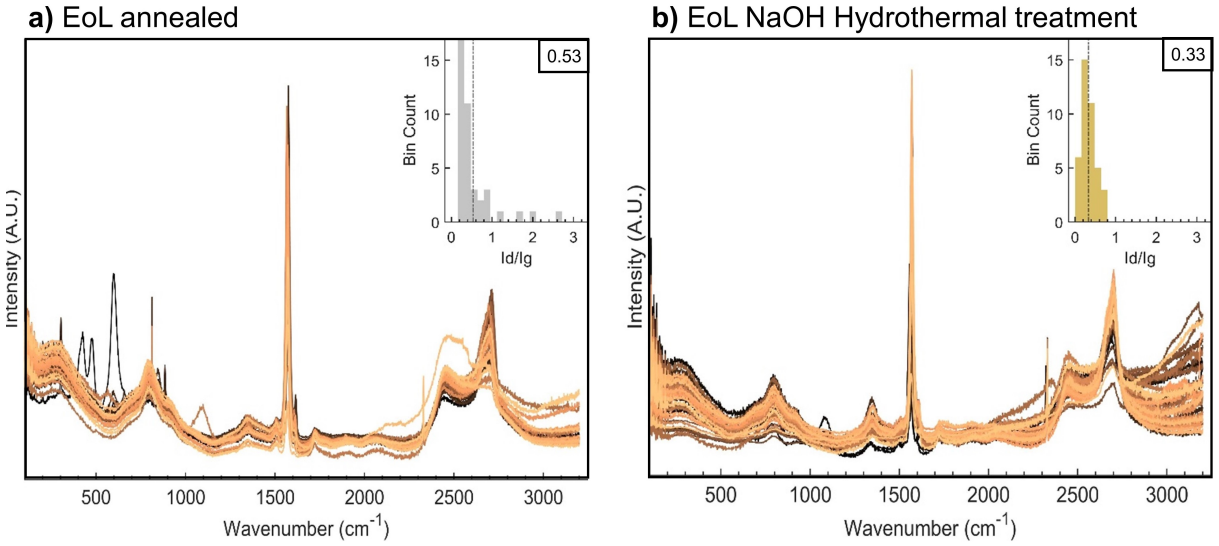


Fig. 6.5. *40 Raman scans taken on graphite recovered from EoL* 1 h *active material either after (a) annealing or (b) hydro-thermal treatment.* I_D/I_G *ratio distributions are given in the top right of each figure. Peak-fittings and integrated intensities were calculated in MATLAB.*[125] *The mean* I_D/I_G *ratio is shown via the dash-dotted black line and is given in the top right corner of each distribution.*

of 0.33; indicating a more consistent and graphitic surface. As seen within the previous SEM study (Figure 6.4) the annealed sample has more salt contamination than the hydro-thermal sample. This is also seen within this study with annealed EoL showing peaks for salt impurities between $300\,\mathrm{cm}^{-1}$-$750\,\mathrm{cm}^{-1}$.[191] More peaks than that found on the pre-thermal treatment EoL scan can be seen below $1000\,\mathrm{cm}^{-1}$ which are likely from salt formation during the heating of SEI, PVDF and metal contaminates. For the hydrothermal treatment, these salts appear to have dissolved within the NaOH solution, leaving the surface of this graphite uncontaminated.

PXRD analysis was also conducted on the obtained graphite as well as the salts recovered via the evaporation of the NaOH solution. The obtained patterns are given in Figure 6.6.

No crystalline impurities can be found on the patterns of both annealed and hydro-thermally treated graphite. This does not indicate that no crystalline impurities are present, just that the amount of impurity is far smaller than the amount of graphite.

The powder obtained after the evaporation of the hydro-thermal solution contained Na_2CO_3 and NaF. There is a lack of $NaOH$ which could suggest all was used to break down PVDF or converted to Na_2CO_3 due to heating. Na_2CO_3 could form from a reaction between the sodium carboxylates, formed from the decomposition of PVDF, with CO_2 within the vessel. NaF appears from the neutralisation of HF formed from the initial dehydrofluorination process.

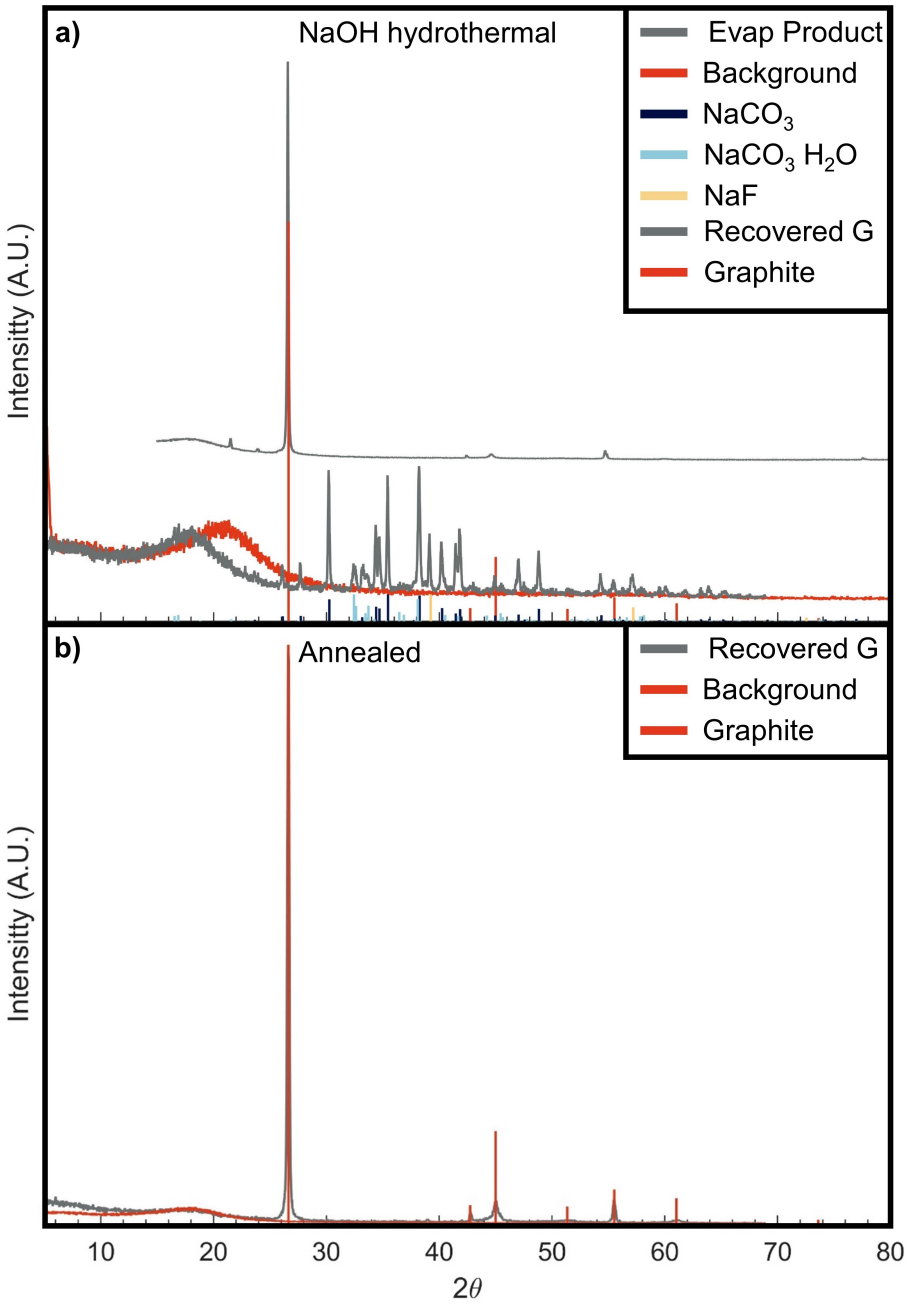


Fig. 6.6. *PXRD patterns obtained for (a) the evaporated salts from the hydrothermal solution on top and the recovered graphite on the bottom. (b) shows the graphite recovered from annealing EoL* 1 h *active material. Vaseline peaks can be found on the hydro-thermal sample (at around* $21.8°$ *and* $23.5°$*) which was used to hold the sample down. Crystallographic Information File files taken from Fayos*[109]*. The background was collected by running a blank scan of the low background holder.*

6.6.2 Electrochemical performance

Both annealing and hydro-thermal treatment of EoL 1 h active material gave powders that, with the addition of CMC/SBR and 2 % carbon black, could create regenerated, recyclable anodes. These anodes were tested electrochemically, where the capacity per cycle and coulombic efficiencies are presented in Figure 6.7. Recast EoL 1 h was also added for comparison. Table 6.3 gives numerical results for the cycling performance.

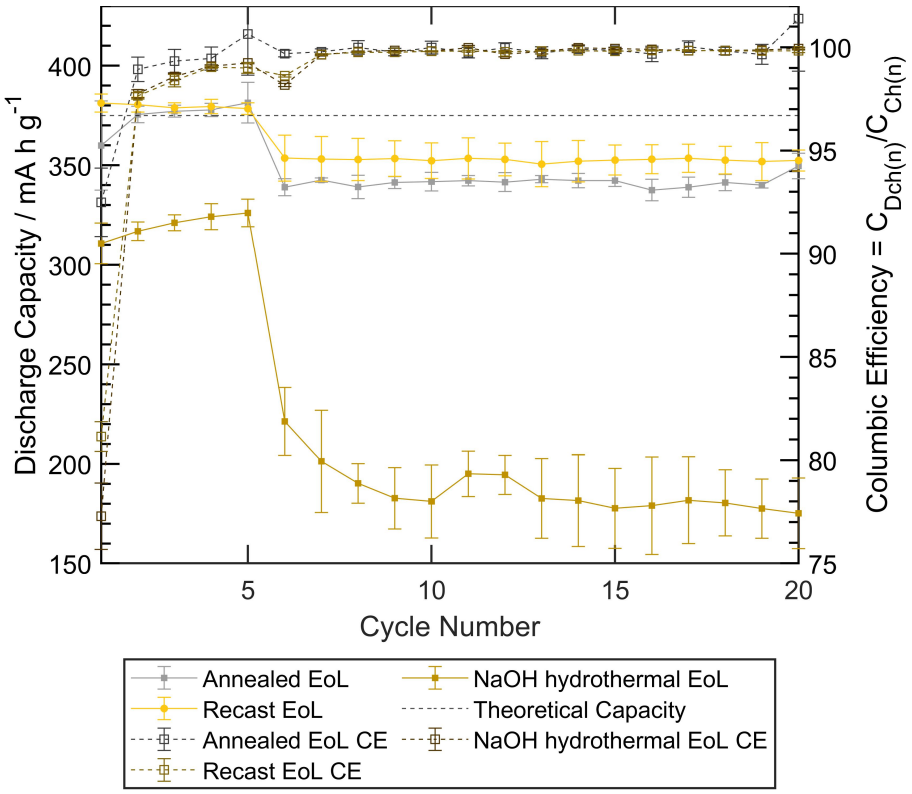


Fig. 6.7. *Specific discharge capacities (referring to the deintercalation of Li^+ from graphite) for triplicate lithium ion half cells made from recast EoL* 1 h *(yellow), hydro-thermally treated EoL* 1 h *(gold) and annealed EoL* 1 h *(black). Using* 372 mA h g^{-1} *as the theoretical capacity, the first five cycles were run at C/20 (18.6* mAg^{-1}*), which was then switched to C/5 (74.4* mAg^{-1}*) for the remaining 15 cycles. The black dotted line represents the theoretical capacity of graphite. The continuous lines represent the specific discharge capacities and relates to the axis on the left. The dotted lines represent the coulombic efficiency and relate to the right axis.*

Table 6.3. *Losses during the electrochemical testing of recast EoL 1 h, hydro-thermally treated EoL* 1 h *and annealed EoL* 1 h *anodes within lithium-ion half cells. Each sample was tested using three half cells; therefore each data point represents an average with a standard deviation.*

Anode material	**First cycle charge capacity**	**First cell irreversible capacity loss**		**C/20 to C/5 capacity loss**		**Capacity loss after 20 cycles**	
	$mA\,h\,g^{-1}$	$mA\,h\,g^{-1}$	% **Loss**	$mA\,h\,g^{-1}$	% **Loss**	$mA\,h\,g^{-1}$	% **Loss**
recast	469.8(97)	88.6(52)	18.86(72)	19.85(35)	4.225(63)	117.4(46)	25.00(47)
Annealed	389(18)	29.0(52)	7.5(17)	41.5(19)	10.66(49)	39(16)	10.1(39)
NaOH Hydro	402.0(52)	91.3(54)	22.7(16)	100.6(11)	25.03(28)	227(21)	56.4(48)

Annealing EoL 1 h drastically decreased the first cycle irreversible capacity loss, almost matching that of the MAGE3 standard tested previously. The CE for the first five formation cycles was also higher than that of the original recast EoL, indicating a stable surface and healthier SEI formation.

Hydrothermally treated EoL 1 h on the other hand, shows decreased cycle performance. First cycle irreversible capacity loss was greater and although the CE is similar to that of recast EoL, discharge capacities decreased dramatically.

In order to study the loss and increase in stability, voltage profiles and dQ/dV plots are given in Figure 6.8.

The first cycle of annealed EoL 1 h (Figure 6.8(c)) looks almost identical to MAGE3 shown previously (Figure 6.3(c)) with the region of SEI formation (around 0.8 V) significantly reduced from that of just recast EoL (Figure 6.3(a)). Industry standard anodes typically have a first cycle irreversible capacity loss of below 10 %, here, annealed EoL 1 h has 7.5 %.[148]

From the dQ/dV plots of annealed EoL 1 h (Figure 6.8(d)), it is evident that the first charge step had an increased overpotential which reduced thereafter, indicating the formation of a stable SEI during the first cycle with no further growth into later cycles. After the first cycle, the increased intensity of the $LiC_{12} \rightarrow LiC_6$ transition (0.08 V on the bottom charge sweep) indicates that potentially full lithiation of the graphite occurs during the first five

formation cycles bar the first. Cycles at C/5 showed no propagating overpotential except that caused by the switch to a faster cycle rate. This indicates stable cycling and potentially good cycle performance if cycled further.

The hydro-thermally treated EoL 1 h voltage profile (Figure 6.8(a)) does not show the distinct phase change plateaus as seen with annealed EoL 1 h. The typical shoulder for SEI seen at 0.8 V is also not seen, instead the charge profile starts with a large dropping curve at around 0.5 V, indicating non-typical side reactions. The latter charge cycles during these formation cycles also show an increased curvature in this region, indicating that further processes are occurring during charging.

A noisy dQ/dV plot was also shown for hydro-thermally treated EoL 1 h. All graphite charging peaks had shifted to lower voltages and discharge peaks to higher voltages, indicating a severe overpotential throughout the cycling of hydro-thermally treated EoL 1 h. This overpotential was so great that during the C/5 cycling, the charge cycle ended before the $\mathrm{LiC_{12}} \rightarrow \mathrm{LiC_6}$ transition reaches equilibrium, which may indicate the drop in discharge capacity seen in Figure 6.8(a). The dQ/dV plot for the first charge cycle did not show an increase in overpotential like that for the well performing MAGE3 and annealed EoL 1 h. This may indicate that the SEI layer growth required to stabilise the cycling of the anode with the electrolyte did not form, leading to an increase in parasitic reactions further into the cycling of the cells.

The increased overpotential for hydrothermally treated EoL 1 h could arise from a poor anode formation, perhaps due to large particles still bound by PVDF. Alternatively, the surface chemistry of the graphite obtained via hydrothermal synthesis may be unfavourable for SEI formation. *Omichi et al.*[224] found that surfaces consisting of dangling bonds in comparison to those that are terminated by hydrogen atoms lead to increased SEI formation and therefore more irreversible capacity loss. *Ng et al.*[225] also found that the presence of oxygen groups on the surface of graphite is crucial for stable SEI formation. This may

distinguish the two heat treatments, with annealing in an oxygen-rich atmosphere forming oxygenated species on the graphite surface for stable SEI formation, while hydrothermal treatment results in a surface that promotes the growth of an unhealthy SEI. The latter causing increased overpotentials in later cycles and continual capacity consumption.

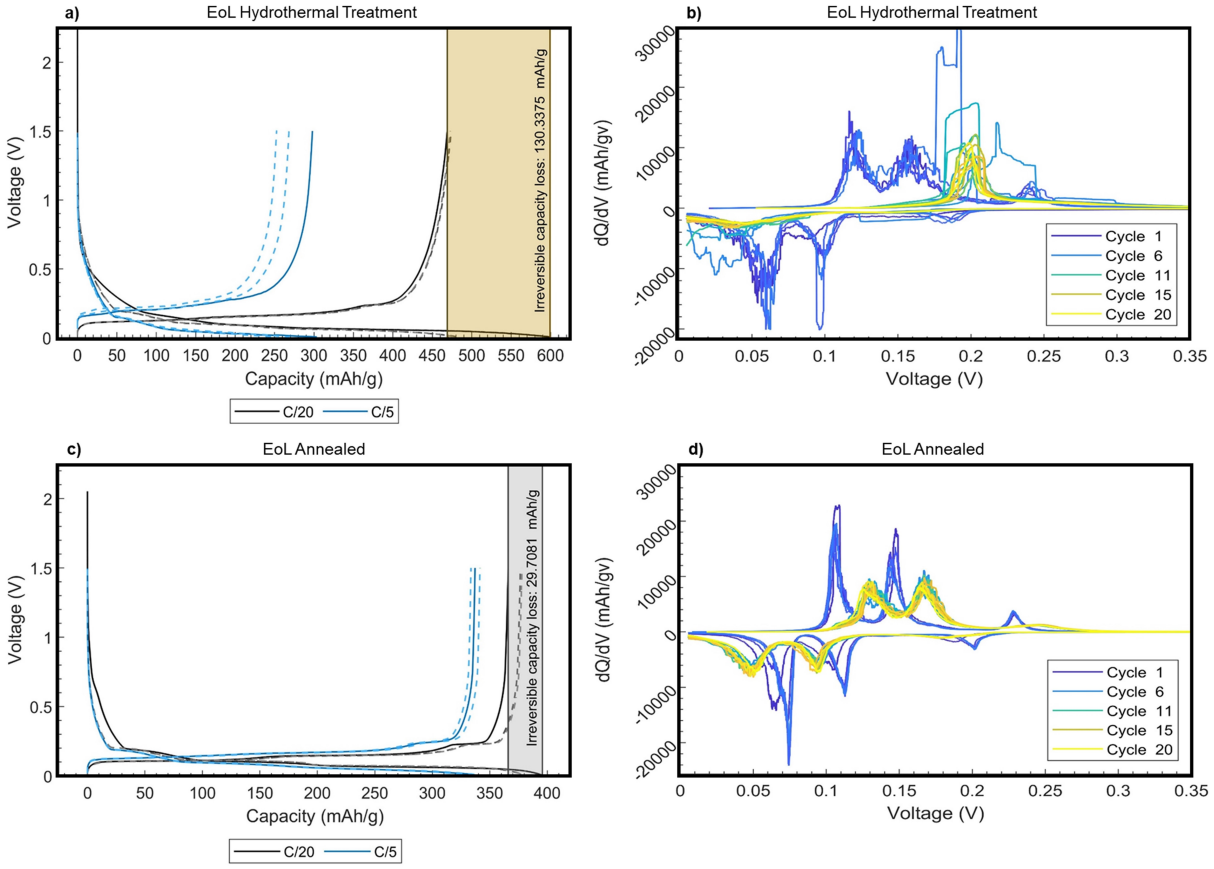


Fig. 6.8. *Capacity plotted against voltage for every cycle of (a) EoL* $1\,\mathrm{h}$ *hydro-thermally treated and (c) Annealed EoL* $1\,\mathrm{h}$*. The black line represents the first five cycles at* $C/20$ *(*$18.6\,\mathrm{mA\,h\,g^{-1}}$*) and the coloured line represent the last 15 cycles conducted at* $C/5$ *(*$74.4\,\mathrm{mA\,h\,g^{-1}}$*). The continuous line represents the first cycle of each cycle rate, the dashed lines represent the second cycle and above. Irreversible capacity is shown via a box on the right. dQ/dV plots for (b) EoL* $1\,\mathrm{h}$ *hydro-thermally treated and (d) Annealed EoL* $1\,\mathrm{h}$ *also shown.*

6.7 | Reuse of all recovered anode material

6.7.1 Annealing recovered anode materials

Annealing EoL 1 h produced an anode with excellent cycling performance. Therefore this same route (annealing to 500 °C for 1 h) was used for all recovered active materials: QCR II, EoL II and EoL III, with 1 h and 2 weeks of air exposure prior to delamination. SEM images of each annealed 1 h air exposed samples and MAGE3 graphite are given in Figure 6.9. 2 week air exposed samples are given in the appendix (Figure 6.15).

The results show that the annealing was successful in unbinding the graphite particles, leaving a fine powder to be used to create a smooth anode slurry. No obvious particle degradation could be found in any sample. Each showed flakes of graphite compressed into a sphericalised particle with no apparent coating over the surface. Similar to the SEM study on treated EoL graphite, white specks could be found on the surface of all recovered graphite, likely to be a mixture of Li, manganese and phosphate salts as discussed within the previous section (Section 6.6.1).

The size and shape of each recovered graphite are similar to that of MAGE3. However, the morphology is slightly different, the recovered graphite particles appear to be comprised of compact clusters with jagged-edges and visible strata whereas the MAGE3 samples are comprised of smooth, smooth-edged pieces clustered together. These differences could originate from the types of graphite used, with the more isotropic nature of MAGE3 suggesting a synthetic origin and the anisotropic crystalline plates of the recovered graphite suggesting an origin from mined NG.[24]

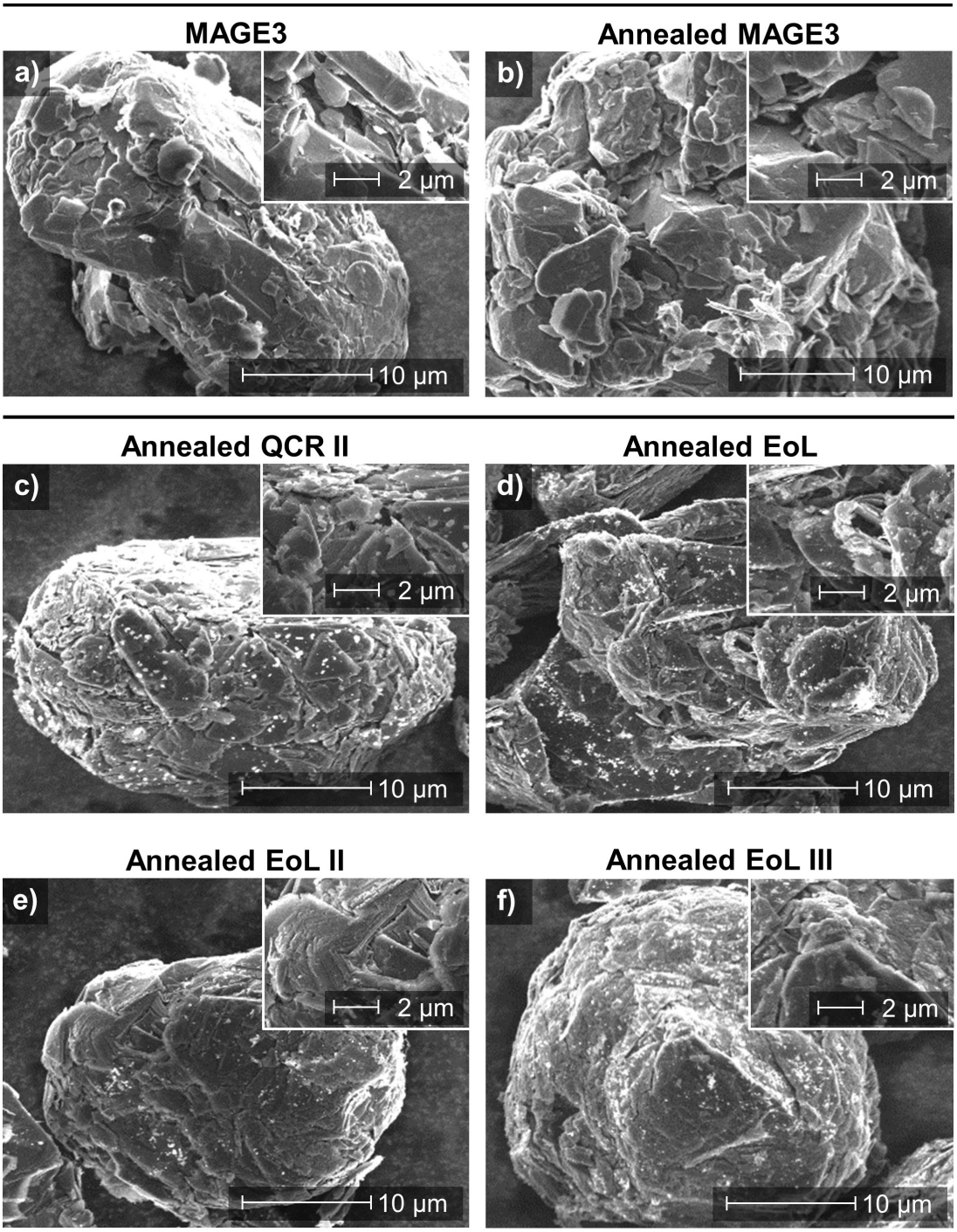


Fig. 6.9. *Large 5000x magnified SEM images with 12000x magnified SEM images in the top right of each. a) MAGE3 particle. b) A particle of MAGE3 after annealing to* $500\,^{\circ}\mathrm{C}$ *for* $1\,\mathrm{h}$. *c) QCR II d) EoL e) EoL II f) EoL III. All graphite was obtained using water delamination after* $1\,\mathrm{h}$ *of air exposure and annealing to* $500\,^{\circ}\mathrm{C}$ *for* $1\,\mathrm{h}$. *Reproduced from Sargent et al.*[121] *with permission from the Royal Society of Chemistry.*

Raman I_D/I_G ratio distributions for each recovered graphite after annealing are given in Figure 6.10. Raman scans for each anode are given in the appendix in Figure 6.16.

Mean I_D/I_G ratios for annealed QCR II, EoL and EoL II show no discernible differences to those obtained after recovery via water delamination. Water delaminated samples gave mean values of 0.66,0.49, 0.53, and 1.48 for QCR II, EoL, EoL II, and EoL III, respectively (shown within Figure 5.10). MAGE3 before annealing gave a mean of 1.79. After annealing, mean I_D/I_G values of 0.64, 0.53, 0.59, 0.83 and 2.29 were obtained for QCR II, EoL, EoL II, EoL III and MAGE3, respectively. However, there was a noticeable difference in the distribution range being much narrower for the annealed samples, suggesting that while the overall ordering has not increased, the homogeneity of the samples appears to have improved, possibly due to the combustion of smaller carbonaceous species.

EoL III did show an increase in ordering with a decrease in average I_D/I_G ratio after annealing (1.48 to 0.83). It is possible that the higher surface area of the de-sphericalised graphite caused these to combust, leaving only the higher ordered, sphericalised graphite.

Annealing MAGE3 under the same conditions did increase the mean I_D/I_G (1.79 to 2.29) as well as the size of distribution, indicating annealing does have an effect on battery-grade graphite.

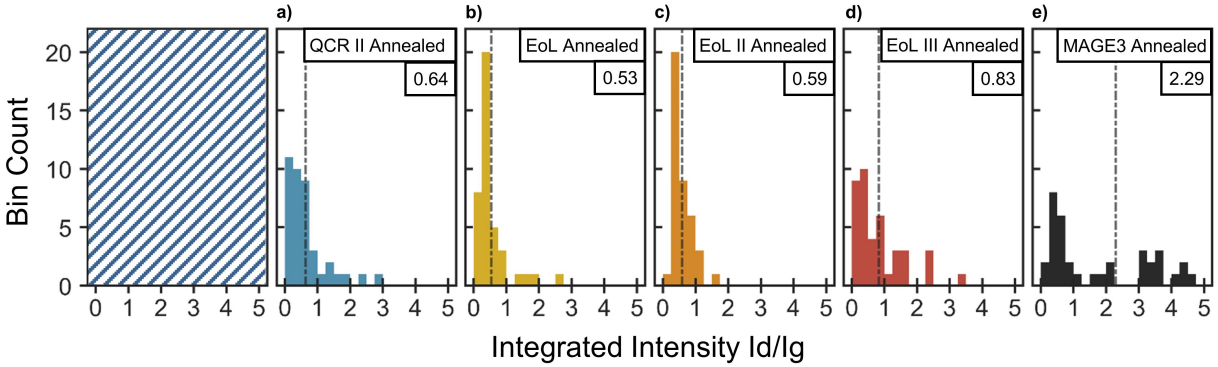


Fig. 6.10. *Distributions of 40 I_D/I_G ratios calculated from randomly distributed Raman scans on (a) QCR II (b) EoL (c) EoL II and (d) EoL III after annealing, each collected active material was annealed to $500\,^{\circ}\mathrm{C}$ for $1\,\mathrm{h}$. For each sample, 20 scans were taken on the annealed active material was delaminated after $1\,\mathrm{h}$ of air exposure and the other 20 were taken on the annealed anode material obtained after 2 weeks of air exposure. e) A distribution obtained after 40 scans on a powder of MAGE3, annealed to $500\,^{\circ}\mathrm{C}$ for $1\,\mathrm{h}$. Peak-fittings and integrated intensities were calculated in MATLAB.[125] The mean I_D/I_G ratio is shown via the dash-dotted black line and is given in the top right corner of each distribution. Reproduced from Sargent et al.[121] with permission from the Royal Society of Chemistry.*

6.7.2 Electrochemical performance

Each annealed recovered active material was used to create a CMC/SBR bound anode which was then electrochemically tested within lithium-ion half cells. The cycling performance of each is given in Figure 6.11 with quantitative values given in Table 6.4. Voltage profiles for one half cell for each anode is given within the appendix in Figures 6.17, 6.18, 6.19 and 6.20.

All recovered graphite showed excellent consistency; all varying around a stable specific capacity close to the theoretical capacity for graphite. All first cycle capacity losses varied around $6\,\%$-$9\,\%$. Differences between the recovered graphite do not vary with sample history but rather active mass loadings and anode thickness, which are given within the experimental section (Table 6.1). For example, EoL III $1\,\mathrm{h}$ has the highest capacity and EoL II 2 weeks has the lowest, which correlates to the active masses of $3.1\,\mathrm{mg\,cm^{-2}}$ for EoL III $1\,\mathrm{h}$ and $6.3\,\mathrm{mg\,cm^{-2}}$ for EoL II 2 weeks. However, the MAGE3 anode sits comfortably

Table 6.4. *Numerical values for losses during electrochemical testing of lithium-ion half cell for annealed active materials. Each sample was tested using three half cells; therefore each data point is an average with its standard error between three cells. Reproduced from Sargent et al.*[121] *with permission from the Royal Society of Chemistry.*

Anode material	First cycle charge capacity $mA\,h\,g^{-1}$	First cycle Discharge capacity $mA\,h\,g^{-1}$	First cell irreversible capacity loss		C/20 to C/5 capacity loss		Capacity loss after 20 cycles	
			$mA\,h\,g^{-1}$	% Loss	$mA\,h\,g^{-1}$	% Loss	$mA\,h\,g^{-1}$	% Loss
QCR II 1 h	382.6(58)	356.5(81)	26.1(33)	6.8(9)	25.0(3)	6.5(1)	34.3(89)	9.0(22)
QCR II 2 weeks	387.7(83)	358.0(59)	29.7(25)	7.7(5)	20.9(9)	5.4(2)	35.4(70)	9.1(16)
EoL 1 h	388.9(176)	359.9(224)	29.0(52)	7.5(17)	41.5(19)	10.7(5)	39.3(163)	10.1(39)
EoL 2 weeks	397.6(78)	366.9(79)	30.7(5)	7.7(2)	30.0(1)	7.5	58.8(62)	14.8(14)
EoL II 1 h	400.9(41)	370.4(4)	30.5(33)	7.6(9)	41.4(28)	10.3(7)	60.2(71)	15.0(20)
EoL II 2 weeks	397.1(35)	363.7(41)	33.4(7)	8.4(2)	38.2(7)	9.6(2)	71.1(48)	17.9(11)
EoL III 1 h	404.2(43)	371.0(38)	33.2(4)	8.2	33.5(8)	8.3(2)	71.0(49)	17.6(14)
EoL III 2 weeks	415.3(32)	375.4(30)	40.0(2)	9.6	17.8(4)	4.3(1)	56.7(32)	13.6(8)
MAGE3	370.9(129)	342.9(117)	27.9(14)	7.5(2)	6.3(3)	1.7(1)	67.2(60)	18.1(12)

within this range of active mass loadings used, cycles at a lower specific capacities than any of the recovered graphite. This may arise from the larger domain sizes of natural graphite (recovered graphite) providing higher specific capacities than synthetic graphite (MAGE3).[226]

Figure 6.11(b) shows no distinct differences in the coulombic efficiency (CE) between any of the cycled cells. Values appear to vary steadily around an excellent value of $99.9\,\%$ for all cells after the initial formation cycles. The CE of the recovered graphite cells match that of the MAGE3, indicating a performance acceptable for battery-grade graphite.

Overall, the excellent electrochemical results displayed here are promising for the development of future anode recycling. If EoL III is considered as an example, before dismantlement a capacity $30\,\%$ of its original value was obtained for its last cycle, while once dismantled, delaminated, annealed, and reconstructed into a new cell, a capacity close to the theoretical was obtained. This result highlights the fact that deteriorated electric car cells are a viable source for high performing battery-grade graphite.

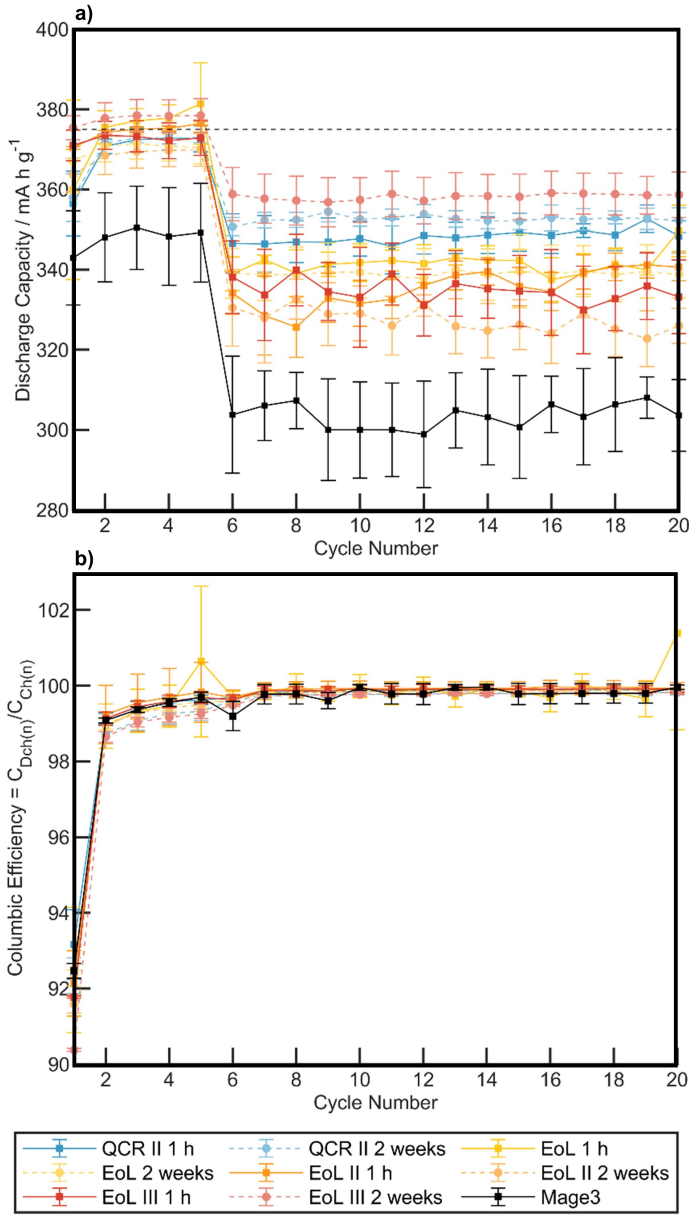


Fig. 6.11. *(a) Graphite discharge specific capacities plotted against cycle number for lithium-ion half cells (using graphite obtained after water delamination and subsequent annealing).* 1 h *and 2 weeks refer to the time exposed to air before delamination. MAGE3 was used as a standard, representing virgin battery-grade graphite. Each data point represents the average of measurements made from three half cells. The first 5 cycles were run at* $C/20$ *(*$18.6\,\mathrm{mA\,g^{-1}}$*) then the remaining 15 were run at* $C/5$ *(*$74.4\,\mathrm{mA\,g^{-1}}$*) using* $372\,\mathrm{mA\,h\,g^{-1}}$ *as the theoretical capacity. The grey dotted line represents the theoretical capacity. (b) Columbic efficiency against cycle number for each obtained graphite and MAGE3. Each point is an average made up of three half cells and the error bars consist of the* 95 % *confidence interval. Reproduced from Sargent et al.*[121] *with permission from the Royal Society of Chemistry.*

6.7.3 Long term cycling

Short term cycling for all recovered anodes showed excellent performance, however this was only to 20 cycles. If this material were to be used within a typical battery, these would be charged and discharged many more times and over a prolonged period of time, which in effect, will exaggerate any degradation method arising from the anode. To test the long term performance of these anodes, lithium-ion half cells were constructed and after cycling for 3 cycles at C/20 (formation cycles), were asymmetrically cycled for 200 cycles at a charge rate of $C/2$ ($186\,\mathrm{mA\,g^{-1}}$) and a discharge rate of $1C$ ($372\,\mathrm{mA\,g^{-1}}$).

Graphite is known to not perform well at high cycle rates, due to a number of slow kinetic transitions including, interfacial diffusion (desolvation and transport through the SEI), particle diffusion (intercalation and movement through the graphene layers) and electrode diffusion (movement through the electrode).[227,228] The particle diffusion limit of graphite ($> 2.64 \times 10^{-10}\,\mathrm{cm^2\,s^{-1}}$ found by *Weng et al.*[228]) is stated to allow for a charge rate of up to 6C for graphite below $10\,\mu\mathrm{m}$ particle size and 2C for those of $20\,\mu\mathrm{m}$, however it is the interfacial diffusion ($10^{-10} - 10^{-12}\,\mathrm{cm^2\,s^{-1}}$ found by *Xu et al.*[227]) that limits the cycle rate. Fast charging leads to a high concentration polarisation at the surface of the particles, leading to parasitic reactions like lithium plating and further electrolyte reduction.[227–229] Therefore, asymmetric testing was used, using a slower rate of charge and a fast rate of discharge, in which these slow kinetics do not excessively hinder the performance.

The cycling performance of QCR II, EoL, EoL III and MAGE3 are shown in Figure 6.12. EoL II was not tested due to time constrains and its similarity in performance during the short-term testing to the other EoL anodes. Table 6.5 shows quantitative data for this cycling performance. The same anode coatings used in the short term study were used for this study, therefore, active mass loadings and thicknesses are also given in Table 6.1.

Table 6.5. *Numerical values for losses during the long term electrochemical testing for lithium-ion half cell testing. Each sample was tested using three half cells; therefore each data point is an average with its standard error between three cells. Reproduced from Sargent et al.*[121] *with permission from the Royal Society of Chemistry.*

Anode material	First cycle discharge capacity $mA\,h\,g^{-1}$	200 Cycle discharge capacity $mA\,h\,g^{-1}$	Capacity loss after 200 cycles	
			$mA\,h\,g^{-1}$	% Loss
QCR II 1 h	249(19)	110.67(52)	138(19)	55.6(32)
QCR II 2 weeks	259(12)	127.5(18)	132(13)	50.8(28)
EoL 1 h	235(29)	65(16)	170(14)	72.2(33)
EoL 2 weeks	150(100)	98(14)	54(91)	36(63)
EoL III 1 h	155.2(13)	94(14)	61(13)	39.2(87)
EoL III 2 weeks	194(12)	140(25)	55(37)	28(18)
MAGE3	94.1(57)	50.0(58)	44.2(73)	46.9(63)

As for the short-term testing, the recovered graphite performs at much higher specific capacities than MAGE3 for all cycles. However, much less stability was shown in the recovered graphite, with discharge capacity decreasing with increased cycle number. This was also paired with more variation in CE and specific discharge capacities between cells, leading to high standard deviations. Significant variation and a dip in discharge capacity can be seen for most anodes, suggesting that additional formation cycles (slow C-rate cycles for SEI formation) may be necessary, as well as equilibration of the cells to the faster cycling conditions. MAGE3, although performing at a lower capacity, shows a very stable performance over the entire cycling period.

Voltage profiles and dQ/dV plots of EoL 1 h and MAGE3 are given in Figure 6.13.

Figures 6.13(a) and (c) show the typical voltage profiles for graphite for the two formation cycles. The typical redox peaks already discussed in Section 6.5 also appear for the two formation cycles within the dQ/dV plots (Figures 6.13(b) and (d)). However, it is likely that more formation cycles are required as consistency in the charge profiles and redox peaks were not acquired before switching to the higher cycle rates.

At the higher cycle rates, the voltage profiles for both EoL 1 h (6.13(a)) and MAGE3 (6.13(b)) are heavily truncated. The distinct plateaus experienced in the formation cycles are not seen and the profiles contain a large slope. For both voltage profiles it appears the charge profiles cuts before the graphite reaches stage III.[24] This is also apparent in the dQ/dV plots (Figures 6.13(b) and (d)) where only one redox peak is present, caused by extreme concentration polarization due to slow Li^+ kinetics.

As no large differences in cycling can be seen within Figure 6.13, The reasoning for the differences in performance may again result from the properties of the graphite established from their origins. The smaller domain sizes typically associated with SG (MAGE3) allows for more Li^+ accessibility to the edge sites and therefore allows for more reversible cycling.[24,227] Whereas NG (recovered graphite) may accept more Li^+ within its domains but the slow kinetics over less area will lead to more side reactions like lithium plating, leading to irreversible loss.[226]

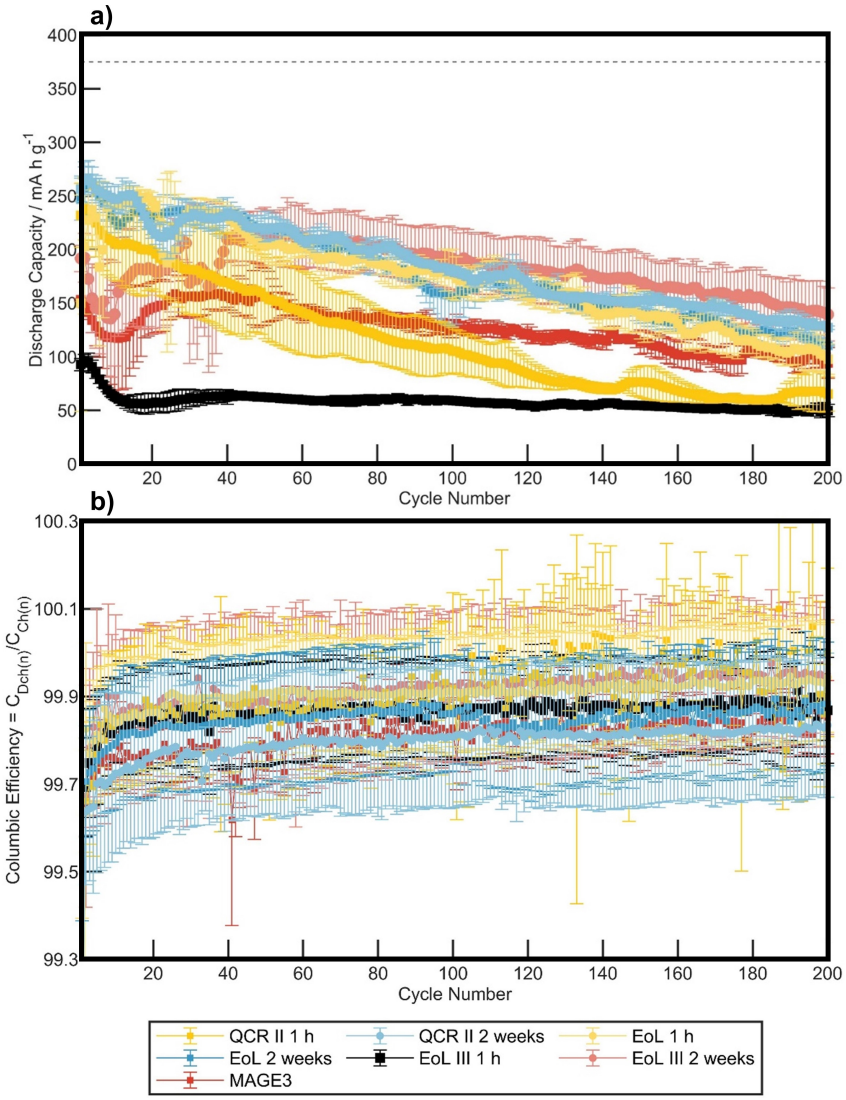


Fig. 6.12. *(a) Graphite discharge specific capacities plotted against cycle number for triplicate Li metal half-cells made from QCR II, EoL and EoL III recovered graphite as well as MAGE3.* $1\,\mathrm{h}$ *and 2 weeks refer to the time exposed to air before delamination. 200 asymmetrical cycles were conducted with a charge rate of* $C/2$ *(*$186\,\mathrm{mA\,g^{-1}}$*) and discharge of* $1C$ *(*$372\,\mathrm{mA\,g^{-1}}$*) after two initial formation cycles at* $C/20$ *(*$18.6\,\mathrm{mA\,g^{-1}}$*) that were omitted from the figure. (b) Columbic efficiency against cycle number for each recovered graphite and MAGE3. Each point is an average and the error bars consist of the* $95\,\%$ *confidence interval. Reproduced from Sargent et al.*[121] *with permission from the Royal Society of Chemistry.*

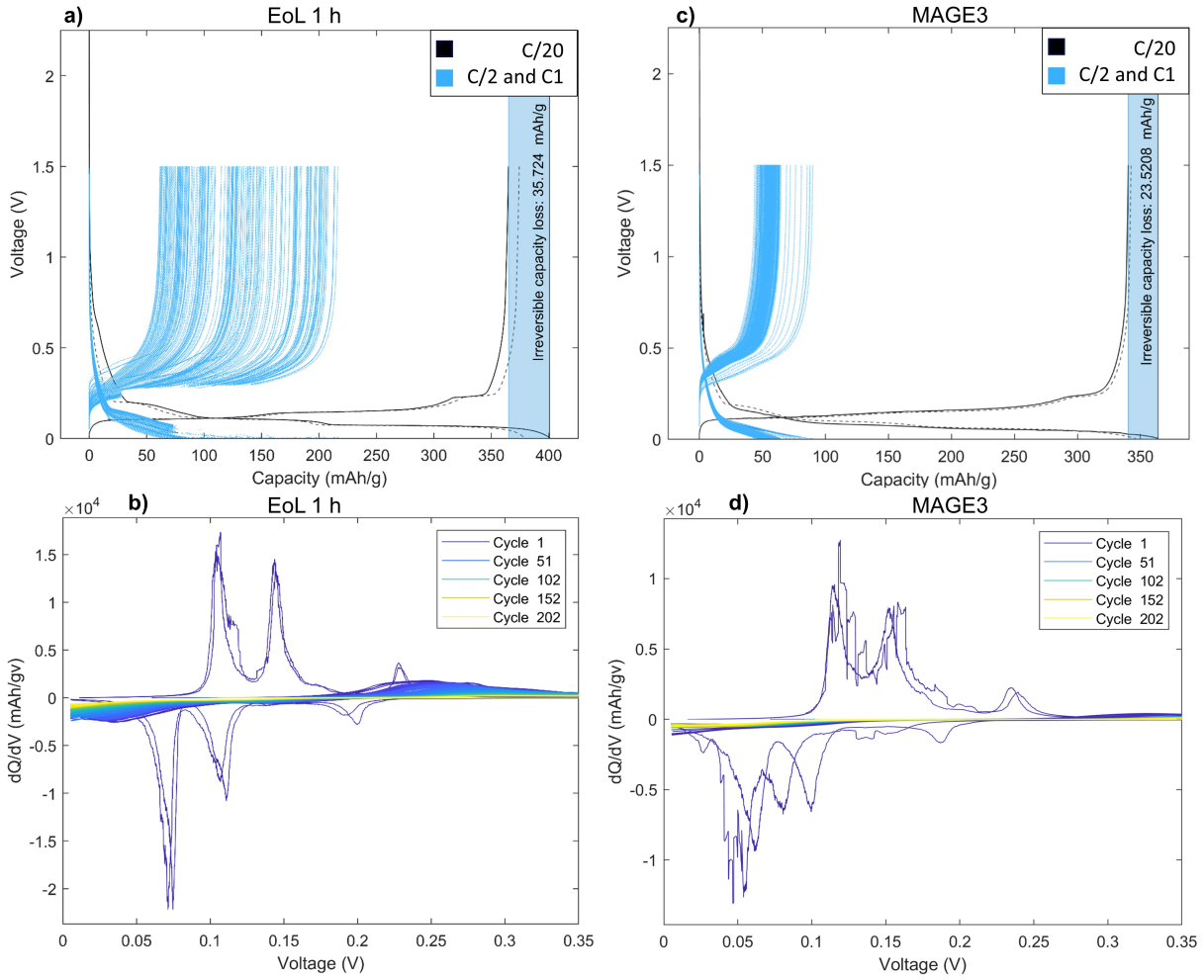


Fig. 6.13. *Capacity plotted against voltage for every cycle on (a) EoL* $1\,\mathrm{h}$ *(time exposed to air before delamination and annealing) and (c) MAGE3. The black line represents the first two cycles at* $C/20$ *(*$18.6\,\mathrm{mA\,g^{-1}}$*) and the coloured line represent the last 200 cycles conducted at a charge rate of* $C/2$ *(*$186\,\mathrm{mA\,g^{-1}}$*) and discharge of* $1C$ *(*$372\,\mathrm{mA\,g^{-1}}$*). The continuous line represents the first cycle of each cycle rate, the dashed lines represents the second and above cycles. Irreversible capacity is shown via a box on the right. dQ/dV plots for (b) EoL* $1\,\mathrm{h}$ *and (d) MAGE3 are also shown.*

6.8 | Chapter conclusion

The graphite obtained from EoL EV cells can be easily recast onto copper foil. The anode created from EoL 1 h performs well within a lithium ion half-cell, showing optimal graphite physical properties. However, a large first cycle capacity loss was experienced, likely caused by surface contamination, which would hinder the use within inventory limited full cells.

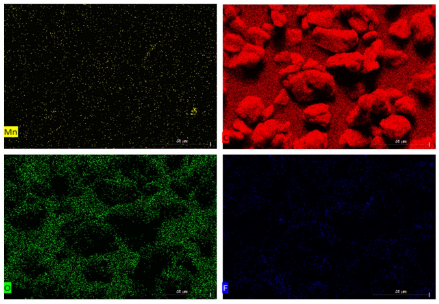
Annealing was a successful technique at removing the surface contamination as well as the PVDF binder, allowing for the subsequent use of the eco-friendlier and water-soluble CMC/SBR binder. Annealing was performed on all recovered active material to investigate the performance of each material in an electrochemical environment. The performance demonstrated by the reclaimed graphite materials was impressive, with consistent capacities closely approaching the theoretical limit. First cycle capacity losses also fell within the range of 6 %-9 %. This shows that EoL anodes can provide a source for high performing battery-grade graphite, helping secure future supplies of this critical raw material and helping to alleviate concerns over future accumulation of battery waste.

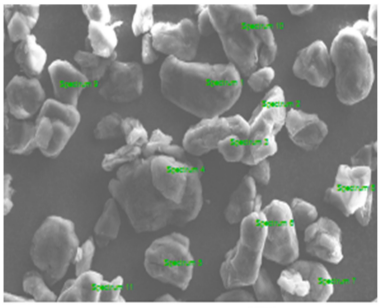
Further testing was conducted at higher cycle rates to 200 cycles. The recovered graphite again performed at higher capacities than MAGE3, a commercial battery-grade graphite standard. However, the capacity of the recovered graphite significantly dropped on extended cycling due to a varying CE. This drop was consistent for all recovered graphite and may have likely been caused by the differences in morphology of the recovered graphite to MAGE3.

Within this chapter, the graphite recovered via water delamination, after annealing, performs well within a half cell environment. Further work is required to prove that the reclaimed graphite would perform similarly within a commercial environment. This would involve full cell analysis compared to current commercial cathodes.

6.9 | Chapter appendix

EoL III 1 hour annealed



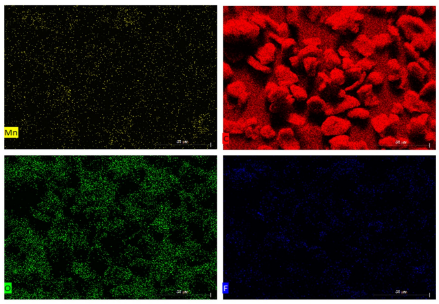


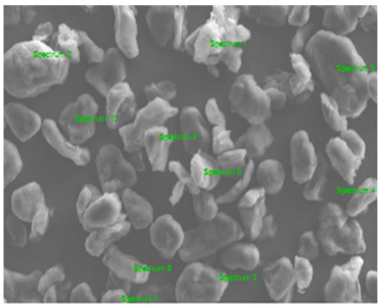
Name	Date	Time	HV [kV]	Mag
Ch 1	01/02/2023	18:11:33	20.0 keV	1500x

Normalized mass concentration [%]

Spectrum	Carbon	Oxygen	Fluorine	Manganese
Spectrum 1	97.83	2.17		
Spectrum 2	74.27	14.58	7.69	3.46
Spectrum 3	94.68	3.30	2.03	
Spectrum 4	97.53	2.47		
Spectrum 5	95.19	2.89	1.92	
Spectrum 6	96.63	3.37		
Spectrum 7	96.04	3.96		
Spectrum 8	92.59	7.41		
Spectrum 9	93.93	2.83	3.23	
Spectrum 10	98.39	1.61		
Spectrum 11	96.31	3.69		
Mean	**93.94**	**4.39**	**3.72**	**3.46**
Sigma	**6.75**	**3.70**	**2.72**	**0.00**
SigmaMean	**2.04**	**1.12**	**0.82**	**0.00**

EoL III 2 weeks annealed





Name	Date	Time	HV [kV]	Mag
Ch 1	01/02/2023	18:51:40	20.0 keV	1500x

Normalized mass concentration [%]

Spectrum	Carbon	Oxygen	Fluorine	Manganese
Spectrum 1	92.63	6.74		0.64
Spectrum 2	94.77	4.34	0.90	
Spectrum 3	95.21	4.79		
Spectrum 4	96.07	3.93		
Spectrum 5	96.53	3.47		
Spectrum 6	92.84	7.16		
Spectrum 7	86.56	3.59	1.25	8.60
Spectrum 8	94.41	4.18		1.40
Spectrum 9	97.14	2.86		
Spectrum 10	96.69	3.31		
Mean	**94.28**	**4.44**	**1.07**	**3.55**
Sigma	**3.12**	**1.44**	**0.25**	**4.39**
SigmaMean	**0.99**	**0.45**	**0.08**	**1.39**

Fig. 6.14. *Elemental mappings were taken using a Zeiss EVO15 VP ESEM with an energy dispersive X-ray spectroscopy detector. 20 kV backscattered electron mode was used. EoL III after* $1\,\mathrm{h}$ *of air exposure before delamination followed by annealing at* $500\,^{\circ}\mathrm{C}$ *for* $1\,\mathrm{h}$ *is shown above and EoL III after 2 weeks of air exposure before delamination followed by the same annealing is shown below.*

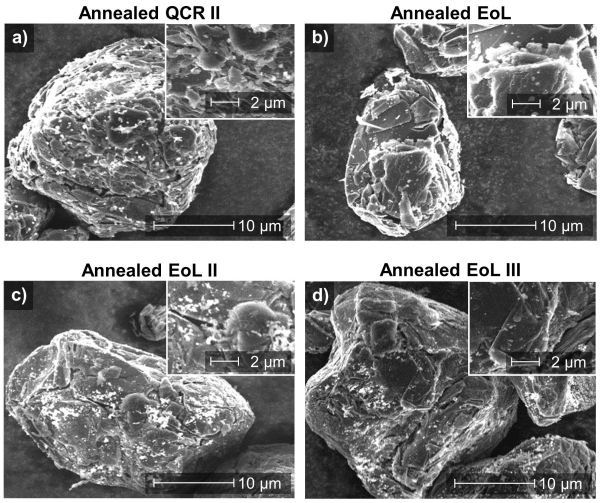


Fig. 6.15. *Large 5000x magnified SEM images with 12000x magnified SEM images in the top right of each. a) QCR II b) EoL c) EoL II d) EoL III delaminated after 2 weeks of air exposure and annealing to* $500\,^{\circ}\mathrm{C}$ *for* 1 h.

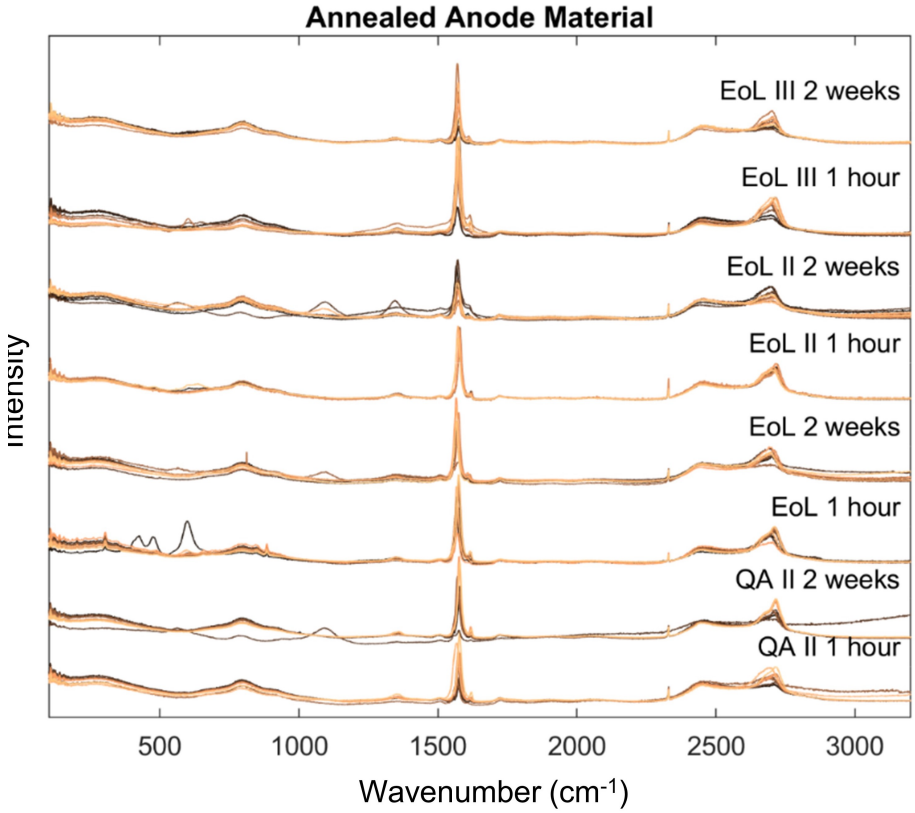


Fig. 6.16. *10 Raman spectra for each recovered graphite after annealing to* $500\,^{\circ}\mathrm{C}$ *for* 1 h. 1 h *and 2 weeks refers to the time exposed to air before water delamination.*

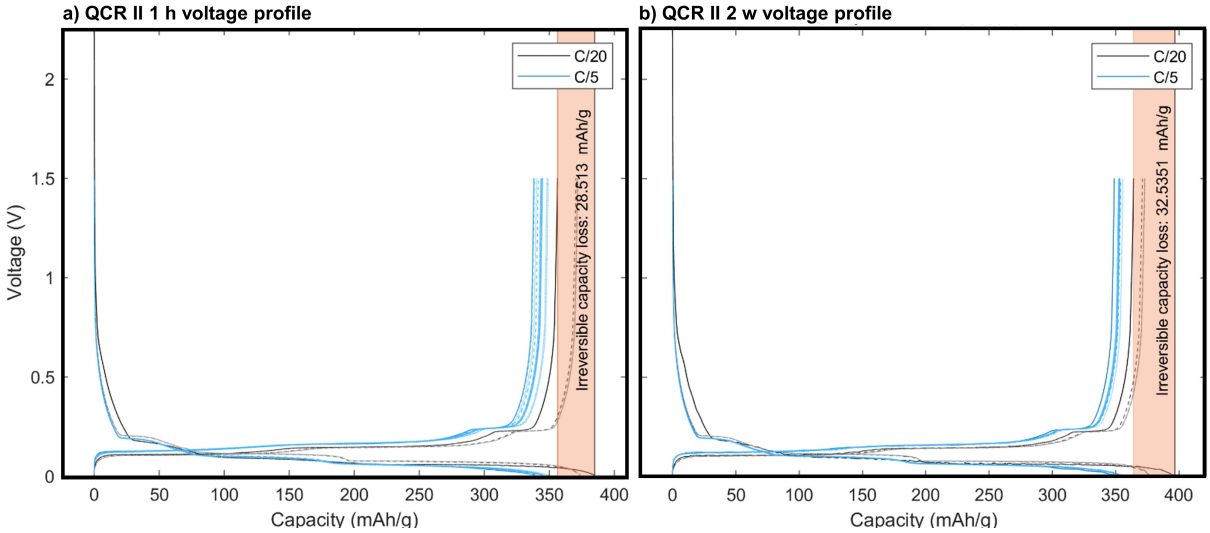


Fig. 6.17. *Voltage profiles of one lithium-ion half cell for both a) QCR II* 1 h *and b) QCR II 2 weeks. 20 cycles were conducted with the first 5 represented in black at C/20 and the following 15 in blue at C/5. The solid black line represents the first cycle, and the irreversible capacity is represented by the orange block.*

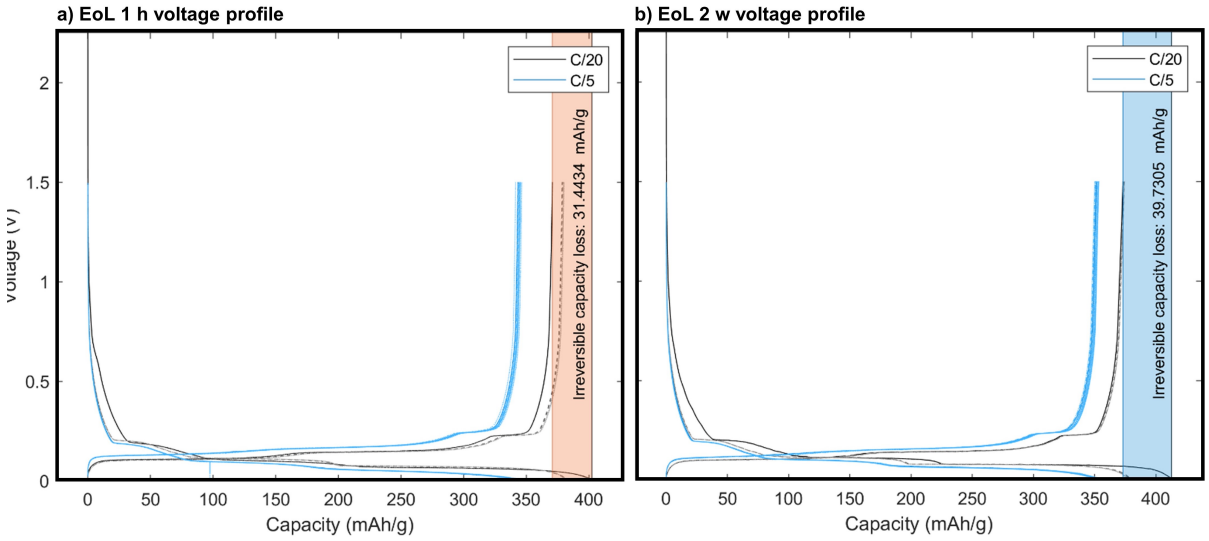


Fig. 6.18. *Voltage profiles of one lithium-ion half cell for both a) EoL* 1 h *and b) EoL 2 weeks. 20 cycles were conducted with the first 5 represented in black at C/20 and the following 15 in blue at C/5. The solid black line represents the first cycle, and the irreversible capacity is represented by the orange and blue block.*

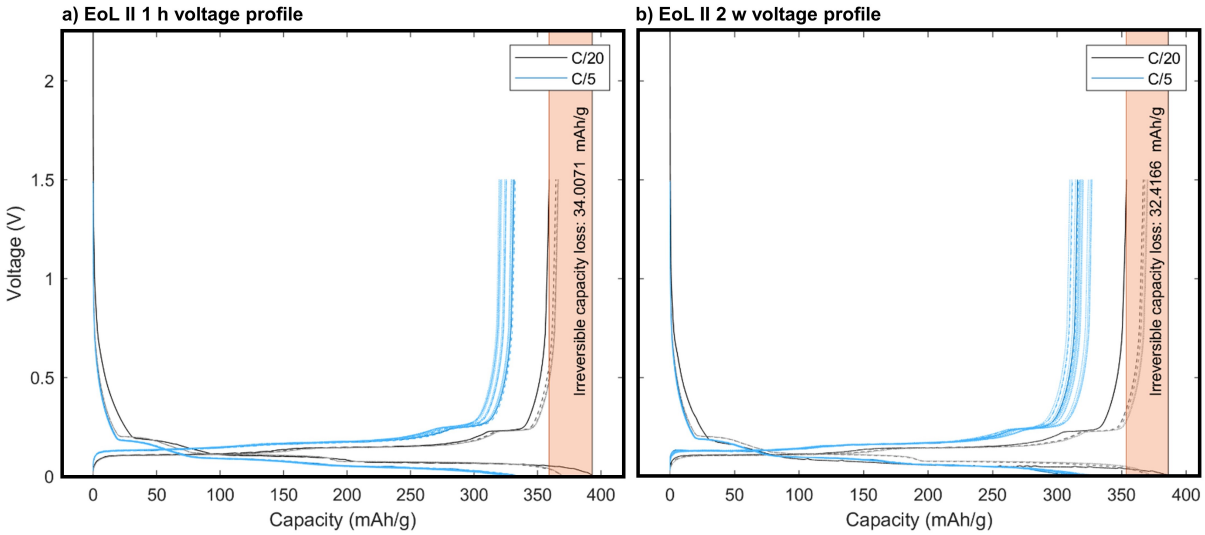


Fig. 6.19. *Voltage profiles of one lithium-ion half cell for both a) EoL II* 1 h *and b) EoL II 2 weeks. 20 cycles were conducted with the first 5 represented in black at C/20 and the following 15 in blue at C/5. The solid black line represents the first cycle, and the irreversible capacity is represented by the orange block.*

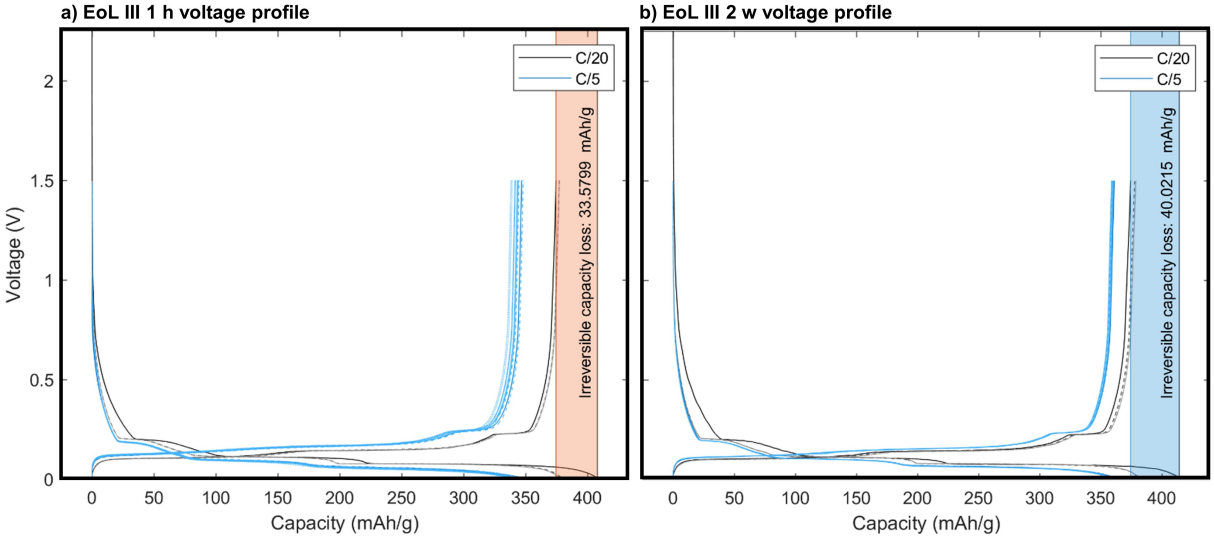


Fig. 6.20. *Voltage profiles of one lithium-ion half cell for both a) EoL III* 1 h *and b) EoL III 2 weeks. 20 cycles were conducted with the first 5 represented in black at C/20 and the following 15 in blue at C/5. The solid black line represents the first cycle, and the irreversible capacity is represented by the orange block.*

CHAPTER 7

Acid delamination

7.1 | Introduction

The previous chapters used water delamination to extract graphite from EV LiB anodes that could be seen in a recycling stream set up in the near future. These chapters were successful in creating a rapid and cost-effective technique that would extract graphite that performed well under electrochemical testing.

An issue that aroses from the proposed technique is that the effectiveness of water delamination decreases with increased air exposure time, where delamination after 4 weeks either did not happen or required more than 2 h of water submersion. This does allow control over how the samples delaminates, but negatively puts pressure on industry to adopt very specific conditions. For instance, cells must be dismantled within an inert atmosphere and washed with anhydrous DMC in order for the technique to work. Current industrial techniques typically involve shredding batteries so adoption to using manual teardowns may be difficult; especially if conducted within an inert atmosphere.[230] If industry were to switch to a direct recycling method it may be more likely to dismantle the cell in air, using isopropyl alcohol (C_3H_8O) to wash off the electrolyte. Therefore, a technique that can delaminate anodes that have been exposed to air for a prolonged period of time would be beneficial.

When an anode is exposed to air, lithiated graphite and SEI components oxidise and hydrolyse in the air, forming components like $LiOH$, Li_2O and Li_2CO_3. These salts, plus

other surface contaminates like manganese salts, LiF, as well as the copper itself, may react with acids to again create local areas of changing temperature and pressure to mechanically cleave the active material from the anode.

Within this chapter, various reagents will be examined to delaminate an EoL anode that has been exposed to air for more than a year.

7.2 | Chapter Aims

Within this chapter, a rapid and cost effective method for delaminating anodes that have been exposed to air for over a year will be investigated. This technique should produce active material that will perform well within an electrochemical environment so that a closed loop battery-grade graphite economy can be established.

7.3 | Experimental

7.3.1 Acid delamination procedure and ICP analysis

LabEoL refers to DMC washed EoL anodes that has been exposed to air for more than a year.

Around $2\,$g of LabEoL was submerged in $80\,$mL of either 0.5 M nitric (diluted $70\,\%$, Sigma Aldrich), sulfuric (diluted $95\,\%$-$97\,\%$, Sigma Aldrich), or hydrochloric acid (diluted $37\,\%$, Sigma Aldrich) with gentle agitation. Within $3\,$min, all active materials had delaminated from the current collector. Both active material and current collector were extracted and washed with DI water over a Buchner funnel.

ICP analysis was conducted on $10\,$mL filtered aliquots of each $20\,$mL delamination solutions of either nitric, sulfuric and hydrochloric acid used to delaminate around $0.35\,$g of LabEoL. Dilutions and measurements were the same as those described in Section 5.4.2.

7.3.2 Graphite characterisation

The collected active material was analysed using Raman and SEM. The techniques used were the same as described in Sections 5.4.5 and 5.4.7.

7.3.3 Electrochemical data collection

The collected anode materials were annealed to $500\,^{\circ}\mathrm{C}$ in air (using a ramp rate of $10\,^{\circ}\mathrm{C\,min^{-1}}$) before coating onto copper foil (MTI corporation, $9\,\mu\mathrm{m}$). Coating methods, coin cell construction and short term electrochemical testing procedures are the same as those described in Section 6.4.3. Electrode information for anodes used within this chapter are given in Table 7.1.

Table 7.1. *Averaged electrode information for each of the three lithium-ion half cells used for the electrochemical testing of each active material within this chapter. All active materials were annealed for* $1\,\mathrm{h}$ *at* $500\,^{\circ}\mathrm{C}$ *in air and casted using CMC/SBR as the binder.*

Graphite used	Active Mass Loading ($\mathrm{mg\,cm^{-2}}$)	Coating thickness (µm)	Coating Porosity (%)
H2O EoL 1 h	5.4(1)	33.3(6)	15.9(4)
H2SO4 LabEoL	9.07(11)	82.7(12)	42.38(86)
HNO3 LabEoL	4.40(10)	38.7(15)	39.4(17)
H2SO4 LabEoL	4.84(13)	56.7(32)	56.7(36)

7.4 | Delamination

Samples of EoL anode exposed to air for more than 1 year (LabEoL) were submerged in separate, gently agitated solutions of DI water as well as 0.5 M HCl, $\mathrm{HNO_3}$ and $\mathrm{H_2SO_4}$ solutions. Water was unable to delaminate the anode even after $2\,\mathrm{h}$ of submersion. The acids however, all delaminated the active material from the current collector within $3\,\mathrm{min}$ of submersion. Small effervescence was observed for each one, suggesting that like water delamination, the process occurs via mechanical cleavage caused by gas production.

ICP analysis was conducted on the delamination solutions collected after submersion of LabEoL anode. These are given in Figure 7.1.

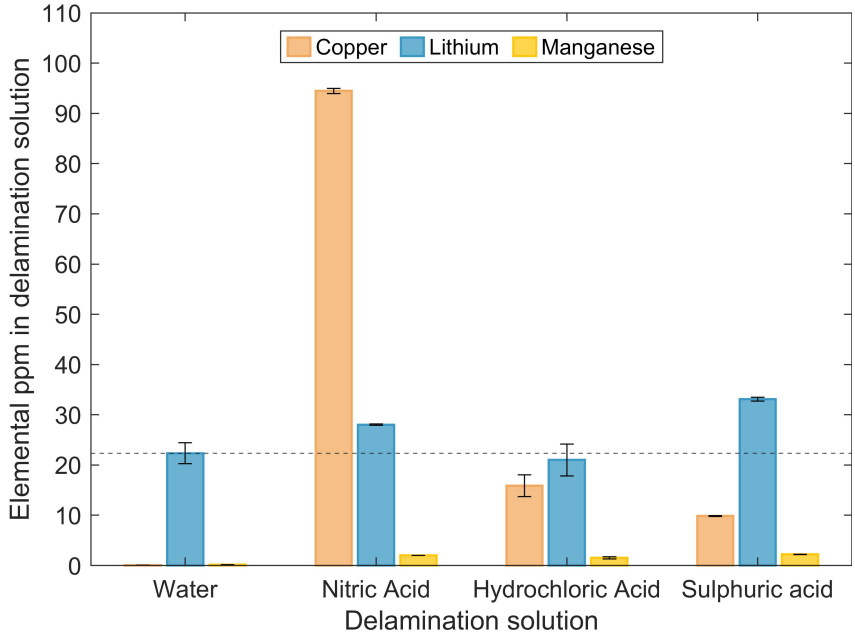


Fig. 7.1. *Copper, lithium and manganese concentrations within* 20 mL *of delamination solution after the submersion of LabEoL. Each anode was cut into a* 10 mm *disk weighing approximately* 0.35 g*. The* 327.393 nm*,* 610.365 nm *and* 257.610 nm *analytical lines were used for copper, lithium and manganese respectively. Error bars represent the standard error between three repeated measurements of the same solution.*

Submersion of LabEoL in water left around 22.4 ppm of lithium within the solution. This is slightly higher than that found during the previous water delamination study (Section 5.5) but did not lead to delamination. This is likely due to the exposure to air, leading to the formation of lithium salts which dissolve in the water but do not produce gas on contact, as discussed in Section 5.5. Water submersion also lead to a very low amount of Mn ($0.20(2)$ ppm) and Cu ($0.040(6)$ ppm) within the solution.

Acid solutions lead to similar, if not higher (for nitric and sulfuric acid) concentrations of lithium within the solutions. There was also an increase in manganese and copper concentrations, particularly for nitric acid which showed a copper concentration of around

94.5(3) ppm, suggesting etching of the current collector. There was also some effervescence observed. Some likely reactions are given below:

$$\mathrm{LiOH_{(s)}} + \text{Acid} \longrightarrow \text{Li Salt} + \mathrm{H_2O_{(l)}} \tag{7.1}$$

$$\mathrm{Li_2O_{(s)}} + \text{Acid} \longrightarrow \text{Li Salt} + \mathrm{H_2O_{(l)}} \tag{7.2}$$

$$\mathrm{LiCO_{3\,(s)}} + \text{Acid} \longrightarrow \text{Li Salt} + \mathrm{CO_{2\,(g)}} + \mathrm{H_2O_{(l)}} \tag{7.3}$$

$$\mathrm{LiF_{(s)}} + \text{Acid} \longrightarrow \text{Li Salt} + \mathrm{HF_{(aq)}} \tag{7.4}$$

Equation 7.3 would produce gasses, leading to delamination. This delamination may also be aided with simultaneous copper etching.

Manganese is typically not very soluble in acids, however, the lower the oxidation state, the more ionic the Mn−O bond is and the higher the dissolution kinetics are.[231,232] Therefore if it is assumed some manganese is present in a +2 oxidation state as proposed from the XPS study in Section 4.5.3, some manganese dissolution in all acids would be expected, as seen experimentally.

Copper is known to react with nitric acid via the following equations:

With dilute nitric acid:

$$3\,\mathrm{Cu_{(s)}} + 8\,\mathrm{HNO_{3\,(aq)}} \longrightarrow 3\,\mathrm{Cu(NO_3)_{2\,(aq)}} + 4\,\mathrm{H_2O_{(l)}} + 2\,\mathrm{NO_{(g)}} \tag{7.5}$$

With concentrated nitric acid:

$$\mathrm{Cu_{(s)}} + 4\,\mathrm{HNO_{3\,(aq)}} \longrightarrow \mathrm{Cu(NO_3)_{2\,(aq)}} + 2\,\mathrm{H_2O_{(l)}} + 2\,\mathrm{NO_{2\,(g)}} \tag{7.6}$$

This results in the high copper concentration after delamination in nitric acid. The nitric oxide gas produced will also aid in delamination. Copper does not react with sulfuric, nitric or hydrochloric acid via a displacement reaction due to the higher reduction potential of copper (Cu^{2+}/Cu, 0.34 V) compared to hydrogen ($2\,H^+/H_2$, 0.00 V). This poses a question as to why

copper content is found in both hydrochloric and sulfuric acid. As found within the SEM study in Section 4.5.2, copper dissolution is an ageing mechanism that coats the surface of the anode with trace amounts of copper. Copper dissolution leads to the formation of Cu^{2+} and Cu^{+} ions within the electrolyte which then appear to deposit on the surface of electrodes as CuO and $Cu(OH)_2$.[233] These products would react with acids under the typical neutralisation reaction, leading to the observation of copper dissolution within the acids.

All acids were successful in cleaving the active material from the current collector. The dissolution of copper and manganese also highlights a potential advantage to acid delamination, metal salt contamination can be removed at the same time as delamination. However, if the condition of the copper current collector is a concern, nitric acid should be avoided.

7.5 | Recovered active material

SEM images were taken of the recovered graphite obtained after acid delamination and are shown in Figure 7.2. Here, not only are no differences seen between each recovered active material, but the images are identical to those obtained within the water delamination study discussed in Section 5.8.3. As discussed before, no degradation is visible on the graphite particles, although a surface coating is visible. There is also a distinct difference between the two sides due to pooling of the PVDF binder during manufacturing.[201,202] EDX and XPS analysis was not conducted but would provide useful insight into the effectiveness of metal contamination removal, or show the presence of alternate salts formed on reaction to the acids.

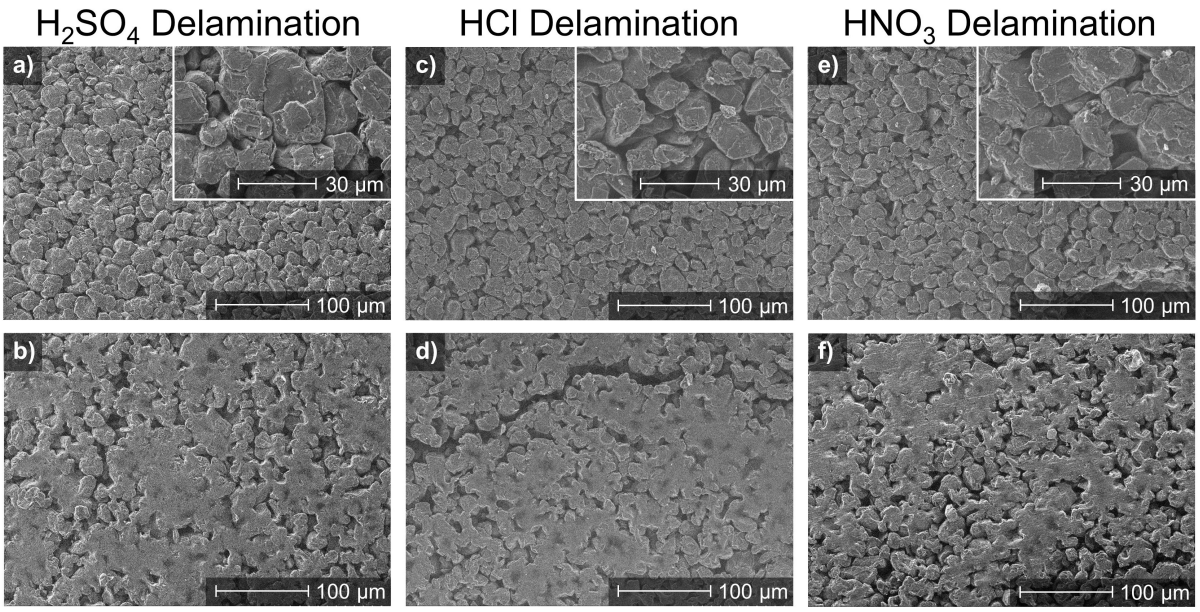


Fig. 7.2. *Large SEM images at 250x magnification with a 5000x magnified SEM image in the top right of each. The face that originally faced the separator and electrolyte for (a) LabEoL delaminated in* H_2SO_4 *(c) LabEoL delaminated in* HCl *and (e) LabEoL delaminated in* HNO_3 *make up the top row. The bottom row shows the face that originally faced the current collector for (b) LabEoL delaminated in* H_2SO_4 *(d) LabEoL delaminated in* HCl *and (f) LabEoL delaminated in* HNO_3*.*

Raman spectroscopy was conducted on the recovered active material and compared to that of water delaminated EoL 1 h. This is shown in Figure 7.3. As discussed in Section 5.8.1, impurity peaks from metal salts contaminating the surface appear at lower wavenumbers. This can be seen on the water delaminated sample but are absent on acid delaminated samples, indicating a removal of inorganic contamination from the surface. These were likely removed during the acid delamination step, given the increased concentration of manganese and copper within the delamination solutions examined using ICP (Section 7.3.1). The pitch coating peak at $800\,\mathrm{cm}^{-1}$ appears at similar intensities for all delaminations.

Distributions for LabEoL delaminated with HNO_3 and H_2SO_4 are almost identical to EoL delaminated after 1 h of air exposure, all showing a left skewed distribution centring around 0.49, 0.50 and 0.52 for EoL 1h, HNO_3 delaminated and H_2SO_4 delaminated LabEoL

respectively. HCl delaminated LabEoL shows a large spread with a higher I_D/I_G ratio (0.77). This value still falls within the range of mean I_D/I_G ratios collected after the water delamination of other anodes (0.49 to 1.48 in Section 5.8.1). Therefore, electrochemical performance may not be hindered.

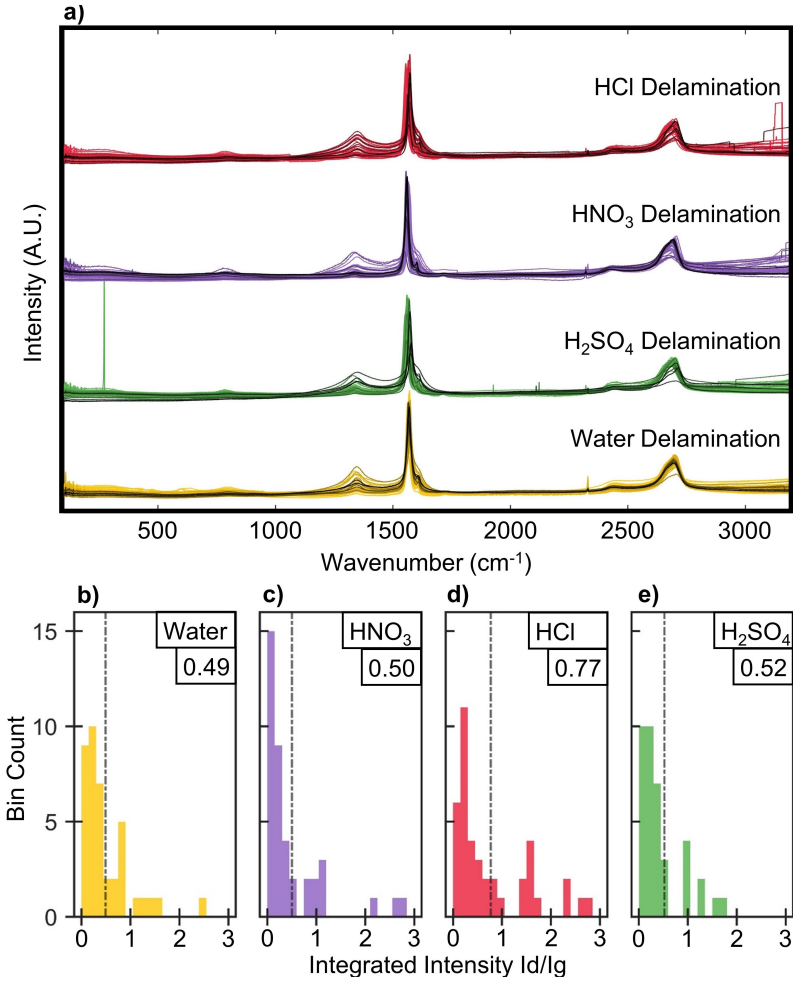


Fig. 7.3. *(a) 40 Raman scans taken on (from the top down) LabEoL delaminated using* HCl, HNO_3 *and H2SO4, EoL delaminated after* 1 h *of air exposure is also given. The calculated* I_D/I_G *ratios were used to create distributions of (b) EoL delaminated after* 1 h *of air exposure (c) LabEoL delaminated in HNO3 (d) LabEoL delaminated in* HCl *and (e) LabEoL delaminated in H2SO4. Peak-fittings and integrated intensities were calculated in MATLAB.*[125] *The mean* I_D/I_G *ratio is shown via the dash-dotted black line and is given in the top right corner of each distribution.*

7.6 | Electrochemical performance

Recovered active materials, via acid delamination, were annealed at 500 °C before coating onto copper foil to create a CMC/SBR bound anode. These anodes were tested within lithium-ion half cells. The cycling performance of each recovered graphite compared to EoL 1 h is shown in Figure 7.4, with quantitative data of losses given in Table 7.2. Voltage profiles and dQ/dV plots for each extracted LabEoL are given in Figure 7.5. Electrode information is given within the experimental (Section 7.3.3).

Table 7.2. *Numerical values for losses during electrochemical testing for lithium-ion half cell testing. Each sample was tested using three half cells, therefore each data point is an average with standard error between three cells.*

Anode material	First cycle charge capacity	First cell irreversible capacity loss		C/20 to C/5 capacity loss		Capacity loss after 20 cycles	
	$mA\,h\,g^{-1}$	$mA\,h\,g^{-1}$	% Loss	$mA\,h\,g^{-1}$	% Loss	$mA\,h\,g^{-1}$	% Loss
H2O	389(18)	29.0(52)	7.5(17)	41.5(19)	10.66(49)	39(16)	10.1(39)
H2SO4	389.7(60)	26.7(11)	6.8(2)	79.0(11)	20.27(28)	138(39)	35.4(96)
HNO3	385.7(11)	28.3(14)	7.35(35)	34.99(57)	9.07(15)	63.4(34)	16.43(92)
HCl	389.64(85)	25.67(59)	6.59(16)	26.64(23)	6.837(59)	51.6(51)	13.3(13)

LabEoL extracted via HCl and HNO_3 delamination performed at specific discharge capacities close to EoL 1 h. These capacities also fell within a similar range to those extracted via water delamination in Section 6.7.2. First cycle capacity losses also fall within the range set by the water delaminated samples. This performance was expected as the previous characterisation of the recovered graphite showed almost identical graphite particles, the only differences being that less metal contamination was observed. The metal contamination had little effect on the short-term electrochemical performance when water delaminated samples were tested but may have affected the long term cycling. Further studies into the long term performance of these acid delaminated samples would determine whether the

drop in performance experienced for the water delaminated samples (in Section 6.7.3) was due to metal contamination or just the morphology of the NG.

Although LabEoL extracted via H_2SO_4 has a first cycle capacity loss similar to those extracted by other acids, the first cycle has a large overpotential on both the charge and discharge. This can be seen in Figure 7.5 which also shows voltage profiles and dQ/dV plots for the other acid delaminated samples. This may be an indication of poor SEI formation or large impedance caused by the anode itself. The following formation cycles show no shifted peaks but all peaks are of lower intensity compared to HNO_3 and HCl. This may indicate a loss of connection of graphite particles, leading to the reduced capacity and overpotential increase at higher cycle rates. To determine whether the loss in capacity is due to poor anode coating causing a loss of connectivity, or if contaminants have led to parasitic reactions, a new anode coating should be fabricated and tested using the same recovered graphite.

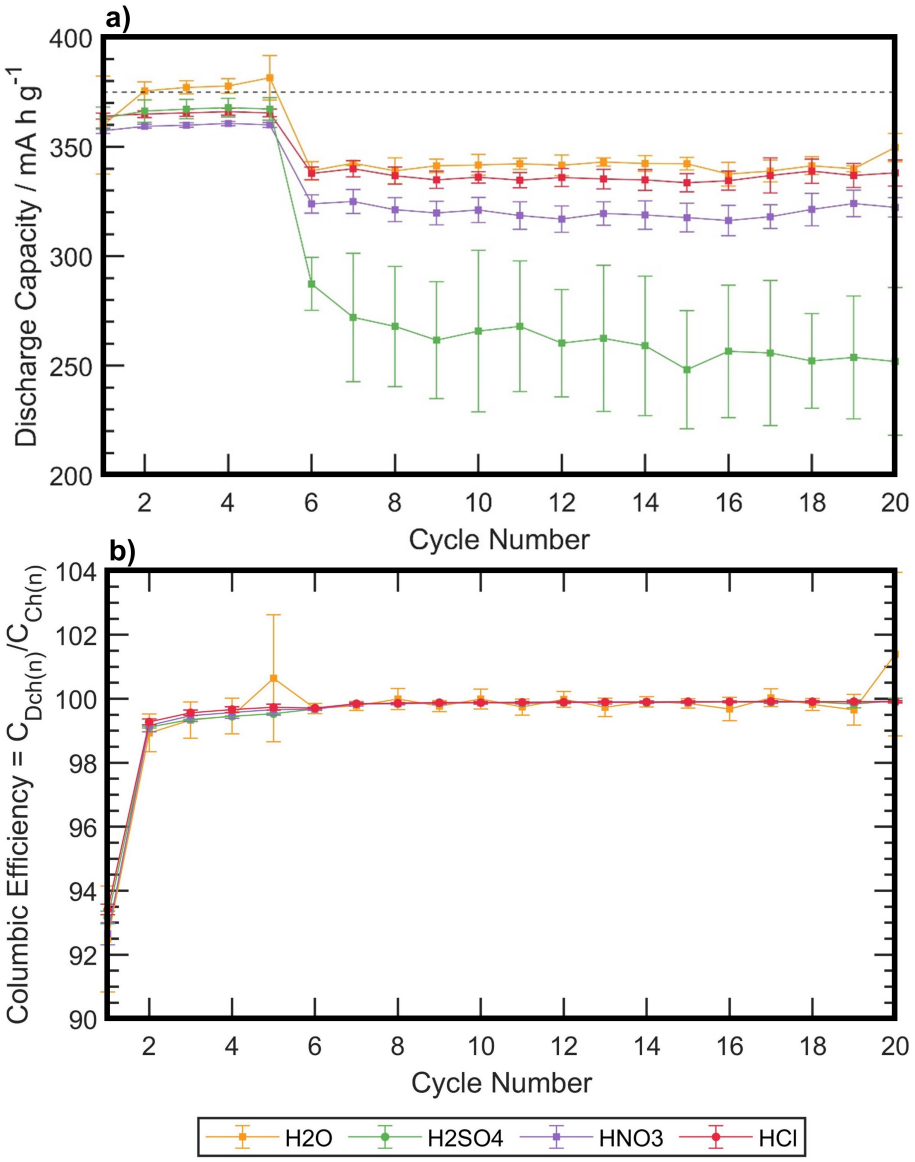


Fig. 7.4. *(a) Graphite discharge specific capacities plotted against cycle number for Li metal half-cells (using graphite obtained after acid delamination and subsequent annealing). Each data point represents the average of measurements made from three half cells. The first 5 cycles were run at* $C/20$ *(*$18.6\,\mathrm{mA\,g^{-1}}$*) then the remaining 15 were run at* $C/5$ *(*$74.4\,\mathrm{mA\,g^{-1}}$*) using* $372\,\mathrm{mA\,h\,g^{-1}}$ *as the theoretical capacity. The grey dotted line represents the theoretical capacity. (b) Columbic efficiency against cycle number for each obtained graphite and MAGE3. Each point is an average made up of three half cells and the error bars consist of the* $95\,\%$ *confidence interval.*

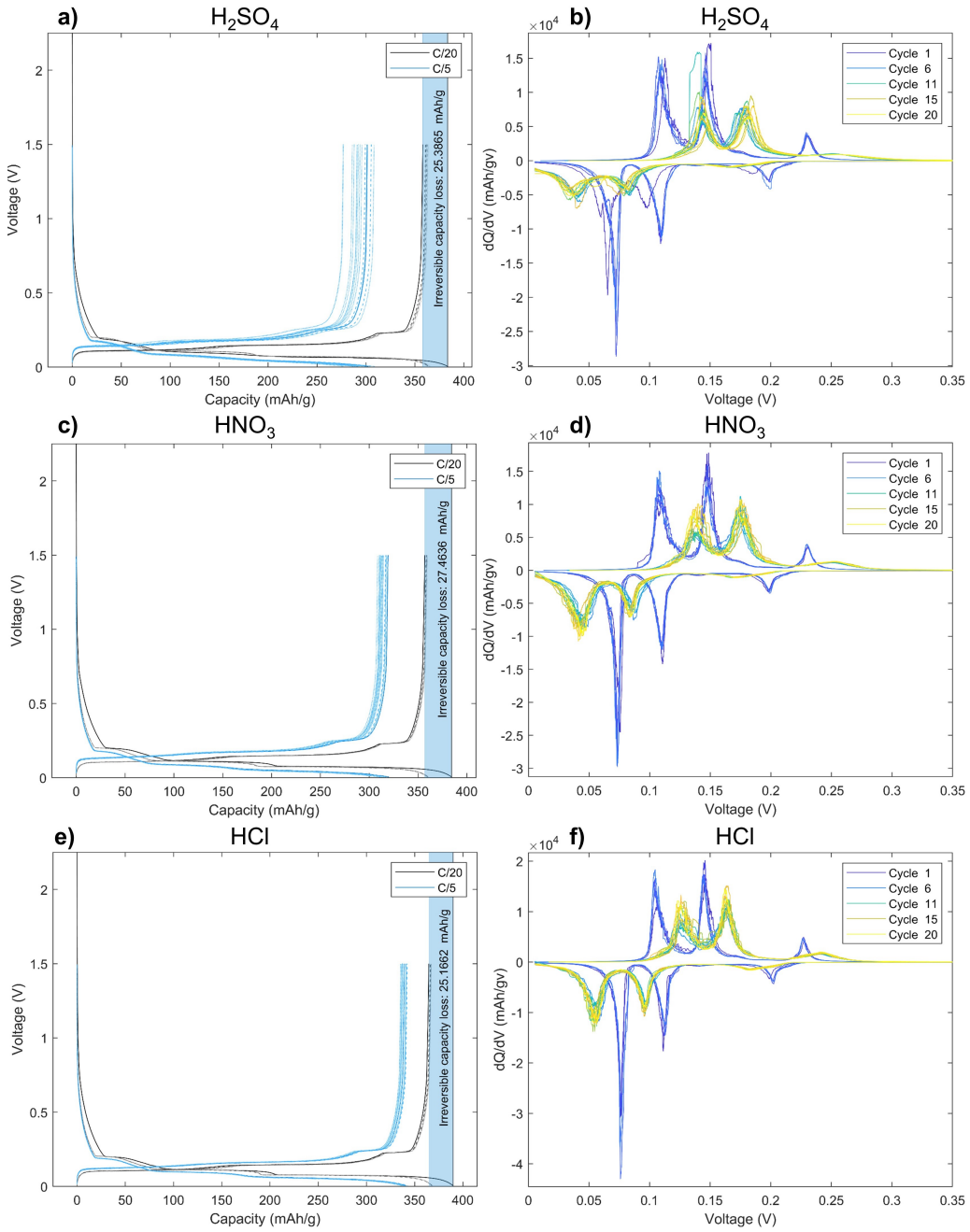


Fig. 7.5. *Capacity plotted against voltage for every cycle on (a)* H_2SO_4*, (c)* HNO_3 *and (e)* H_2SO_4 *delaminated LabEoL. The black line represents the first five cycles at C/20 (18.6* mAg^{-1}*) and the coloured line represent the last 15 cycles conducted at C/5 (74.4* mAg^{-1}*). The continuous line represents the first cycle of each cycle rate, the dashed lines represent the second and above cycles. Irreversible capacity is shown via a box on the right. The dQ/dV plots for (b)* H_2SO_4*, (d)* HNO_3 *and (f)* H_2SO_4 *delaminated LabEoL are also given.*

7.7 | Chapter conclusion

In this chapter, an alternative delamination technique was explored to extract graphite from EoL anodes that had been exposed to air for an extended period of time. The motivation for this exploration was the limitation observed in the effectiveness of water delamination with air exposure time, necessitating specific conditions for successful application. Acid delamination emerged as a promising method, not only overcoming the challenges associated with prolonged air exposure, but also removing metal salt contamination from the surface of the anodes.

The observed effervescence during acid delamination suggested a mechanism similar to water delamination, involving mechanical cleavage induced by heat and gas production. ICP analysis revealed varying concentrations of copper, lithium, and manganese, suggesting that the process may be more complicated than water delamination and the composition of the gas may vary. For instance, the reaction of nitric acid and copper will produce nitrous oxide.

Characterisation of the recovered active material through SEM and Raman spectroscopy indicated no significant differences compared to water delamination. However, acid delamination demonstrated enhanced cleaning of inorganic contamination from the surface, as evidenced by the absence of impurity peaks in Raman spectra.

Electrochemical testing of the recovered active materials showed promising performance. LabEoL extracted via HCl and HNO_3 delamination exhibited discharge capacities close to those of water delamination, suggesting that metal contamination had minimal impact on short-term electrochemical performance.

Overall, this chapter highlights an alternate method for the recycling of graphite via a direct recycling route. With acid delamination, there is no need for dismantling and storage within an inert atmosphere and it provides a rapid method for both extracting and rejuvenating

the graphite. All acids worked well, however if the complete preservation of the copper current collector is a requirement, nitric acid should not be used. A disadvantage to this technique compared to water delamination is the use of acids and subsequent treatment of the associated waste.

CHAPTER 8

Colloidal silica delamination

8.1 | Introduction

With a theoretical capacity of $4200\,\mathrm{mA\,h\,g^{-1}}$ and a relatively high abundance, silicon is considered a promising future anode material. However, the $300\,\%$ volume expansion experienced during lithiation caused by the alloying of lithium with the silicon to create a final formula of $Li_{22}Si_5$, causes cracking and pulverisation of the anode during each cell discharge. This causes a constant loss of lithium inventory and increased resistance via the continual production of an SEI layer on the freshly exposed surface as well as a loss of active material via disconnections due to this pulverisation. The low electronic conductivity and diffusion coefficient of lithium ions also results in purely silicon anodes finding little commercial success.[234–236]

Silica (SiO_2), silicon monoxide (SiO) and silicon sub-oxide (SiO_x) are all also electrochemically active. Upon lithiation: Li_xSi, Li_4SiO_4 and Li_2O form, with the latter two suppressing the volume expansion. Instead of $300\,\%$, SiO increases by $\sim 150\,\%$ and SiO_2 increases by $\sim 100\,\%$. SiO_x will expand to a percentage between these two values. Theoretical capacities vary from $1965\,\mathrm{mA\,h\,g^{-1}}$ for SiO_2 to $2680\,\mathrm{mA\,h\,g^{-1}}$ for SiO. Even though these capacities are less, the lower volume expansions make these materials more likely to be useful as anode materials. An anode of pure silicon oxides has yet to be made, which is due to the low electrical conductivity (caused by the strong ionic Si-O bonds), and low coulombic

efficiency caused by the volume expansion.[237] However, silicon and silicon sub-oxide blend with graphite make up the third generation of commercialised EV LiB anodes already on the road.[238] 5 % silicon is added to the carbon anodes of the Panasonic cells used in the Tesla X EV.[238,239]

Blends with graphite have been proven to be a successful first step into the adoption of silicon; where the graphite provides a buffer to the volume expansion, provides electrical conductivity and aids in stabilising SEI formation.[24,240] The ratio of C/Si balances capacity versus cycle life, with the more silicon added giving a higher capacity but a lower cycle life.[240] A ratio of 1:0.2 of C/Si was found to perform well with decent coulombic efficiency by *Ren et al.*[241].

Academic literature into the development of silicon anodes has seen a large uptake; with developments into silicon morphology, electrode engineering and novel binders in order to improve CE.[242] Some of these developments include silicon quantum dots anchored on graphene,[243] silicon nanotubes within carbon nanotubes,[244] and silicon nanoparticles encapsulated by amorphous titanium oxide TiO_2 formed via a sol-gel method[245]. Although very interesting and providing a vast improvement to CE whilst providing very high capacity, the practicality of applying these techniques on a commercial scale is questionable, due to the high cost, difficult implementation and lack of long term testing. Another issue arises as whilst silicon is one of the most abundant elements on earth, the use of metallic silicon within the steel, glass, solar panels, electronics and now batteries industry has caused the EU to categorise it as a critical raw material.[63]

Silica is very abundant, one of the main constituent of sand.[246] Also under certain conditions, such as after high energy mechanical milling, it has proven to be electrochemically active.[246] The amorphization or nano-sizing of silica particles within a blend is required for good performance due to its stability as an oxide.[246,247] The strong $Si{-}O$ bond leads to high first cycle capacity loss and low electrical conductivity, and if present as large particles,

leads to complete inactivity within a LiB.[248] If conditions are correct, during the first cycle the following conversions will occur:[247–249]

$$SiO_2 + 4\,Li^+ + 4\,e^- \longrightarrow 2\,Li_2O + Si \tag{8.1}$$

$$2\,SiO_2 + 4\,Li^+ + 4\,e^- \longrightarrow Li_4SiO_4 + Si \tag{8.2}$$

$$5\,SiO_2 + 4\,Li^+ + 4\,e^- \rightleftharpoons {}_2Li_2Si_2O_5 + Si \tag{8.3}$$

$$Si + XLi^+ + Xe^- \rightleftharpoons Li_xSi \tag{8.4}$$

Where Equations 8.1 and 8.2 occur at around $0.25\,V$ and are irreversible, leading to capacity loss.[249] These irreversible reactions lead to the *in-situ* formation of electrochemically reversable Si, therefore making these reactions a necessity.[249] The formed Si is then de/lithiated in further cycles via Equation 8.4.[247,249] The theoretical capacity of silica can be calculated to be $1965\,mA\,h\,g^{-1}$, if $Li_{22}Si$ is considered as the final product. However, due to Equations 8.1 and 8.2 and other inevitable irreversible reactions, capacities this high has not been seen within the literature.[246–249]

Silica utilised in anode research has come from a number of sources including quartz, rice husks and geothermal sludge.[237] The mechanics of water delamination, however, have also revealed a promising new potential source: colloidal silica solutions. Colloidal silica is a stable diffusion of silica particles within an aqueous medium.[250,251] A silica colloid can be made by controlled precipitation of silica using sodium silicate and sulfuric acid as well as other methods like milling and peptization of silica powder.[250,251] Colloidal silica allows for the suspension of nanoparticles of controllable sizes typically below $100\,nm$. Colloidal silica is used for various applications like rheological modifiers, fillers and additives in paints, coatings and additives.[250,251] Aggregation of silica particles can be caused by increasing the pH.[250] As water delamination increases the pH, if conducted in colloidal silica, nano silica particles may precipitate and coat the recovered active material. Not only recovering graphite

to sustain a circular economy but up-scaling the anode material to suit the ever-developing chemistry of LiBs.

Within this chapter, delamination of EoL anode will be conducted in colloidal silica solution in order to coat the active material in nano sized silica particles. The collected active material will be electrochemically tested in order to determine any benefits.

8.2 | Chapter aim

Water delamination has proven to be an effective and quick method for obtaining graphite from gen-1 LiBs. However, current-generation batteries use Si/C blends, therefore even though battery-grade graphite can be obtained, this may not have adequate economical value for adoption. Therefore, an attempt to improve the recovered active material by the addition of nanoparticulate silica will be made.

Delamination within colloidal silica will be used to both recover the active material and up-scale it within a single step.

Within this chapter, the effectiveness of delamination and the electrochemical performance of colloidal silica obtained graphite will be analysed. Changes to the delamination procedure will be investigated in order to improve electrochemical performance.

8.3 | Experimental

8.3.1 Colloidal silica delamination procedure

EoL anode was stored within an argon glovebox until required. Once required, the anode was washed in DMC via the process given in Section 4.4.1. All delaminations took place just after 1 h or air exposure.

Delamination of around 2 g of EoL anode were conducted in lightly agitated 80 mL solutions. Five solutions were used: 100 % colloidal silica (41.4 g of silica), 50 % colloidal silica (20.7 g of silica), 20 % colloidal silica (8.3 g of silica), 5 % colloidal silica (2.1 g of silica) and 1 % colloidal silica (0.4 g of silica), where the 100 % colloidal silica consisted of LUDOX® AS-40 colloidal silica (40 wt.% silica suspension in water). The other solutions consisted of the same solution but diluted to 50 %, 20 %, 5 % and 1 % with DI water.

Active material was collected and dried, collected copper current collector was washed and dried.

8.3.2 Graphite treatment

EoL active material collected via the delamination using 20 % colloidal silica was either annealed or broken apart via ball milling. Annealing followed a similar procedure as that in previous chapters: annealing to 500 °C for 1 h using a 10 °C min^{-1} ramp rate. Milling was conducted using a Fritsch pulverisette 7 planetary ball mill with 14 zirconia ball bearings and span at 600 rpm for 15 min.

8.3.3 Graphite characterisation

Active material was characterised with TGA using the same technique as that described in Section 6.4.1.

SEM images were collected using a Hitachi tabletop TM4000Plus under similar conditions as described in Section 5.4.7, however, using a high sensitivity four segment BSE detector.

8.3.4 Electrochemical data collection

Coating methods, coin cell construction and short term electrochemical testing procedures are the same as those described in Section 6.4.3. All anodes were casted with NMP,

except annealed EoL delaminated in 20 % colloidal silica which used water, CMC and SBR. Electrode information for anodes used within this chapter are given in Table 8.1.

Table 8.1. *Averaged electrode information for each of the three lithium-ion half cells used for the electrochemical testing of each active material within this chapter.*

Graphite used	Active Mass Loading (mg cm^{-2})	Coating thickness (µm)	Coating Porosity (%)
EoL 0 % SiO_2	5.4(1)	33.3(6)	15.9(4)
EoL 1 % SiO_2	3.23(21)	120.0(10)	63.84(54)
EoL 5 % SiO_2	2.01(33)	83.0(10)	67.55(82)
EoL 20 % SiO_2	2.83(24)	64.0(10)	40.31(63)
EoL 50 % SiO_2	1.81(37)	70.0(10)	63.60(92)
EoL 100 % SiO_2	2.17(31)	95.0(10)	67.77(72)
EoL 20 % SiO_2 2% CB	1.95(34)	54.0(10)	47.82(89)
EoL 20 % SiO_2 Annealed	5.46(12)	70.0(10)	59.24(85)
EoL 20 % SiO_2 BM	7.079(94)	88.0(10)	61.29(70)

8.4 | Colloidal silica delamination

8.4.1 Delamination

Delamination of EoL after 1 h of air exposure was successful in 100 % colloidal silica solution (40 wt.% silica). The rate of delamination was noticeably longer with the production of larger bubbles; evidently the viscosity of the solution slightly hindered the delamination process. Delamination was also conducted in 50 %, 20 %, 5 % and 1 % colloidal silica in water, all of which showed successful delamination of the graphite.

Each sample was left in the delamination solution for 1 h before removal, and the anode material exhibited a noticeable reflective quality compared to those extracted via water delamination.

8.4.2 TGA of recovered material

Table 8.2 shows the amount of PVDF and active material within each collected anode material from the colloidal silica delamination of EoL exposed to air for 1 h.

Table 8.2. *Percentage masses of PVDF compared to active material within a sample of obtained anode material. Values were calculated from TGA plots given in Figure 8.6 within the appendix.*

Sample	PVDF	Active Material
EoL	4.11	95.89
EoL 1 % SiO2	4.79	95.21
EoL 5 % SiO2	4.63	95.37
EoL 20 % SiO2	4.02	95.98
EoL 50 % SiO2	4.33	95.67
EoL 100 % SiO2	4.36	95.64

It was expected that the higher concentration of colloidal silica would increase the amount of silica deposited on the anode material, therefore leading to a reduction of the percentage of PVDF. Via TGA there was no consistency in the variation of mass percentage between different concentrations of colloidal silica. There are a number of reasons this may have happened: either the amount of silica added is very small and is not detectable within the error of the TGA or the amount of silica deposited on the material is not controlled by the concentration of the delamination solution; perhaps time and temperature have a greater effect.

8.4.3 Electrochemical performance

As a proof of concept and to reduce the number of steps to reach a recycled battery, colloidal silica delaminated anode materials were recast onto copper and the performance of these newly formed anodes were tested electrochemically. The voltage profiles for the first five cycle conducted at $10\,\mathrm{mA\,g^{-1}}$ are shown in Figure 8.1. EoL delaminated in water is used as a comparison. Capacities and capacity losses experienced for the first five cycles at $10\,\mathrm{mA\,g^{-1}}$ and fifteen cycles at $75\,\mathrm{mA\,g^{-1}}$ are given in Table 8.3. Electrode information is given in the experimental section in Table 8.1.

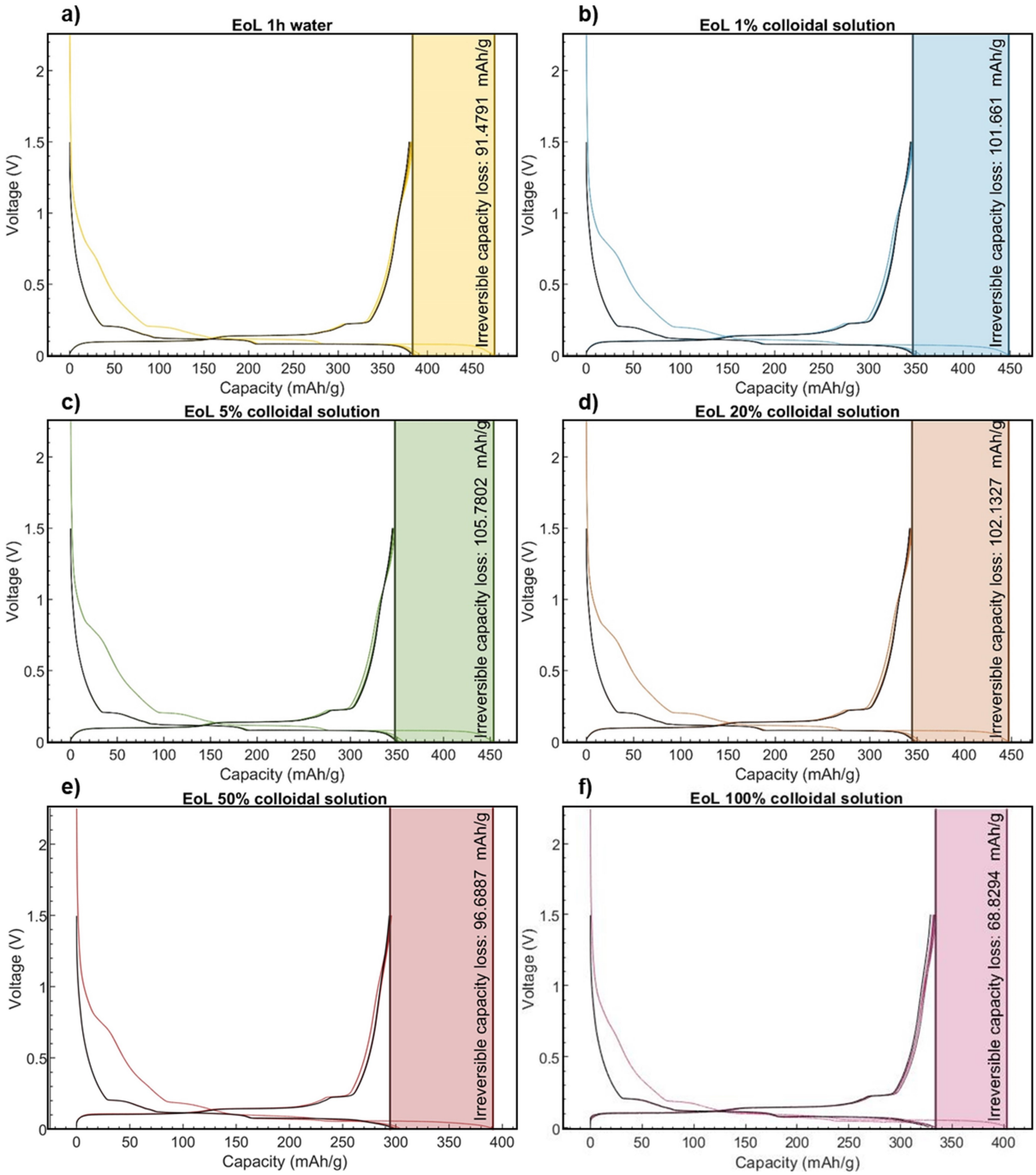


Fig. 8.1. *Voltage profiles of the first five cycles of (a) water delaminated EoL,(b) EoL delaminated in* $1\,\%$ *colloidal silica solution,(c) EoL delaminated in* $5\,\%$ *colloidal silica solution,(d) EoL delaminated in* $20\,\%$ *colloidal silica solution,(e) EoL delaminated in* $50\,\%$ *colloidal silica solution and (f) EoL delaminated in* $100\,\%$ *colloidal silica solution. All were run at* $10\,\mathrm{mA\,g^{-1}}$ *and represent the best performance of three half cells.*

Table 8.3. *Numerical values for losses during electrochemical testing for lithium-ion half cell testing. Each sample was tested using three half cells; therefore each data point is an average with its standard error between three cells.*

Anode material	First cycle charge capacity mA h g^{-1}	First cycle discharge capacity mA h g^{-1}	First cycle irreversible capacity loss mA h g^{-1}	First cycle irreversible capacity loss % loss	Discharge capacity after 5 cycles mA h g^{-1}	Discharge capacity after 20 cycles mA h g^{-1}
EoL 0 % SiO2	469.8(97)	381.2(45)	88.6(52)	18.86(72)	378.4(29)	352.4(52)
EoL 1 % SiO2	427.0(19)	328.5(21)	98.5(13)	23.06(30)	326.0(21)	305.7(51)
EoL 5 % SiO2	420(22)	322(16)	98.1(59)	23.33(22)	320(16)	302(15)
EoL 20 % SiO2	445.9(23)	343.1(28)	102.8(11)	23.06(30)	340.4(28)	319.2(48)
EoL 50 % SiO2	430.0(10)	324.59(95)	105.31(95)	24.50(20)	323.98(68)	205(16)
EoL 100 % SiO2	384.38(46)	318.6(15)	65.8(11)	17.11(31)	314.5(27)	247(17)

Electrochemical performance for all anodes collected via colloidal silica delamination were worse than that obtained after water delamination on all counts. For EoL delaminated in 1 %, 5 %, 20 % and 50 % colloidal silica, first cycle irreversible loss had risen from around 18 % to around 23 %. Specific capacities obtained after five formation cycles at 10 mA g^{-1} were consistently lower for the colloidal silica obtained EoL. This was further exaggerated after fifteen cycles at 75 mA g^{-1}. The reduced performance may be highlighted by the much larger electrolyte reduction peak starting at 0.8 V. The shape of the voltage profiles after the first cycle also resembles more the cycling of graphite rather than a Si/C blend. A sloped profile would be expected for an Si/C blend.[236] Also expected for the first cycle of a Si/C blend is a small plateau at around 1.4 V for SEI formation and two more plateau at 0.4 V and 0.2 V representing the formation of Li_2O and the (de)lithiation of lithium silicide respectively.[236]

The dQ/dV plots tell a similar story. Figure 8.2 shows differential plots for recast EoL 1 h and EoL delaminated in 20 % colloidal silica solution (other differential plots are given in Figure 8.7 within the appendix). Both these figures are almost identical, with the only differences being a slight increase in overpotential for the first two large graphite charge peaks at around 0.2 V and 0.18 V for EoL delaminated in a 20 % colloidal silica solution.

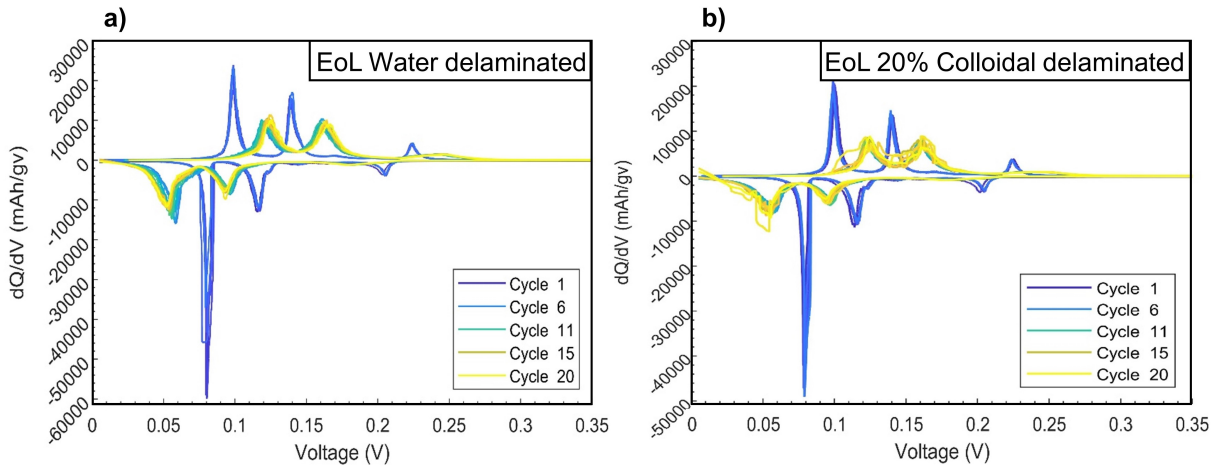


Fig. 8.2. *dQ/dV plots for (a) recast EoL* $1\,\mathrm{h}$ *and (b) EoL* $1\,\mathrm{h}$ *delaminated in* $20\,\%$ *colloidal silica solution.*

This data suggests that the added silica does not participate electrochemically. Instead, the silica reduces the amount of active material and acts as a surface for increased electrolyte reduction, leading to increased resistance and lower cell capacity.

Interestingly, the first cycle irreversible capacity loss for EoL was reduced via delamination in $100\,\%$ colloidal silica. The reason for this is unknown. Nevertheless, this does not lead to great efficiency, the capacity of EoL $100\,\%$ SiO_2 decreases quickly and drastically. Evidently a stable SEI was not formed.

8.4.4 SEM images

In order to determine why the silica did not participate electrochemically, images of the anode material collected via colloidal silica delamination were collected via SEM. 30x magnified images are given in Figure 8.3 with 300x magnified images given in the appendix in Figure 8.8.

Silica particles are indicated by the white crystals found on top of the anode material. They appear white due to their lack of electrical conductivity and increased electron density.

These particles appear to adhere more to the surface that face the current collector, likely due to the increased PVDF content providing increased van der Waals attraction.

The particle size range varies from approximately 0.05 mm to 1 mm. These particles are far too big to participate electrochemically; as stated in the introduction (Section 8.1), the low electrical conductivity in larger particles leads to complete electrochemical inactivity within a LiB.[248] Presumably, these inactive particles lead to the loss in electrochemical performance.

It was expected that varying the colloidal silica concentration would vary the amount and size of silica crystals that deposit onto the anode material. This appears to be the case between the $100\,\%$, $50\,\%$ and $20\,\%$ colloidal silica solution, however lower concentrations seem to have little affect on the amount and size of particles, as determined via SEM.

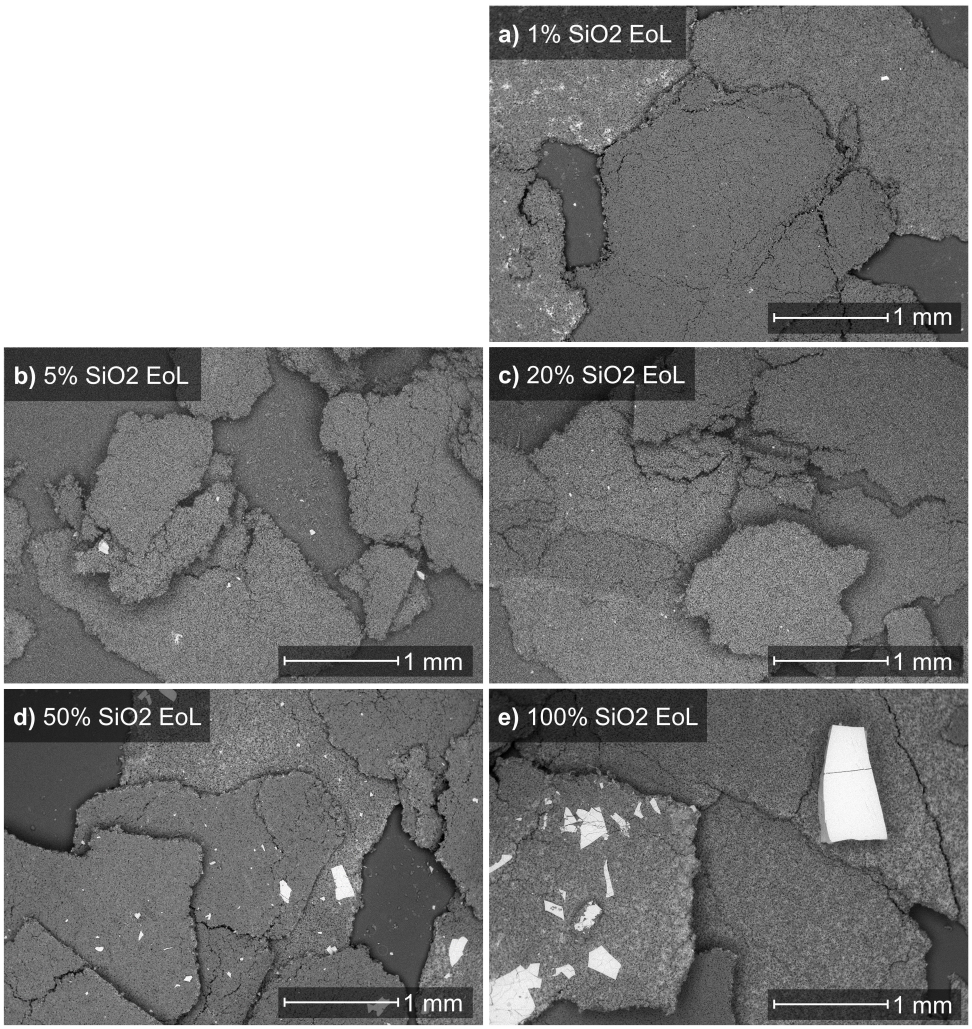


Fig. 8.3. *SEM images, taken at 30x magnification using a BSE detector, for EoL anode material collected via delamination in (a)* $1\,\%$ *colloidal silica,(b)* $5\,\%$ *colloidal silica,(c)* $20\,\%$ *colloidal silica,(d)* $50\,\%$ *colloidal silica, and (e)* $100\,\%$ *colloidal silica solution with water.*

8.5 | Steps to improvement

Simple improvements can be made to the collected anode material. Within this study, three steps were taken; adding a small percentage of CB to increase electrical conductivity, annealing to remove the binder and replace it with CMC/SBR which is known to adhere better to silica particles,[236] and milling to reduce the size of the silica particles.

8.5.1 SEM images

SEM images of annealed and milled EoL anode materials delaminated in $20\,\%$ colloidal silica are shown in Figure 8.4.

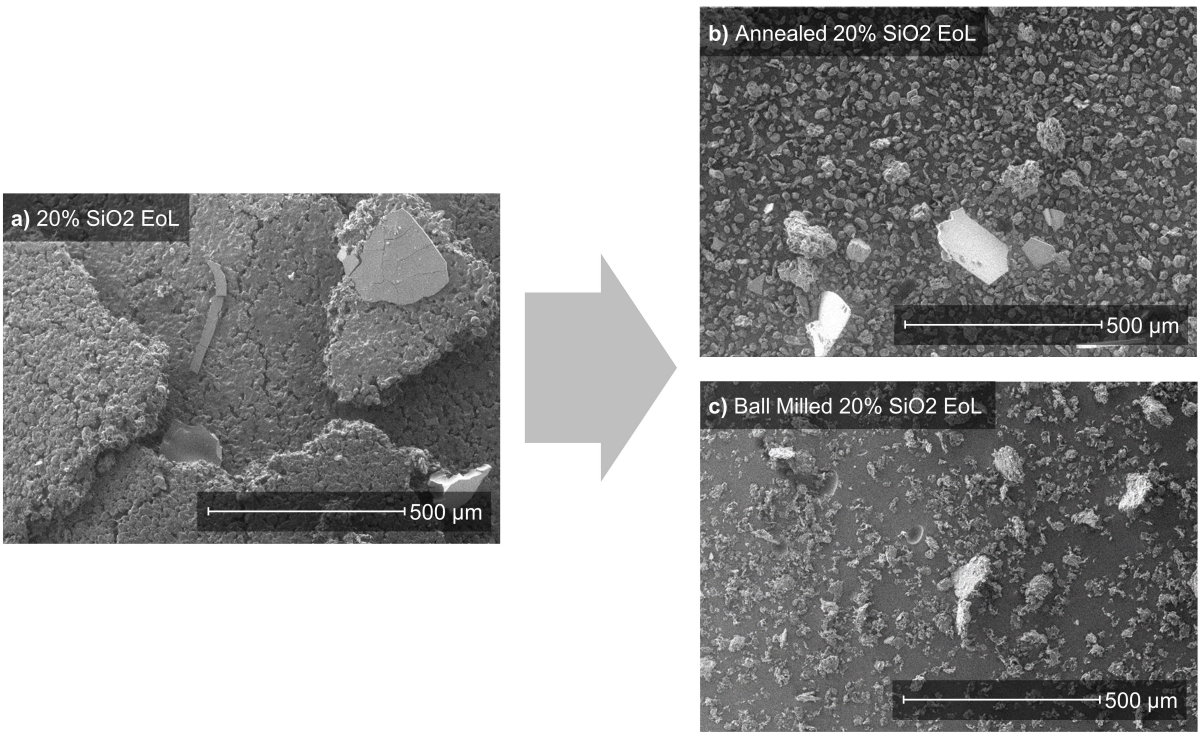


Fig. 8.4. *SEM images taken at a magnification of 100x for EoL delaminated in* $20\,\%$ *colloidal silica (a) pre-processed, (b) annealed to* $500\,^{\circ}\mathrm{C}$ *for* $1\,\mathrm{h}$*, and (c) ball milled at* $600\,\mathrm{rpm}$ *for* $10\,\mathrm{min}$*.*

Annealing successfully unbound the anode material particles, as seen in previous chapters. The size and shape of silica particles remained unchanged, indicating that annealing does not affect the silica particles. Ball milling, however, was successful at both unbinding the anode material and reducing the size of the silica particles. In fact, no silica particles could be found using SEM, indicating very small silica particles that may be integrated within the clumps of graphite particles. It must be noted, milling would not remove the PVDF binder, therefore, redundant material would be present if a new binder is used. Recasting is a potential option for creating rejuvenated anodes from the ball milled material.

8.5.2 Electrochemical performance

The electrochemical performance of $20\,\%$ colloidal silica delaminated EoL anode material after the addition of $2\,\%$ CB, annealing to $500\,^{\circ}\mathrm{C}$ for $1\,\mathrm{h}$ and milling for $15\,\mathrm{min}$ at $600\,\mathrm{rpm}$, separately, were analysed (plotted in Figure 8.5 and quantified in Table 8.4). The $2\,\%$ CB added EoL was recast using the PVDF content within the anode material, whereas the annealed and ball milled sample were bound with fresh CMC/SBR binder. Electrode information is given within the experimental (Section 8.3.4).

Table 8.4. *Numerical values for losses during electrochemical testing for lithium-ion half cell testing. Each sample was tested using three half cells; therefore each data point is an average with its standard error between three cells. EoL* $20\,\%$ SiO_2 *BM samples are an average of two half cells.*

Anode material	First cycle charge capacity $\mathrm{mA\,h\,g^{-1}}$	First cycle discharge capacity $\mathrm{mA\,h\,g^{-1}}$	First cycle irreversible capacity loss $\mathrm{mA\,h\,g^{-1}}$	First cycle irreversible capacity loss % loss	Discharge capacity after 5 cycles $\mathrm{mA\,h\,g^{-1}}$	Discharge capacity after 20 cycles $\mathrm{mA\,h\,g^{-1}}$
EoL 20 % SiO2 2 % CB	416.7(77)	332.8(60)	83.9(20)	20.12(22)	333.2(43)	232(50)
EoL 20 % SiO2 Annealed	327.5(27)	294.1(17)	33.4(14)	10.21(34)	295.3(14)	240(18)
EoL 20 % SiO2 BM	369.7(16)	281.61(98)	87.18(74)	23.64(22)	279.53(61)	232.4(38)

Adding CB marginally improved the first cycle capacity loss (originally around $23\,\%$ in the untreated anode material and now sitting at around $20\,\%$) whereas ball milling did not

improve this performance. As seen previously, annealing did significantly reduced the loss giving a first cycle capacity loss of around $10\,\%$.

Addition of CB would lead to increased overall electrical conductivity reducing any overpotential on the surface of the anode, hopefully leading to less harmful SEI formation. It appears the effect of this addition was not stronger than the negative effects the silica particles create as capacity loss is still greater than that of the water delaminated EoL (around $18.9\,\%$ loss compared to around $7.5\,\%$).

Milling did not electrochemically activate the silica particles. The remnants of PVDF also likely led to the worsened performance.

The drastic improvement to irreversible capacity loss via annealing has already been seen within Section 6.7.1. However, the irreversible capacity shown for this annealed sample is still larger than that obtained for the water delaminated sample (around $10\,\%$ compared to around $7.5\,\%$). This again, is likely due to the silica particles acting as a surface for excessive SEI formation.

All anodes exhibited lower capacities after five cycles, with even more pronounced reductions after twenty cycles compared to the untreated EoL $20\,\%$ SiO_2 sample. This demonstrates no improvement in performance following further treatment.

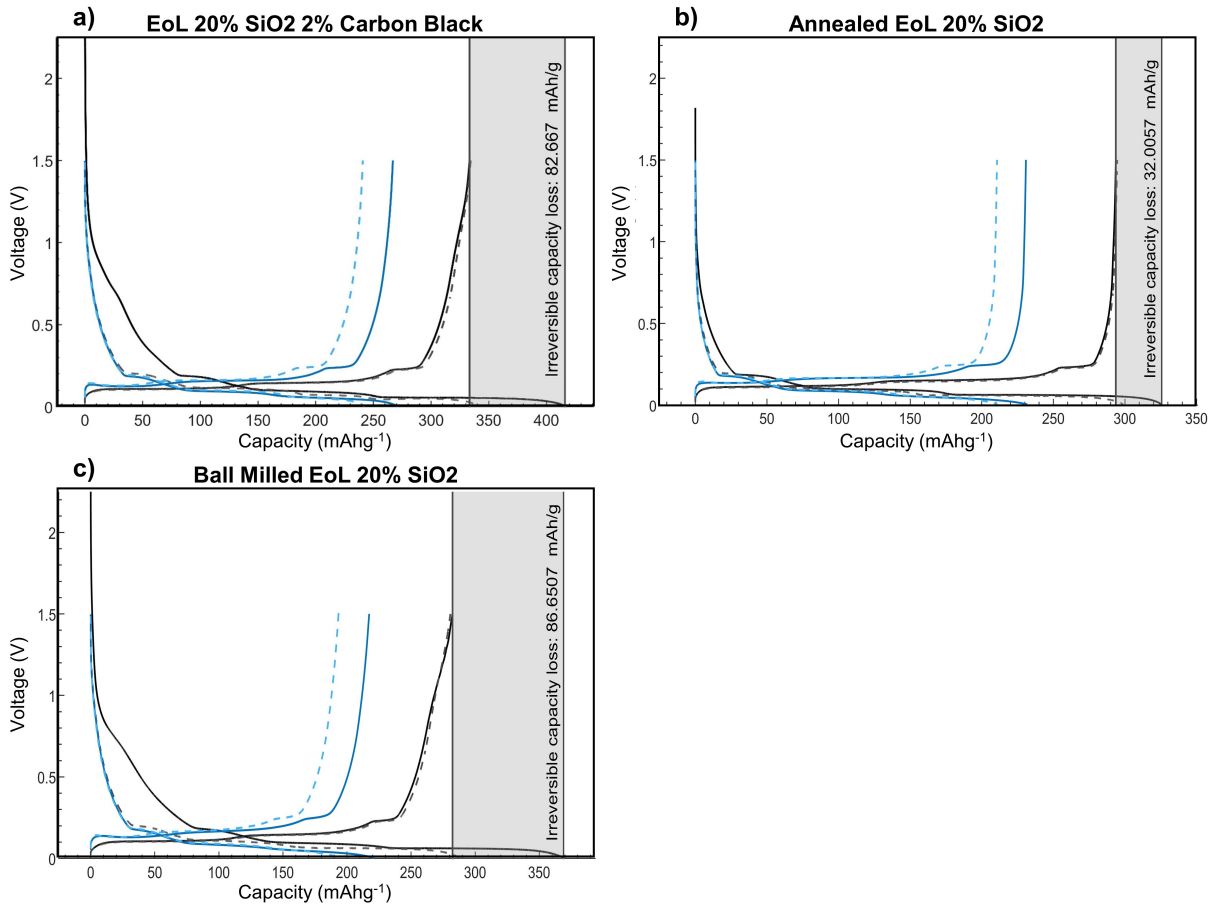


Fig. 8.5. *Voltage profiles of the first five cycles of EoL delaminated in* $20\,\%$ *colloidal silica solution either (a) bound with PVDF with the addition of* $2\,\%$ *CB,(b) bound with CMC/SBR after annealing to* $500\,^{\circ}\mathrm{C}$ *for* $1\,\mathrm{h}$ *or (c) bound with CMC/SBR after milling for* $15\,\mathrm{min}$ *at* $600\,\mathrm{rpm}$. *All were ran at* $10\,\mathrm{mA\,g^{-1}}$ *for five cycles then* $75\,\mathrm{mA\,g^{-1}}$ *for fifteen cycles. Only the first three cycles of each rate are shown and represent the best performance of three half cells.*

8.6 | Chapter conclusion and future work

Although silica could be added to the anode via colloidal silica delamination, the silica did not appear to participate electrochemically due to its large size. Instead, the silica appears to function as a surface for further degradation. Efforts to improve the performance were also in vain. Electrochemical testing showed a worsened performance than standard recovered anode material.

Questions may also be raised to the methodology of the attempted improvements. Recasting of the milled sample would have been more beneficial, as by using this technique, no redundant material would have been left in the active material. Annealing was a technique already established to reduce first cycle capacity loss, via the previous chapters. The combination of all three techniques may have been more appropriate as this would remove organic contamination, allow the use of a more effective binder, and reduce the size of silica particles within one anode.

This chapter was successful in highlighting the fact that material can be combined with the anode material upon delamination, leading to potential routes for future work. Firstly, a colloidal solution of SiO_x could be used. Here a SiO_x/graphite blend could be extracted, which would likely be more electrochemically active due to being less electrically insulating. Another potential route would be to add more silica to the anode material. Next, magnesiothermic reduction could be used to reduce this silica into porous silicon.[252] Silicon readily alloys with lithium and the porous nature will help reduce volume expansion, which will already be aided by the graphite blend. Magnesiothermic reduction involves heating magnesium with silica at around $500\,^{\circ}$C-$950\,^{\circ}$C under argon to create MgO and silicon. MgO can then easily be removed by washing with hydrochloric acid.[252] If paired with colloidal silica delamination two benefits may occur; firstly, non-critical silica can be used to create high capacity silicon containing batteries and secondly, the heating process may decompose

the PVDF binder and organic contamination and thereby rejuvenating the graphite within the same step. However, many side reaction or a lack of decomposition may occur, and so this would require a more detached study, which was not possible in the time constraints of this PhD.

8.7 | Chapter appendix

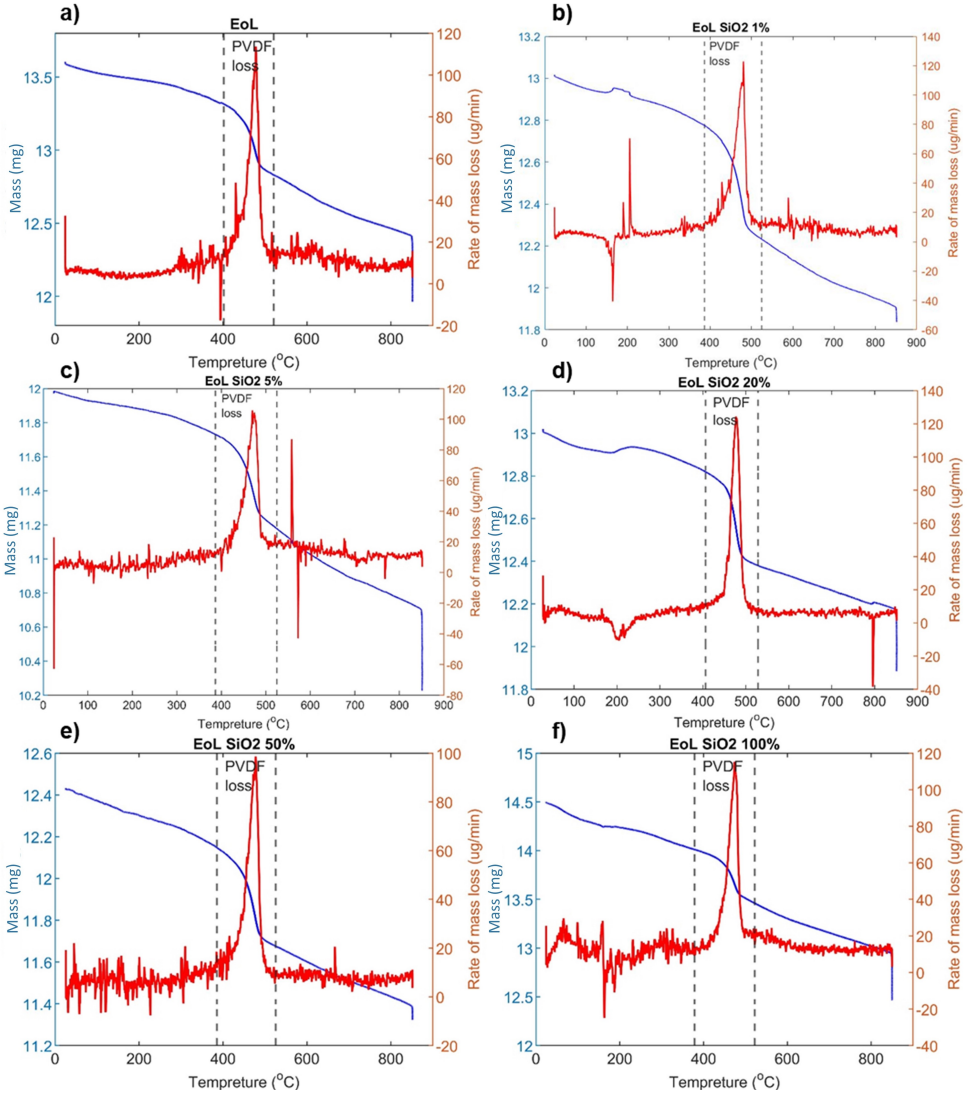


Fig. 8.6. *Mass loss (blue line, left axis) and rate of mass loss (red line, right access) for* 1 h *air exposed EoL anode material delaminated in (a) water,(b)* 1 % *colloidal silica,(c)* 5 % *colloidal silica,(d)* 20 % *colloidal silica,(e)* 50 % *colloidal silica, and (f)* 100 % *colloidal silica. Each was heated to* 900 °C *at a rate of* 10 °C min^{-1}.

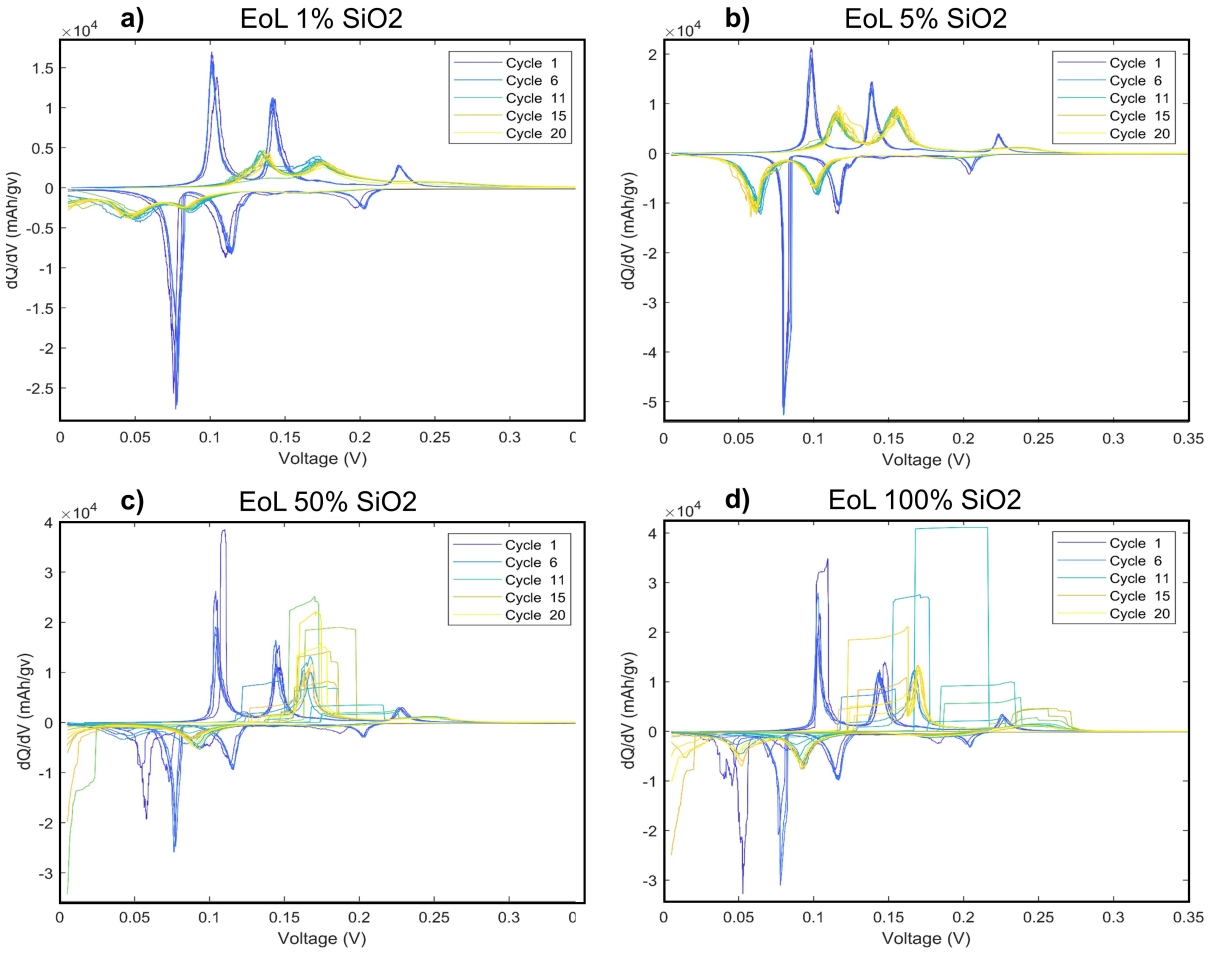


Fig. 8.7. *dQ/dV plots for EoL* 1 h *delaminated in (a)* 1 % *colloidal silica solution,(b)* 5 % *colloidal silica solution,(c)* 50 % *colloidal silica solution, and (d)* 100 % *colloidal silica solution.*

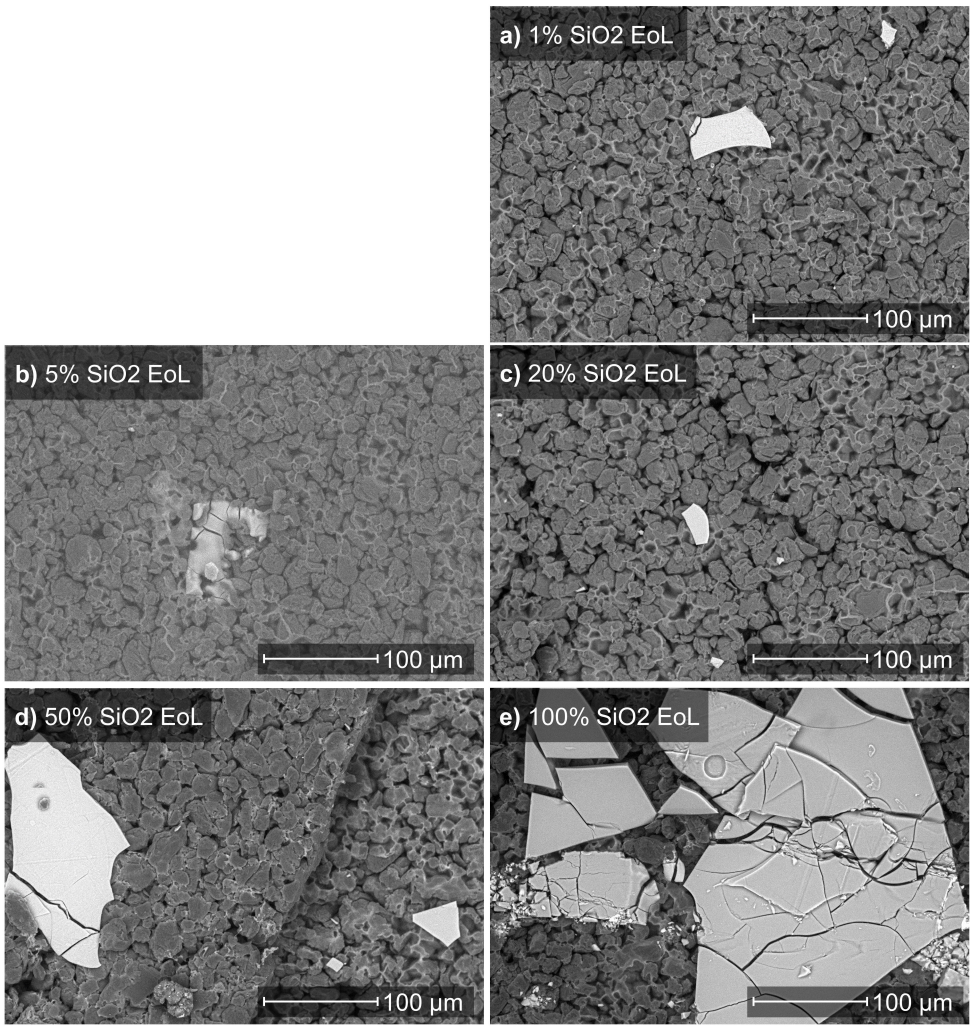


Fig. 8.8. *SEM images, taken at 300x magnification using a BSE detector, for EoL anode material collected via delamination in (a)* $1\,\%$ *colloidal silica,(b)* $5\,\%$ *colloidal silica,(c)* $20\,\%$ *colloidal silica,(d)* $50\,\%$ *colloidal silica, and (e)* $100\,\%$ *colloidal silica solution with water.*

CHAPTER 9

Overall discussion

This work has addressed the observed gap in industrial LiB recycling, where although graphite is labelled as a critical resource by certain governing bodies and its production is energetically and climate costing, it currently is not recycled. As reviewed in Chapter 1, studies within research have extracted graphite from deteriorated LiBs, however have used this graphite as a precursor for less ordered material such as graphene or amorphous carbons. Currently, there is a lack in research that obtains this graphite and reuses it for the purpose it was designed for - electrochemistry. It is advantageous to reuse the graphite from LiBs as it is specifically engineered for that use case: sphericalised and pitch coated. It also has the potential to reduce the overall carbon cost of the LiB industry by reducing the amount of virgin material required to satisfy demand.

As explored in Chapter 1, there are two reasons why this gap may exist. Firstly, it is believed that the graphite from EoL batteries are heavily deteriorated and no longer fit-for-purpose within a battery due to excessive side reactions. It is predicted that graphite particles crack and exfoliate during cycling, leading to a larger surface area for side reactions. This is also why EoL graphite is used as a precursor for graphene-like materials. The second reason is that the PVDF binder used in first generation batteries makes it challenging to remove the graphite from the copper current collector, particularly, in an environmentally friendly way, without the use of toxic solvents, or to do this in a cost effective manner. The

latter is required as the price of virgin graphite currently is relatively cheap. Both points were address in this work.

In Chapter 4, the morphology and characteristics of anodes that would typically be found within an industrial recycling stream were studied to observe the extent and range of degradation present in order to determine whether recycling the material is worthwhile. This included, a representation of process scrap obtained during the manufacturing process of a battery (QCR and QCR II), a used battery from a gen-1 electric Nissan Leaf (EoL), as well as batteries that experienced higher than normal use cases and therefore were more deteriorated (EoL II and EoL III). Ageing mechanisms described within the literature were observed on the EoL batteries as well as the fully discharged QCR anode. The dominate ageing mechanisms appeared to be SEI formation, metal contamination and disconnection of active material caused by the expansion and shrinkage of the graphite during cycling. No particle cracking, exfoliation or structural changes were observed within the graphite which contrasted that already reported.[34,50–58] Studies within literature were either computationally based or laboratory based and therefore may represent an exaggerated form of ageing which would not be present during normal use. As ageing appeared to only affect the surface of the graphite particles, it was determined that graphite from deteriorated cells could potentially be reusable within the battery industry.

It was also discovered that trace amounts of lithiated graphite remained in the anode, even after discharging the cells to a SoC of zero before dismantling. The presence of small amounts can be attributed to the fact that the voltage was not dropped to zero during discharging. Additionally, the presence of electronically isolated components would further contribute to the retention of lithium content. Submersion of these anodes in water after limited exposure to standard atmospheric conditions caused clean delamination of the anode film from the current collector (Chapter 5). Also observed was effervescence and an increase in pH which was rationalised by the production of hydrogen and lithium hydroxide

from the hydrolysis of lithiated graphite. The production of hydrogen would generate similar conditions to those used for ultrasonic delamination of the anode that was seen within the literature.[84–86] Here acoustic vibrations generate bubbles that collapse at the surface of the anode to generate changes in pressure and temperature. The hydrogen production on the surface of the anode would create a similar effect. Thus, we further demonstrated the use of this as a delamination technique to reclaim graphite, addressing the second challenge associated with graphite recycling.

Via this route, delamination could be achieved with only water and no energy input. This delamination technique also presented three additional benefits, the collection of copper, collection of lithium and cleaning of the graphite surface. The copper foil could be collected undamaged, however oxidised. Lithium could be extracted from the delamination water, the recycling of lithium is prominent within industry due to its large market demand created by the LiB industry. Not only could this incentivise the recycling of graphite but also indicates lithium that may be lost during current industrial practices. Water delamination was able to remove most surface contamination on the graphite, however some metal contamination remained and the PVDF binder still bound the particles together.

Two caveats were also present for this technique. Firstly, the production of hydrogen may become an issue if taken to a larger scale. Secondly, the longer the anodes were left under standard atmospheric conditions, the less effective the delamination became. This was due to the lithiated graphite reacting with the air and the moisture to create lithium salts that would dissolve when submerged but not produces the needed hydrogen for delamination. It is unlikely that material will be stored under inert conditions for long periods of time within an industrial set-up. Therefore, a technique for delaminating samples with prolonged exposure to air was studied within Chapter 7. For a sample exposed to air for more than a year, submersion into 0.5 M mineral acids was just as effective as water submersion after

minimum air exposure. This delamination provided graphite with less metal contamination however the copper foil was slightly etched.

After delamination, electrochemical testing was conducted to determine the re-usability of the obtained graphite (discussed in Chapter 6). First, the obtained graphite was directly recast onto the copper foil using NMP and inserted into a lithium-ion half-cell. Although consistent cycling was observed, the first cycle capacity loss was high. Improvements to the performance was made via a heat treatment step to $500\,^{\circ}\mathrm{C}$ for $1\,\mathrm{h}$. This removed any remaining surface contamination as well as the PVDF binder. After casting, this rejuvenated graphite onto copper using water soluble CMC and SBR binder, the electrochemical performance was again tested using lithium-ion half-cells. All anodes showed excellent performance, including EoL III, which originated from a cell that only had $30\,\%$ of its original capacity remaining before dismantlement. Therefore, showing that graphite can easily be obtained from used LiBs, providing a source for high performing battery-grade graphite, helping to secure future supplies of this critical raw material.

Finally, in Chapter 8, the first steps towards converting EoL graphite to current high end anodes was made via the addition of silicon. This was achieved by delaminating the anode within a colloidal silica solution. The aim was to produce graphite with nanoparticles of silica attached to the surface. However, the silica particles were too large to be electrochemically active and only reduced the capacity of the recovered anode.

CHAPTER 10

Conclusion and future work

10.1 | Conclusion

The overall aim of this work was to address the gap in graphite recycling within the LiB recycling industry in order to establish a circular economy.

Anodes of varying SoH were studied to determine whether the graphite from EV cells entering a recycling stream could be reused within the LiB industry. Within the literature, it was proposed that ageing occurs via many degradation mechanisms, particularly on the anode and the graphite. Some examples being particle cracking, graphite exfoliation, and a loss of graphitic structure. Within this study, these degradation pathways were not found. Instead, the dominate ageing mechanisms for cells used in a real application were SEI formation, metal contamination, and a loss of connectivity within the anode. As the structure of the graphite from even the most deteriorated cells remained similar to that of virgin battery-grade graphite, it was determined that reuse of recovered graphite would be possible.

In order to create a scalable graphite recycling technique, it must be environmentally friendly and cost effective. These aims address the need to establishing a clean circular economy and the current low economics for graphite. This work presented the delamination of anode material from the current collector (and therefore easy collection of graphite) via a simple submersion in water, addressing the two requirements. Trace amounts of lithiated

graphite within the anodes react with water to produce hydrogen and lithium hydroxide. The change in pressure resulting from the hydrogen production leads to the cleavage of the anode material. This presents a simple technique that not only separates the anode from the current collector, but also washes the graphite surface and allows for the extraction of lithium from the delamination water. Lithiated graphite will also react with the air and the moister within, therefore the effectiveness of delamination will decrease with increased air exposure. To remedy this, delamination within acid solutions was also studied and showed excellent delamination efficiency. Within acid, gas is produced through the reactions of acid with lithium salts and the copper, leading to a similar delamination.

Studies within the literature use recovered graphite as a precursor for less ordered materials. However, fewer studies focus on reusing the graphite within a lithium ion cell. As proven before, the graphite extracted from used LiBs are structurally similar to virgin battery-grade graphite. Therefore, within this work reuse of the recovered graphite was conducted. The performance of the graphite when directly inserted into a cell was stable, however, lead to a large first cycle irreversible capacity loss. Using a heat treatment step ($500\,^{\circ}$C for 1 h) leads to much better performance. Recovered graphite performed close to the theoretical limit for graphite and similarly to commercial battery-grade graphite. Signalling optimism regarding the benefits of recycling and reuse of graphite within the battery industry.

To finish, steps were made towards up-cycling the material to generate a higher capacity anode. This was conducted by delaminating anodes in colloidal silica solutions to attach nanoparticles of silica to the graphite. However, the silica particles were too large to be electrochemically active.

In summary, this work has demonstrates the feasibility of recycling and reusing graphite from used EV batteries and highlighted its potential to match the quality of commercial battery-grade graphite. This work may help to both reduce the future accumulation of waste and to relieve pressure on future demand.

10.2 | Future work

This work encompassed a method to recycle graphite from lithium pouch cells and demonstrated that the electrochemical performance matched the quality of commercial battery-grade graphite. These electrochemical studies, however, were only conducted within a half cell environment with lithium metal as the reference electrode. This means that the voltage range in which the tests were conducted would not match that of a commercially used cell. As well as this, in a full cell, lithium inventory is limited, therefore side reactions like SEI formation would have a more detrimental effect. Small amounts of metal contamination did remain on the graphite particles, however, these particles were unreactive within the used voltage range. When used in a full cell, this may tell a different narrative. Therefore, further work should be directed towards pairing the recovered graphite with commonly used cathode material. This would present a much more representative performance than what has been presented here.[253] Full cell analysis would also allow for a longer lifetime study as the performance of the cell is not limited by the degradation mechanisms of the lithium metal.[212]

Within this work, it was demonstrated that an entire anode sheet could be easily delaminated using a bath of water. The cells used within this study contained 18 anode sheets and if this method were to be up-scaled, multiple cells would be dismantled and delaminated within a short period of time. Although the technique had no potential risks within the scale used within this work due to the small amount of hydrogen produced, the production at a larger scale may cause a potential risk. For scale up, it would be important to study the amount of gas produced via this techniques and strategies to remedy the risk. Differences in cell OCV will also change the amount of lithiated graphite within an anode and therefore, the amount of produced hydrogen gas. An avenue of hydrogen quantity analysis

will be to vary the OCV of cells before dismantlement. This will allow a study into the safe limits of battery charge for water delamination.

The final chapter made progress towards up-cycling the recovered graphite to create a higher capacity anode. Delamination within a solution of colloidal silica was conducted with the aim of attaching silica nanoparticles to the surface of the graphite. These silica particles would add additional capacity to the anode. However, the silica particles were not nano-sized and due to the poor electrical conductivity of silica, did not participate electrochemically. Therefore this chapter showed that material could be added to the graphite surface via the delamination but did not upcycle the graphite. Two approaches for further work could be made, either create a colloidal solution of particles that will precipitate out as a more electrochemically active material, or alter the silica already attached to the graphite. The former could be conducted by varying the conditions of the colloidal solution (*i.e.* pH and temperature) to produce smaller particles, or a colloidal solution of silicon suboxide could be used, a more electrochemically active variant of silica. Magnesiothermic reduction is a technique that reduces silica to create porous silicon.[252] This could be used on the obtained silica covered recovered graphite to produce a porous silicon/graphite blend. As temperatures of between $500\,^{\circ}$C-$950\,^{\circ}$C are required for this technique, an added benefit may be the combined combustion of the PVDF binder and remnant surface contamination with the reduction of the silica. However, the combination of the two reactions may also lead to a number of unwanted side reactions. Further work would be required.

In summary, further work is required in order to address the creation of a circular economy. This would entail further electrochemical testing of the recovered graphite in real use cases, (*i.e.* within a full cell) to determine if any other side reactions would occur. Up-scaling the water delamination technique is also required, however a study on the hydrogen production is required in order to not induce any risks. Lastly, to align with the high-end materials entering the market and to further incentivise the collection of used graphite,

successful integration of silicon into the recycling process is a potential avenue. This could either be achieved by altering the colloidal solution, or the use of additional processing to electrochemically activate the deposited silica particles.

CHAPTER 11

Publication list

- **Reclamation and reuse of graphite from electric vehicle lithium-ion battery anodes via water delamination.** Alexander Sargent, Zoe Henderson, Alex Walton, Ben Spencer, Luke Sweeney, Wendy Flavell, Paul Anderson, Emma Kendrick, Peter Slater and Phoebe. Allan. *J. Mater. Chem. A, 2023, 11, 9579–9596.*

- Drafted Paper. **Direct recycling of 2nd generation EV production scrap cathode materials.** Emily Giles, Abbey Jarvis, Alexander Sargent, Paul Anderson, Phoebe Allan, and Peter Slater.

- Drafted Paper. **Probing the cause of capacity fade in large-format Li-ion pouch cells through multimodel characterisation.** Emily Giles, Kieran O'Regan, Abbey Jarvis, Rosie Madge, Alexander Sargent, Beatrice Browning, Luke Sweeney, Anton Zorin, Roberto Sommerville, Stefan Michalik, Phil Chater, Peter Slater, Phoebe Allan, Dan Reed, Emma Kendrick, Paul Anderson.

- Drafted Paper. **Lithium ion battery ageing viewed with SEM and EDX.** Alexander Sargent, Wing Wong, Roberto Sommerville, James Batten, Emma Kendrick, Yu-Lung Chiu, Peter Slater and Phoebe Allan.

CHAPTER 12

References

[1] S. Ruben, Proc. Electrochem. Soc. Meeting, Chicago, 1947.

[2] B. Scrosati, *J. Solid State Electrochem.*, 2011, **15**, 1623–1630.

[3] K. Mizushima, P. C. Jones, P. J. Wiseman and J. B. Goodenough, *Mater. Res. Bull.*, 1980, **15**, 783.

[4] M. S. Whittingham, *J. Electrochemical Soc.*, 1976, **123**, 31.

[5] K. Mizushima, P. Jones, P. Wiseman and J. Goodenough, *Solid state ion.*, 1981, **7**, 314–321.

[6] A. Yoshino, K. Sanechika and T. Nakajima, *Secondary battery, US4668595A, US Patent*, 1986.

[7] E. Nevelius, *Press release: The Nobel Prize in Chemistry 2019, (Accessed: 2023-05-03)*, 2019, https://www.nobelprize.org/prizes/chemistry/2019/press-release/.

[8] J. B. Goodenough, *Nature Electronics*, 2018, **1**, 204–204.

[9] J. B. Goodenough and K. S. Park, *J. Am. Chem. Soc.*, 2013, **135**, 1167–1176.

[10] R. Ali, *History of mobile phones and the first mobile phone, (Accessed: 2024-01-03)*, 2023, https://www.uswitch.com/mobiles/guides/history-of-mobile-phones/.

[11] M. Spencer-Green, *iPhone, You Phone, We All Wanna iPhone, (Accessed: 2024-10-28)*, 2007, https://www.wired.com/2009/06/dayintech-0629/.

[12] C. Pillot, *The Rechargeable Battery Market and Main Trends 2016-2025*, Avicenne Energy Technical Report, 2017.

[13] C. J. Orendorff, *Electrochem. Soc. Interface*, 2012, **21**, 61–65.

[14] A. Tornheim and D. C. O'Hanlon, *J. Electrochem. Soc.*, 2020, **167**, 110520.

[15] G. Pistoia, *Batteries for Portable Devices*, Elsevier, Amsterdam, 1st edn, 2005.

[16] J. W. Fergus, *J. Power Sources*, 2010, **195**, 939–954.

[17] F. Liu and X. Chuan, *RSC Adv.*, 2021, **11**, 16633–16644.

[18] A. M. Haregewoin, A. S. Wotango and B. J. Hwang, *Energy Environ. Sci.*, 2016, **9**, 1955–1988.

[19] B. R. Kim, J. H. Kim and J. S. Im, *Mater.*, 2022, **15**, 4713.

[20] L. H. Saw, Y. Ye and A. A. Tay, *J. Cleaner Production*, 2016, **113**, 1032–1045.

[21] G. Harper, R. Sommerville, E. Kendrick, L. Driscoll, P. Slater, R. Stolkin, A. Walton, P. Christensen, O. Heidrich, S. Lambert, A. Abbott, K. Ryder, L. Gaines and P. Anderson, *Nature*, 2019, **575**, 75–86.

[22] H. Zhang, Y. Yang, D. Ren, L. Wang and X. He, *Energy Storage Mater.*, 2021, **36**, 147–170.

[23] A. J. Green, E. H. Driscoll, P. A. Anderson, E. Kendrick and P. R. Slater, *J. Mater. Chem. A*, 2024, **12**, 7321–7328.

[24] J. Asenbauer, T. Eisenmann, M. Kuenzel, A. Kazzazi, Z. Chen and D. Bresser, *Sustainable Energy Fuels*, 2020, **4**, 5387–5416.

[25] L.-Q. Chen, *MRS Bulletin*, 2019, **44**, 520–523.

[26] J. Witt, *Nissan LEAF Battery Replacement Guide, (Accessed: 2024-01-10)*, 2022, https://www.recurrentauto.com/research/nissan-leaf-battery-replacement.

[27] G. E. Blomgren, *J. Electrochem. Soc.*, 2017, **164**, A5019–A5025.

[28] Electric Vehicle Database, *Useable battery capacity of electric vehicles, (Accessed: 2024-01-10)*, 2024, https://ev-database.org/uk/cheatsheet/useable-battery-capacity-electric-car.

[29] L. L. Driscoll, A. Jarvis, R. Madge, J.-M. Price, R. Sommerville, F. S. Tontini, M. Bahri, B. L. Mehdi, E. Kendrick, N. D. Browning, P. K. Allan, P. A. Anderson and P. R. Slater, *ChemRxiv*, 2023, 1–16.

[30] J. Marshall, D. Gastol, R. Sommerville, B. Middleton, V. Goodship and E. Kendrick, *Metals*, 2020, **10**, 773.

[31] M. A. Pimenta, G. Dresselhaus, M. S. Dresselhaus, L. G. Cançado, A. Jorio and R. Saito, *Phys. Chem. Chem. Phys.*, 2007, **9**, 1276–1290.

[32] A. H. R. Palser, *Phys. Chem. Chem. Phys.*, 1999, **1**, 4459–4464.

[33] D. Surovtseva, E. Crossin, R. Pell and L. Stamford, *J. Ind. Ecology*, 2022, **26**, 964–979.

[34] B. Moradi and G. G. Botte, *J. Appl. Electrochem.*, 2016, **46**, 123–148.

[35] G. Barber, *The Surprising Climate Cost of the Humblest Battery Material, (Accessed: 2024-01-14)*, 2022, https://www.wired.com/story/the-surprising-climate-cost-of-the-humblest-battery-material/.

[36] B. Ulrich Hofmann, *Trans. Faraday Soc.*, 1938, **34**, 1017–1021.

[37] J. R. Dahn, *Phys. Rev. B*, 1991, **44**, 9170–9177.

[38] J. B. Goodenough and Y. Kim, *Chem. Mater.*, 2010, **22**, 587–603.

[39] S. J. An, J. Li, C. Daniel, D. Mohanty, S. Nagpure and D. L. Wood, *Carbon*, 2016, **105**, 52–76.

[40] HM Government, *Net Zero Strategy: Build Back Greener*, HM Government Technical Report, 2021.

[41] European Commission, *Delivering the European Green Deal, (Accessed: 2024-01-27)*, 2021, https://commission.europa.eu/strategy-and-policy/priorities-2019-2024/european-green-deal/delivering-european-green-deal_en.

[42] The White House, *Building a clean energy economy guidebook Version 2*, 2023.

[43] G. Erbach, U. Jochheim and V. Seppälä, *China's climate change policies State of play ahead of COP27*, European Parliamentary Research Service Technical Report, 2022.

[44] A. Biferno, H. Shaftel, S. Callery, R. Jackson, D. Bailey and S. Callery, *Global climate change vital signs of the planet, (Accessed: 2024-01-27)*, 2023, https://climate.nasa.gov/.

[45] N. Kittner, F. Lill and D. M. Kammen, *Nature Energy*, 2017, **2**, 17125.

[46] Department for Energy Security and Net Zero, *2022 UK greenhouse gas emissions, Provisional figures*, 2023.

[47] S. Gifford, *The Road to Electrification - from the Internal Combustion Engine to the Battery Electric Vehicle*, The Faraday Institution Technical Report, 2022.

[48] N. Morris, I. Ellerington, A. Paterson, M. Howard and S. Gifford, *UK electric vehicle and battery production potential to 2040*, The Faraday Institution Technical Report, 2019.

[49] T. Parry and S. Reynolds, *Vehicle Licensing Statistics: Annual 2020*, Department for Transport Technical Report, 2021.

[50] J. L. Yang, X. X. Zhao, W. H. Li, H. J. Liang, Z. Y. Gu, Y. Liu, M. Du and X. L. Wu, *eScience*, 2022, **2**, 95–101.

[51] Y. Qiao, H. Zhao, Y. Shen, L. Li, Z. Rao, G. Shao and Y. Lei, *Recycling of graphite anode from spent lithium-ion batteries: Advances and perspectives*, 2023.

[52] C. R. Birkl, M. R. Roberts, E. McTurk, P. G. Bruce and D. A. Howey, *J. Power Sources*, 2017, **341**, 373–386.

[53] S. Bhattacharya and A. T. Alpas, *Carbon*, 2012, **50**, 5359–5371.

[54] A. P. Monasterial, P. J. Weddle, K. Atkinson, D. S. Wragg, A. M. Colclasure, F. L. E. Usseglio-Viretta, N. Seitzman, J.-S. Park, J. Almer, K. Smith and D. P. Finegan, *Small Sci.*, 2023, **3**, 2200067.

[55] T. C. Bach, S. F. Schuster, E. Fleder, J. Müller, M. J. Brand, H. Lorrmann, A. Jossen and G. Sextl, *J. Energy Storage*, 2016, **5**, 212–223.

[56] C. Zhan, T. Wu, J. Lu and K. Amine, *Energy Environ. Sci*, 2018, **11**, 243–257.

[57] I. Rey, C. Vallejo, G. Santiago, M. Iturrondobeitia and E. Lizundia, *ACS Sustainable Chem. Eng.*, 2021, **9**, 14488–14501.

[58] H. C. W. Parks, A. M. Boyce, A. Wade, T. M. M. Heenan, C. Tan, E. Martínez-Pañeda, P. R. Shearing, D. J. L. Brett and R. Jervis, *J. Mater. Chem. A*, 2023, **11**, 21322–21332.

[59] P. Keil, S. F. Schuster, H. Hesse, R. Arunachala, C. Von Lüders and A. Jossen, *3rd Electromobility Challenging Issues conference*, 2015, 1–5.

[60] R. Sommerville, P. Zhu, M. A. Rajaeifar, O. Heidrich, V. Goodship and E. Kendrick, *Resources Conservation Recycling*, 2021, **165**, 105219.

[61] Battery University, *BU-1003a: Battery Aging in an Electric Vehicle, (Accessed: 2024-01-27)*, 2019, https://batteryuniversity.com/article/bu-1003a-battery-aging-in-an-electric-vehicle-ev.

[62] International Energy Agency, *Global EV Outlook 2023: Trends in batteries*, 2023.

[63] M. Grohol and C. Veeh, *Study on the Critical Raw Materials for the EU 2023*, European Commission Technical Report, 2023.

[64] H. Mitchell, F. Maubrey, N. Garret and F. Tang, *The Battery Revolution: Balancing Progress with Supply Chain Risks*, RCS Global Technical Report, 2016.

[65] J. Hu, J. Zhang, H. Li, Y. Chen and C. Wang, *J. Power Sources*, 2017, **351**, 192–199.

[66] J. Heelan, E. Gratz, Z. Zheng, Q. Wang, M. Chen, D. Apelian and Y. Wang, *J. Organomet. Chem.*, 2016, **68**, 2632–2638.

[67] A. Walton, P. Anderson, G. Harper, J. Beddington, A. Abbott, A. Bloodworth, D. OudeNijeweme, E. Schofield, F. Wall, N. Glover, R. Chaddock, R. Gross, R. Lee, R. Grimes, R. Lewis, V. Gibson, P. McGuiness and R. Ogrin, *Securing technology-critical metals for Britain*, University of Birmingham Technical Report, University of Birmingham, 2021.

[68] M. Kaya, *Circular Economy*, 2022, **1**, 100015.

[69] Circular Energy Storage Research and Consulting, *Circular Energy Storage, (Accessed:2024-05-12)*, 2022, https://circularenergystorage.com/articles/2022/9/7/a-tsunami-or-a-drop-in-the-ocean-how-to-calculate-the-volumes-of-lithium-ion-batteries-available-for-recycling.

[70] B. Huang, Z. Pan, X. Su and L. An, *J. Power Sources*, 2018, **399**, 274–286.

[71] S. M. Shin, N. H. Kim, J. S. Sohn, D. H. Yang and Y. H. Kim, *Hydrometallurgy*, 2005, **79**, 172–181.

[72] T. Georgi-Maschler, B. Friedrich, R. Weyhe, H. Heegn and M. Rutz, *J. Power Sources*, 2012, **207**, 173–182.

[73] ReCell Advanced Battery, *Recycling, (Accessed: 2024-01-31)*, 2024, https://recellcenter.org/research/.

[74] J. Meyer, S. Beardsmore, J. Mills, S. Raevskiy, P. Smith, R. Parlons and J. Williams, *Industry Research note, Graphite Q2 2018*, Spangel Technical Report, 2018.

[75] S. Rothermel, M. Evertz, J. Kasnatscheew, X. Qi, M. Grützke, M. Winter and S. Nowak, *ChemSusChem*, 2016, **9**, 3473–3484.

[76] J. Dunn, L. Gaines, M. Barnes, J. Sullivan and M. Wang, *Material and Energy Flows in the Materials Production, Assembly, and End-of-Life Stages of the Automotive Lithium-Ion Battery Life Cycle*, Argonne National Laboratory Technical Report, 2014.

[77] A. Bennett, *Graphite demand from EV battery sector forecast to rise over 35% in 2022, (Accessed: 2024-01-26)*, 2022, https://www.fastmarkets.com/insights/graphite-demand-from-ev-battery-sector-forecast-to-rise-over-35-in-2022/.

[78] L. Yang, L. Yang, G. Xu, Q. Feng, Y. Li, E. Zhao, J. Ma, S. Fan and X. Li, *Sci. Rep*, 2019, **9**, 9823.

[79] Altilium, *Altilium delivers its next generation graphite from EV Battery Recycling, bringing us one step closer to achieving full anode circularity in batteries, (Accessed: 2024-01-28)*, 2023, https://altilium.tech/2023/08/07/.

[80] A. Gupta, *Lohum Cleantech's green mission, (Accessed: 2024-01-28)*, 2023, https://lohum.com/media/news/a-force-to-reckon-with/.

[81] M. L. Divya, S. Natarajan and V. Aravindan, *Batteries Supercaps*, 2022, **5**, e202200046.

[82] R. Saneie, H. Abdollahi, S. Ghassa, D. Azizi and S. Chehreh Chelgani, *J. Sustainable Metallurgy*, 2022, **8**, 386–397.

[83] O. Buken, K. Mancini and A. Sarkar, *RSC Advances*, 2021, **11**, 27356–27368.

[84] L. Li, L. Zhai, X. Zhang, J. Lu, R. Chen, F. Wu and K. Amine, *J. Power Sources*, 2014, **262**, 380–385.

[85] L.-P. He, S.-Y. Sun, X.-F. Song and J.-G. Yu, *Waste Management*, 2015, **46**, 523–528.

[86] C. Lei, I. Aldous, J. M. Hartley, D. L. Thompson, S. Scott, R. Hanson, P. A. Anderson, E. Kendrick, R. Sommerville, K. S. Ryder and A. P. Abbott, *Green Chem.*, 2021, **23**, 4710–4715.

[87] P. Atkins and J. D. Paila, *Atkins Physical Chemistry*, Oxford University Press, 10th edn, 2014.

[88] M. Weller, T. Overton, J. Rourke and F. Armstrong, *Inorganic Chemistry*, Oxford University Press, Oxford, 6th edn, 2014.

[89] D. Tuschel, *Raman Spectroscopy and Polymorphism, (Accessed: 2023-12-06)*, 2019, https://www.spectroscopyonline.com/view/raman-spectroscopy-and-polymorphism.

[90] A. Jorio, L. G. Cançado and L. M. Malard, *2D Materials*, Cambridge University Press, 2017, 71–89.

[91] S. Reich and C. Thomsen, *Philos. Trans. R. Soc. London, Ser. A*, 2004, **362**, 2271–2288.

[92] R. Kostić, M. Mirić, T. Radić, M. Radović, R. Gajić and Z. V. Popović, *Acta Physica Polonica A*, 2009, **116**, 718–721.

[93] O. Beyssac and M. Lazzeri, *European Mineralogical Union Notes in Mineralogy*, 2012, **12**, 415–454.

[94] A. Sadezky, H. Muckenhuber, H. Grothe, R. Niessner and U. Pöschl, *Carbon*, 2005, **43**, 1731–1742.

[95] T. Jawhari, A. Roid and J. Casado, *Carbon*, 1995, **33**, 1561–1565.

[96] F. Delarue, J. N. Rouzaud, S. Derenne, M. Bourbin, F. Westall, B. Kremer, K. Sugitani, D. Deldicque and F. Robert, *Astrobiology*, 2016, **16**, 407–417.

[97] P. Puech, M. Kandara, G. Paredes, L. Moulin, E. Weiss-Hortala, A. Kundu, N. Ratel-Ramond, J. Plewa, R. Pellenq and M. Monthioux, *J. Carbon Res. C*, 2019, **5**, 69.

[98] Renishaw plc., *renishaw, (Accessed: 2024-03-11)*, 2024, https://www.renishaw.com/en/renishaw-enhancing-efficiency-in-manufacturing-and-healthcare--1030.

[99] Thermo Fisher Scientific., *Thermo Fisher Scientific: Electron Microscopy 101, (Accessed: 2024-03-11)*, 2024, https://www.thermofisher.com/blog/materials/electron-microscopy-101/.

[100] J. F. Moulder, W. F. Stickle, P. E. Sobol and K. D. Bomben, *Handbook of X-ray Photoelectron Spectroscopy*, Perkin-Elmer Corporation, 1992.

[101] S. Malmgren, K. Ciosek, R. Lindblad, S. Plogmaker, J. Kühn, H. Rensmo, K. Edström and M. Hahlin, *Electrochim. Acta*, 2013, **105**, 83–91.

[102] S. Malmgren, K. Ciosek, M. Hahlin, T. Gustafsson, M. Gorgoi, H. Rensmo and K. Edström, *Electrochim. Acta*, 2013, **97**, 23–32.

[103] I. Bloom, J. Bareño, N. Dietz Rago, F. Dogan, D. G. Graczyk, Y. Tsai, S. R. Naik, S. D. Han, E. Lee, Z. Du, Y. Sheng, J. Li, D. L. Wood, L. A. Steele, J. Lamb, S. Spangler, C. Grosso and K. Fenton, *J. Power Sources*, 2018, **385**, 156–164.

[104] T. S. Pathan, M. Rashid, M. Walker, W. D. Widanage and E. Kendrick, *J. Phys. Energy*, 2019, **1**, 044003.

[105] S. Jiao, X. Ren, R. Cao, M. H. Engelhard, Y. Liu, D. Hu, D. Mei, J. Zheng, W. Zhao, Q. Li, N. Liu, B. D. Adams, C. Ma, J. Liu, J.-G. Zhang and W. Xu, *Nature Energy*, 2018, **3**, 739–746.

[106] L. Somerville, J. Bareño, P. Jennings, A. McGordon, C. Lyness and I. Bloom, *Electrochim. Acta*, 2016, **206**, 70–76.

[107] J. Piwowarczyk, R. Jędrzejewski, D. Moszyński, K. Kwiatkowski, A. Niemczyk and J. Baranowska, *Polymers*, 2019, **11**, 1629.

[108] B. F. Spencer, S. A. Church, P. Thompson, D. J. H. Cant, S. Maniyarasu, A. Theodosiou, A. N. Jones, M. J. Kappers, D. J. Binks, R. A. Oliver, J. Higgins, A. G. Thomas, T. Thomson, A. G. Shard and W. R. Flavell, *Faraday Discussions*, 2022, **236**, 311–337.

[109] J. Fayos, *J. Solid State Chem.*, 1999, **148**, 278–285.

[110] A. N. Popova, *Coke Chem.*, 2017, **60**, 361–365.

[111] N. Chadha, P. Saini and R. Sharma, *Indian J. Pure Appl. Phys.*, 2017, **55**, 625–629.

[112] D. Harvey, *Instrumental Analysis*, LibreTexts, 2024.

[113] Microtrac Retsch GmbH, *Microtrac Particle Characterization, (Accessed: 2024-03-11)*, 2024, https://www.microtrac.com/knowledge/.

[114] M. D. Levi and D. Aurbach, *J. Electroanal. Chem.*, 1997, **421**, 79–88.

[115] K. Egorov, W. Zhao, K. Knemeyer, A. N. Filippin, A. Giraldo and C. Battaglia, *ACS Appl. Mater. Interfaces*, 2023, **15**, 20075–20080.

[116] N. Elgrishi, K. J. Rountree, B. D. McCarthy, E. S. Rountree, T. T. Eisenhart and J. L. Dempsey, *J. Chem. Ed.*, 2018, **95**, 197–206.

[117] A. Smith, P. Stüble, L. Leuthner, A. Hofmann, F. Jeschull and L. Mereacre, *Batteries Supercaps*, 2023, **6**, e202300080.

[118] H. Fujimoto, T. Yamaki, K. Shimoda, S. Fujinami, T. Nakatani, G. Kano, M. Kawasaki, Z. Ogumi and T. Abe, *J. Electrochem. Soc.*, 2022, **169**, 070507.

[119] C. Yuqin, H. Li, W. Lie and L. Tianhong, *J. Power Sources*, 1997, **68**, 187–190.

[120] C. Schmitt, A. Kube, N. Wagner and K. A. Friedrich, *ChemElectroChem*, 2022, **9**, 43–51.

[121] A. T. Sargent, Z. Henderson, A. S. Walton, B. F. Spencer, L. Sweeney, W. R. Flavell, P. A. Anderson, E. Kendrick, P. R. Slater and P. K. Allan, *J. Mater. Chem. A*, 2023, **11**, 9579–9596.

[122] J. Wang, *Looming EV raw materials supply crunch has OEMs eyeing battery recycling and production scrap, (Accessed: 2024-03-06)*, 2024, https://www.spglobal.com/mobility/en/research-analysis/ev-raw-materials-supply-crunch-battery-recycling.html.

[123] Benchmark Mineral Intelligence, *Battery production scrap to be main source of recyclable material this decade, (Accessed: 2024-03-06)*, 2022, https://source.benchmarkminerals.com/article/battery-production-scrap-to-be-main-source-of-recyclable-material-this-decade.

[124] P. S. Attidekou, Z. Milojevic, M. Muhammad, M. Ahmeid, S. Lambert and P. K. Das, *J. Electrochem. Soc*, 2020, **167**, 160534.

[125] The MathWorks Inc., *MATLAB (2020a) (Accessed: 2023-09-05)*, 2023, https://www.mathworks.com.

[126] T. O'Haver, *peakfit.m (Accessed: 2023-09-05)*, 2018, https://uk.mathworks.com/matlabcentral/fileexchange/23611-peakfit-m.

[127] J. D'Errico, *fminsearchbnd.m (Accessed: 2023-09-05)*, 2012, https://uk.mathworks.com/matlabcentral/fileexchange/8277-fminsearchbnd-fminsearchcon.

[128] A. Regoutz, M. Mascheck, T. Wiell, S. K. Eriksson, C. Liljenberg, K. Tetzner, B. A. D. Williamson, D. O. Scanlon and P. Palmgren, *Rev. Sci. Instruments*, 2018, **89**, 073105.

[129] B. Spencer, S. Maniyarasu, B. Reed, D. Cant, R. Ahumada-Lazo, A. Thomas, C. Muryn, M. Maschek, S. Eriksson, T. Wiell, T. Lee, S. Tougaard, A. Shard and W. Flavell, *Appl. Surface Sci.*, 2021, **541**, 148635.

[130] N. Fairley, V. Fernandez, M. Richard-Plouet, C. Guillot-Deudon, J. Walton, E. Smith, D. Flahaut, M. Greiner, M. Biesinger, S. Tougaard, D. Morgan and J. Baltrusaitis, *Appl. Surface Sci. Adv.*, 2021, **5**, 100112.

[131] D. J. H. Cant, B. F. Spencer, W. R. Flavell and A. G. Shard, *Surface Interface Analysis*, 2022, **54**, 442–454.

[132] G. Mercurio, O. Bauer, M. Willenbockel, B. Fiedler, T. Sueyoshi, C. Weiss, R. Temirov, S. Soubatch, M. Sokolowski and F. S. Tautz, *Phy. Rev. B*, 2013, **87**, 121409.

[133] Bruker, *DIFFRAC.EVA (Accessed:2024-02-26)*, 2024, https://www.bruker.com/en/products-and-solutions/diffractometers-and-x-ray-microscopes/x-ray-diffractometers/diffrac-suite-software/diffrac-eva.html.

[134] M. Wojdyr, *J. Appl Crystallography*, 2010, **43**, 1126–1128.

[135] A. Coelho and Coelho Software, *TOPAS Academic V7, (Accessed: 2024-02-26)*, 2012, http://www.topas-academic.net/.

[136] R. Sharma, N. Chadha and P. Saini, *Indian J. Pure Appl. Phy.*, 2017, **55**, 625–629.

[137] A. Kashima, S. Urashima and H. Yui, *Meteoritics Planetary Sci.*, 2024, **59**, 338–350.

[138] H. Yang, X. Li, Y. Wang, M. Mu, X. Li and G. Kou, *Sci. Rep.*, 2016, **6**, 37611.

[139] J. Hyun Kim, S. Min Jane Han, W. Sik Yoo, W. Sik Yoo Jae Hyun Kim Seung Min Han and S. Min Han, *J. Micro/Nanolith. MEMS MOEMS*, 2014, **13**, 011205–011214.

[140] Renishaw, *inVia ™ research-grade confocal Raman microscopes*, 2023, 1–26.

[141] J. S. Okasinski, I. A. Shkrob, A. Chuang, M.-T. F. Rodrigues, A. Raj, D. W. Dees and D. P. Abraham, *Phys. Chem. Chem. Phys.*, 2020, **22**, 21977–21987.

[142] S. J. Goldie, M. T. Degiacomi, S. Jiang, S. J. Clark, V. Erastova and K. S. Coleman, *ACS Nano*, 2022, **16**, 16109–16117.

[143] A. Wróblewska, A. Dużyńska, J. Judek, L. Stobiński, K. Żerańska, A. P. Gertych and M. Zdrojek, *J. Phys. Condensed Matter*, 2017, **29**, 475201.

[144] H. Charalambous, D. P. Abraham, A. R. Dunlop, S. E. Trask, A. N. Jansen, T. R. Tanim, P. R. Chinnam, A. M. Colclasure, W. Xu, A. A. Yakovenko, O. J. Borkiewicz, L. C. Gallington, U. Ruett, K. M. Wiaderek and Y. Ren, *J. Power Sources*, 2021, **507**, 230253.

[145] F. Leng, C. M. Tan and M. Pecht, *Sci. Rep.*, 2015, **5**, 12967.

[146] T. Waldmann, A. Iturrondobeitia, M. Kasper, N. Ghanbari, F. Aguesse, E. Bekaert, L. Daniel, S. Genies, I. J. Gordon, M. W. Löble, E. De Vito and M. Wohlfahrt-Mehrens, *J. Electrochem. Soc.*, 2016, **163**, A2149–A2164.

[147] S. Schweidler, L. de Biasi, A. Schiele, P. Hartmann, T. Brezesinski and J. Janek, *J. Phys. Chem. C*, 2018, **122**, 8829–8835.

[148] C. Fear, D. Juarez-Robles, J. A. Jeevarajan and P. P. Mukherjee, *J. Electrochem. Soc.*, 2018, **165**, A1639–A1647.

[149] R. Jung, F. Linsenmann, R. Thomas, J. Wandt, S. Solchenbach, F. Maglia, C. Stinner, M. Tromp and H. A. Gasteiger, *J. Electrochem. Soc.*, 2019, **166**, A378–A389.

[150] C. Zhan, J. Lu, A. Jeremy Kropf, T. Wu, A. N. Jansen, Y. K. Sun, X. Qiu and K. Amine, *Nature Commun.*, 2013, **4**, 2437.

[151] J. Wandt, A. Freiberg, R. Thomas, Y. Gorlin, A. Siebel, R. Jung, H. A. Gasteiger and M. Tromp, *J. Mater. Chem. A*, 2016, **4**, 18300–18305.

[152] K. Kobayashi, *Nuclear Instruments and Methods in Phys. Res. A*, 2009, **601**, 32–47.

[153] Y. Wang, S. Nakamura, M. Ue and P. B. Balbuena, *J. Am. Chem. Soc.*, 2001, **123**, 11708–11718.

[154] X. Yu and A. Manthiram, *Energy Environ. Sci.*, 2018, **11**, 527–543.

[155] V. R. Rikka, S. R. Sahu, A. Chatterjee, P. V. Satyam, R. Prakash, M. S. R. Rao, R. Gopalan and G. Sundararajan, *J Phys. Chem. C*, 2018, **122**, 28717–28726.

[156] A. Missyul, I. Bolshakov and R. Shpanchenko, *Powder Diffraction*, 2017, **32**, S56–S62.

[157] H. Badenhorst, *Carbon*, 2014, **66**, 674–690.

[158] J. Y. Howe, C. J. Rawn, L. E. Jones and H. Ow, *Powder Diffraction*, 2003, **18**, 150–154.

[159] J. E. Sabisch, A. Anapolsky, G. Liu and A. M. Minor, *Resources Conservation Recycling*, 2018, **129**, 129–134.

[160] Umicore, *Umicore history, (Accessed: 2024-02-27)*, 2024, https://www.umicore.com/en/about/history.

[161] POSCO international, *POSCO International homepage, (Accessed: 2024-02-27)*, 2017, https://www.poscointl.com/eng/.

[162] L. Gaines, J. Zhang, X. He, J. Bouchard and H. E. Melin, *Batteries*, 2023, **9**, 360.

[163] Z. J. Baum, R. E. Bird, X. Yu and J. Ma, *ACS Energy Lett.*, 2022, **7**, 712–719.

[164] M. Herstedt, D. P. Abraham, J. B. Kerr and K. Edström, *Electrochim. Acta*, 2004, **49**, 5097–5110.

[165] B. H. Toby and R. B. Von Dreele, *J. Appl Crystallography*, 2013, **46**, 544–549.

[166] D. A. Wetz, B. Shrestha, P. M. Novak and S. Donahue, 2014 17th International Symposium on Electromagnetic Launch Technology, 2014, 1–7.

[167] L. Baudino, C. Santos, C. F. Pirri, F. La Mantia and A. Lamberti, *Adv. Sci.*, 2022, **9**, 2201380.

[168] J. W. An, D. J. Kang, K. T. Tran, M. J. Kim, T. Lim and T. Tran, *Hydrometallurgy*, 2012, **117-118**, 64–70.

[169] D. Bradley, L. Munk, H. Jochens, S. Hynek and K. Labay, *A Preliminary Deposit Model for Lithium Brines*, U.S. Geological Survey Technical Report, 2013.

[170] D. Garrett, *Handbook of Lithium and Natural Calcium Chloride*, Elsevier, 2004, 214.

[171] F. Annunzi, C. Nicolella, R. S. Stella, M. Lenzi and F. Signorini, *Chem. Eng. Transactions*, 2023, **98**, 207–212.

[172] E. G. Pinna, M. Ruiz, M. W. Ojeda and M. H. Rodriguez, *Hydrometallurgy*, 2017, **167**, 66–71.

[173] H. Li, H. Li, J. Liang, H. Yan and Z. Cai, *Crystals*, 2021, **11**, 1163.

[174] D. J. Shin, S. Joo, D. Lee and S. M. Shin, *Canadian J. Chem. Eng.*, 2022, **100**, 3760–3767.

[175] Y. Idemoto, W. Richardson, James, N. Koura, S. Kohara and Loong C, *J. Phys. Chem. Solids*, 1998, **59**, 363–376.

[176] C. Keffer, A. Mighell, F. Mauer, H. Swanson and S. Block, *J. Am. Chem. Soc*, 1967, **6**, 4513.

[177] E. Smith and G. Dent, *Modern Raman Spectroscopy: A Practical Approach*, John Wiley & Sons Ltd., 2nd edn, 2019.

[178] C. Hinshelwood, *Proc. R. Soc. Lond. A*, 1922, **102**, 318–328.

[179] G. Kalita, M. E. Ayhan, S. Sharma, S. M. Shinde, D. Ghimire, K. Wakita, M. Umeno and M. Tanemura, *Corrosion Sci.*, 2014, **78**, 183–187.

[180] D. Becker, *All About Flex: Copper Grain Direction, (Accessed: 2023-11-06)*, 2018, https://iconnect007.com/index.php/article/108284/all-about-flex-copper-grain-direction/.

[181] MTI Corporation, *Copper Foil with Various Width and Thickness as Battery Current Collector: from 4.5μm, to 25μm, (Accessed: 2023-11-06)*, 2023, https://www.mtixtl.com/EQ-bccf-16mm.aspx(2023-11-06).

[182] J. Peng, B. Chen, Z. Wang, J. Guo, B. Wu, S. Hao, Q. Zhang, L. Gu, Q. Zhou, Z. Liu, S. Hong, S. You, A. Fu, Z. Shi, H. Xie, D. Cao, C. J. Lin, G. Fu, L. S. Zheng, Y. Jiang and N. Zheng, *Nature*, 2020, **586**, 390–394.

[183] S. Hong, C. Liu, S. Hao, W. Fu, J. Peng, B. Wu and N. Zheng, *npj Flexible Electronics*, 2022, **6**, 17.

[184] Y. Tang, C. A. Roberts, R. T. Perkins and I. E. Wachs, *Surface Sci.*, 2016, **650**, 103–110.

[185] T. Boyadzhieva, V. Koleva, E. Zhecheva, D. Nihtianova, L. Mihaylov and R. Stoyanova, *RSC Adv.*, 2015, **5**, 87694–87705.

[186] H. J. Seong and A. L. Boehman, *Energy Fuels*, 2013, **27**, 1613–1624.

[187] S. Roscher, R. Hoffmann and O. Ambacher, *Anal. Methods*, 2019, **11**, 1224–1228.

[188] C. S. Casari, A. Li Bassi, A. Baserga, L. Ravagnan, P. Piseri, C. Lenardi, M. Tommasini, A. Milani, D. Fazzi, C. E. Bottani and P. Milani, *Phys. Rev. B*, 2008, **77**, 195444.

[189] M. Kazanci, P. Fratzl, K. Klaushofer and E. P. Paschalis, *Calcif. Tissue Int.*, 2006, **79**, 354–359.

[190] W. Weber, V. Kraft, M. Grützke, R. Wagner, M. Winter and S. Nowak, *J. Chromatogr. A*, 2015, **1394**, 128–136.

[191] L. Cabo-Fernandez, A. R. Neale, F. Braga, I. V. Sazanovich, R. Kostecki and L. J. Hardwick, *Phys. Chem. Chem. Phys.*, 2019, **21**, 23833–23842.

[192] M. A. Cabañero, M. Hagen and E. Quiroga-González, *Electrochim. Acta*, 2021, **374**, 127487.

[193] A. Spivak, N. Solopova, V. Cerantola, E. Bykova, E. Zakharchenko, L. Dubrovinsky and Y. Litvin, *Phys. Chem. Minerals*, 2014, **41**, 633–638.

[194] S. J. Goldie, S. Bush, J. A. Cumming and K. S. Coleman, *ACS Appl. Nano. Mater.*, 2020, **3**, 11229–11239.

[195] M. Biesinger, *Graphite XPS fitting model, (Accessed: 2023-11-08)*, 2021, www.xpsfitting.com.

[196] Casa Software Ltd., *CasaXPS User's Manual for Version 2.0*, Acolyte Science, Cheshire, 1st edn, 2001.

[197] D. J. Morgan, *Surf Interface Anal.*, 2023, **55**, 567–571.

[198] T. R. Gengenbach, G. H. Major, M. R. Linford and C. D. Easton, *J. Vac. Sci. Technol. A*, 2021, **39**, 013204.

[199] J. Park, S. Suh, S. Tamulevičius, D. Kim, D. Choi, S. Jeong and H. J. Kim, *Nanomaterials*, 2022, **12**, 2625.

[200] S. Kursunoglu and M. Kaya, *Physicochem. Probl. Miner. Process.*, 2014, **50**, 41–55.

[201] M. Baunach, S. Jaiser, S. Schmelzle, H. Nirschl, P. Scharfer and W. Schabel, *Drying Technol.*, 2016, **34**, 462–473.

[202] J. Kumberg, M. Müller, R. Diehm, S. Spiegel, C. Wachsmann, W. Bauer, P. Scharfer and W. Schabel, *Energy Technol.*, 2019, **7**, 1900722.

[203] R. K. Iyer and J. Kelly, *Updated production inventory for LiB battery anodes for GREEY Model, and Review of Advanced Battery Chemistries*, Argonne National Laboratory Technical Report, 2022.

[204] MacKenzie Wood, *Main uses of Carbon and Graphite, (Accessed: 2023-11-13)*, 2022, https://ecga.net/main-uses-of-graphite/.

[205] Magnis Energy Technologies Limited., *Graphite Market, (Accessed: 2023-11-13)*, 2023, https://magnis.com.au/graphite-market/.

[206] Benchmark Mineral Intelligence Limited, *What to expect for graphite in 2023?, (Accessed: 2023-11-13)*, 2023, https://source.benchmarkminerals.com/article/what-to-expect-for-graphite-in-2023.

[207] J. P. Yen, C. C. Chang, Y. R. Lin, S. T. Shen and J. L. Hong, *J. Electrochem. Soc.*, 2013, **160**, A1811–A1818.

[208] G. Zhang, Z. Du, Y. He, H. Wang, W. Xie and T. Zhang, *Sustainability*, 2019, **11**, 2363.

[209] B. Markey, M. Zhang, I. Robb, P. Xu, H. Gao, D. Zhang, J. Holoubek, D. Xia, Y. Zhao, J. Guo, M. Cai, Y. S. Meng and Z. Chen, *J. Electrochem. Soc.*, 2020, **167**, 160511.

[210] C. D. Reynolds, P. R. Slater, S. D. Hare, M. J. Simmons and E. Kendrick, *Mater. Design*, 2021, **209**, 109971.

[211] F. Yang, D. Wang, Y. Zhao, K.-L. Tsui and S. J. Bae, *Energy*, 2018, **145**, 486–495.

[212] J. Xiao, Q. Li, Y. Bi, M. Cai, B. Dunn, T. Glossmann, J. Liu, T. Osaka, R. Sugiura, B. Wu, J. Yang, J.-G. Zhang and M. S. Whittingham, *Nature Energy*, 2020, **5**, 561–568.

[213] S. Scott, Z. Islam, J. Allen, T. Yingnakorn, A. Alflakian, J. Hathaway, A. Rastegarpanah, G. D. Harper, E. Kendrick, P. A. Anderson, J. Edge, L. Lander and A. P. Abbott, *Next Energy*, 2023, **1**, 100023.

[214] A. J. de Jesus Silva, M. M. Contreras, C. R. Nascimento and M. F. da Costa, *Heliyon*, 2020, **6**, e04573.

[215] A. Kriston, I. Adanouj, V. Ruiz and A. Pfrang, *J. Power Sources*, 2019, **435**, 226774.

[216] O. Clemens and P. R. Slater, *Rev. Inorg. Chem*, 2013, **33**, 105–117.

[217] K. Guérin, J. P. Pinheiro, M. Dubois, Z. Fawal, F. Masin, R. Yazami and A. Hamwi, *Chem. Mater.*, 2004, **16**, 1786–1792.

[218] S. Zulfiqar, M. Zulfiqar, M. Rizvi, A. Munirt and I. C. Mcneil, *Polymer Degradation Stability*, 1994, **43**, 423–430.

[219] Z. Ju, S. Zhang, Z. Xing, Q. Zhuang, Y. Qiang and Y. Qian, *ACS Appl. Mater. Interfaces*, 2016, **8**, 20682–20690.

[220] G. Zhang, M. Wen, S. Wang, J. Chen and J. Wang, *RSC Adv*, 2018, **8**, 567–579.

[221] N. Cornea, *Rev. Chim. (Bucharest)*, 2011, **62**, 923–925.

[222] M. F. Rabuni, N. M. Nik Sulaiman, M. K. Aroua and N. A. Hashim, *Ind. Eng. Chem. Res.*, 2013, **52**, 15874–15882.

[223] L. Pagliaro and D. A. Lowy, *La Granja*, 2019, **29**, 17–31.

[224] K. Omichi, G. Ramos-Sanchez, R. Rao, N. Pierce, G. Chen, P. B. Balbuena and A. R. Harutyunyan, *J. Electrochem. Soc.*, 2015, **162**, A2106–A2115.

[225] S. Ng, C. Vix-Guterl, P. Bernardo, N. Tran, J. Ufheil, H. Buqa, J. Dentzer, R. Gadiou, M. Spahr, D. Goers and P. Novák, *Carbon*, 2009, **47**, 705–712.

[226] S. L. Glazier, J. Li, A. J. Louli, J. P. Allen and J. R. Dahn, *J. Electrochem. Soc.*, 2017, **164**, A3545–A3555.

[227] W. Xu, C. Welty, M. R. Peterson, J. A. Read and N. P. Stadie, *J. Electrochem. Soc.*, 2022, **169**, 010531.

[228] S. Weng, G. Yang, S. Zhang, X. Liu, X. Zhang, Z. Liu, M. Cao, M. N. Ateş, Y. Li, L. Chen, Z. Wang and X. Wang, *Nano-Micro Lett.*, 2023, **15**, 215.

[229] W. Yourey, Y. Fu, N. Li, V. Battaglia and W. Tong, *J. Electrochem. Soc.*, 2019, **166**, A1432–A1438.

[230] A. Sonoc, J. Jeswiet and V. K. Soo, *Procedia CIRP*, 2015, **29**, 752–757.

[231] E. B. Godunov, A. D. Izotov and I. G. Gorichev, *Inorg. Mater.*, 2017, **53**, 831–837.

[232] J. Peng, L. Giordano, T. C. Davenport and Y. Shao-Horn, *Chem. Mater.*, 2022, **34**, 7774–7787.

[233] C. E. Hendricks, A. N. Mansour, D. A. Fuentevilla, G. H. Waller, J. K. Ko and M. G. Pecht, *J. Electrochem. Soc.*, 2020, **167**, 090501.

[234] Y. F. Yang, J. L. Yang, F. Pan and Y. Cui, *Chinese J. Struct. Chem.*, 2020, **39**, 16–19.

[235] M. Jo, S. Sim, J. Kim, P. Oh and Y. Son, *Nanomaterials*, 2022, **12**, 1956.

[236] Y. Xiong, H. Xing, Y. Fan, Y. Wei, J. Shang, Y. Chen and J. Yan, *RSC Advances*, 2021, **11**, 7801–7807.

[237] M. S. Al Ja'farawy, D. N. Hikmah, U. Riyadi, A. Purwanto and H. Widiyandari, *J. Electronic Mater.*, 2021, **50**, 6667–6687.

[238] M. Lavigne Philippot, D. Costa, G. Cardellini, L. De Sutter, J. Smekens, J. Van Mierlo and M. Messagie, *J. Energy Storage*, 2023, **60**, 106635.

[239] J. Van Mierlo, M. Berecibar, M. El Baghdadi, C. De Cauwer, M. Messagie, T. Coosemans, V. Jacobs and O. Hegazy, *World Electric Vehicle J.*, 2021, **12**, 20.

[240] P. Nzereogu, A. Omah, F. Ezema, E. Iwuoha and A. Nwanya, *Appl. Surface Sci. Adv.*, 2022, **9**, 100233.

[241] W. Ren, Z. Zhang, Y. Wang, Q. Tan, Z. Zhong and F. Su, *J. Mater. Chem. A*, 2015, **3**, 5859–5865.

[242] L. Sun, Y. Liu, R. Shao, J. Wu, R. Jiang and Z. Jin, *Energy Storage Mater.*, 2022, **46**, 482–502.

[243] B. Wang, X. Li, B. Luo, L. Hao, M. Zhou, X. Zhang, Z. Fan and L. Zhi, *Adv. Mater.*, 2015, **27**, 1526–1532.

[244] B. Hertzberg, A. Alexeev and G. Yushin, *J. Am. Chem. Soc*, 2010, **132**, 8548–8549.

[245] J. Yang, Y. Wang, W. Li, L. Wang, Y. Fan, W. Jiang, W. Luo, Y. Wang, B. Kong, C. Selomulya, H. K. Liu, S. X. Dou and D. Zhao, *Adv. Mater.*, 2017, **29**, 1700523.

[246] W. S. Chang, C. M. Park, J. H. Kim, Y. U. Kim, G. Jeong and H. J. Sohn, *Energy Environmental Sci.*, 2012, **5**, 6895.

[247] Q. Sun, B. Zhang and Z.-W. Fu, *Appl. Surface Sci.*, 2008, **254**, 3774–3779.

[248] Y. Han, X. Liu and Z. Lu, *Appl. Sci.*, 2018, **8**, 1245.

[249] B. Guo, J. Shu, Z. Wang, H. Yang, L. Shi, Y. Liu and L. Chen, *Electrochem. Commun.*, 2008, **10**, 1876–1878.

[250] J. Bałdyga, M. Jasińska, K. Jodko and P. Petelski, *Chem. Eng. Sci.*, 2012, **77**, 207–216.

[251] H. M. Lim, J. Lee, J. H. Jeong, S. G. Oh and S. H. Lee, *Eng.*, 2010, **02**, 998–1005.

[252] J. Entwistle, A. Rennie and S. Patwardhan, *J. Mater. Chem. A*, 2018, **6**, 18344–18356.

[253] I. de Meatza, I. Urdampilleta, I. Boyano, I. Castrillo, I. Landa-Medrano, S. Sananes-Israel, A. Eguia-Barrio and V. Palomares, *J. Electrochem. Soc.*, 2023, **170**, 010527.